UNIVERSITÀ
DEGLI STUDI
DI PADOVA

Università degli Studi di Padova
Dipartimento di Fisica e Astronomia “Galileo Galilei”

SCUOLA DI DOTTORATO DI RICERCA IN SCIENZA E INGEGNERIA DEI MATERIALI
CICLO XXVII

Development of an Optofluidic Platform in Lithium Niobate

Direttore della Scuola : Ch.mo Prof. Gaetano Granozzi

Supervisore: Prof. Cinzia Sada

Dottorando: Gianluca Pozza

Abstract

Optofluidics is a promising interdisciplinary research and technological field, thanks to its wide potential of application in sector like medicine, chemistry, biology and environmental science. In this context the study of innovative materials including their properties, their efficiency, their limits and their possibility of leading to miniaturized devices is the key point for the overcoming of currently adopted strategies. A promising material that could satisfy new optofluidic requirements is Lithium Niobate ($LiNbO_3$ - LN) thanks to its excellent optical and nonlinear optical properties.

In this work we demonstrated for the first time the applicability of the Lithium Niobate as a high intagrable and tailorable substrate for optofluidics. As a matter of fact, we developed all the several stages that can be interconnected to realize a platform with complex optofluidic functionalities: from the droplets generation and manipulation, to their transfer through a microfluidic channel directly engraved on the crystal substrate, to the droplets optical analysis stage.

In particular in this thesis we present the first high performant T-Junction droplet generator completely engraved in LN, and the first Ti in-diffused channel waveguide coupled with a microfluidic channel in the same substrate. Furthermore a study on the wetting properties of the Lithium Niobate is discussed.

Concerning the optical stage we discuss the realization of optical frequency converter realized in LN, which plays a key role in the development of our optofluidic platform. In fact it can be used to integrate a laser source in the green-blue range that could found application particularly in the biological field. Moreover we present the first frequency converter in the PPLN configuration realized in Zirconium doped LN, a dopants that prevent the optical damage and therefore could increase the intensity of work and the efficiency of conversion of the devices. Also we implemented the process to produce single-mode channel waveguide by Ti in-diffusion as interconnection stage for the optical circuit.

Concluding, we were able to implement a well-equipped tool-box for the incorporation of different devices on the same substrate, demonstrating for the first time the integration of all the different stages in a single substrate, and paving the way to an extreme optofluidic integration in Lithium Niobate.

Riassunto

L'optofluidica è un promettente settore di ricerca interdisciplinare con altrettante interessanti applicazioni tecnologiche. Questo grazie al suo ampio potenziale in settori quali la medicina, la chimica, la biologia e le scienze ambientali. In questo contesto uno studio di materiali innovativi che includa le loro proprietà, la loro efficienza, i loro limiti e la loro possibilità di produrre dispositivi miniaturizzati è fondamentale per superare le attuali strategie adottate. Un materiale promettente per soddisfare i requisiti dell'optofluidica è il Niobato di Litio (LN o $LiNbO_3$), un materiale conosciuto per le sue eccellenti proprietà ottiche lineari e non lineari e che qui discutiamo per la prima volta in un contesto optofluidico.

In questo lavoro abbiamo dimostrato l'applicabilità del Niobato di Litio come substrato altamente integrabile e adattabile per l'optofluidica. Abbiamo infatti sviluppato tutti i diversi stadi che possono essere interconnessi per realizzare una piattaforma con funzionalità complesse optofluidiche: dalla produzione di gocce, alla loro manipolazione, al loro trasporto in canali microfluidici realizzati nel cristallo, fino all'analisi ottica delle stesse. In particolare nella tesi sono presentati il primo generatore di gocce a giunzione a T completamente fabbricato su Niobato di Litio e la prima guida d'onda a canale in Titanio diffuso accoppiata con un canale. Infine abbiamo proposto il primo studio completo sulla bagnabilità del Niobato di Litio.

Per quanto riguarda lo stadio ottico, abbiamo realizzato dei convertitori di frequenza ottica, dispositivi che giocano un importante ruolo nel progetto, in quanto possono essere usati come sorgenti laser integrate con emissione nell'intervallo verde-blu, uno spettro che trova molte applicazioni nell'ambito biologico. In questo contesto abbiamo realizzato il primo convertitore di frequenza con configurazione PPLN realizzato su Niobato di Litio drogato Zirconio, un nuovo tipo di drogante che prevenendo il danno ottico è in grado di aumentare l'intensità di lavoro e l'efficienza di conversione di questi dispositivi. Abbiamo infine implementato il processo per produrre guide ottiche a canale monomodo per diffusione di Titanio, dispositivi necessari per connettere le diverse parti del circuito ottico.

In conclusione con questo lavoro abbiamo implementato un'ampia categoria di dispositivi, per la prima volta tutti contemporaneamente integrabili su un singolo substrato. Abbiamo perciò aperto la strada verso un'elevata integrazione di funzionalità optofluidiche su Niobato di Litio.

Contents

Chapter 3: Optical Stage

“Solo dopo aver conosciuto la superficie delle cose
- conclude-
ci si può spingere a cercare quel che c'è sotto.
Ma la superficie delle cose è inesauribile”
Italo Calvino – Palomar

Introduction

1. Optofluidic Platform in Lithium Niobate

1.1. Optofluidics

Optofluidics is a new analytical field based on the synergistic coupling of optics and microfluidics that provides a number of unique characteristics for enhancing the sensing performance and simplifying the design of microsystems. It is well known that optics has long been used to analyse biological and chemical samples. In recent decades, optical sensing systems have evolved to microdevices, such as on-chip waveguides and resonators in order to get greater compactness and efficient integration. This period has also seen the emergence of microfluidics, which enables small-volume sample handling for performing automated functions such as particle sorting and separation, cell culturing and concentration gradient formation. Optofluidics has found a broad range of applications since its debut about 10 years ago, as described by Erickson et al [1] and Schmidt and Hawkins [2], as well as in other recent publications [3]–[6]. In particular, optofluidics is well suited for biological/chemical detection and analysis in extremely small detection volumes (femtolitres to nanolitres) because it integrates sample preparation and delivery with the analytical mechanism. However, the majority of the optical functions demonstrated in microfluidic systems are not fully integrated since they use external micro-optical systems, or hybrid embedding of optical fibers, which, while providing much flexibility, do not offer the robustness, stability, operator-independence, and potential for mass manufacture of fully integrated approaches. Also integrated optics is widely used in biosensing and chemical sensing research, but there have been rather few demonstrations in true microfluidic systems. Until recently, most integrated optical circuits consisted of only one or two devices, but the field appears to be maturing with a drive for standardization of materials, devices and interfaces, allowing much denser integration. The confluence of integrated optics with integrated fluidics in the future ‘‘lab-on-a chip’’ (LoC) shows great potential [7], as LoC presents great benefits in terms of reagent and sample consumption; speed, precision, and automation of analysis; cost

and ease of use. With the result of a rapid escalation and adoption of microfluidic approaches. Many optical properties, such as refractive index, fluorescence, Raman scattering, absorption and polarization, can be exploited individually or in combination to generate the sensing signal. Detection can be carried out in either the linear [8]–[11] or nonlinear optical regime [12], [13]. More recently, the adaptation of traditional analytical chemistry technologies such as chromatography and electrophoresis to optofluidic devices further increases their functionality in biological/chemical analysis [14]–[18]. Furthermore, optofluidic microsystems can also employ optical forces as non-contact means for trapping, manipulation, and separation in microsystems; and moreover for driving pumps. Thus further enhances the system's analytical capabilities [19]. The use of light for ''optoporation'' of cells in microsystems has also been demonstrated [20]. Nonetheless, the full integration of optical functions within microfluidic chips is at the starting stage, and this work aims to highlight approaches and new application to materials (i.e. Lithium Niobate), which may contribute to further miniaturization and integration.

Many excellent reviews [3], [5], [6] describe various optofluidic architectures developed over the past years in different fields: microfluidics [21] for cell manipulation and analysis [22], μTAS (micro Total analysis systems) [23], optical manipulation [24], and optofluidic devices for non-chemical applications [3].

1.2. Opto-microfluidic in Lithium Niobate

Microfluidic technology holds great promise as it can perform typical laboratory applications using a fraction of the volume of reagents in significantly less time. Reagents can be significantly reduced from millilitres and microliters to nanolitres and femtolitres whereas hours of reaction time could be decreased to few seconds or less [25]. Applications for microfluidics have significantly advanced from its root in micro-analytical chemistry to include high throughput screening, biological analysis of cells and proteins and reaction kinetics and mechanism studies [26]. Due to the high surface area to volume ratios, the reaction times are faster and the independent control of each droplet can be exploited to realise micro-reactors that can be

individually transported, mixed and analysed. Thanks to its scalability and parallel processing, the droplets microfluidics has been used in a wide range of applications including the synthesis of biomolecules, drug delivery and diagnostic testing and bio-sensing [27][28]. Although novel micro-fabrication techniques are continuously being developed and micro-chemical systems are established by integrating micro-devices with appropriate fluidic interfacing scheme, the incorporation of chemical and physical sensors perfectly integrated with the micro-reactor stage is still under debate although the optical VIS-NIR methods are the most used to get quantification and chemical identification. The most commonly used materials for micro-reactors based device (such as ceramics, polymers, stainless steel, glasses, silica and silicon) in fact, seem to prevent the fully integration the microfluidic and optical functionalities in the VIS-NIR region although presenting bio- and micro-machining compatibility. As a matter of fact several examples of sensors for reaction temperature, residence time and stoichiometry have been reported [29] as well as systems for in-situ reaction monitoring with fluorescent measurements, with line ultraviolet spectroscopy, with inline infrared and Raman spectroscopy [26][30]. In this scenario, the integration of a large number of different stages on a single substrate chip is a key point for promoting new insights in many applications that need portable devices to speed the analysis and allow investigation of new phenomena [3][31]. Among the others, even Lithium Niobate crystals have been proposed in microfluidics since allows for high efficient acoustic waves generation able to move droplets on the substrate in a very controlled way [32], flow mixing and pumping [33], pyroelectric [34] and photogalvanic [35] particle trapping. Quite surprisingly, all the above mentioned applications were realized without producing a microfluidic circuit directly on $LiNbO_3$ substrates and without the integration of optical sensing stages although it is a material thoroughly exploited in the photonic and integrated optics industry. As a matter of fact waveguides and a large number of integrated electro-optical devices such as switches, modulators and directional couplers are still commercial in $LiNbO_3$ and diffractive optical elements such as holographic filters and multi/demultiplexers were proposed by exploiting its photorefractive effect strongly enhanced by local doping with metal impurities [36].

1.3. The project

The present project aims to combine the excellent properties and versatility of Lithium Niobate crystals and the powerful tools of the droplet-based microfluidics in order to realise an integrated microfluidics prototype on the same substrate with tailored functionalities and a high level of integration that has not been reported yet in literature. The platform include a stage for the droplets generation (every droplet could act as microreactor); an optofluidic junction in which every single droplet is analyzed by an optical probe (luminescence or IR/VIS absorption) in waveguides; a stage with a coherent light emitting source (realized with a frequency converter); and a spectral analysis stage realized with Bragg reticle (realized by a holographic or machining technique). The realization of the platform will allow the study in depth of the physics of the system, the characterization of the material both for its fluidic and optical properties, the improvement of the microfabrication techniques, and also to project an optical circuit for molecular sensing. Finally, the testing of the prototype will underline the potentiality of the Lithium Niobate as a multi-functional substrate for microfluidic, with the related applicative spillovers. Moreover the frequency converter that the project aims to realize represents the first stage for obtaining an integrated coherent light emitting source in an optofluidic platform working at high intensities and tailored wavelength. In particular the device prototype that the group intends to obtain is constituted by a periodic pattern of ferroelectric domains (PPLN) realized on a z-cut $LiNbO_3$ substrate in a waveguide configuration in order to assure a spatially confined frequency conversion. The proposed prototype could also be realized on substrates suitably doped in order to have an enhanced optical damage resistance in a waveguide configuration [37] and therefore a high conversion efficiency.

1.4. Objectives

The main objective of the project consists in the development of several interconnected stages that, starting from the droplet generation and manipulation, consider the droplets transfer through micro-channels to an integrated optical stage; where the optical properties of the droplets constituents are monitored and detected using the integrated laser source

(PPLN or Zr:PPLN), and analytical stages (photorefractive or nanofabricated gratings).

The project objectives concern:

1) The realization of a microfluidic circuit on lithium niobate crystals. T-junctions geometry is used in order to exploit the mixing properties of two different fluids to get droplets with controlled properties (size, shape and rates of production). The droplets act as micro-reactors and therefore contain reagents to study or detect;
2) The realization of an optical stage integrated on the same substrate to fine illuminate a given droplet and detect the optical signal therein generated. The pump signal is generated in a waveguide-based-frequency converter in the visible range. The optical signal detection is aimed to be spectral resolved in order to follow the reaction dynamics and select the reaction product.

The project therefore aims to demonstrate the feasibility of an opto-microfluidic circuit that conjugates portability, high efficiency and high integration, that up to now have not been reported yet on the same substrate. Finally it aims to open new perspectives on opto-microfluidics integration by increasing the number of integrable functionalities such as particle trapping (by the pyroelectric properties of $LiNbO_3$), droplets movement by the acoustic wave generation and micro-pumps integration (by exploiting the $LiNbO_3$ piezoelectric properties).

1.5. The Platform outline

The optimal configuration between the microfluidic device and the optical stage will be studied to allow the light coupling and detection. The prototype will be realized and tested on doped-water/oil system, where fluorescent molecules emitting at a selected wavelength (in the visible and in the NIR infrared spectral region) are dispersed and checking the change in the droplet constituents concentration by analysing the relative intensity of a selected emitted (luminescent/absorption) line.

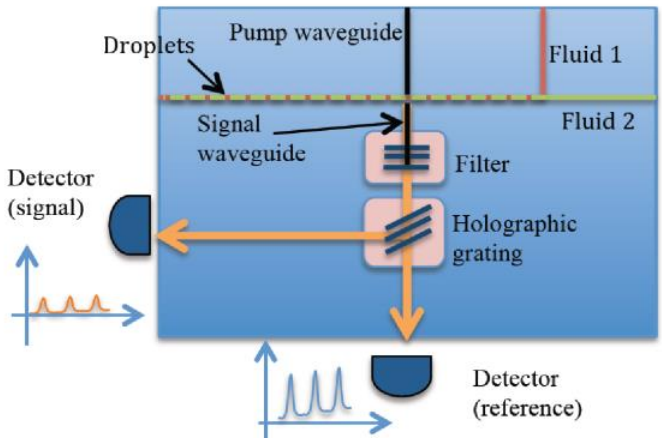

FIGURE 1 SCHEME OF AN OPTOFLUIDIC DEVICE INTEGRATED IN LITHIUM NIOBATE

1.5.1. Fluidic Stage

The project considers the realisation of microchannels of the typical size suitable for microfluidics applications (10^2 μm) in a T-junction configuration exploiting the interaction of immiscible fluids in order to form droplets. The system is designed in order to guarantee uniform droplets generation focusing on the fine control of the size, shape and monodispersion by altering the fluids flow rate and the surface energy between the liquids, for these purpose the variation of the concentration of a surfactant was studied. The circuit pattern is realized by a femtosecond laser ablation technique able to produce high quality structures with flat channel walls, a prerequisite to obtain an efficient coupling at the waveguide – liquid interface. The micromachining with a self-polishing saw was also explored in order to get flatter channel walls. A preliminary systematic study of the wetting properties of lithium niobate was required for a proper use of this material in microfluidics since in the literature these properties have not been investigated in details.

1.5.2. Optical Stage

The optical circuit is divided in three different parts:

The laser source, in which the nonlinear optical properties of Periodically Poled Lithium Niobate (PPLN) crystals, the Zirconium doping, and the waveguides fabrication are combined to obtain a waveguide-based-frequency converter in the visible range for an efficient Second Harmonic Generation

(SHG). The frequency generated is controlled by the period of the PPLN grating.

The channel-waveguide coupling stage, that is the more critical part of the project, where the droplets are illuminated and excited by the pump laser signal, and then the droplet emitted signal is collect and transferred to the analytical stage.

The analytical stage, where the optical signal emitted from the excited droplets is filtered and elaborated using gratings obtained with photorefractive effect or nanofabrication technique (such as Focused Ion Beam, FIB). The period grating will be optimized depending on the wavelength needed to be monitored in the micro-reactor.

The different stages are connected by optical waveguides defined by the photolithographic process and obtained by the standard Ti-indiffusion process.

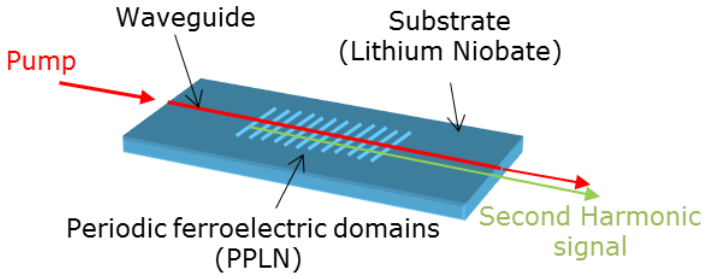

FIGURE 2 WAVEGUIDE-BASED FREQUENCY CONVERTER (QUASI PHASE-MATCHING SECOND HARMONIC GENERATION) IN LITHIUM NIOBATE

1.6. Results

At the conclusion of the thesis all the different devices and stages necessary to the realization of an optofluidic platform were fabricated and characterized, also first studies on light coupling in the waveguide/channel system were obtained in the final part of the thesis. In particular we achieved:

1) the realisation of a microfluidic circuit in lithium niobate crystals made of micro-channels and T-junctions with characteristic sizes of 100 μm and lengths up to a few centimetres;

2) the characterization of lithium niobate as a substrate for microfluidics applications, with particular detail on the surface/interface physics;
3) The realization of an optical stage in lithium niobate crystals. This stage requires the fabrication of PPLN frequency converter in congruent and Zr doped Lithium Niobate, optical waveguides, holographic grating, and Bragg grating integrated together.
4) The first characterization of the light transmission through the waveguide/channel junction;

The final step will concern the design and integration of the microfluidic stage and the optical stage to allow the realisation of an optofluidic circuit to analyse the droplets microreactors products.

1.7. Future Perspectives

The great versatility of the lithium niobate crystals allows the possibility of study the integration of new functionalities such as particle trapping (by the pyroelectric or the photorefractive properties of $LiNbO_3$), droplet movement by the acoustic wave generation and micro-pumps integration (by exploiting the $LiNbO_3$ piezoelectric properties). The application of these opto-microfluidic circuits in biology has a strong impact especially if one considers the need of integrated optical detection of signals for example of blood constituents: due to the coagulation, in fact, many analysis are hardly performed and need post-chemical action of the blood. The exploitation of microfluidics and the droplets technique, instead, will prevent the blood coagulation while the integration of an optical stage can allow the in-situ analysis with rapid response and no need of chemical treatment. This is only an application, similar results can be obtained in a full integrated circuit in agro-alimentary problems for detecting bacteria, in the direct optical detection in bio-analysis [38] or for obtaining optical sensor chip for medical point of care and in many other applications of interest in pharmaceutical and chemical analysis [26] such as photo-initiated and catalyst initiated polymerization, therapeutic agent delivery, biomolecule synthesis, diagnostic chips, and drug discovery [25] actually performed in hybrid circuit where the microfluidic circuit is

coupled with external stages (optical stage, pumps, particle trapping systems).

Apart from the integration of a tailored laser source in an optofluidic platform the project also presents several future developments concerning the realisation of a visible light emitting source with a tailored wavelength depending on the realised periodic pattern of the PPLN structure and the combination of this pattern with a waveguide configuration allow for the development of many different optical devices. Several examples of PPLN based devices have already been demonstrated as efficient visible coherent sources with application in the biomedical, industrial, spectroscopic, and telecom fields. The possibility of improving the photorefractive resistance of such a system would allow extending the range of the available SH powers. Moreover the waveguide geometry allows for a more compact and stable packaging. Therefore, as a first general future development we have the potential extension of the already present application of PPLN based devices to higher operating power and more compact devices. A potential approach consists in realizing more sophisticated domain structures, where several periodicities are simultaneously present. This would allow more complicated nonlinear process, enabling the simultaneous conversion of a suitable pump beam into several signals at different wavelengths in the visible; this is of great interest for the realization of a more complex optical analysis in optofluidic device or for the integration of RGB laser sources to be used in the next generation of laser displays or mobile projectors. A very interesting application is represented by the integration of these sources in a monolithic Mach Zehnder interferometer [39], which was recently proposed as a very promising configuration for space applications, such as DOAS spectroscopy for space application and can result very promising for medical and biomedical field. More sophisticated applications take advantage of the possibility of design the PPLN system to enable a QPM frequency halving process; this is of interest for the realization of brilliant correlated photon sources, of great interest for quantum computing and cryptography.

1.8. Acknowledgement:

We kindly acknowledge the Ca.Ri.Pa.Ro foundation for financing the research by the Excellence Projects “Integrated opto-microfluidic prototype on lithium niobate crystals for sensing applications” (call 2011-2012), and “Integrated visible frequency converter based on doped periodically poled lithium niobate crystals with enhanced optical damage resistance” (call 2008-2009).

And the COST action MP1205 “Advances in Optofluidics: Integration of Optical Control and Photonics with Microfluidics”.

2. Lithium Niobate

2.1. Introduction

In this section Lithium Niobate properties will be described with special care to its structure, its manipulation process, the behavior of ferroelectric domains, and the role of dopants and defects respectively. The knowledge of the material used for the platform is important to understand the reasons of its choice, and moreover to explain the problems and solutions we met in its handling.

In the field of integrated optics Lithium Niobate ($LiNbO_3$) is a well-known ferroelectric crystal thanks to its good optical and structural properties, which make it a suitable material for realizing different optical components, such as light waveguides, holographic wavelength filters, Second Harmonic generators and so on [40]–[44]. Consequently, lithium niobate is surely a promising candidate for applications also in the field of Optofluidics, a research area which aims to integrate all typical lab processing [42] on a single device, by combining the potentialities offered by optics and the tools typical of microfluidics [45]. Indeed, the passive materials most commonly used in microfluidics, like poly-dimethilsiloxane (PDMS) or elastomers, require the use of external equipment or the combination with various materials in order to realize the desired stages for droplet movement and optical analysis. As a matter of fact, often mechanical parts as well as external metallic electrodes have to be implemented in microfluidic devices to characterize droplets or actuate them, thus making these conventional methods less flexible and efficient than those exploiting optical approaches. Therefore, the capability to realized a microfluidic device in a material like $LiNbO_3$, where different optical stages can be easily implemented, represents a key point for promoting new insights in many applications [3][31]. As a matter of fact, lithium niobate has been also proposed for microfluidic applications, since it is easily bondable to polymeric materials and allows for creating micro-pumps, by exploiting its piezoelectric properties or by realizing high efficient surface acoustic waves (SAW) generators [32], [46]. Moreover, in the last years trapping experiments have been successfully performed at

the surface of lithium niobate crystals on droplets and particles dissolved in oils [43], [47]–[49], by exploiting the excellent photovoltaic properties of this material, thus paving the way for its use also in the microfluidic field based on optically-driven manipulation phenomena.

In this section Lithium Niobate structure, properties, and synthesis are discussed in order to introduce the reader to the lithium niobate fields and to the main features that are useful to know to understand the following chapters.

2.2. Lithium Niobate

Lithium niobate (LN, $LiNbO_3$) is a synthetic dielectric material which does not exist in nature. It is a ferroelectric trigonal crystal first synthesized and described in 1928 by Zachariasen [50] and since the sixties – when for the first time large and homogeneous crystals were grown using the Czochralski technique [51], [52] – it has found growing interest and applications with thousands of publications in very different fields and tons of crystals grown every year for optical and acoustical applications. It has excellent optical, mechanical, and physical properties as wide transparency range; birefringence; high piezoelectric, pyroelectric, electro-optical, and nonlinear optical coefficients; photovoltaic and photorefractive behaviour; chemical and mechanical stability; photo-acoustic properties; insolubility in water or organic solvents; and high melting point. A number of review [53] have been published about LN properties and processing. A detailed review of physical and chemical of lithium niobate has been given by Rauber 1978 [54], also the physical, chemical, structural and optical properties were systematizes by Prokhorov and Kuz'minov [55]. $LiNbO_3$ crystals are well known for their low acoustic losses and so are used as excellent substrate for surface acoustic wave devices. Furthermore, important applications are based on the electro-optic, nonlinear optical, piezoelectric, and pyroelectric properties with high coefficients for specific effects and devices (optical amplitude modulators, optical phase modulators, second-harmonic generators, Q-switches, beam deflectors, phase conjugators, dielectric waveguides, memory elements, holographic data processing devices, and others) [53]. For the optical stage of the project we are interested to the nonlinear optical properties for the

frequency converter, and in the waveguides fabrication using ion in-diffusion [50]. Instead for what regards the fluidic properties, at the best of our knowledge, systematic studied have not been done yet. In this field only works on surface-acoustic device and properties are particular developed and also interesting for future micro-pump application in our platform [32], but are beyond the aims of this work.

2.2.1. Crystal growth

FIGURE 3 A BOULE OF LITHIUM NIOBATE GROWN BY CZOCHRALSKI TECHNIQUE

The LN crystals are usually prepared by the standard Czochralski (CZ) technique, i.e. crystals are obtained from the solidification at the interface between the solid and liquid phase. In this project the crystal that were used are both commercial and home-growth using a CZ furnace installed at the Padova Physics Department, which allowed also doping the material with different kind of dopants and different concentration. The first step of CZ method is the preparation of the starting material: a mixture of pure $LiNbO_3$ powders with congruent composition and, if necessary, the chosen dopant concentration are put in a platinum crucible and heated above its melting temperature for some hours, in order to achieve good melt homogeneity, then cooled slowly to the growth temperature. A pure LN crystal seed (typical dimension 4mm x 4mm x 3cm) is then slowly approached to the liquid surface, in order to avoid large temperature gradients. When the seed come into contact with the liquid, the temperature is finely tuned to equilibrium (i.e. no mass variations in the crucible). Only after equilibrium is reached, the pulling process can start: the seed is lifted out from the melt, kept in rotation to compensate the convective currents within the melt and favour the melt homogenization. In the first stage of the growth the mass variation is

controlled so that the growing crystal diameter increases linearly with time giving the so called crystal shoulder. When the crystal diameter increases up to the desired value (in our case 1 inch), the growth parameters are fixed so that a constant mass variation is maintained in time. When the liquid is nearly finished, the crystal is detached and the growth chamber is cooled down till the freezing of the melt. At this point the crystal is lowered again, in order to touch the solidified melt and create an electrical contact: the poling of the boule is then performed by applying a constant current of some tenth of mA to the crystal crucible system inside the growth furnace while cooling it down to room temperature. The result of this process is the creation of a single domain crystal boule. The whole system will be kept at controlled temperature, and feedback methods are provided in order to maintain good quality and uniformity. In fact, constant rotation and pulling speed are maintained during the growth process, while monitoring the growth speed (in practice the crystal diameter) through a balance. It is worth mentioning that if a growth process is performed from a melt with non-congruent composition (look at section 2.2.2), the different composition of the crystal causes a progressive variation in the lithium content of the liquid phase, and the composition of the crystal itself. Particular care need to be therefore devoted to test the homogeneity distribution of the dopant within the crystal in order to get homogeneous crystals. The process is optimized varying systematically and with a very fine tune the growth parameters such as the pulling rate (1-12 mm/h), the rotational rate (5-30 rounds per minute), the crystallographic growth axis and the dopant concentration in order to obtain high reproducibility and high homogeneity along the crystal. Particular care is be also devoted to obtain crystal with very low dislocation and defect densities and post annealing treatments in controlled atmosphere are performed to reduce the possible presence of colour centers and residual stresses and assure that the sample is well oxidized, a condition necessary to achieve a good resistance against optical damage (i.e. photorefractivity). The poled crystals are then oriented by X-Rays methods, cut and polished to obtain mono-domain slices of optical quality.

2.2.2. Composition

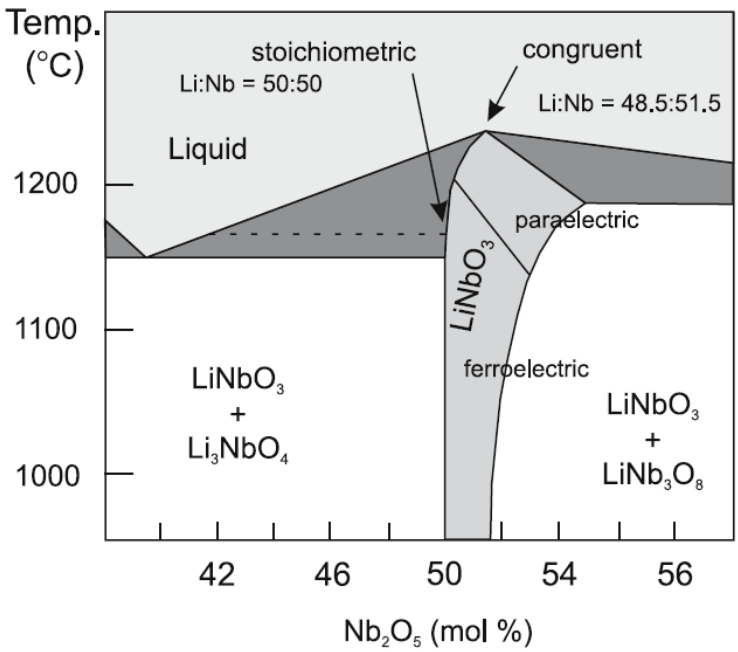

FIGURE 4 . PHASE DIAGRAM LITHIUM NIOBATE [36]

Lithium niobate is one of the four compounds of the pseudo-binary system $Li_2O–Nb_2O_5$, besides $Li_2Nb_{28}O_{71}$, Li_3NbO4 and the lithium triniobate $LiNb_3O_8$, and it is colorless and insoluble in water and organic solvents. The phase diagram of the $Li_2O–Nb_2O_5$ system (Figure 4), reveals a maximum of the liquidus-solidus curve at approximately 48.45% Li_2O (congruent composition), whereas for 50% Li_2O (stoichiometric composition) no singularity exists. Lithium Niobate crystals grown by Czochralski technique have a congruently melting composition which has an Li deficiency of about 1.5% compared to the stoichiometric one [36]. In this congruent point the melt and the growing crystal have the same composition, so crystals grown in this conditions show the highest bulk uniformity. Several physical and optical properties strongly depend on the concentration of lithium and niobium ratio, like the phase transition temperature, birefringence, the photovoltaic effect, phase-matching temperature, and UV band edge [36]. The high sensitivity of these properties to a non-uniform composition of crystals is the reason for the preference of congruent $LiNbO_3$ in optical applications, this because it easier to grown homogeneous congruent crystals compared to the stoichiometric one. Therefore commercial $LiNbO_3$ are usually congruent crystals grown by Czochralski technique (section 2.2.1).

2.2.3. Structure

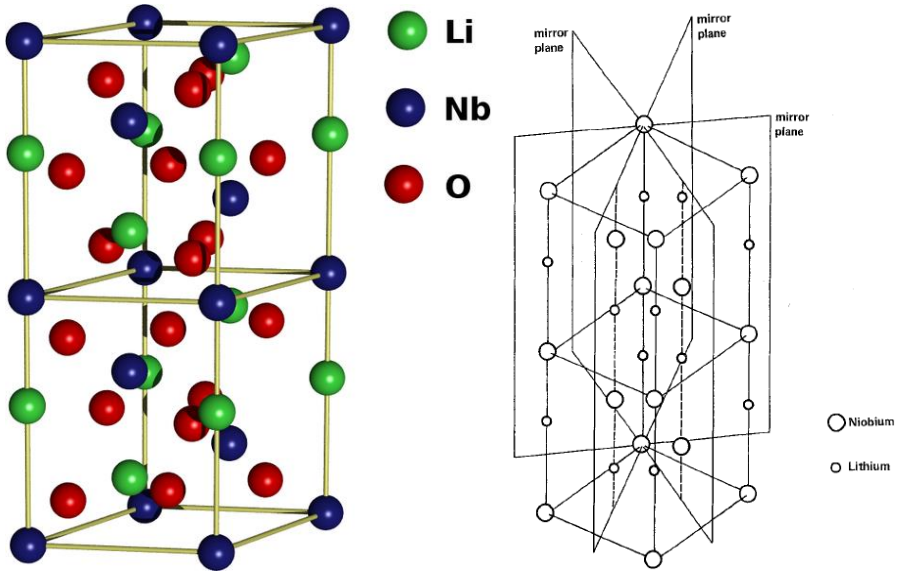

FIGURE 5 (LEFT) REPRESENTATION OF LITHIUM NIOBATE CELL; (RIGHT) MIRROR PLANES OF THE LN CELL [50]

$LiNbo_3$ belong to the ABO_3-type ferroelectric [36], its structure, at temperatures below the ferroelectric Curie temperature (1142.3 ±0.7°C for congruent crystal [56], is a distorted hexagonal close-packed configuration of oxygen atoms, which has the octahedral sites filled one third by lithium atoms, one third by niobium atoms, and one third with vacancies. Along the principal axis direction (c) the atoms occur in the following order: Nb, vacancy, Li, Nb, vacancy, Li [53]. In the paraelectric phase, above Curie's temperature, the primitive cell does not present a dipole because Lithium ions lie in the oxygen layer and Niobium ions are centered between oxygen layers. Under the critical temperature elastic forces of the crystal become dominant and constrain lithium and niobium ions into polar new positions. This shift of ions relative to the oxygen octahedral is the cause of the spontaneous polarization of Lithium Niobate that at T of about 25°C is 0,71 C/m^2. The ferroelectric phase's cell is member of the trigonal system crystal, in fact it exhibits three-fold rotation symmetry about its c axis. Moreover, it shows three mirror symmetry planes that are 60° apart and intersect forming a three-fold rotation axis. These two symmetry operations classify $LiNbO_3$ belonging to the 3m point group (C6v in Schtnflies notation) [53], and

furthermore it is member of the R3c space group [57]. In the paraelectric phase the crystal transforms to the centrosymmetric space group R3m [36].

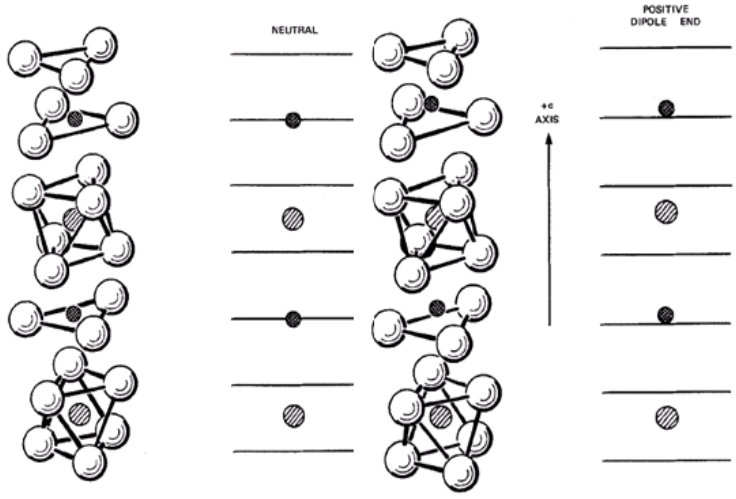

FIGURE 6 ON THE LEFT IS RAPPRESENTED THE PARAELECTRIC PHASE OF LITHIUM NIOBATE; ON THE RIGHT THE FEROELECTRICT PHASE [53]

In the trigonal system the setting of the crystallographic axes is not unambiguous, three different cells can be chosen: hexagonal, rhombohedral or orthohexagonal [36]. For most applications the orthohexagonal cell is preferred, and tensor components of properties are given respecting these axes. In this case the three axes are mutually orthogonal and their directions are settled in the following way. The threefold axis is z, the axis y lies in the mirror plane, and the axis x is orthogonal to both of them. Piezoelectric and spontaneous polarization are properties of only z and y axes, and by convention their positive ends correspond to the plane negative charged under a uniaxial compression. Moreover, the z axis is also pyroelectric and by convention its positive end corresponds to the plane negative charged on heating the crystal. The x axis in this setting is non-polar. Experimentally it is easy to find the y axis in usual congruent crystals grown by the Czochralski technique along the polar axis z (0°-crystals), because the mirror planes correspond on the cylindrical boule surface as three facets aligned along the growth axis oriented mutually by exactly 120°, y axis connect the boule axis to the facets.

2.2.4. Intrinsic Defect

As explained, in the polar phase structure the octahedral interstitials are one-third filled by Li ions, one-third by Nb ions and one-third are empty (vacancy). The Li octahedron is larger, than the Nb one, the distances between a Li ion and the closest oxygen ions are 206.8 and 211.2 pm, whereas those for an Nb ion are 188.9 and 211.2 pm, respectively [57]. A larger size of the Li octahedron may qualitatively explain a predominant incorporation of impurity ions onto Li sites. As seen from the phase diagram (Figure 4), the congruently melting (Li-deficient) composition corresponds to the oxide concentrations 48.45 mol.% Li_2O and 51.55 mol. % Nb_2O_5 with the ratio [Li]/[Nb] = 0.94. Correspondingly, the congruent $LiNbO_3$ (denoted often as CLN) contains about 6% empty Li sites in the lattice. Therefore $LiNbO_3$ is to some extent a unique oxide containing no oxygen vacancies. Further experimental studies have shown that with decreasing Li_2O content, i.e., increasing concentration of V_{Li}, the density of $LiNbO_3$ increases [58]. To overcome this paradox, it is assumed that Nb ions incorporate partially on the Li sites [36]. This is very probable, because an Nb^{5+} ion has a smaller ion radius than Li^+. Therefore, the Li-deficient crystal may be formally explained with a Nb surplus, or, in other words, a decreasing Li content is accompanied by an increasing content of the heavier Nb. The existence of such a stacking fault, Nb on a Li site, Nb antisite was repeatedly proved by structure studies, which formed the basis for defect models in $LiNbO_3$. According to precise data of X-ray and neutron diffraction only 1% of the Li sites are occupied by Nb, whereas about 4% of the Li sites are empty (Li vacancies) [36]. These data supported the Li site vacancy model in which an Nb antisite is compensated by four V'_{Li}, in this model a congruent LiNbO3 is described as

$$\{[\mathrm{Li}]_{1-5x}[\mathrm{Nb_{Li}}]_x[\mathrm{V_{Li}}]_{4x}\}[\mathrm{Nb_{Nb}}]\mathrm{O_3}$$

where the group in the braces corresponds to the population of the Li sites. Nowadays, the Li site vacancy model is commonly accepted as valid and considerations of all defect reconstructions in $LiNbO_3$ are discussed in its framework.

2.3. Properties

In this section general properties of lithium niobate are presented to give a basic summary of the characteristic of the crystal. We give particular attention for the non-linear optical phenomena that occur in the material, such as the second harmonic generation and the photorefractive effect. Principal characteristics of Lithium Niobate are presented in the following table.

Property	
Congruent composition[56]	48.38 mol.% Li_2O
Congruent melting point[56]	1250°C
Curie temperature [56]	1142,3 ± 0,7 °C
Point group [56]	3m
Space group[56]	R3c
Lattice constants (hexagonal) [56]	a_H= 5,151 Å; c_H=13,866 Å
Density[56]	4,65 g/cm^3
Dielectric constants[56] (at 25°C)	Unclumped ε_{11}=85; ε_{33}=28,7 Clumped ε_{11}=44; ε_{33}=27,9
Spontaneous polarization[56]	71 μC cm^{-2}
Pyroelectric coefficient (25°C)[36]	-8,3x10^{-5} C/°Cm^2
Piezoelectric strain coefficients[56] (at 25° x 10^{-12}C/N)	d_{15}=69,2; d_{31}=-0,85; d_{22}=20,8; d_{33}=6,0

TABLE 1. PHYSICAL, CHEMICAL, AND ELECTRICAL PROPERTIES OF LITHIUM NIOBATE

2.3.1. Pyroelectric effect

Lithium niobate is a pyroelectric solid which exhibits a change in the spontaneous polarization as a function of the temperature. The relation between the change in temperature (ΔT) and the change in the spontaneous polarization (ΔP) is linear and can be written as $\Delta P = \boldsymbol{p}\Delta T$, where $\boldsymbol{p}$ is the pyroelectric tensor. In lithium niobate this effect is due to the movement of Li and Nb ions relative to the oxygen planes and, since they move only in the direction parallel to the c-axis, the pyroelectric tensor has the form

$$\boldsymbol{p} = \begin{bmatrix} \mathbf{0} \\ \mathbf{0} \\ \boldsymbol{p_3} \end{bmatrix}$$

EQUATION 1

where p_3 =-8,3 x 10^{-5} C/m^{2}K [53] and the negative sign indicates that upon cooling the +c crystal face will become positively charge.

Pyroelectricity in Lithium Niobate could be used to manipulate or dispense liquid at microscale or nanoscale, compared to conventional electro-wetting devices, the pyroelectric effect allowed to have an electrode-less and circuit-less configuration [34], [59]–[61].

2.3.2. Piezoelectricity

A piezoelectric crystal is a solid that exhibits an induced polarization when a mechanical stress is applied. The relationship between polarization and stress is linear and may be written as

$$P_i = \sum_{j,k} d_{i,j,k}\, \sigma_{j,k}$$

EQUATION 2

where the vector P_i is the induced polarization, $\sigma_{j,k}$ is the second-rank stress tensor, and $\sigma_{j,k}$ is the third-rank piezoelectric tensor. Since the lithium niobate is a 3m point group symmetry crystal, all tensors describing the physical properties of lithium niobate must have at least that symmetry (Neumann's principle). The application of Neumann's principle to the $\sigma_{j,k}$ tensor followed by the use of the reduced-subscript notation gives

$$d_{i,j,k} = \begin{bmatrix} 0 & 0 & 0 & 0 & d_{15} & -2d_{22} \\ -d_{22} & d_{22} & 0 & d_{15} & 0 & 0 \\ d_{31} & d_{31} & d_{33} & & 0 & 0 \end{bmatrix}$$

EQUATION 3

Note that $d_{15}=d_{24}$, $d_{22}=-d_{21}=(-d_{16})/2$, and $d_{31}=d_{32}$. So we can describe the piezoelectric effect with four independent coefficients d_{15}, d_{22}, d_{31}, and d_{33} [53]. Measured values for these quantities are presented in Table 1.

A piezoelectric crystal also exhibits a strain under the application of an electric field. This is called the converse piezoelectric effect. It can be shown that the coefficients connecting the induced strain and the applied electric field are identical to those connecting the induced polarization and the applied stress in the direct piezoelectric effect [62]. The converse piezoelectric effect is expressed as

$$S_{i,k} = \sum_{i} d_{i,j,k}\, E_i$$

EQUATION 4

where $S_{i,k}$ is the second-rank strain tensor.

2.3.3. Permittivity and refractive indices

The relationship between the electric displacement **D** and the electric field **E** is linear and can be written as $\mathbf{D}=\hat{\varepsilon}\mathbf{E}$, where $\hat{\varepsilon}$ is the second-rank permittivity tensor. Due to the crystallographic structure and the symmetry properties of lithium niobate, its permittivity tensor, in the orthohexagonal cell, can be represented by a 3 x 3 matrix with the form

$$\hat{\varepsilon} = \begin{bmatrix} \varepsilon_{11} & 0 & 0 \\ 0 & \varepsilon_{22} & 0 \\ 0 & 0 & \varepsilon_{33} \end{bmatrix}$$

EQUATION 5

where it is notable that only the diagonal elements are not-zero and that the permittivity has the same value for any electric direction perpendicular to the c-axis. Permittivity is often given in terms of the permittivity of the vacuum (ε_0), obtaining the so called relative permittivity or dielectric constant (ε_r), whose values are reported in Table 1. At optical frequencies the permittivity of a material is usually described in terms of its refractive index. In particular the lithium niobate presents two refractive indices, an extraordinary one (n_e) and an ordinary one (n_o), which refer respectively to the z axis and to the x and y axes of the crystal. The dependence of the refractive indices on the temperature, the light wavelength and the composition of the material is taken into account in the relation proposed by Schlarb and Betzeler in their

paper [63], where the Sellmeier equations (Equation 6) are further generalized. In particular the Schlarb's approach is valid not only for pure $LiNbO_3$ crystals, but also in the case of doping with optical damage-resistant ions, allowing exploiting the refractive indices as a sensitive method to determine the composition of the material.

$$n^2 = A_1 + \frac{A_2 + B_1 F}{\lambda^2 - (A_3 + B_2)^2} + B_3 F - A_4 \lambda^2$$

EQUATION 6

Where n is the refractive index, λ is the wavelength in vacuum in nm, A_x and B_y are experimentally determined coefficients and F is a factor depending on temperature expresses in °C.

$$F = (T - 24.5)(T + 570.5)$$

EQUATION 7

The crystal is transparent between 320 nm and 5000 nm (Figure 7).

Parameter of Sellmeier	n_e	n_o
A_1	4,582	4,9048
A_2	9,921 x 10^4	1,1775 x 10^5
A_3	2,109 x 10^2	2,1802 x 10^2
A_4	2,194 x10^{-8}	2,7153 x 10^{-8}
B_1	5,2716 x 10^{-2}	2,2314 x 10^{-2}
B_2	-4,9142 x 10^{-5}	-2,9671 x 10^{-5}
B_3	2,2971 x10^{-7}	2,1429 x 10^{-8}

TABLE 2. PARAMETERS OF SELLMEIER FOR LITHIUM NIOBATE [56]

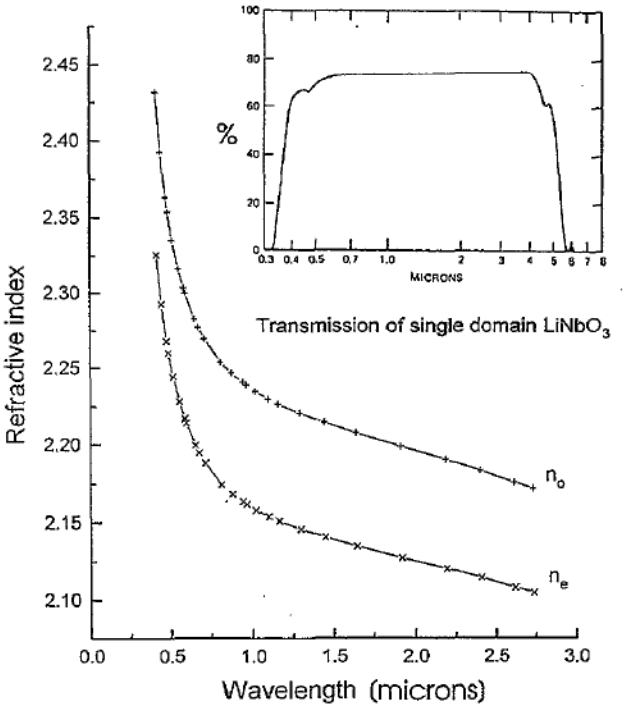

FIGURE 7 REFRACTIVE INDEX AND TRANSMITTANCE (%) OF LITHIUM NIOBATE [64]

2.3.4. Second Harmonic Generation

Second-Harmonic Generation (SHG) could be seen like a quantum-mechanical process in which the contemporary interaction of two photons of frequency ω causes the creation of a single photon of frequency 2ω (Figure 8). This process, in appropriate conditions, could be so efficient to completely convert an incident radiation to its second harmonic. One of the most used applications of SHG is converting the Nd:YAG radiation at λ =1.064 μm to 532 nm.

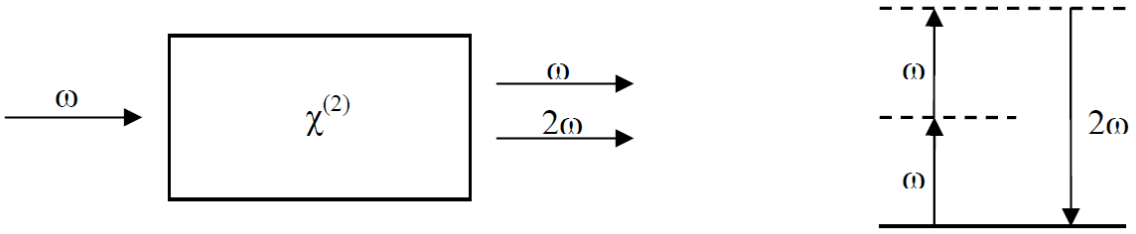

FIGURE 8 SCHEMATIC EXPLANATION OF SECOND HARMONIC GENERATION

SHG is a parametric phenomenon, this means that there is not any variation of quantum-state of our system during the transition between initial and final states. So no energy exchange occurs between incident radiation and

material. Therefore, crystal functions like a "catalyst" that permits Energy Exchange from a mode to another without absorption.

Property	pm V^{-1}
Non-linear-optical coeff. (at 1,06 μm) [36]	d_{33}=34; d_{31}=6; d_{22}=3

TABLE 3. NON-LINEAR OPTICAL COEFFICIENTS OF LITHIUM NIOBATE

For intense fields the simple relation $P = \varepsilon_0 \chi E$ is no longer valid and several contributions have to be taken into account to work out the induced polarization P of the material. Effectively we must use the expanded form

$$P(r,t) = \varepsilon_0 \sum_i \overline{\chi_\iota} E^i(r,t) = \sum_i P_i\,(r,t)$$

EQUATION 8

And it is important to note that the susceptibility is a tensor of i^{th} rank. Therefore, if the term $\varepsilon_0 \chi_2 E^2$ is sufficiently large, then the fundamental wave generates a second harmonic. The scale of the nonlinearities is controlled by the crystal structure and the polarization of the incoming light, in fact second order phenomena like SHG and electro-optic effect (Pockels) occur only in crystal without the inversion center. We can quantify the SHG performance for a particular material or crystal orientation by introducing the nonlinear coefficients $d_{ijk} = \chi_{ij}/2$ to obtain:

$$\begin{bmatrix} P_x(2\omega) \\ P_Y(2\omega) \\ P_Z(2\omega) \end{bmatrix} = \begin{bmatrix} 0 & 0 & 0 & 0 & d_{31} & -d_{22} \\ -d_{22} & d_{22} & 0 & d_{33} & 0 & 0 \\ d_{31} & d_{31} & d_{33} & & 0 & 0 \end{bmatrix} \cdot$$

$$\cdot \begin{bmatrix} E_x^2(\omega) & E_y^2(\omega) & E_z^2(\omega) & 2E_y(\omega)E_z(\omega) & 2E_x(\omega)E_z(\omega) & 2E_x(\omega)E_y(\omega) \end{bmatrix}$$

EQUATION 9

With the matrix simplified by symmetry, in this case by Lithium Niobate symmetry (Neumann's principle). The sign of the nonlinear coefficient determines the sense of the polarization and the overall efficiency of such harmonic generation is given [64] as

$$\eta = \frac{P_{2\omega}}{P_{\omega}} = 2\left(\frac{\mu}{\varepsilon_0}\right)^{\frac{3}{2}} \frac{\omega^2 d^2 l^2}{n(\omega)^2 n(2\omega)} \frac{\sin^2(\Delta k l/2)}{(\Delta k l/2)} \frac{P_{\omega}}{A}$$

EQUATION 10

$$\Delta k = k_{2\omega} - 2k_{\omega}$$

EQUATION 11

where P_{ω} and $P_{2\omega}$, are the fundamental and the SH powers respectively, d the nonlinear coefficient, l the interaction length, n the refractive index, k the wavevector of the fundamental in the medium, and A the cross sectional area of the pump beam. The efficiency expression emphasizes that ideally Δk=0, which can only occur if

$$2k(\omega) = k(2\omega) \rightarrow n_{2\omega} = n_{\omega} \text{ (Phase Matching)}$$

EQUATION 12

A failure in minimizing Δk means that there will be destructive interference between wavelengths generated at different points in the crystal. Thus, there is a spatial coherence length given by

$$l_c = \frac{2\pi}{\Delta k} = \frac{\lambda}{4(n_{2\omega} - n_{\omega})}$$

EQUATION 13

To achieve the phase Matching condition (Equation 12), in a non-linear crystal such as $LiNb0_3$ the natural birefringence could be used to equate the n_e and n_o indices for two polarizations of light, whose wavelengths differ by a factor of two. In the case of lithium niobate this condition occurs at a pump wavelength of 1100 nm (Figure 7). For negatively birefringent crystals ($n_o > n_e$) the use of a pure ordinary wave for the pump is called type I phase matching. Where the incident wave is a combination of ordinary and extraordinary polarizations, the phase matching is called type II. However, if the incident wave is inclined at an angle relative to the primary optic axis of the crystal then the birefringence can be reduced, and hence phase matching achieved, at longer wavelengths. Practically, phase matching can be achieved if one rotates the crystal so that, using the index variation, the direction of propagation of the pump wave is at the correct angle with respect to the

optic axis. Another way to achieve phase matching is to use the temperature dependence of the refractive index. The temperature-dependencies of the refractive index are given by the Sellmeier equations (Equation 6). However in the next section a better method to achieve SHG for every frequency desired is discussed.

Quasi-Phase Matching

As previously discussed, when the wave-vector mismatch Δk between the pump and the generated waves is zero, the interaction is phasematched and the generated intensity grows quadratically as the waves propagate through the crystal. This condition is however difficult to be reached although exploiting the birefringence and temperature/angle tuning [65]. On the other hand, if Δk is not zero due to the material optical dispersion, the fundamental and the SH waves travel with different velocity: in particular, the coherence length l_c is the distance for which the fundamental waves and the generated waves build a phase difference of π and the newly generated SH waves interfere destructively with the present ones (Figure 9). If the interaction is not phasematched, the second harmonic intensity oscillates between zero and a very limited value along the sample, with a period equal to two times the coherence length. The maximum power obtainable is therefore quite small, independently of the converter length. The quasi-phasematching (QPM) is an alternative approach to conventional methods, that does not require Δk=0 and allows to access the highest components of the nonlinear optical tensor. It is most commonly implemented by periodically reversing the sign of the nonlinear coefficient with a period matching an even multiple of coherence lengths. In this way at each domain, the newly SH waves sum up constructively with those already present so that the SH intensity grows monotonically along the sample. In ferroelectric crystals such as Lithium Niobate, this task can be achieved by periodically inverting the spontaneous polarization of the material therefore creating a regular grating of ferroelectric domains. This procedure gives the so-called Periodically Poled Lithium Niobate (PPLN) crystals: the maximum efficiency is obtained for the first QPM order i.e. using a grating pattern having a period of 2lc. That in our case, for a frequency conversion between 1064 nm and 532 nm at room temperature is equal to 6,8 μm.

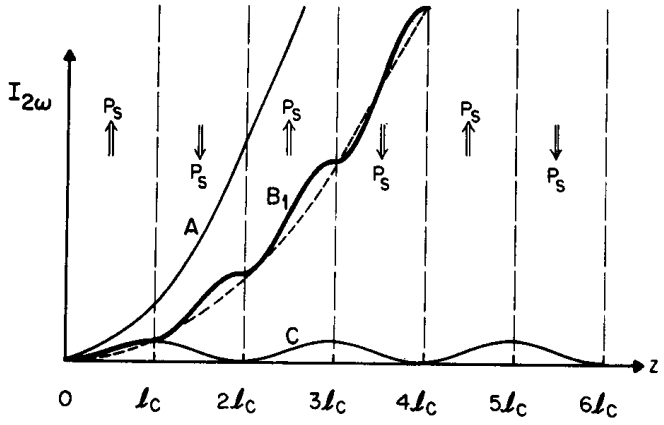

FIGURE 9 GRAPHIC OF THE INTENSITIES OF THE SECOND HARMONIC SIGNAL IN CONDITION OF PHASE MATCHING (QUADRATIC GROWTH), OUT FROM THE PHASE MATCHING (SINUSOIDAL BEHAVIOR) AND QUASI-PHASE MATCHING (INTERMEDIATE BEHAVIOR), WHERE L_c IS THE COHERENCE LENGTH

A significant advantage of quasi-phase matching is that any interaction within the transparency range of the material can be quasi-phase matched at a specific temperature, even interactions for which birefringent phase matching is impossible. Another benefit is that the interacting waves can be chosen so that coupling occurs through the largest element of the second rank tensor. In $LiNbO_3$, quasi-phase matching with all waves polarized parallel to the z axis yields a gain enhancement over the birefringent phase-matched process of $(2d_{33}/\pi d_{31})^2 \approx 20$ [66]. Quasi-phase matching is a useful technique for extending the range of available nonlinear optical materials. Using planar processing methods from the microelectronics industry, such as lithography, one can inexpensively fabricate practical microstructured materials for QPM interactions. The ability to pattern QPM structures allows the nonlinear material to be engineered for the desired interaction.

The condition of quasi-phase matching become [67]

$$\Delta k = k_{2\omega} - 2k_{\omega} - K_m$$

EQUATION 14

$$K_m = \frac{2\pi m}{\Lambda}$$

EQUATION 15

Where K_m is the grating wave vector, Λ is the period of the grating, and m is the QPM order. Therefore to calculate the period of the grating for a certain wavelength we have

$$\Lambda_n = m\Lambda = 2ml_c = \frac{m\lambda}{2(n_{2\omega} - n_{\omega})}$$

EQUATION 16

And the efficiency of the QPM-SHG will be [64]

$$\eta = \frac{P_{2\omega}}{P_{\omega}} = 2\left(\frac{\mu_0}{\varepsilon_0}\right)^{\frac{3}{2}} \frac{\omega^2 d_{eff}^2 l^2}{n(\omega)^2 n(2\omega)} \frac{P_{\omega}}{Wt}$$

EQUATION 17

where d_{eff} is the effective nonlinear coefficient, W the width of the waveguide that transport the incident light, and t the thickness of the guiding layer. The formula above will be explained in detail in appendix 2

Fabrication methods and results and more information about the realization and characterization of frequency doubler devices in Lithium Niobate doped with Zirconium and undoped are extensively discussed in chapter 3.

2.3.5. Electro-optical effect

Another second order optical phenomenon that characterized Lithium Niobate is the Electro-optical effect. It consists on the change of the refractive index when the crystal is subjected to an electric field. Usually this effect is discussed in terms of optical indicatrix, an ellipsoidal surface whose major and minor axes of the central section normal to the light propagation direction represent the principal refractive indices of the material. The behavior of the indicatrix can be expressed in function of the electric fields as a power (Equation 18).

$$\Delta\left(\frac{1}{n^2}\right)_{ij} = \sum_k r_{ijk} E_k + \sum_{k,l} s_{ijkl} E_k E_l + \dots$$

EQUATION 18.

where r_{ijk} and s_{ijkl} are the coefficients relative to the linear and quadratic electro-optic effects, usually named respectively Pockels effect and Kerr

effect. Although Lithium Niobate presents high linear electro-optic effect, higher-order terms can be neglected, because in this material no quadratic electro-optical effect can be significatively observed for applied electric fields up to 65kV/mm [68]. Due to the symmetry of the Lithium Niobate, its linear electro-optic tensor $\hat{r}$ results:

$$\hat{r} = \begin{bmatrix} 0 & -r_{22} & r_{13} \\ 0 & r_{22} & r_{13} \\ 0 & 0 & r_{33} \\ 0 & r_{42} & 0 \\ r_{42} & 0 & 0 \\ -r_{22} & 0 & 0 \end{bmatrix}$$

EQUATION 19

In Table 4 we report the value of the Pockels effect coefficients measured in clamped or unclamped mode, in fact the mechanical strains can affect the refractive index via elasto-optic effect leading to different measurements. The elasto-optical effect can be expressed as

$$\left(\frac{1}{n^2}\right)_{ij} = p_{ijkl} u_{kl}$$

EQUATION 20

where p_{ijkj} and u_{kl} are the elasto-optic coefficients and mechanical strains, respectively.

Property		pm V^{-1}				
		r_{11}	r_{22}	r_{33}	r_{51}	r_z
Electro-optical coeff. (at 633 nm) (Crystal Technology, Inc.)	**Unclamped**	10	7	33	33	18
	Clamped	9	3	31	28	19

TABLE 4.ELECTRO-OPTICAL COEFFICIENTS OF LITHIUM NIOBATE

2.3.6. Photorefractivity

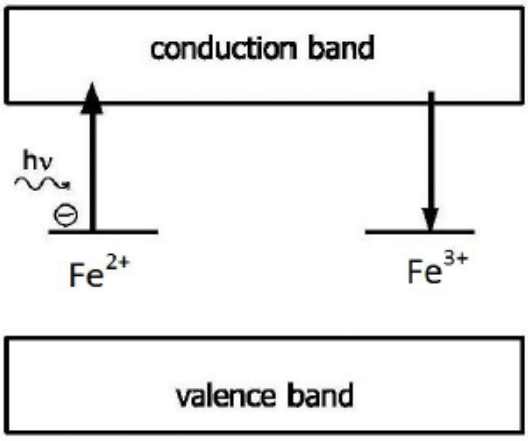

FIGURE 10 BAND SCHEME OF THE ONE-CENTER CHARGE TRANSPORT PROCESS

The photorefractive effect is an optically induced change of the refractive index that appears starting from low intensities (10 mW cm^{-2} for blue–green light in $LiNbO_3$:Fe) [36], and shows no intensity threshold. It is produced by a combination of effects that occur in three steps: photoexcitation of charge, charge migration followed by an electro-optic effect (linear or quadratic). The charge migration may be produced by diffusion, drift, bulk photovoltaic effect, or a combination of these effects. In Lithium Niobate the dominant charge migration mechanism is the photovoltaic effect and the dominant electro-optic mechanism is the linear effect (Pockels effect). Therefore the variation of the refractive index is due to the Pockels effect arising from an electric field generated by a non-homogeneous distribution of charge inside and outside the illuminated zone of the crystals. The induced change of the refractive index can be detrimental when light propagates in the material, leading to the so called optical damage. The negative consequences are the wave-front damage, a strong scattering of a transmitting light-wave, and an instability or loss of lasing when $LiNbO_3$ crystals are used as a solid state laser medium. The photovoltaic effect, the first step of the photorefractivity, is strictly dependent on concentration of doping impurities and crystal defect. In fact they could form donor and acceptor levels inside the band gap of Lithium Niobate from while electron transition may occur promoting free charge which diffuse from the illuminated area to the dark area, where the electrons decay to the acceptor levels. This lead to a charge difference

between the illuminated area and the dark area with the arising of an associated electric field. As a matter of fact, this effect can be significatively enhanced by doping the material with ions which act as photorefractive centers, such as the iron, that, with its two possible valence states (Fe^{2+} and Fe^{3+}), can behave as donor and as acceptor for the free charge carriers. Two models could explain these phenomena: one-centre model and two-centre model. The one-center charge-transport model [37] was the first model developed at the beginning of the studies on photorefractive effect and it is still valid in many situations. In this model only a single type of photorefractive dopants is considered, which presents two possible valence states acting both as donor or as acceptor for the carriers. This is the case of iron impurities which are incorporated in Lithium Niobate with the possible valence state Fe^{2+} and Fe^{3+}, behaving respectively as filled or empty trap. The one-center model is illustrated in Figure 10.

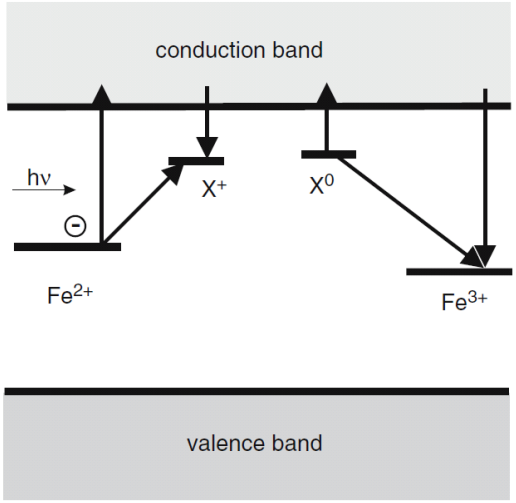

FIGURE 11 CHARGE TRANSPORT SCHEME IN A TWO-CENTER MODEL. Fe^{2+} AND Fe^{3+} ARE FILLED AND EMPTY DEEP ELECTRON TRAPS. X^0 AND X^+ ARE FILLED AND EMPTY SHALLOW ELECTRON TRAPS.

However, at high light intensities ($I > 10^2 W/cm^2$) the one-center model is not valid [36], these suggesting the need of developing a new approach to the charge transport scheme, and to its consideration on the base of a two (or more) center model. The most simple and obvious is a transport scheme assuming the participation of an additional (secondary) shallow electron trap, which is empty in the equilibrium state (Figure 11). Two-center charge-transport model could explains the fundamental role of Fe_{Li}^{3+} and Nb_{Li}^{4+} as causes of the photorefractive effect, with the former serving as the dominant

electron trap and the second as secondary electron trap respectively. This model is generally accepted and is always used for interpretation on the photoconductivity and photorefraction in $LiNbO_3$.

For our aims photorefractive effect can play the role of a problem and a resource. This because on one hand the optical damage can limited the usefulness of the crystals, giving rise to decollimation and scattering of laser beams in devices such as modulators and frequency doublers. On the other the photorefractivity could be very useful for the realization of holographic gratings, holographic data storage, interference filters, image processing, and so on. Finally recent studies demonstrated also a direct optofluidic application of photorefractivity, such as optoelectronic tweezers [48], or electrophoretic and dielectrophoretic particle manipulation [49] exploiting the interaction between a laser source, particles and a Fe:LN substrate.

3. Microfluidics

3.1. Microfluidic

Microfluidics is a branch of knowledge that studies the manipulation and the behavior of small quantities of liquid (in the range of 10^{-9} and 10^{-12} litres) either in channels with dimensions of tens to hundreds micrometers [69] or in open configuration as droplets. It is worth mentioning both as technology and as science: the first exploits the small size, for example the ability to use small volume of reagents and samples, the low cost of a fluidic microchip and the short time for analysis; but the second concern their behavior in the fluid dynamics at low Reynolds number (section 3.2.2), that ensures laminar flow regimes and a high control of the parameters involved. Thus, high control and short length scales can be exploited to reach short time scales regarding rapid mixing and short reaction times. The impact of the microfluidics in biology, medicine, chemistry, material science and other fields is the analogous of the use of integrated circuits in electronics. As a matter of fact, the miniaturization process has affected and still affects many research fields, it is a technological effort of great importance that has brought quite a few advantages in different areas, including portability, parallel processing, and small volumes. This gives rise to the idea of a "Lab on a chip": the possibility to reduce a whole laboratory in a single microfluidic chip which makes step by step all the process phases. This kind of technological effort requires that engineering, chemistry and material science participate in the micro-fabrication research, whereas the flow dynamic studies and the influence of capillarity and interfacial phenomena involve mostly physics.

The high surface to volume ratio, characteristic of the microfluidic channel, implies that the interfacial effects play a great role in the dynamics of the system. The capillary effects are further amplified in the droplet microfluidics, that is the production and manipulation of discrete volumes with the use of immiscible phases [25]. The presence of liquid droplets or gas bubbles in a liquid, adds a new degree of complexity to the system. However, droplet microfluidics presents many advantages compared to the single phase flow, for example the absence of interaction with the microchannel walls of the

droplet/bubble fluid, the possibility to rapid mixing in each droplet and the absence of cross-contamination between adjacent droplets. In particular the control of microfluidic flows together with the use of two immiscible fluids can produce droplets with a very low dispersion in size.

In this work, we focused on the production of controlled droplets by using a T-junction geometry for the first time engraved in Lithium Niobate. The role of this geometry in the droplets generation will be discussed in (chapter 2). In the next section a basic theory of microfluidic is presented to enable the understanding of the phenomena and behaviors of our fluidic devices.

3.2. Theory

The change of the surface to volume ratio after the miniaturization of fluids dimensions changes significantly the behavior of hydrodynamic systems. In fact at a micrometric scale volume contributions (such as gravity and inertia) decrease their importance or become completely negligible as the surface driven effects (such as capillarity) become more important and tend to govern the behavior of microfluidic systems. In the following, important concepts necessary to understand the formation and the flow of droplets in microfluidic channels are briefly introduced.

3.2.1. Navier-Stokes and Hagen-Poiseuille equations

For Newtonian fluids (liquid for which the viscosity does not depend on the stress state and velocity of the flow) in single-phase flow, the Navier-Stokes equation for incompressible fluids is expressed as

$$\rho\left(\frac{\partial \boldsymbol{u}}{\partial t} + (\boldsymbol{u}\cdot\boldsymbol{\nabla})\boldsymbol{u}\right) = -\boldsymbol{\nabla}\mathrm{p} + \mu\Delta\mathbf{u} + \mathbf{f}$$

NAVIER-STOKES EQUATION 21

Where ρ is the density, **u** is the velocity, p is the pressure, μ is the dynamic viscosity and **f** is the resultant of any other forces per unit volume. To describe the flow in a circular microchannel it is convenient to

- use cylindrical coordinates;
- assuming a steady state of the system;

- assuming the radial and the swirl components of the fluid velocity to be zero (propagation just in the direction of the channel);
- assuming axisymmetric flow, the velocity of the flow just depends on the distance from the centre of the channel;
- assuming that the velocity of the liquid do not change along the direction of propagation.

Therefore, integrating and considering the boundary no slip condition (at the channel wall the flow velocity is zero) a parabolic velocity profile is obtained, with the maximum velocity in the center of the channel. Integrating the flow profile over the pipe cross section the Hagen-Poiseuille equation is achieved [70].

$$\Delta p = \frac{8 \cdot \mu \cdot L \cdot Q}{\pi \cdot r^4}$$

HAGEN-POISEUILLE EQUATION 22

where Q is the volumetric flow rate that passes the channel, r is the radius and Δp is the pressure difference between two points of the channel separated by the distance L.

The Hagen-Poiseuille equation gives the pressure drop along a circular pipe filled with a Newtonian fluid[70]. It is only valid for circular cross sections, for rectangular cross sections there is no exact analytical solution known. One approximation used to solve the problem is to look at the cross section and use a circle with the same surface taking its diameter as hydrodynamic diameter and insert it into the Hagen-Poiseuille equation.

3.2.1.1. Hydrodynamic resistance

According to Hagen-Poiseuille equation the volume flux Q in a given channel depends linearly on the pressure gradient Δp. In analogy to the Ohm's law the hydrodynamic resistance of a microfluidic channel can be introduced. The hydrodynamic resistance R is defined by the relation [71]:

$$\Delta p = R \cdot Q_m$$

EQUATION 23

where Δp is the pressure difference along the channel and $Q_m = Q \cdot \rho$ is the mass flux (where ρ is the density of the fluid).

3.2.1.2. Limits of the Hagen-Poiseuille equation

It is clear that all the drawn conclusions are only valid generally as long as the assumptions made in section 3.2.1 are fulfilled. Especially for high velocities, pipe diameters above a threshold (or viscosities below a certain threshold) the flow can become turbulent due to small disturbances. Those turbulent flows in pipes have a higher resistance than the one predicted by the Hagen-Poiseuille equation. Hence the derived equations can be applied only for laminar flow or rather, using the concept that is introduced in the following section, for small Reynolds numbers. Moreover, the linearity of the Navier-Stokes equations is not valid in the presence of droplets or bubbles on account of the presence of interfaces that cause instabilities and nonlinearities like the deformation of interfaces and the splitting or merging of droplets.

3.2.2. Dimensionless numbers

The most important dimensionless number in fluid dynamics is the Reynolds number

$$Re = \frac{\rho U L}{\mu}$$

REYNOLDS NUMBER EQUATION 24

where ρ is the fluid density, μ its dynamic viscosity, U is the mean velocity and L the typical length scale of the channel (the equivalent diameter). The value of Re gives the idea of relative importance of the inertia to viscous stress in the system. Microfluidic devices work at low Reynolds numbers (Re<1) that assure laminar flow [71].

Another dimensionless number is the Weber number

$$We = \frac{\rho U^2 L}{\sigma}$$

WEBER NUMBER EQUATION 25

where σ is the interfacial tension between the two phases. This number compares inertia to interfacial tension and usually it is lower than 1 in microfluidics.

The Bond number gives the comparison between gravity and interfacial tension:

$$Bo = \frac{\Delta \rho g L^2}{\sigma}$$

BOND NUMBER EQUATION 26

where Δρ is the difference in fluid densities and g the gravity acceleration. Bo<<1 means that gravity effects can be ignored.

The relative strength between viscosity and interfacial tension is expressed by the Capillary number [72]

$$Ca = \frac{\mu U}{\sigma}$$

CAPILLARY NUMBER EQUATION 27

where μ is the larger dynamic viscosity in the system. A low value of Ca indicates that the stress due to the interfacial tension is strong compared to the viscous stress. In this condition droplets minimize their surface forming spherical shape if there are not geometrical constraints. At high value of Ca deformation of the droplet surface can be observed. In droplet microfluidics Ca is usually comprised in the range from 10^{-5} to 1.

3.2.3. Interfacial energy

The interfacial energy is defined by the interfacial tension σ ([σ]=N/m or J/m^2). The interfacial tension determines the change in interfacial energy δW that is needed to increase the liquids interface by a surface element δA.

$$\delta W = \sigma \delta A$$

EQUATION 28

Interfacial energy can be controlled using surfactants, amphiphilic molecules (i.e. with a part hydrophilic and another hydrophobic) [73]. Generally a higher surfactant concentration leads to a lower interfacial energy, with a concentration limit called critical micellar concentration (cmc) after which micelles are generated (micelles are aggregates of surfactant molecules oriented in an energetically efficient way) [71]. The decrease of the interfacial energy makes it easier to create droplets, that because the

capillary number increases lowering the surface tension, making it easier to deform the meniscus. Moreover surfactants stabilize the interface once it is formed against coalescence, allowing the production of time stable emulsions [74].

3.2.4. Droplets transport

Up to this point, channels containing just one fluid were discussed. But for the later experiments there is a second important situation: rectangular channels that carry a fluid (continuous phase) and droplets of a different fluid (dispersed phase). After a droplet is generated in a channel, it is carried downstream by the continuous phase and its shape is determined by both: surface tension effects that act to minimize the surface of the droplet, and the geometry constraints. When its equivalent diameter is greater than the diameter of the channel, the shape change forming a plug. For a circular channel the plug assumes a circular cross section with a film of the continuous phase of constant thickness that wets the walls. If the channel has a rectangular cross section, this thickness in not constant and the phase fills also the corners like in Figure 12. Both experiments [75] and numerical simulations [76] confirm that the thickness which separates droplets from the walls is of the order from 1% to 5% of the channel's half height. Note that the presence of the continuous phase prevents the direct contact between plugs and the wall.

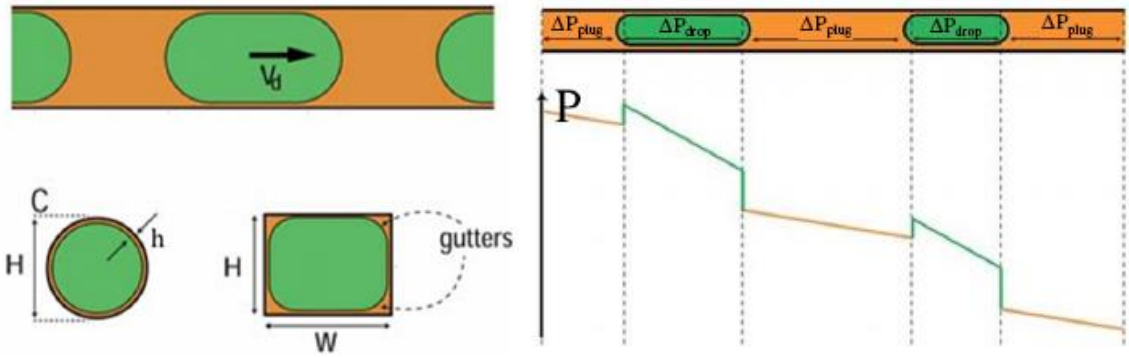

FIGURE 12 (LEFT) TYPICAL SHAPE OF A DROPLET IN A MICROUIDIC CHANNEL FROM FRONT AND CROSS SECTION PERSPECTIVES. (RIGHT) AN EXAMPLE OF PLUG TRAIN IN A MICROUIDIC CHANNEL AND THE PRESSURE TREND ALONG IT [77]

The continuous phase layer influences also the velocity of the droplet along the channel, in fact for circular channel the droplet move faster than the oil [75], while for rectangular channel it moves slower than the carrier fluid,

usually the velocity difference keeps below the 6% for typical microfluidic capillary numbers ranging from 10^{-6} and 1 [78]. The typical output of the droplet production in microfluidics is the "plug train": a sequence of droplets of constant size and constant spacing (Figure 12). As long as droplets are confined and their order is preserved, so that they can be seen as independent reactors. Furthermore, we emphasize that at each interface between the two phases corresponds a Laplace pressure (Δp_L) due to curvature of the surface

$$\Delta p_L = \sigma \left(\frac{1}{R_1} + \frac{1}{R_2} \right)$$

EQUATION 29

Where σ is the interfacial tension, and R_1 and R_2 the radius of curvature of the droplet surface respectively. Therefore, the total pressure along the channel is nonlinear but it evolves with discrete steps as shown in Figure 12.

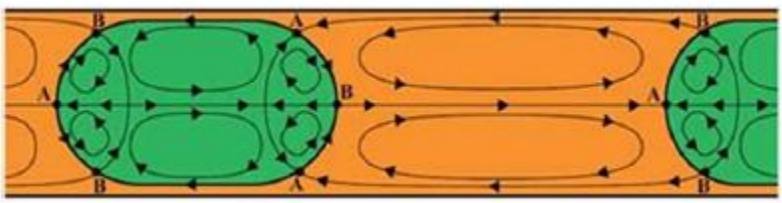

FIGURE 13 FLOW FIELD INSIDE AND OUTSIDE THE DROPLET PRODUCE FAST MIXING [77].

Finally, another important feature of confined droplets is related to the fast self-mixing induced inside the droplet volume and the possibility to droplets handling by active or passive methods. Mixing inside micro-droplets also benefits from the internal vortex circulation directed by channel geometry. The geometrical factor is as much important in droplet fusion or splitting, for example through width variation or bifurcation. They takes part in the passive methods, while active methods for handling of droplets include the use of electrodes or laser heating to induce droplets merging or separation, also photorefractivity of lithium niobate can be used for these purposes [48].

Bibliography

[1] D. Erickson, D. Sinton, and D. Psaltis, "Optofluidics for energy applications," *Nat. Photonics*, vol. 5, no. 10, pp. 583–590, Sep. 2011.

[2] H. Schmidt and A. R. Hawkins, "The photonic integration of non-solid media using optofluidics," *Nat. Photonics*, vol. 5, no. 10, pp. 598–604, Aug. 2011.

[3] D. Psaltis, S. R. Quake, and C. Yang, "Developing optofluidic technology through the fusion of microfluidics and optics.," *Nature*, vol. 442, no. 7101, pp. 381–6, Jul. 2006.

[4] C. Monat, P. Domachuk, and B. J. Eggleton, "Integrated optofluidics: A new river of light," *Nat. Photonics*, vol. 1, no. 2, pp. 106–114, Feb. 2007.

[5] X. Fan and I. M. White, "Optofluidic Microsystems for Chemical and Biological Analysis.," *Nat. Photonics*, vol. 5, no. 10, pp. 591–597, Oct. 2011.

[6] H. C. Hunt and J. S. Wilkinson, "Optofluidic integration for microanalysis," *Microfluid. Nanofluidics*, vol. 4, no. 1–2, pp. 53–79, Sep. 2007.

[7] J. W. Hong and S. R. Quake, "Integrated nanoliter systems.," *Nat. Biotechnol.*, vol. 21, no. 10, pp. 1179–83, Oct. 2003.

[8] D. Yin, D. W. Deamer, H. Schmidt, J. P. Barber, and A. R. Hawkins, "Single-molecule detection sensitivity using planar integrated optics on a chip," *Opt. Lett.*, vol. 31, no. 14, p. 2136, 2006.

[9] F. Eftekhari, C. Escobedo, J. Ferreira, X. Duan, E. M. Girotto, A. G. Brolo, R. Gordon, and D. Sinton, "Nanoholes as nanochannels: flow-through plasmonic sensing.," *Anal. Chem.*, vol. 81, no. 11, pp. 4308–11, Jun. 2009.

[10] M. Huang, A. A. Yanik, T.-Y. Chang, and H. Altug, "Sub-wavelength nanofluidics in photonic crystal sensors.," *Opt. Express*, vol. 17, no. 26, pp. 24224–33, Dec. 2009.

[11] Y. Guo, H. Li, K. Reddy, H. S. Shelar, V. R. Nittoor, and X. Fan, "Optofluidic Fabry–Pérot cavity biosensor with integrated flow-

through micro-/nanochannels," *Appl. Phys. Lett.*, vol. 98, no. 4, p. 041104, 2011.

[12] J. C. Galas, C. Peroz, Q. Kou, and Y. Chen, "Microfluidic dye laser intracavity absorption," *Appl. Phys. Lett.*, vol. 89, no. 22, p. 224101, 2006.

[13] Y. Sun, S. I. Shopova, C.-S. Wu, S. Arnold, and X. Fan, "Bioinspired optofluidic FRET lasers via DNA scaffolds.," *Proc. Natl. Acad. Sci. U. S. A.*, vol. 107, no. 37, pp. 16039–42, Sep. 2010.

[14] Z. Wang, K. Swinney, and D. J. Bornhop, "Attomole sensitivity for unlabeled proteins and polypeptides with on-chip capillary electrophoresis and universal detection by interferometric backscatter.," *Electrophoresis*, vol. 24, no. 5, pp. 865–73, Mar. 2003.

[15] H. Zhu, I. M. White, J. D. Suter, M. Zourob, and X. Fan, "Integrated refractive index optical ring resonator detector for capillary electrophoresis.," *Anal. Chem.*, vol. 79, no. 3, pp. 930–7, Feb. 2007.

[16] S. I. Shopova, I. M. White, Y. Sun, H. Zhu, X. Fan, G. Frye-Mason, A. Thompson, and S. Ja, "On-column micro gas chromatography detection with capillary-based optical ring resonators.," *Anal. Chem.*, vol. 80, no. 6, pp. 2232–8, Mar. 2008.

[17] Y. Sun, J. Liu, D. J. Howard, G. Frye-Mason, A. K. Thompson, S. Ja, and X. Fan, "Rapid tandem-column micro-gas chromatography based on optofluidic ring resonators with multi-point on-column detection.," *Analyst*, vol. 135, no. 1, pp. 165–71, Jan. 2010.

[18] S. J. Lee and M. Moskovits, "Visualizing chromatographic separation of metal ions on a surface-enhanced Raman active medium.," *Nano Lett.*, vol. 11, no. 1, pp. 145–50, Jan. 2011.

[19] D. Erickson, X. Serey, Y.-F. Chen, and S. Mandal, "Nanomanipulation using near field photonics.," *Lab Chip*, vol. 11, no. 6, pp. 995–1009, Mar. 2011.

[20] J. S. Soughayer, T. Krasieva, S. C. Jacobson, J. M. Ramsey, B. J. Tromberg, and N. L. Allbritton, "Characterization of Cellular Optoporation with Distance," *Anal. Chem.*, vol. 72, no. 6, pp. 1342–1347, Mar. 2000.

[21] D. Erickson and D. Li, "Integrated microfluidic devices," *Anal. Chim. Acta*, vol. 507, no. 1, pp. 11–26, Apr. 2004.

[22] C. Yi, C.-W. Li, S. Ji, and M. Yang, "Microfluidics technology for manipulation and analysis of biological cells," *Anal. Chim. Acta*, vol. 560, no. 1–2, pp. 1–23, Feb. 2006.

[23] P. S. Dittrich, K. Tachikawa, and A. Manz, "Micro total analysis systems. Latest advancements and trends.," *Anal. Chem.*, vol. 78, no. 12, pp. 3887–908, Jun. 2006.

[24] K. Dholakia and P. Reece, "Optical micromanipulation takes hold," *Nano Today*, vol. 1, no. 1, pp. 18–27, Feb. 2006.

[25] S.-Y. Teh, R. Lin, L.-H. Hung, and A. P. Lee, "Droplet microfluidics.," *Lab Chip*, vol. 8, no. 2, pp. 198–220, Feb. 2008.

[26] J. P. McMullen and K. F. Jensen, "Integrated microreactors for reaction automation: new approaches to reaction development.," *Annu. Rev. Anal. Chem. (Palo Alto. Calif).*, vol. 3, pp. 19–42, Jan. 2010.

[27] P. Watts and S. J. Haswell, "The application of micro reactors for organic synthesis.," *Chem. Soc. Rev.*, vol. 34, no. 3, pp. 235–46, Mar. 2005.

[28] G. N. Doku, W. Verboom, D. N. Reinhoudt, and A. van den Berg, "On-microchip multiphase chemistry—a review of microreactor design principles and reagent contacting modes," *Tetrahedron*, vol. 61, no. 11, pp. 2733–2742, Mar. 2005.

[29] D. J. Quiram, K. F. Jensen, M. A. Schmidt, P. L. Mills, J. F. Ryley, M. D. Wetzel, and D. J. Kraus, "Integrated Microreactor System for Gas-Phase Catalytic Reactions. 1. Scale-up Microreactor Design and Fabrication," *Ind. Eng. Chem. Res.*, vol. 46, no. 25, pp. 8292–8305, Dec. 2007.

[30] L. Novak, P. Neuzil, J. Pipper, Y. Zhang, and S. Lee, "An integrated fluorescence detection system for lab-on-a-chip applications.," *Lab Chip*, vol. 7, no. 1, pp. 27–9, Jan. 2007.

[31] M. L. Sin, J. Gao, J. C. Liao, and P. K. Wong, "System Integration - A Major Step toward Lab on a Chip.," *J. Biol. Eng.*, vol. 5, p. 6, Jan. 2011.

[32] J. Friend and L. Y. Yeo, "Microscale acoustofluidics: Microfluidics driven via acoustics and ultrasonics," *Rev. Mod. Phys.*, vol. 83, no. 2, pp. 647–704, Jun. 2011.

[33] M. K. Tan, L. Y. Yeo, and J. R. Friend, "Rapid fluid flow and mixing induced in microchannels using surface acoustic waves," *EPL (Europhysics Lett.*, vol. 87, no. 4, p. 47003, Aug. 2009.

[34] S. Grilli and P. Ferraro, "Dielectrophoretic trapping of suspended particles by selective pyroelectric effect in lithium niobate crystals," *Appl. Phys. Lett.*, vol. 92, no. 23, p. 232902, 2008.

[35] M. Esseling, F. Holtmann, M. Woerdemann, and C. Denz, "Two-dimensional dielectrophoretic particle trapping in a hybrid crystal/PDMS-system.," *Opt. Express*, vol. 18, no. 16, pp. 17404–11, Aug. 2010.

[36] T. Volk and M. Wöhlecke, *Lithium Niobate*, vol. 115. Berlin, Heidelberg: Springer Berlin Heidelberg, 2008.

[37] G. Nava, P. Minzioni, W. Yan, J. Parravicini, D. Grando, E. Musso, I. Cristiani, N. Argiolas, M. Bazzan, M. V. Ciampolillo, A. Zaltron, C. Sada, and V. Degiorgio, "Zirconium-doped lithium niobate: photorefractive and electro-optical properties as a function of dopant concentration," *Opt. Mater. Express*, vol. 1, no. 2, p. 270, May 2011.

[38] G. Gauglitz, "Direct optical detection in bioanalysis: an update.," *Anal. Bioanal. Chem.*, vol. 398, no. 6, pp. 2363–72, Nov. 2010.

[39] G. G. Bentini, M. Bianconi, a. Cerutti, M. Chiarini, G. Pennestrì, C. Sada, N. Argiolas, M. Bazzan, and P. Mazzoldi, "Integrated Mach-Zehnder micro-interferometer on LiNbO3," *Opt. Lasers Eng.*, vol. 45, no. 3, pp. 368–372, Mar. 2007.

[40] C. Denz, K.-O. Muller, T. Heimann, and T. Tschudi, "Volume holographic storage demonstrator based on phase-coded multiplexing," *IEEE J. Sel. Top. Quantum Electron.*, vol. 4, no. 5, pp. 832–839, 1998.

[41] S. Breer and K. Buse, "Wavelength demultiplexing with volume phase holograms in photorefractive lithium niobate," *Appl. Phys. B Lasers Opt.*, vol. 66, no. 3, pp. 339–345, Mar. 1998.

[42] Y. L. Lee, N. E. Yu, C. Jung, B.-A. Yu, I.-B. Sohn, S.-C. Choi, Y.-C. Noh, D.-K. Ko, W.-S. Yang, H.-M. Lee, W.-K. Kim, and H.-Y. Lee, "Second-harmonic generation in periodically poled lithium niobate waveguides fabricated by femtosecond laser pulses," *Appl. Phys. Lett.*, vol. 89, no. 17, p. 171103, 2006.

[43] M. Jubera, A. García-Cabañes, J. Olivares, A. Alcazar, and M. Carrascosa, "Particle trapping and structuring on the surface of

LiNbO3:Fe optical waveguides using photovoltaic fields.," *Opt. Lett.*, vol. 39, no. 3, pp. 649–52, Feb. 2014.

[44] M. C. and F. A.-L. M. Carrascosa, *Infrared Holography for Optical Communications*, vol. 86. Berlin, Heidelberg: Springer Berlin Heidelberg, 2003.

[45] L. Pang, H. M. Chen, L. M. Freeman, and Y. Fainman, "Optofluidic devices and applications in photonics, sensing and imaging.," *Lab Chip*, vol. 12, no. 19, pp. 3543–51, Oct. 2012.

[46] M. F. Schneider, Z. Guttenberg, S. W. Schneider, K. Sritharan, V. M. Myles, U. Pamukci, and A. Wixforth, "An acoustically driven microliter flow chamber on a chip (muFCC) for cell-cell and cell-surface interaction studies.," *Chemphyschem*, vol. 9, no. 4, pp. 641–5, Mar. 2008.

[47] H. A. Eggert, F. Y. Kuhnert, K. Buse, J. R. Adleman, and D. Psaltis, "Trapping of dielectric particles with light-induced space-charge fields," *Appl. Phys. Lett.*, vol. 90, no. 24, p. 241909, 2007.

[48] M. Esseling, A. Zaltron, N. Argiolas, G. Nava, J. Imbrock, I. Cristiani, C. Sada, and C. Denz, "Highly reduced iron-doped lithium niobate for optoelectronic tweezers," *Appl. Phys. B*, vol. 113, no. 2, pp. 191–197, Apr. 2013.

[49] M. Esseling, A. Zaltron, C. Sada, and C. Denz, "Charge sensor and particle trap based on z-cut lithium niobate," *Appl. Phys. Lett.*, vol. 103, no. 6, p. 061115, 2013.

[50] Y. N. Korkishko and V. A. Fedorov, *Ion Exchange in Single Crystals for Integrated Optics and Optoelectronics*. Cambridge International Science Publishing, 1999.

[51] A. A. BALLMAN, "Growth of Piezoelectric and Ferroelectric Materials by the CzochraIski Technique," *J. Am. Ceram. Soc.*, vol. 48, no. 2, pp. 112–113, Feb. 1965.

[52] S. Fedulov, Z. Shapiro, and L. PB, "GROWTH OF CRYSTALS OF LINBO3 LITAO3 AND NANBO3BY CZOCHRALSKI METHOD," *Sov. Phys. Crystallogr. USSR*, vol. 10, no. 2, p. 218, 1965.

[53] R. S. Weis and T. K. Gaylord, "Lithium niobate: Summary of physical properties and crystal structure," *Appl. Phys. A Solids Surfaces*, vol. 37, no. 4, pp. 191–203, Aug. 1985.

[54] Rauber and Armin, "Chemistry and physics of lithium niobate," *Curr. Top. Mater. Sci.*, vol. 1, no. 481–601, 1978.

[55] A. Prokhorov and Y. S. Kuz'minov, "Physics and Chemistry of Lithium Niobate," *Bristol, Hilger*, 1990.

[56] "Lithium Niobate optical crystals datasheet," *Cryst. Technol. Inc.*

[57] S. C. Abrahams and P. Marsh, "Defect structure dependence on composition in lithium niobate," *Acta Crystallogr. Sect. B Struct. Sci.*, vol. 42, no. 1, pp. 61–68, Feb. 1986.

[58] P. Lerner, C. Legras, and J. P. Dumas, "Stoechiométrie des monocristaux de métaniobate de lithium," *J. Cryst. Growth*, vol. 3–4, pp. 231–235, Jan. 1968.

[59] S. Grilli, L. Miccio, V. Vespini, a. Finizio, S. De Nicola, and P. Ferraro, "Liquid micro-lens array activated by selective electrowetting on lithium niobate substrates," *Opt. Express*, vol. 16, no. 11, p. 8084, May 2008.

[60] P. Ferraro, S. Grilli, L. Miccio, and V. Vespini, "Wettability patterning of lithium niobate substrate by modulating pyroelectric effect to form microarray of sessile droplets," *Appl. Phys. Lett.*, vol. 92, no. 21, p. 213107, 2008.

[61] P. Ferraro, S. Coppola, S. Grilli, M. Paturzo, and V. Vespini, "Dispensing nano-pico droplets and liquid patterning by pyroelectrodynamic shooting.," *Nat. Nanotechnol.*, vol. 5, no. 6, pp. 429–35, Jun. 2010.

[62] J. F. Nye, *Physical properties of crystals : their representation by tensors and matrices*. Oxford : Clarendon Press, 1985, p. 329.

[63] U. Schlarb and K. Betzler, "Refractive indices of lithium niobate as a function of temperature, wavelength, and composition: A generalized fit," *Phys. Rev. B*, vol. 48, no. 21, pp. 15613–15620, Dec. 1993.

[64] M. Houe and P. D. Townsend, "An introduction to methods of periodic poling for second-harmonic generation," *J. Phys. D. Appl. Phys.*, vol. 28, no. 9, pp. 1747–1763, Sep. 1995.

[65] R. L. Byer, *Nonlinear Optics*. San Francisco, 1977.

[66] L. E. Myers, R. C. Eckardt, M. M. Fejer, R. L. Byer, W. R. Bosenberg, and J. W. Pierce, "Quasi-phase-matched optical

parametric oscillators in bulk periodically poled LiNbO_3," *J. Opt. Soc. Am. B*, vol. 12, no. 11, p. 2102, Nov. 1995.

[67] M. M. Fejer, G. a. Magel, D. H. Jundt, and R. L. Byer, "Quasi-phase-matched second harmonic generation: tuning and tolerances," *IEEE J. Quantum Electron.*, vol. 28, no. 11, pp. 2631–2654, 1992.

[68] M. Luennemann, U. Hartwig, G. Panotopoulos, and K. Buse, "Electrooptic properties of lithium niobate crystals for extremely high external electric fields," *Appl. Phys. B Lasers Opt.*, vol. 76, no. 4, pp. 403–406, Apr. 2003.

[69] G. M. Whitesides, "The origins and the future of microfluidics.," *Nature*, vol. 442, no. 7101, pp. 368–73, Jul. 2006.

[70] F. M. White, *Fluid Mechanics*, 4th ed. 2003.

[71] P. Tabeling, *Introduction to Microfluidics*. Oxford University Press, 2005.

[72] T. Squires and S. Quake, "Microfluidics: Fluid physics at the nanoliter scale," *Rev. Mod. Phys.*, vol. 77, no. 3, pp. 977–1026, Oct. 2005.

[73] J.-C. Baret, "Surfactants in droplet-based microfluidics.," *Lab Chip*, vol. 12, no. 3, pp. 422–33, Feb. 2012.

[74] J. H. Xu, S. W. Li, J. Tan, Y. J. Wang, and G. S. Luo, "Controllable preparation of monodisperse O/W and W/O emulsions in the same microfluidic device.," *Langmuir*, vol. 22, no. 19, pp. 7943–6, Sep. 2006.

[75] L. W. Schwartz, H. M. Princen, and A. D. Kiss, "On the motion of bubbles in capillary tubes," *J. Fluid Mech.*, vol. 172, no. -1, p. 259, Apr. 2006.

[76] A. L. HAZEL and M. HEIL, "The steady propagation of a semi-infinite bubble into a tube of elliptical or rectangular cross-section," *J. Fluid Mech.*, vol. 470, Nov. 2002.

[77] C. N. Baroud, F. Gallaire, and R. Dangla, "Dynamics of microfluidic droplets.," *Lab Chip*, vol. 10, no. 16, pp. 2032–45, Aug. 2010.

[78] F. Jousse, G. Lian, R. Janes, and J. Melrose, "Compact model for multi-phase liquid-liquid flows in micro-fluidic devices.," *Lab Chip*, vol. 5, no. 6, pp. 646–56, Jun. 2005.

Fluidic stage

1. Preface

Lithium Niobate (LN, $LiNbO_3$) could be a suitable functional material in the field of optofluidics, in fact as discussed previously (Chapter 1) its optical properties and applications have been studied in depth in the past years, giving to Lithium Niobate a leading position as a material for photonics. Moreover, recently also microfluidic and optofluidic application has been found for the crystal, from the fabrication of integrated micropump, to electrowetting, to optical trapping. Nonetheless, at the best of our knowledge, there are not published studies in which Lihtium Niobate is used as substrate for microfluidic, but always as a co-operating material with other classical materials for microfluidic, in particular polydimethylsiloxane (PDMS). In this chapter we discuss the realization of the first microfluidic circuit completely engraved in Lithium Niobate. The prototype is made of several interconnected stages that, starting from the droplet generation and manipulation, consider the droplets transfer through a microfluidic channel directly engraved on the Lithium Niobate substrate to an integrated analysis stage (Chapter 3) where the optical properties of the droplets constituents are monitored and detected.

In the first section of this chapter theory, geometries, and models of the microfluidic droplets generation are discussed, with particular attention to the T-junction geometry. Then, in the second section, the fabrication of microfluidic circuits in Lithium Niobate is presented, and moreover a systematic study of the wetting properties of lithium niobate is discussed since in the literature these properties have not been investigated in details. Finally in the third section we discuss the characterization of the performances of two T-junction droplet generators in comparison to standard microfluidic circuits.

1.1. Microfluidic circuit

The project regards the realization of microchannels in y-cut and z-cut $LiNbO_3$ crystals with characteristic sizes in the range of 50-250 μm and lengths up to a few centimetres. The circuit is fabricated in a T-junction geometry in order

to create a droplet generator. The system is designed to guarantee uniform droplets generation, focusing on the fine control of the size, shape and monodispersion by altering the fluids flow rate, the channels geometries, and the interface energies. A femtosecond laser at 800 nm was used to create microfluidic circuits on lithium niobate substrates by means of laser ablation, later the circuits were sealed by the means of a PDMS layer with inlet and outlet reservoir (Figure 1). The PDMS was used for the testing since the final device is closed by a LN top. The microfluidic performance was characterized in a wide range of droplet generation frequencies, from few Hz to about 1 kHz.

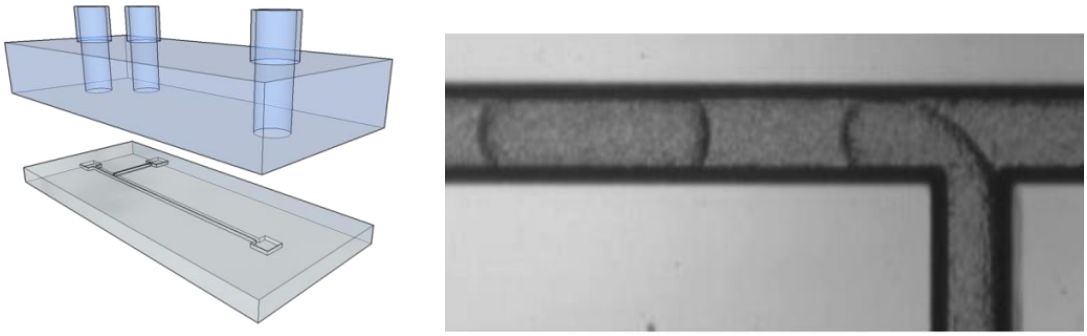

FIGURE 1. LEFT) AN EXPLODED VIEW DRAWING OF THE DROPLET GENERATOR, WITH THE T-JUNCTION ENGRAVED IN THE LITHIUM NIOBATE AND THE PDMS COVER WITH THE THREE INLETS; RIGHT) A MICROSCOPE IMAGE OF THE T-JUNCTION DURING THE DROPLET PRODUCTION IN THE SQUEEZING REGIME

1.2. Objectives

The principal objectives of the fluidic stage of our project are relative to the complete fabrication and characterization of the droplets generator, with particular attention to the roughness of the walls of the channel, which is a fundamental parameter for coupling optical waveguides with the fluidic stage. This result was achieved by several steps:

• Preliminary study of different techniques for the fabrication of channels in Lithium Niobate, with particular attention to sidewall surface quality, realization time, and flexibility of the circuit design; (section 3.3)

• Realization of microfluidic T-junctions devices on y-cut and z-cut Lithium Niobate crystals, optimizing all the necessary stage, from the control of

wettability of surface by their functionalization, to the better way to seal and deliver liquids to the circuit; (sections 3.3, 3.5, and 3.6)

- A detailed characterization of the T-junction prototypes investigating different flow rates of the dispersed and continuous phases, and different interface energy. (Section 4)

2. Droplets microfluidic

2.1. Introduction

In the past years great efforts have been directed towards the development of droplet based microfluidics, since it allows overcoming problems typical of continuous microfluidics, such as surface effects which lead to axial dispersion of liquids and the difficulty to obtain fast and efficient mixing of fluids. Moreover, each droplet can be thought as an isolated liquid compartment where chemical or biological syntheses take place, so this approach significantly reduces the risk of cross contamination between different droplets and facilitates single-cell analysis. Also, the possibility to produce such kind of flow in a microfluidic device increases the control of the parameters which come into play; hence it allows a great control of the outcomes. Finally, droplet microfluidics has the ability to perform a large number of reactions without increasing device size or complexity [1] and it is characterized by a high versatility connected to the generation and manipulation of discrete droplets inside micro-devices [2]. For all the mentioned reasons and thanks to their scalability and parallel processing, droplets based systems have been used in a wide range of applications [3]–[6], such as the drug delivery, diagnostic testing, bio-sensing [7] and the synthesis of biomolecules such as protein and DNA [8]–[10].

The key point of the droplet-based microfluidics is the control of the two-phase flow in a microfluidic device in order to produce and manage discrete volumes of fluids. The main elements are two immiscible fluids and a microchannel, where the dispersed phase is the fluid that forms the droplet, and the continuous phase is the fluid that carries the droplets downstream and that completely wets the channel walls. In the case of a hydrophobic channel, water is the dispersed fluid that creates droplets and oil constitutes the continuous phase: this is the so called W/O condition, which means Water-in-Oil droplets. On the contrary we have O/W condition (Oil-in-Water droplets) when the channels are hydrophilic. The two-phase flow properties in micro-devices rely on three groups of parameters: the channel geometry, the fluids properties and the flows conditions. All these factors appear in some

important dimensionless numbers that describe the global behaviour of the system. As a subcategory of microfluidics, droplet microfluidic inherits the same features of standard microfluidics, but also new dynamic problems rise. First of all microfluidic devices operate at low Reynolds numbers that assure a laminar flow. In the single-phase flow this means the linearity of the Navier-Stokes equations, but the presence of interfacial tension, deformable interfaces and the complexity of singular events as merging or splitting of droplets, introduce elements of instability and nonlinearity otherwise not present in standard microfluidics [11]. The evidence of that is the presence of different regimes that can appear in the same channel upon varying the flow parameters in the experiments (Figure 2). In the transition from one regime to the other, small changes in the conditions produce great differences on the output. This behaviour is related to the fact that modification in the drop geometry couples back to flow profile and can amplify initially small variations [12]. Therefore, the interfacial energy became an important parameter because of the high surface to volume ratio. This effect can be found between the immiscible phases and also between the continuous phase and the channel walls. Although the presence of instabilities does not enable to predict the system behaviour at all scales, microfluidics allows to produce droplets in a controlled and reproducible manner [12], varying a few driven parameters in definite ranges. Achieving stability in the production of droplets means size monodispersion of droplets and there is a great interest in such control ability for potential applications in chemistry, biology and material science.

In conclusion droplets can be easily generated, transported and manipulated by playing with geometry, fluids and eventually other integrated devices. Moreover the mixing inside the droplets happens in short time in comparison to classical procedures; in fact classic microfluidics presents limitations in the mixing of two liquids, because at the microscale (low Reynolds number) diffusion dominates on turbulence. Droplets can plug this gap and bring possible new applications. For this reasons droplet microfluidics has become an excellent platform for Lab-on-a-Chip applications.

In this section we analyse all these aspects and discuss their effects on droplet dynamics, focusing on the main features of droplet microfluidics.

Later we present a detailed treatment of the droplet production in the T-Junction geometry, which is the one used in this project.

2.2. Droplets generator

The high surface to volume ratio increases the importance of the interfacial effects, hence the choice of the chip material and fluids and the geometry factor play a great role. Direct agitation of immiscible fluids forms the traditional top-down method of droplets production or emulsion, but it causes a broad size droplet distribution [13]. On the other hand, geometry constraints devices have shown the generation of highly monodispersed droplets with a size variation smaller than 2% [14]. There are different droplets formation techniques; here we will focus on the three main passive methods: Co-flow system, Flow-focusing, and T-junction devices; with particular attention to the last one. In all cases the dispersed phase is injected in the device where it comes in contact with the carrier phase that is independently driven. The junction zone is particularly important; its design should optimize the reproducibility of droplet production. The shape of the channel evidently influences the local flow field, which can deform the interface causing the droplet break-up. The size of the droplet is the result of the competition between the viscous shear stress and the pressure of the external flow on the one hand, and the capillary pressure resisting deformation on the other [12]. Furthermore, another important parameter is the frequency of droplets generation, which is related to the volumetric flow rate of the dispersed fluid. In general T-junction devices are exploited to work at low frequency even though they permit to vary it in a wide range, whereas Flow Focusing devices work in general at higher rate of droplet production, never below 100 Hz. Both assure a good monodispersion.

In this project the T-junction geometry in rectangular channels was chosen for the realization of the droplet generator in our platform. This because on one hand it is a simple shape to reproduce in a substrate of Lithium Niobate in comparison to flow-focusing, in the other a great amount of studies has been reported in bibliography about this technique, therefore our results can be compared to a strengthened literature. Moreover T-shaped is typically

implemented since the droplet formation is periodic and regular over a wide range of flow rates

Some examples of droplet size and frequency for different T-junction generators are shown in Table 7. In the next sections we present the three different droplet generators.

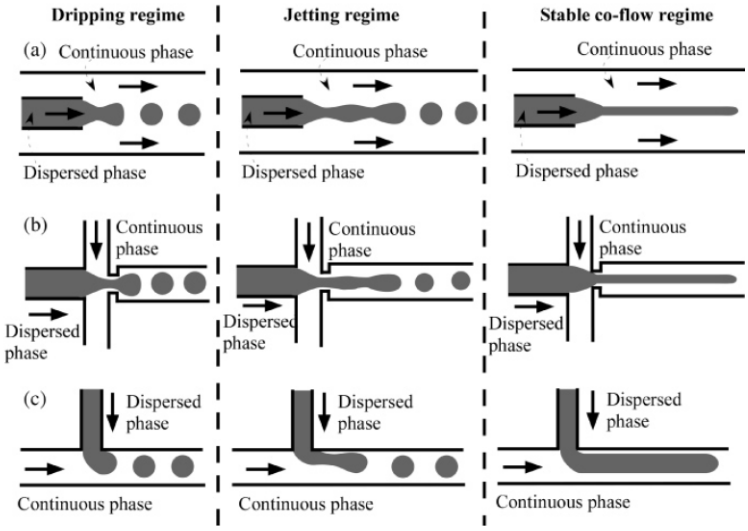

FIGURE 2 THREE DIFFERENT PASSIVE DROPLET GENERATORS ARE REPRESENTED: (A) CO-FLOW STREAMS, (B) FLOW FOCUSING, (C) T-JUNCTION. IN HORIZONTAL ARE REPORTED THREE DIFFERENT FLOW REGIMES: DRIPPING ON THE LEFT, JETTING ON THE CENTER, AND CO-FLOW ON THE RIGHT.

2.2.1. Co-flowing

As it can be seen in Figure 2(a) this configuration is obtained using two concentric capillaries: the dispersed phase is injected with a needle into another co-flowing immiscible fluid. This geometry was first proposed by Cramer et al. [15] in 2004. With this set-up three different regimes are distinguished: dripping, jetting, and co-flowing. In the former drops are formed close to the capillary, in the second they break-up downstream from an extended liquid jet, in the last two different flows coexist. The first regime can be controlled externally by the continuous phase mean velocity. The transition between the regimes is linked to a critical value of velocities that depends on the dispersed phase flow rate, on the viscosity, and on the interfacial tension. The performance of this kind of devices are good, with dispersion lower than 1% and frequency of production of the kHz, however it cannot be used to produce plugs as the squeezing regime is not achievable, and therefore it is not suitable for our application.

2.2.2. T-junction

A typical example of T-junction is shown in Figure 2(c). It was first proposed by Thorsen et al. [11] and it consists of two perpendicular channels, one for each phase, forming a T-shaped junction generating a cross-flow condition. Droplets form in that junction and in general three different regimes can be obtained varying both the flow rate ratio and the width channel ratio ($\Lambda=w_c/w_d$) as summarized in Figure 3. The first regime, called squeezing (Figure 1-right), occurs when the dispersed phase obstructs the channel as the droplet grows, thus restricting the flow of the continuous phase. This restriction produces an increase of the dynamic pressure upstream of the droplets that generates a force necking the interface and pinching off the droplets [12]. This configuration generally occurs at low velocity of both phases and for $\Lambda\sim1$. A second regime is the dripping one: droplets break up when the shear stress overcomes the interfacial tension. The easiest way to obtain this regime is when $\Lambda\ll1$ and the velocity of the continuous phase are high enough (bigger than the dispersed phase mean velocity) [16]. The jetting regime occurs when both phases have high velocities and it appears as stable parallel flowing streams. In this configuration droplets are formed by the instability at the flat interface and their size is not controlled. The influence of both flow rate ratio and the geometry factor is not trivial at all. Since this generator is that used in this thesis, a more detailed explanation of the T-junction can be found in section 2.3.

2.2.3. Flow-focusing device

As shown in Figure 2(b), in this kind of geometry the dispersed phase is squeezed by two opposite streaming flows of the continuous phase. The flow-focusing device was first proposed by Anna et al. [17] where both monodisperse and polydisperse emulsions were produced. Differently from the T- junction the large number of possible configurations does not allow the development of simple scaling laws, while phase diagrams are usually produced changing flow rates or pressure to study the general output and characterize the single device. Four main regimes can be identified: squeezing, dripping, jetting and thread formation.

2.3. T-junction: theory and models

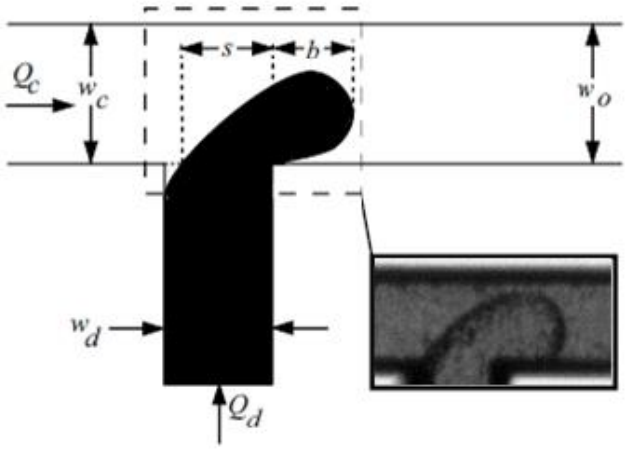

FIGURE 3. SCHEME OF THE GEOMETRICAL PARAMETERS TYPICAL OF A T-JUNCTION AND OF THE DROPLET FORMATION IN THE SQUEEZING AND DRIPPING REGIMES, ALSO Q_c AND Q_D ARE THE FLOW RATE OF THE CONTINUOUS PHASE AND THE DISPERSED PHASE RESPECTIVELY

In this section we present a brief introduction of the models developed to describe this kind of device. In fact, the mechanism of break-up of droplets strongly influences their final size, therefore several numerical [18]–[20] and experimental studies [21][22] discuss the models of the pinch-off, analysing the strength of the forces involved in it. A better and general characterization of microfluidic device for droplets generation and manipulation was given by Seeman et al. [23]. In this thesis and in particular in our later discussion (section 4) we refer to the model proposed by Cristopher et al. [21] in which the process of droplet formation is analysed in the frame of the competition between the local fluid shear stress, that acts to deform the interface, and the capillary pressure ΔP_L, which resists to that deformation. In particular the authors investigate the transition between regimes, from squeezing to dripping. The model is an extension of a previously one developed by Garstecki et al. [22], which is valid only in the squeezing regime. Instead Christopher model is valid for the squeezing and for the dripping regimes; therefore it is useful to know that the transition from the two regimes occurs when the shear stress is exactly balanced by the Laplace pressure, so that the shear stress affects the size of droplets before they obstruct the channel. The transition is found at a critical capillary number $Ca^* \approx 0.015$ [21], therefore the pure squeezing regime is achieved for $Ca \ll Ca^*$. We report in

Figure 3 the circuit parameters taken in account in this section and in the article [21]. The model is divided in two stages: in the first the dispersed phase (water in our setup) grows inside the continuous phase channel, in the second we have the detachment of the droplets from the junction with the constriction of the neck (s in Figure 3) until the detachment. Christopher analyses the contribution to the droplet length of each of these two stages. During the first stage the growing of the droplet is controlled by three forces:

• Capillary force, which contrasts the interface deformation and therefore the break-up of the droplet. This force is due to the pressure difference between the head and the tail of the droplet along the flux direction that is calculated from the Laplace equation.

$$F_\sigma \approx \left[-\sigma\left(\frac{2}{b}+\frac{2}{h}\right)+\sigma\left(\frac{1}{b}+\frac{2}{h}\right)\right]bh \approx -\sigma h$$

EQUATION 1

where σ is the surface tension between the two liquids, b the droplet length, and h is the depth of the channels.

• Viscous force, due to the shear stress between the two fluxes, and it is calculated as the product of the viscosity of the continuous and dispersed phases and the shear rate γ due to the flowing of the continuous phase between the droplet and the upper wall (approximately w_c-b) of the continuous phase cannel. γ is approximated as the ratio between the velocity of the continuous phase (u_{gap}) at the interface with the dispersed phase, and the width of the shrinkage between the droplet and the channel wall as w_c-b.

$$F_\tau \approx \mu_c \frac{u_{gap}}{(w_c-b)}bh \approx \mu_c \frac{Q_c}{h(w_c-b)^2}bh \approx \frac{Q_c b \mu_c}{(w_c-b)^2}$$

EQUATION 2

• When Λ≥1/2 or Λ~1 the emerging droplet is influenced by the confinement within the microchannel. The obstruction of the channel by the droplet gives an additional force F_p exerting on the interface due to the increasing resistance of the continuous flow in the region between the droplet and the wall [22].

$$F_p \approx \Delta p_c bh \approx \frac{\mu_c Q_c b^2}{(w_c - b)^3}$$

EQUATION 3

Where Δp_c is the Hagen-Poiseuille pressure acting on the droplet while the channel is being closed by the droplet growing. The approximation is valid for $h >> w_c - b$ that is valid for the squeezing regime. Moreover when $\Lambda = {w_d}/{w_c} < 1/5$ the emerging droplets do not interact with the downstream microchannel walls and remain unconfined by the channel [24]. In this configuration the dependence of the droplet size on the dispersed phase flow rate is less consistent and it should depend only on the capillary number.

When the three contributions get balanced, i.e. the capillary force cannot contrasts the other forces, the second stage begin and the droplet neck start shrinking until its break-up. Therefore we can calculated two contributions to the final droplet length, the first that is relative to the first stage of the droplet grown until the compensation of the three forces can be derived resolving the equation $F_p + F_\tau + F_\sigma = 0$ in function of b:

$$(1 - \bar{b})^3 = \bar{b} \cdot Ca$$

EQUATION 4

where $\bar{b} \equiv {b}/{w_c}$ and Ca is the Capillary Number, it is notable from this equation that Ca is a fundamental parameter for the control of the droplet size.

The second length contribution is relative to the break-up stage in which we assume that the shrinking rate of the neck is equal to the continuous phase velocity [21] $u_{squeeze} \approx u_c = {Q_c}/{w_c h}$. Moreover the rate of grown of the droplet during the breakup phase can be approximate as $u_{growth} \approx {Q_d}/{bh} = {u_d \Lambda}/{b}$, where $\Lambda = {w_d}/{w_c}$ and $u_d = {Q_d}/{w_d h}$. The contribution to the final droplet length of the second phase is then calculated using Equation 4 and estimating the time of detachment $t_{squeeze} \approx {w_d}/{u_{squeeze}}$ and the rate of droplet growing u_{growth}.

Finally from the sum of the two different length contributions we obtain the expression of Christopher et al. for the droplet length in a T-Junction generator:

$$\hat{L} = \bar{b} + \frac{\Lambda}{\bar{b}}\phi$$

EQUATION 5

Where $\phi = {Q_d}/{Q_c}$ and $\hat{L} = {L}/{w_c}$ which is an effective length.

The expression for $\bar{b} \to 1$ and $\Lambda = \alpha$, where α is a constant factor of order 1 [22], tends to Garstecki et al. equation:

$$\hat{L} = 1 + \frac{\alpha}{\bar{b}}\phi$$

EQUATION 6

From the Equation 5, Christopher et al. proposed two relations that are important for the discussion of our results:

• The relation between Ca and the frequency of droplet production f:

$$\bar{f} = \bar{\beta} \cdot Ca^{\alpha}$$

EQUATION 7

where $\bar{f} = f t_{cap}$ is an effective frequency, $t_{cap} = {\mu_c w_c}/{\sigma}$, and $\bar{\beta}$ is the proportional coefficient. This relation is valid for viscosity ratio $\lambda = {\mu_d}/{\mu_c}$ between 1/6 and 1/350, and for Ca values between 0.04 and 0.001 [21].

• The relation between the droplet volume V, Ca and the fluxes ratio φ between the two liquid phases:

$$\hat{V} = \frac{\phi}{\bar{\beta}} \cdot Ca^{1-\alpha}$$

EQUATION 8

where $\hat{V} = {V}/{w_c{}^2 h}$ is an effective volume.

These relations will be used in the discussion of the devices performances in the characterization section (4.2).

2.4. Fluids and Materials

The choice of the liquids used in a microfluidic circuit is an important task. As a matter of fact, the properties of the liquids, first of all the viscosity and the surface tension, affect significantly the performances and the microfluidic characteristics of the circuit. In particular, for our purpose, viscosity and surface tension are relevant in the droplets generation phase, as discussed in the previous section, and are taken into account in the Capillary number that control the length of the droplets (Equation 4), their volume (Equation 8), and their generation frequency (Equation 7). Typically, in the literature water is used for the disperse phase and different kind of oil for the continuous phase, this because water is a suitable fluid for lot of application, since both biology experiments and chemistry reactions are in most cases performed in aqueous systems. Moreover it is possible to control the surface tension between the immiscible liquids using surfactant, amphiphilic molecules that are able to decrease the surface energy of a liquid.

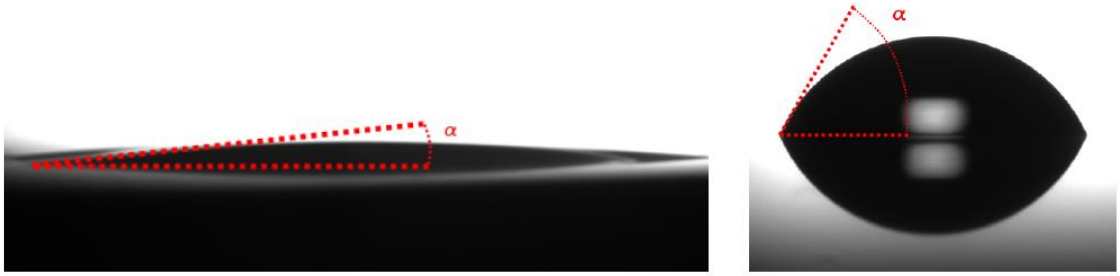

FIGURE 4 (LEFT) CONTACT ANGLE BETWEEN LN AND HEXADECANE (RIGHT) CONTACT ANGLE BETWEEN LN AND WATER

To prevent the Co-flow regime it is important that the continuous phase wet completely the channels walls and that the dispersed phase do not wet them. Therefore the interaction between the material in which the channels are realized and the liquids is fundamental in the realization of the devices. The coefficient of wettability k is the parameters used to measure this kind of interaction between a liquid and a solid surface. The coefficient is defined by the Young's Law from the angle that a droplet forms on the surface of a solid (Figure 4):

$$k = \cos \alpha_c = \frac{\sigma_{sg} - \sigma_{ls}}{\sigma_{lg}}$$

EQUATION 9

where α_c is the angle between the solid surface and the interface liquid-gas, σ_{ls} is the surface tension at the solid-liquid interface, σ_{sg} at the solid-gas interface, and σ_{lg} at the liquid-gas interface. The measurement of α_c for different solids and liquids is used to determine a scale of wettability where 0° is total wettability and angle >90° are reached by hydrophobic surfaces. Therefore to avoid Co-flow regime in a T-Junction we need to measure the contact angle between each liquids and the surface material, in our case Lithium Niobate, finding the best condition to achieve hydrophobic and lipophilic surfaces.

For what concern the solid materials, a large number of microfluidic devices are fabricated using PDMS (polydimethylsiloxane), an elastomeric, transparent and inexpensive polymer. Also other materials can compose the channel, like glass or silicon. They better withstand the swelling and the deformation in the presence of strong organic solvent, but at the price of a more complicated manufacturing process. PDMS is hydrophobic, hence it is a good choice to obtain W/O configuration because it prevents the dispersed phase from adhering to the channel walls [13]. The wetting control between the channel and the continuous phase is important in switching between W/O and O/W configuration. The functionalization of PDMS, glass and silicon usually can be used to change the superficial chemical properties of surfaces bonding a layer of molecules that can change the wettability of the material, so that with a hydrophobic functionalization W/O configuration is achieved, on the contrary O/W is reached with a hydrophilic functionalization of the channel surfaces (section 3.6).

Lithium Niobate wettability properties and its microstructuration are discussed in the next chapter, in order to demonstrate its applicability in the microfluidic field.

3. T-Junction in Lithium Niobate

3.1. Introduction

In this section we discuss for the first time, at best of our knowledge, the realization of a microfluidic device in Lithium Niobate crystals by means of femtosecond laser ablation at a wavelength of 800 nm. In particular, as part of our project, a droplet generator system has been fabricated due to the recent interest of scientific community on this research area. Among the main droplets generation devices, the T-junction geometry has been chosen as reference for this work, thanks to its simple realization and the capability to produce a rich and complex scenario of stable droplets patterns: [18][22] and references therein. A feasibility study of the microstructuration techniques for the realization of microchannel in Lithium Niobate is presented. The comparison between these different techniques supports the exploitation of laser ablation to get microfluidics device engraved in lithium niobate crystals (0). After that, we discuss all the steps that are necessary for the realization of a complete microfluidic device, from the sealing of the channel with a PDMS layer, to the functionalization of the walls of the channels. In the first section we present the preliminary study about the wettability of the lithium niobate as a starting point for its application in microfluidics.

3.2. Wettability of Lithium Niobate

As previously explained (2.4) one of the most important parameters in microfluidic is the contact angle between a liquid and a solid. A parameter that is directly related to the value of the surface tensions of the system (Equation 9) and therefore is able to give a measure of the wettability between a solid and a liquid. The contact angle is defined as the angle made by the intersection of the liquid/solid interface and the liquid/air interface. A high contact angle indicates a low solid surface energy or chemical affinity. In particular we are interested on the hydrophilicity and lipophilicity of the Lithium Niobate as, how discussed in section 2.4, we want a material that is lipophilic (as the majority of the solids) and hydrophobic. Therefore we collect

measurements of the contact angle of distilled water and hexadecane, the liquids chosen for the droplets generation. The measure of the contact angle was achieved with a software (developed by Lafsi group - Padova) able to fit the surface profile of a droplet, which allows the user to measure the contact angle. The droplets were deposited by a syringe pointed vertically down onto the sample surface, and two high resolution cameras captures the image at 90° one from the other. The volume of the droplets was 500 nL and the $LiNbO_3$ samples were all cleaned before the measurements using a simple procedure: soap and water, distilled water, isopropanol, and acetone under sonication. Moreover, the measures were taken on 6 different crystallographic surfaces of lithium niobate ±x, ±y, and ±z. For each of these faces more than 10 droplets were drop off and photographed by the two cameras along the two different crystallographic axes laying on the surface. All this attention to the crystallography of the crystal was necessary to estimate the effect of the crystal anisotropy on the surface energy of the crystals, in order to discover eventual phenomena that could affect the droplets generation and carriage in the $LiNbO_3$ microchannels. In fact, it is well known from literature that positive and negative faces of the z [25], [26] and y [27] surfaces have different chemical behaviour, starting from their etching rates that strongly depend from the crystallographic plane [28]. Finally the contact angles were measured also for LN functionalizated with a hydrophobic Self Assembled Monolayer (SAM), using Octadecyltrichlorosilane (OTS) with the same procedure discussed in section 3.6. The results of these measurements are reported in Figure 5 and Figure 6.

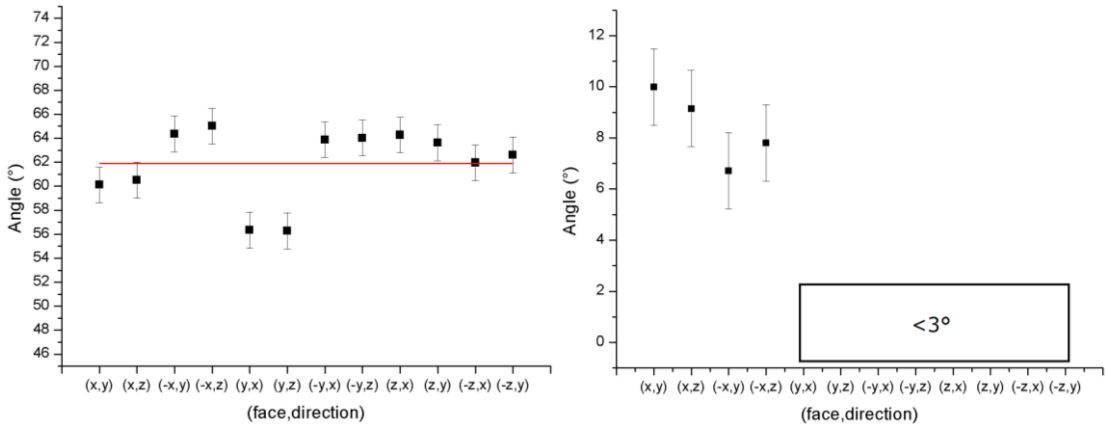

FIGURE 5 CONTACT ANGLES FOR THE DIFFERENT CRYSTALLOGRAPHIC FACES AND DIRECTIONS OF CONGRUENT LITHIUM NIOBATE FOR DISTILLED WATER (LEFT) AND HEXADECANE (RIGHT). IN RED THE VALUE OF THE AVERAGE CONTACT ANGLE.

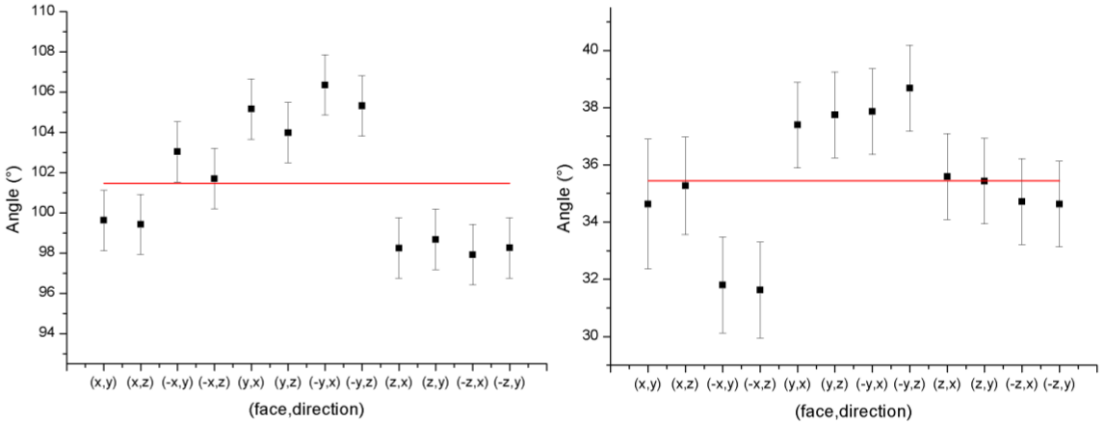

FIGURE 6 CONTACT ANGLES FOR THE DIFFERENT CRYSTALLOGRAPHIC FACES AND DIRECTIONS OF CONGRUENT LITHIUM NIOBATE FUNCTIONALIZATED WITH OTS FOR DISTILLED WATER (LEFT) AND HEXADECANE (RIGHT). IN RED THE VALUE OF THE AVERAGE CONTACT ANGLE.

As it can be seen in Figure 5 Lithium Niobate results to be extremely lipophilic and moderately hydrophobic with a contact angle between between 10° and 0° with the hexadecane and 65° and 56° with the water, so that it could be a good substrate for the W/O configuration. As expected (Figure 6) the OTS functionalization affect the wettability of the Lithium Niobate in all the direction, obtaining an enhancement of the contact angle of about 40° for the water and of about 30° for the hexadecane.

It is difficult to discuss these results, as the wettabilities are probably affected by different phenomena which could change the surface energies of the crystallographic planes during different sets of measurement: umidity, pressure and temperature. Moreover, also pyro- and piezo-electric effects can change the value of contact angles under pressure or temperature fluctuations, since they can lead to electro-wetting phenomena as net charge arise. Since the measurements do not follow the reproducibility condition, the statistical error cannot be used. Therefore we estimate an error of 1,5° from the sensibility.

Moreover only the measurements of the angles on the same surface are comparable, as they were taken from the same sets of droplets, one for each of the two cameras. Therefore we can derive the value of the compatibility parameter [29] for the couples (x,y)(x,z); (-x,y)(-x,z); (y,x)(y,z); (-y,x)(-y,z); (z,x)(z,y); (-z,x)(-z,y). The compatibility parameter for all this contact-angle couples results compatible in each condition (water, hexadecane, OTS functionalization), with value always lower than 0,8. Therefore the results

suggest that on every face the wettability is isotropic. Unfortunately we cannot discuss the other couples of faces and directions, as the low reproducibility of the measurements prevents their comparison. Consequently further studies are necessary to measure a possible anisotropy of the different faces. But the control of pressure, temperature and humidity needs to be done in a glow-box. In Table 1 we report the average value for alla the crystallographic direction.

	Water	Hexadecane
Congruent	62±1°	10° - total wetting
OTS	101±1°	35±1°

TABLE 1 AVERAGE VALUE OF ALL THE CRYSTALLOGRAPHIC DIRECTIONOF THE CONTACT ANGLE FOR WATER AND HEXADECANE IN LITHIUN NIOBATE CONGRUENT AND FUNCTIONALIZATED WITH OTS.

3.3. Microfabrication in Lithium Niobate

One of the main challenges of our project was the fabrication of micrometric channels in Lithium Niobate. As a matter of fact, very few studies realized structures of hundreds of micrometres in such kind of material [30], and the majority of the works on microfabrication in Lithium Niobate concerns the realization of ridge waveguides of few micrometres [31]–[37]. Therefore we start from a feasibility study of different techniques starting from what has been proposed in literature for optical devices. We take into account several techniques: wet etching, mechanical micromachining, ion implantation, Focused Ion Beam lithography (FIB), Reactive Ion Etching (RIE), laser ablation. For some of them we discuss only the results reported in literature, for other we present also some experiments and results we achieved. The choice of the fabrication technique was subjected to different parameters: time of fabrication, flexibility of the circuit pattern realizable, costs, quality of the channels, and reproducibility. Moreover, since the material is proposed as an optofluidic substrate also the optical quality of the walls of the channels is fundamental, especially for the good coupling between the waveguides and the droplets in the final device. Therefore the femtosecond laser ablation is discussed in-depth as it got the best results and was chosen for the realization of our platform. Since our purpose was not a complete characterization of these techniques applied to Lithium Niobate this section cannot be considered a definitive response to the problem.

3.3.1. Etching

A method often used for microstructuring of $LiNbO_3$ surface is the chemical etching process, which is also exploited to realize low-loss ridge waveguides [33]. Lithium Niobate is an extremely chemically stable material, so that only a bath in hydrofluoric acid is able to etch the crystal. Usually a solution of $HF:HNO_3$ in a 1:2 ratio is used, as it gives fewer defects and a lower roughness of the surfaces after the etching. In fact the main advantage of this technique is the quality of the sidewalls, since it has been optimized for optical purpose. However, this approach has two main disadvantages: the first is that the etching rate strongly depends on the crystallographic axes of the material [28], so that the material removal is asymmetric, furthermore the maximum etching rate is achievable on the -z face and it is about 1μm/h at room temperature [25], so that the realization of a microfluidic device with the same depth of the T-junctions used in this work would require tens of hours. Moreover, we need a technique able to realize channels on y-cut and x-cut crystals, because the realization of photorefractive reticle is efficient only in orientations different front the z axes; but this kind of orientation have etching rate even slower than –z surface (some nm/min at room temperature [28]).

We tried to solve these problems improving the wet etching with a previous step able to increase the etching rate and the isotropy of the process. It is known that the proton exchange (PE) in lithium niobate crystals is able to increase the etching rate of the material of about one thousand times [38] [32]. This is because a phase transition related to the process [39]. Another advantage of this treatment is that it diffusion in step-like [39], which would allow to obtain rectangular channels. So we made some tries using as source of proton benzoic acid at 240°C

$$LiNbO_3 + xC_6H_5COOH \leftrightarrow Li_{-x}H_xNbO_3 + xC_6H_5COOLi$$

First experiment realized on y-cut samples exhibit, as expected [32], a serious surface damage y due to the strain that occurred in the crystal. Therefore we repeat the PE treatment adding 1% mol. of C_6H_5COOLi to the benzoic acid (buffered PE), so that the reaction became less aggressive. The surface of the sample was not damage, but the diffusion time slow down as reported in Table 2.

	Diffusion Coefficient [$\mu m^2/h$]
Benzoic Ac. 230°C y-cut	1,52
Benzoic Ac. 230°C y-cut buffered 1%	0,08
Benzoic Ac. 230°C x-cut	0,10

TABLE 2 PROTON EXCHANGE DIFFUSION COEFFICIENT IN LITHIUM NIOBATE CALCULATED FOR DIFFERENT ORIENTATION AND CONDITION [39].

Therefore we tried PE with x-cut sample that, as expected from literature [38], does not exhibit surface damage. However also in this case the proton diffusion is too slow. Moreover we found that the PE stops at a depth of about 3 μm also after days of treatments at high temperature [40], this is due to an opposite electric field caused by the strain of the PE phase and the piezoelectric effect. Therefore the realization of channels of tens or hundreds of micrometres seems to be impossible, a solution to this problems could be proton exchange electrically assisted [41], becoming complicated with respect to other approaches and therefore less competitive. In fact the chemical etching process showed to require the combination with too much preparation steps: the realization of a suitable mask at the surface of the $LiNbO_3$ substrate by means of conventional lithography for the PE; the PE at high temperature and under an electric field for long time (days), and finally the etching in extremely hazardous solutions. This makes the whole fabrication process extremely complex and time consuming and not suitable for our purpose.

3.3.2. Micromachining - optical grade dicing

As an alternative, we tried to realize microfluidic channels by using a precision blade for optical grade dicing (thanks to MISTER lab of the IMM CNR of Bologna) as also proposed by Chauvet et al. [30], but even after several optimization steps the best roughness we were able to achieve on the bottom of the channel, Ra = (0.53 ± 0.01) μm (Figure 7), was almost a factor of two greater than the value obtained in the channels made by laser ablation (see section 3.4.1). Moreover, even if the optical grade dicing showed to be a good method to realize smooth vertical walls [35], as showed by SEM images (Figure 8); this technique cannot be exploited to realize a microfluidic device with an arbitrary shape and therefore it is mainly useful to create only

straight channels or waveguides. In addition the width of each single channel is strictly conditioned by the thickness of the blade.

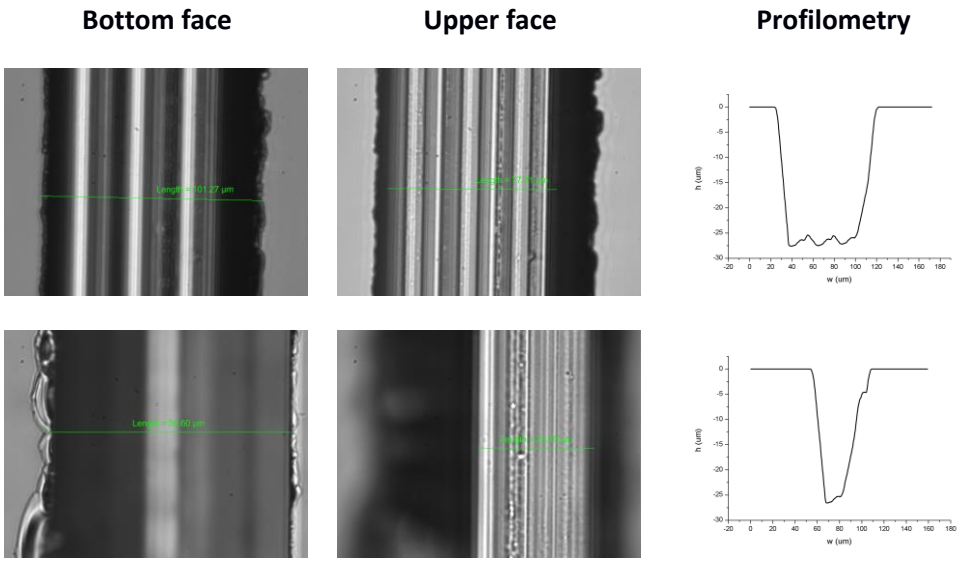

FIGURE 7. THE IMAGES OF THE BOTTOM SIDES AND THE UPPER SIDES OF TWO CHANNELS FABRICATED WITH OPTICAL GRADE DICING ARE REPORTED. THE NOMINAL VALUES OF DEPTH FOR BOTH IS 25 µm AND THE WIDTH IS 100 µm FOR THE FIRST AND 25 µm FOR THE SECOND. THE CHANNELS ARE CUT ALONG THE Z DIRECTION. ON THE RIGHT ALSO THEIR PROFILOMETRY IS REPORTED.

Furthermore, as it can be easily seen in the figures above, the quality of the upper edges of the channel were not good, an important feature considering the implementation of surface waveguides and their coupling with the channel walls. Hiwever this problem can be probably solved using a protective layer during the cut. Nevertheless, optical grade dicing could be a good solution for the realization of low roughness sidewalls and - although femtosecond laser ablation is more suitable for the realization of complex geometry as the T-junction - a cooperation between the two technique, the first for the droplets generation stage and the second for the analytical stage, could be a possible solution in the case the roughness of the femtosecond technique exhibits unsatisfactory results.

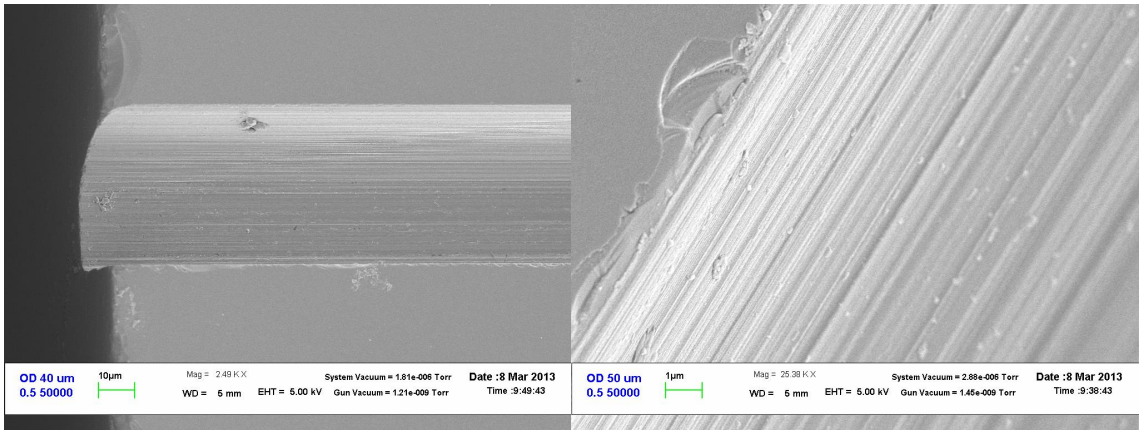

FIGURE 8. SEM IMAGES OF A CHANNEL FABRICATED WITH OPTICAL-GRADE DICING, ON THE RIGHT A PARTICULAR OF THE WALLSIDE

3.3.3. Other techniques

A lot of other different techniques have been used to produce waveguides: reactive ion etching (RIE) [42], ion beam wet etching enhancement [43], and focused ion beam lithography (FIB) [44]. In the following we briefly discuss the reasons of their exclusion as channels fabrication methods:

Reactive Ion Etching: Different efforts based on RIE on Lithium Niobate using SF_6, CF_4, and CHF_3 plasmas have been reported in literature, with etching rates of up to 50 nm/min and a $LiNbO_3$/Cr selectivity of 0.25 obtained on a variety of $LiNbO_3$ substrates[45][46]. More recently, the introduction of high density plasma tools such as inductively coupled plasma (ICP) enhanced the etching ability of this systems, and ICP etchers were introduced to etch $LiNbO_3$ using SF_6 and mixed CHF_3/Ar plasma [42], significantly increasing the etching rate up to 190 nm/min, with a mask selectivity of 10 over NiCr, good surface smoothness, and near-vertical sidewall angle [42]. However, at the best of our knowledge, the realization of structures of hundreds of micrometres have not been reported in literature since now, and surely new studies are necessary to optimize this technique for our purposes. Therefore, ICP-RIE is a notable process that can be taken in consideration as a valid alternative to femtosecond laser ablation.

Ion Beam damage: A study on the enhancement of the etching rate in samples of $LiNbO_3$ damaged by ion beam exposure was recently proposed by Bianconi et al. [43]. The study exhibits a very high etching selectivity of the heavily damaged ion implanted substrate regions, with an etching rate of up

to 100 nm/s. However, this process seems to be more suitable for sub-micro machining of $LiNbO_3$ crystals than for our purpose, with a depth of damage of 2 μm for Ti ions at 12.5 MeV.

Focused Ion Beam lithography: FIB technique allows obtaining a good roughness (few nanometres) of the channel walls as reported in [44]. However, the FIB milling process is mainly suitable for realizing nanochannels, since its material removal rate is several orders of magnitude smaller than the values typical of micromachining by femtosecond laser ablation. Sridhar et al. [44] report a milling time of 30s to realize a nanochannel that is 100μm long, 100nm wide and 100 nm deep (volume equals to 1 μm^3), an order of magnitude that is too far from our volume (equals to 5.4×10^8 μm^3).

In Table 3 a comparison between the three suitable techniques for the fabrication of microfluidic device in lithium niobate is reported. Therefore, methods and characterization of the femtosecond laser technique are reported in the following section, where an accurate study is presented.

Technique	Optical quality	Pattern flexibility	Sidewall Angle
Femtosecond Laser Ablation	Good (Ra~50 nm)	Every pattern, in prospect 3D and embedded structures could be made [47]	Vertical
ICP-RIE	Good	Every superficial pattern compatible with the lithographic mask	Near vertical
Optical grade Dicing	Good	Only superficial and straight structures	Vertical

TABLE 3 COMPARISON BETWEEN THE TECHCNIQUES THAT, AFTER THE FEASIBILITY STUDY, RESULT SUITABLE FOR THE FABRICATION OF MICROFLUIDIC STRUCTURES IN LITHIUM NIOBATE

3.4. Laser Ablation

The result of our feasibility study on different techniques for the Lithium Niobate microstructuration is the choice of femtosecond laser ablation. Since it allows realizing fluidic circuits at the micrometre scale in a reasonable time, with any desired geometry and good quality of the channels walls. Our results support the exploitation of laser ablation as a suitable technique to get microfluidics device engraved in lithium niobate crystals, so that

subsequent integration of several optical stages can be foreseen, thus paving the way for the realization of powerful optofluidic devices on this material.

In the following section we discuss the realization and characterization of channels and T-junction devices on $LiNbO_3$ substrates by means of laser ablation, a femtosecond laser at 800nm was used to create the microfluidic circuits, using different scanning velocities (100-500 μm/s) and laser pulse energies (1-20 μJ). All the fabrication processes were realized at the "Nonlinear Photonics Group" of prof. C. Denz (Institute of Applied Physics of the University of Münster, Germany) and then characterized at the Physics and Astronomy Department of the University of Padova.

3.4.1. Experimental and characterization

A pure y-cut $LiNbO_3$ sample with congruent composition was cut from a commercial wafer (Crystal Tech.) polished on both sides. The T-junction was realized on the +y face of the $LiNbO_3$ sample by using a Ti:Sapphire femtosecond laser (Coherent Inc.), with an operating wavelength of 800nm, 1 kHz repetition rate and 120fs pulse length. The laser beam was focused at the surface of the crystal by using a 50x ultralong working distance microscope objective (NA=0.55) and the workstation was equipped with a computer-controlled XYZ translation stage, which allows moving the $LiNbO_3$ sample with high spatial resolution. The addressed volume of the microfluidic channels was scanned successively with a resolution of 10 micron and 15 micron in the horizontal and vertical direction, respectively. The tool path was optimized to achieve flat boundaries and even surfaces. Moreover, a constant air flux was maintained at the upper surface of the sample during the micromachining process, in order to eject the ablated material out of the channels.

Several tests were performed to study the laser ablation process on lithium niobate by varying the values of scanning velocity (50-1000μm/s) and energy (1-20 μJ) used to engrave the T-junction, in order to find the best parameters to be used in our particular experimental set-up. Figure 9 to Figure 12 illustrates the microscope images of U-grooves (200 x 250 μm^2) realized with the femtosecond laser by using different parameters. For each structure the bottom of the engraved areas (Figure 9), the corresponding

upper edges (Figure 10), the sidewall (Figure 11) and the lateral edges (Figure 12) are shown.

The nominal depth of the U-grooves was set to 100 μm, but the images of the lateral edges in Figure 12 clearly show that its final value strongly depends on the pulse energy used during the micromachining process, as expected since the ablation depth increases with increasing energy fluence. For example, the effective depth was reduced by a factor of two in the U-groove realized with energy of 1μJ and a speed of 500μm/s. Indeed, in this case $LiNbO_3$ is not completely crumbled and removed from the microchannel, thus preventing the further ablation of the underlying material in the micromachined area and significantly decreasing the quality of the channel walls. Although good quality microchannels could be realized with the same pulse energy of 1μJ by simply decreasing both the scanning speed and the step between parallel lines, this will result in an extremely time-consuming process. On the contrary, the images of the upper edges in fFigure 10 show that a slow scanning speed has to be avoided if a pulse energy of 20μJ is used, since slivers are produced during the micromachining process resulting in scratches at the edges of the channel. This problem could be avoided by using faster scanning speeds, but in this case the surfaces of the channel walls present more defects and irregularities and some dark debris still exist (Figure 11). Therefore, to shorten the preparation time of the microfluidic circuit and obtain high quality walls of the channels, the scanning speed and the energy pulse used to create the investigated T-junctions were set to 5μJ and 500μm/s, respectively. Moreover, the quality of the boundaries and surfaces of the ablated area were significantly improved by further scanning each final U-groove with a 4-times higher resolution. The T-junction was then cleaned in ultrasonic baths of water, isopropanol and acetone.

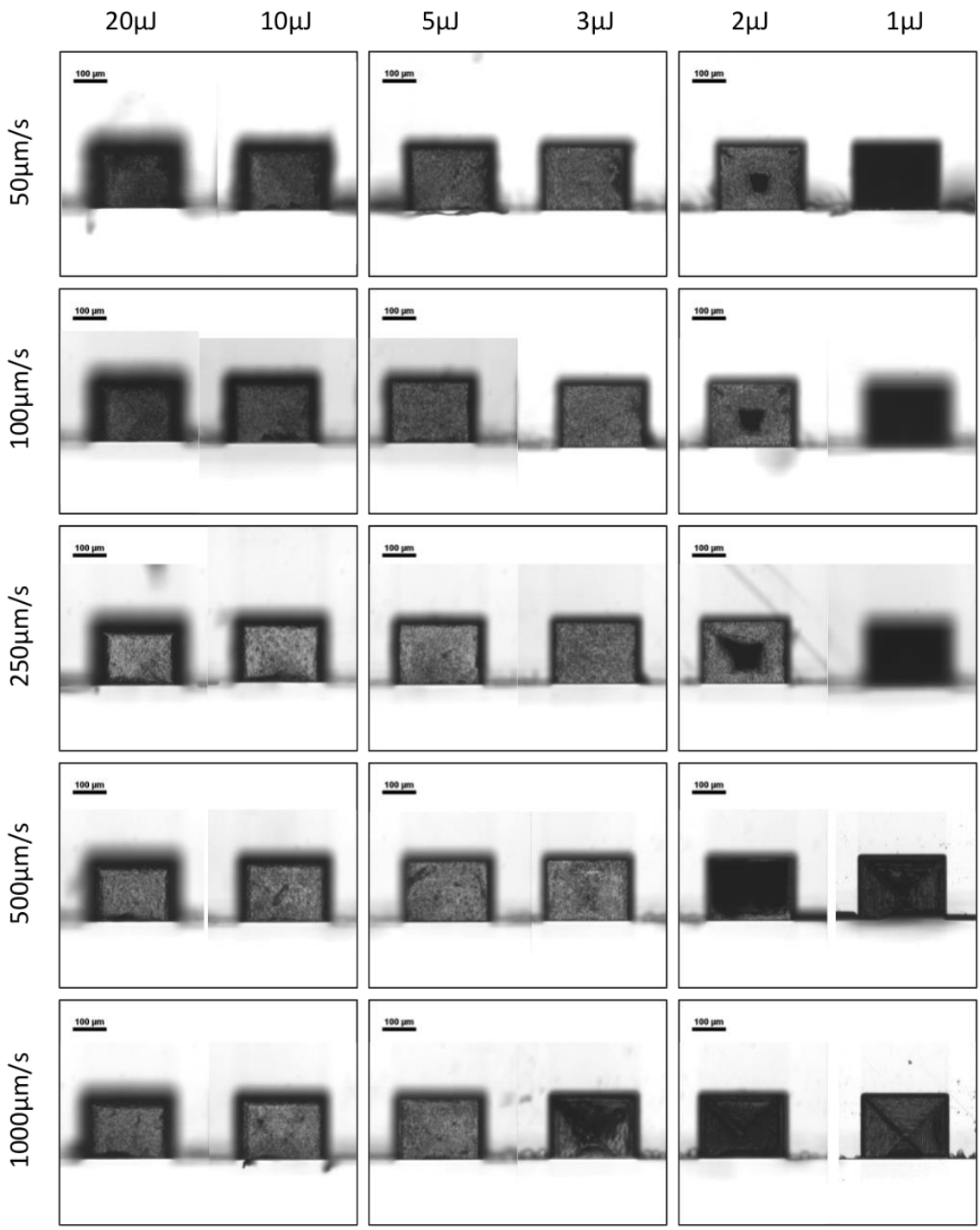

FIGURE 9 MICROSCOPE (40X) IMAGES OF U-GROOVE REALIZED AT THE EDGE OF A Y-CUT LN SAMPLE, BY USING DIFFERENT SCANNING SPEEDS AND DIFFERENT VALUES OF THE ENERGY PULSE. FOR EACH STRUCTURE THE BOTTOM SIDES OF THE ENGRAVED AREAS IS SHOWN.

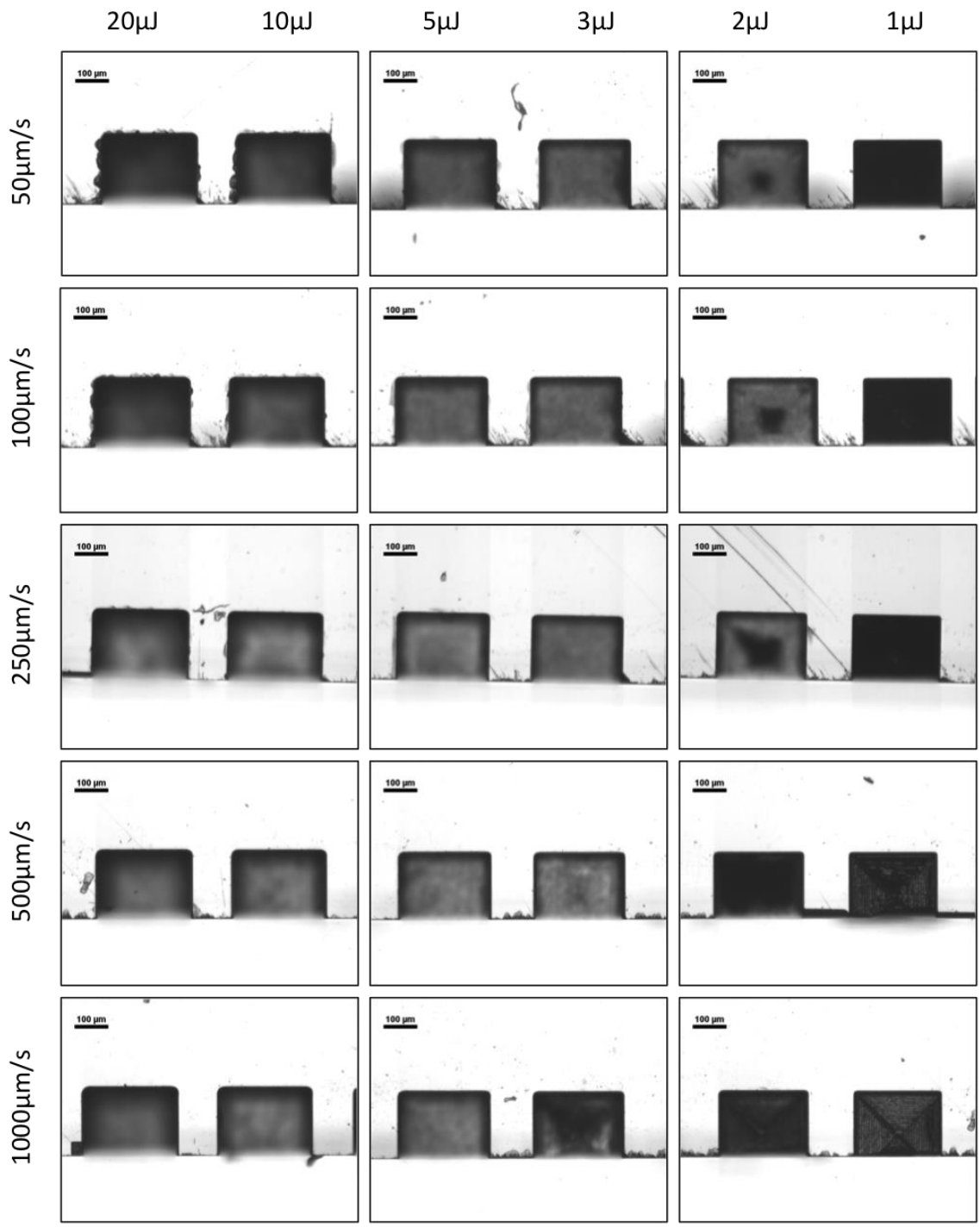

FIGURE 10 MICROSCOPE (40X) IMAGES OF U-GROOVE REALIZED AT THE EDGE OF A Y-CUT LN SAMPLE, BY USING DIFFERENT SCANNING SPEEDS AND DIFFERENT VALUES OF THE ENERGY PULSE. FOR EACH STRUCTURE THE UPPER EDGES OF THE ENGRAVED AREAS ARE SHOWN.

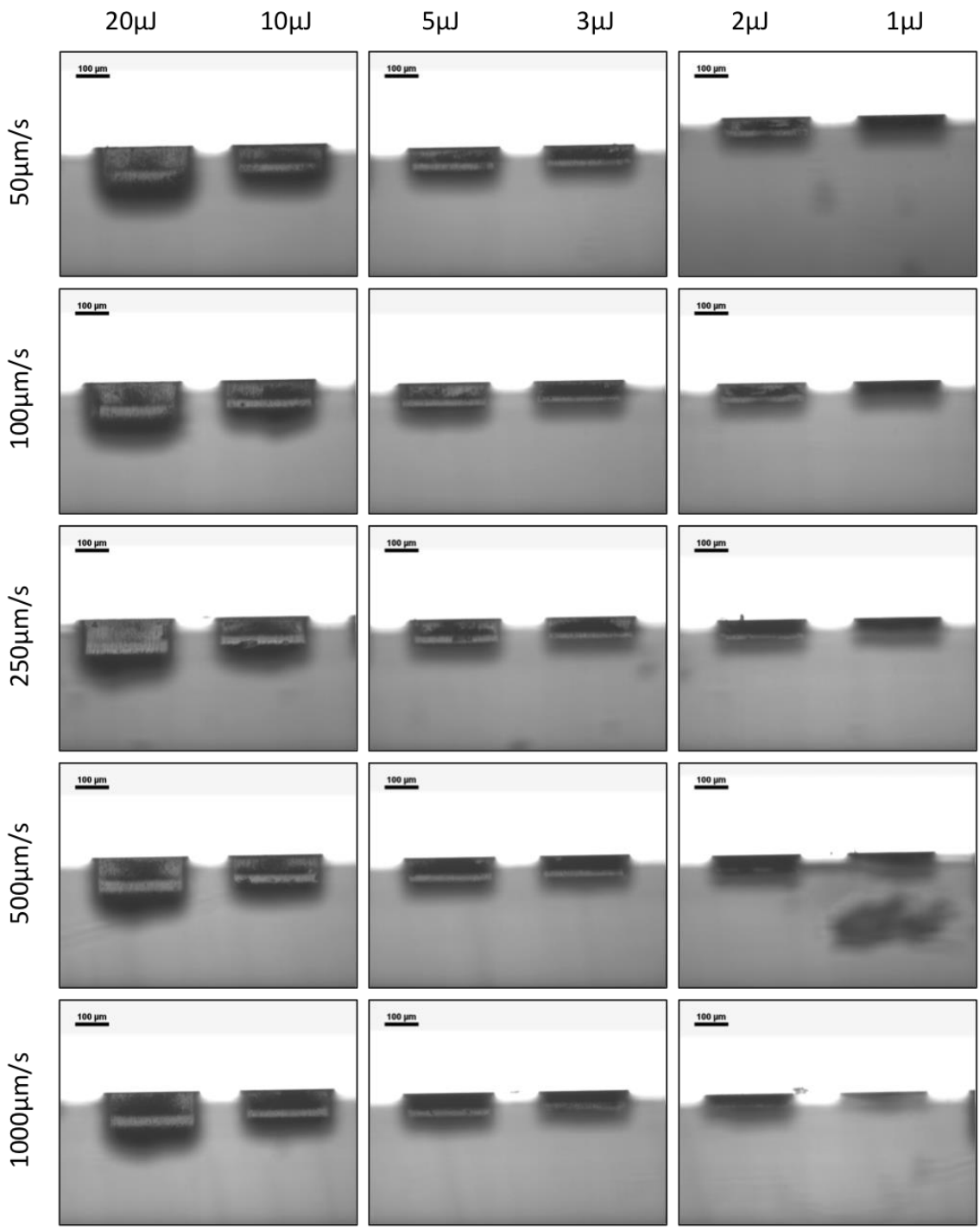

FIGURE 11 MICROSCOPE (40X) IMAGES OF U-GROOVE REALIZED AT THE EDGE OF A Y-CUT LN SAMPLE, BY USING DIFFERENT SCANNING SPEEDS AND DIFFERENT VALUES OF THE ENERGY PULSE. FOR EACH STRUCTURE THE SIDEWALLS OF LATERAL VIEWS ARE SHOWN.

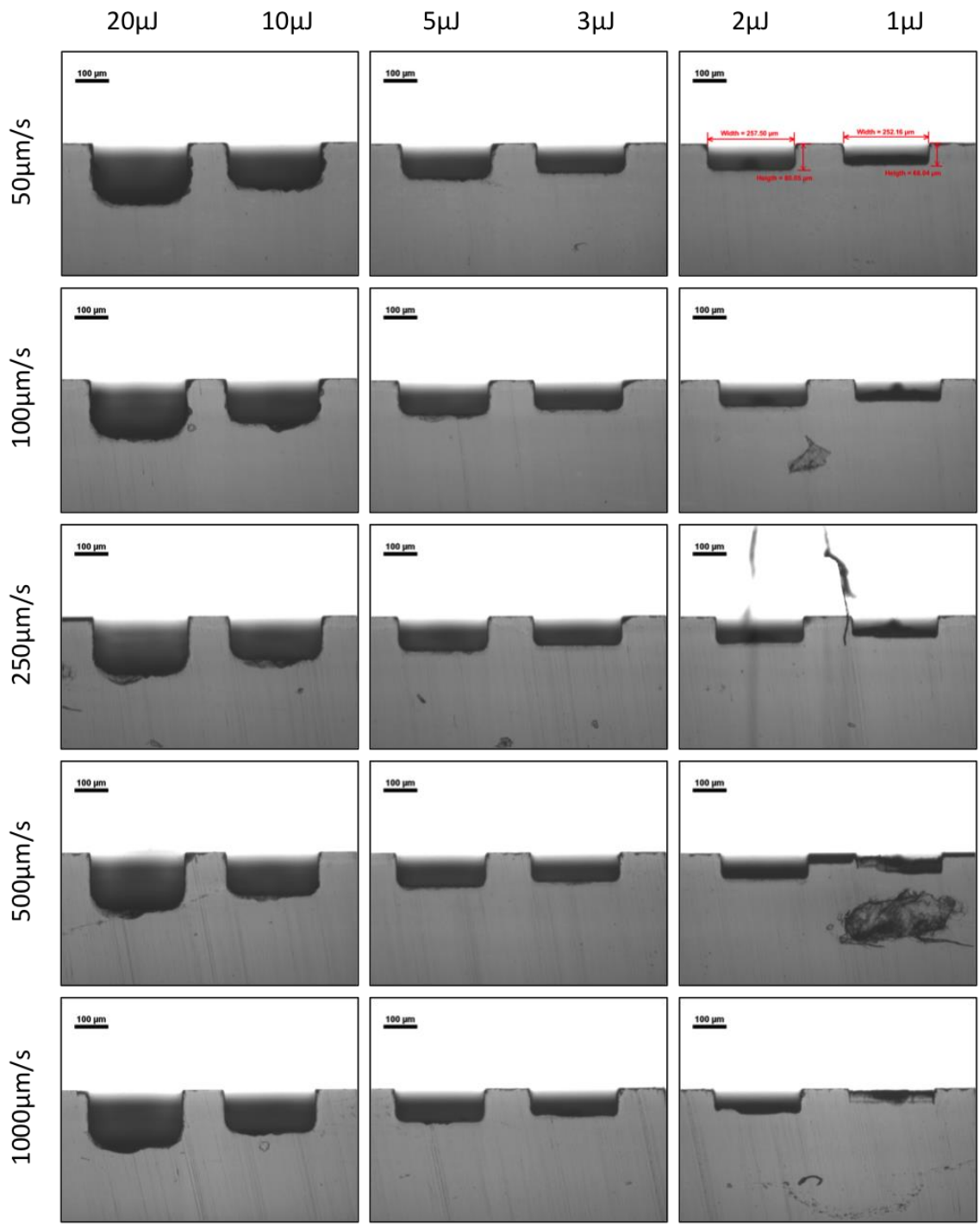

FIGURE 12 MICROSCOPE (40X) IMAGES OF U-GROOVE REALIZED AT THE EDGE OF A Y-CUT LN SAMPLE, BY USING DIFFERENT SCANNING SPEEDS AND DIFFERENT VALUES OF THE ENERGY PULSE. FOR EACH STRUCTURE THE EDGES OF THE LATERAL VIEWS ARE SHOWN.

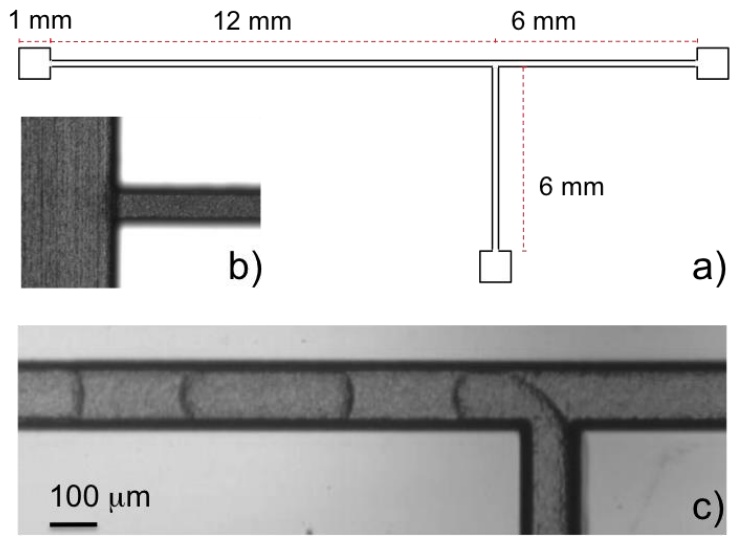

FIGURE 13 (A) SCHEME OF THE FINAL T-JUNCTION; (B) TOP VIEW OF THE CONNECTION BETWEEN THE MICROCHANNEL AND THE INLET RESERVOIR; C) TOP VIEW OF THE T-JUNCTION FOR DROPLET GENERATION. THE T-JUNTION WAS REALIZED WITH A SCANNING SPEED OF 500 μM/S AND ENERGY OF 5μJ

The scheme of the final circuit is reported in Figure 13, where the microscope images of the inlet reservoir and the T-shape droplet generator are also shown. For the two investigated T-junctions (TJ1 and TJ2 respectively) the sizes of the microchannels have been measured by using a surface profilemeter (KLA Tencor P-10) and the corresponding values are listed in Table 4; the reservoirs have an area of $1mm^2$ and the same depth of the microfluidic channel. The widths of the channels have a spread at least of 5% and a depths spread of 1%, moreover we achieved values near the nominal ones, resulting in a good quality and uniformity of the channel sections, and of the pattern writing.

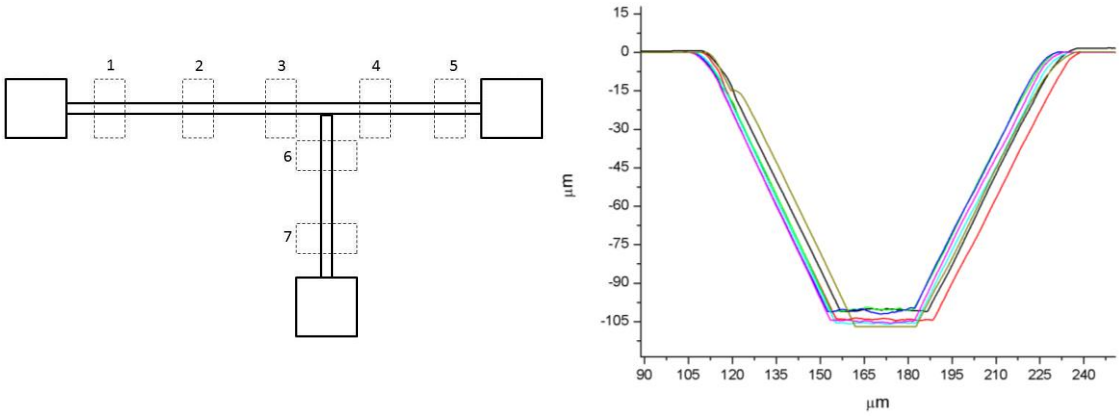

FIGURE 14 ON THE LEFT THE SCHEME OF THE REGION IN WHICH THE T-JUNCTIONS WERE MEASURED WITH PROFILOMETRY. ON THE RIGHT AN EXAMPLE OF T-JUNCTION PROFILE COMPARED (TJ2).

T-junction	w_c (μm)	h(μm)
TJ1	126 ± 2	89 ± 6
TJ2	125 ± 3	100 ±1

TABLE 4. SIZES OF THE MICROCHANNELS FOR THE T-JUNCTIONS TJ1 AND TJ2. THE VALUES OF WIDTH (W_C) AND DEPTH (H) WERE OBTAINED USING A SURFACE PROFILOMETER.

The profilometer was also exploited to estimate the roughness Ra relative to the bottom of each microfluidic channel, thus comparing the obtained value with those relative to other techniques. In particular, in the analysed T-junctions the mean roughness was estimated to be Ra = (0.26 ± 0.02) μm. Even if the roughness of our T-junction does not compromise the microfluidic performances of our device, obviously it needs to be improved to allow combining the fluidic channels with optical components. As a matter of fact, we are currently investigating also the roughness of the lateral walls of the channels made by laser ablation, being this parameter crucial for developing optofluidic devices on $LiNbO_3$. With this aim AFM (Atomic Force Microscopy) measurements were done, both on the lateral face and the bottom face of the U-groove structures. First results reported in Figure 15 exhibit an average roughness (Ra) of 51,2 nm for the sidewall and a Ra of 170 nm for the bottom face. Moreover the two surfaces have also different structures with the first composed of little structures that could be due to re-deposition of ablated material, or to re-grown of the surface itself; the bottom surface have bigger structure that are probably related to the focus dimensions and the resolution of the technique. Further studies, also on the surface composition, will be implemented.

Furthermore, an improvement of the surface quality could be necessary to optimize the coupling between channel and waveguide, therefore the idea is to combine the laser ablation procedure with a post-treatment of the ablated surfaces, by means of chemical etching process or magnetorheological polishing method [48][49], in order to recover the optical quality of the channel walls. In particular, the etching process has been already exploited in optofluidic devices realized by femtosecond laser ablation on fused silica: in [47][50] the authors obtained a sidewall roughness less than 30 nm and a larger roughness of about 200 nm on the bottom of the channels, which is comparable with our results.

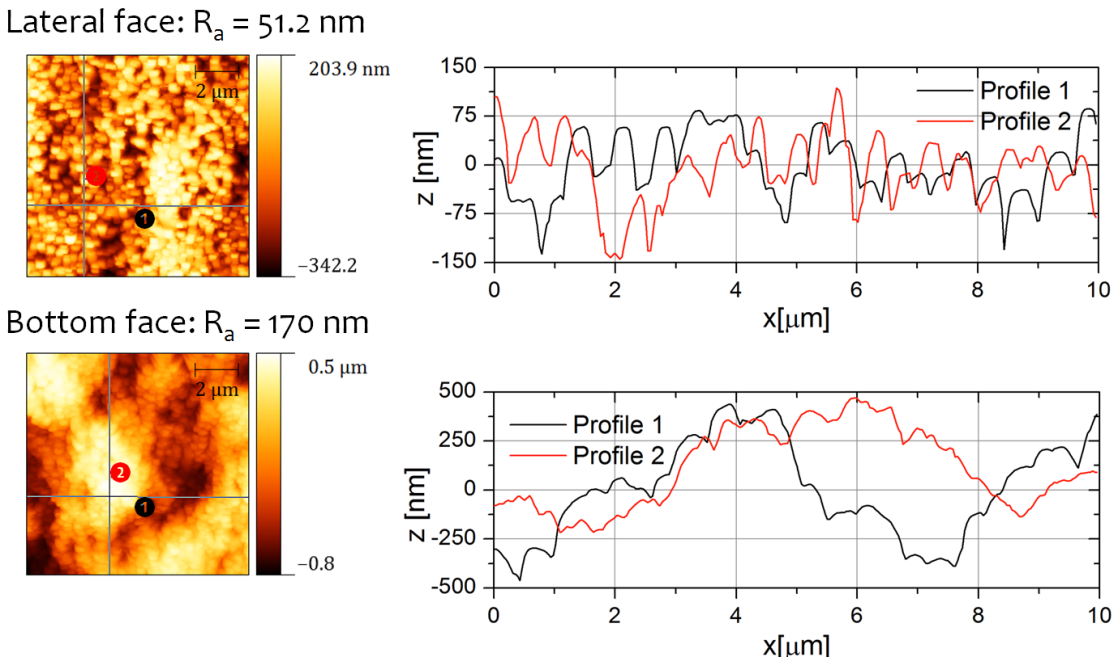

FIGURE 15 AFM IMAGES AND PROFILOMETRY OF THE LATERAL FACE (UP) AND THE BOTTOM FACE (BOTTOM) OF A U-GROOVE STRUCTURE FABRICATED BY LASER ABLATION IN A Y-CUT LN CRYSTAL (5 µJ, 500 µm/s). FOR EACH THE VALUE OF THE AVERAGE ROUGHNESS (R_A) IS REPORTED.

Therefore as a prelimary step the ablated U-grooves discussed previously were etched in a solution of EtOH-HNO_3-HF 8:2:1, since this solution give a better surface quality after the etching [33], monitoring the effect of the etching with microscopy took at different time (5, 10, 35, 95, 300, and 720 minutes). The results of this study are reported in Figure 16 where we show the images of the lateral surface of the U-groove structures taken after 5, 10 and 35 minutes of etching. The times of etching showed are the most important; as after 35 minutes the samples start being too much damaged and therefore less transparent. The bath of 10 minutes seems to give the best results in terms of cleanness as most of the dark regions, which are probably residual of the ablated material, were dissolved. On the contrary, the quality of the lateral surface roughness does not exhibit improvement and therefore this treatment seems not able to achieve more transparent and less light-scattering samples. Therefore this treatment of the ablated structures could be useful only for the cleaning of the samples showing the dark regions. Therefore the combination of laser treatment and etching should be study using the radiation only to damage the crystal, without ablating the material.

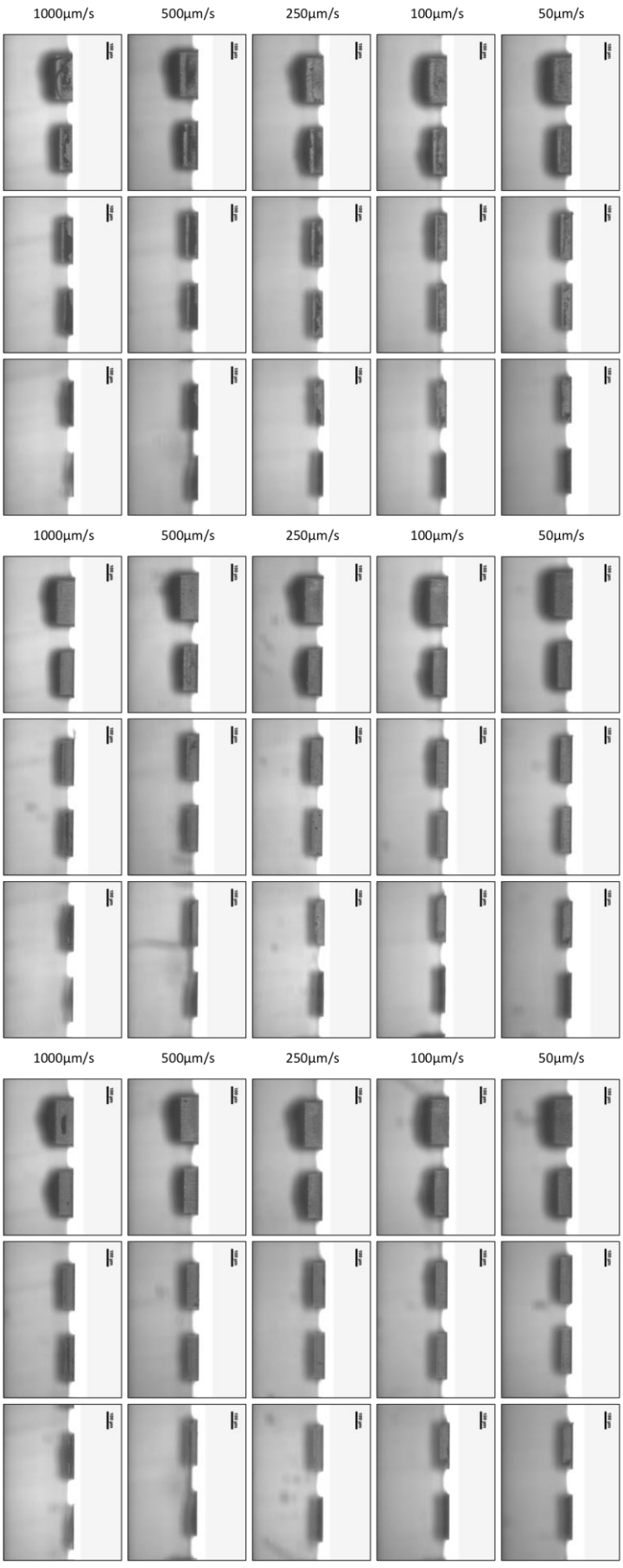

Figure 16 In the figures the U-grove samples discussed previously where etched in a solution of $EtOH/HNO_3/HF$ for three different times: **5** minutes (on the left) **10** minutes (on the center), **35** minutes (on the right)

3.5. Sealing of the channels

For the first performance tests the two T-junctions were sealed with a thick layer of polydimethylsiloxane (PDMS), where the inlets and the outlet for the flowing liquids were previously realized (Figure 1). In the final prototype the closure will be achieved with a Lithium Niobate top. PDMS was chosen because it is the principal polymer used in microfabrication due to its excellent properties that make it suitable as a stamp material and as a structural material: it is optically transparent, it is inexpensive and durable, it is chemically inert, it is isotropic and homogeneous, it does not swell with humidity, and it has good thermal stability. To bond the LN and the PDMS surfaces, they both underwent an O_2-plasma treatment (plasma system FEMTO) for 60 s at 200 W, with an oxygen flow rate of 10 sccm at $3x10^{-3}$ mbar. As it happens also for other oxide materials (glass, quartz), it probably took place a condensation reaction between the hydroxyl groups of both the materials when the surfaces got in contact, and became covalently bonded. Different adhesion proofs were implemented on the different orientations of the crystal (x, y, and z-cut) without observing particular anisotropies of behaviour. The adhesion between PDMS and LN results good, as the channels resisted to flux rate of 380 μl/min and more before start leaking.

Moreover, it was easier to remove the PDMS in case of necessity, as mechanical peeling was successful in most cases and the eventual residual layer was removed with acid bath (HNO_3, HCl, or diluted HF in the hardest cases) without affecting the $LiNbO_3$ thanks to its chemical stability.

The layer of PDMS was fabricated using a soft lithographic method. We use, as substrate for the polymerization, a crystal of silicon treated with Trichloro(1H,1H,2H,2H-perfluorooctyl) silane vapour to passivate the master surface, and so to facilitate the PDMS removal once cured. The liquid prepolymer of PDMS was mixed with a cross-linking agent (Syligard 184) in a 1:10 weight ratio, and then poured on the silicon surface. In that way after the solidification of the polymer under a treatment of 1 hour at 90°C, the PDMS layer was peeled off, and the surface in contact with the silicon resulted extremely smooth, improving the adhesion with the Lithium Niobate. For the fabrication of the inlets and outlets used to carry the liquids in the devices, pipes of polyethylene with an internal diameter of 0,5 mm were

used. In particular they were attached on the silicon layer before pouring the PDMS prepolymer, and in that way directly bonded to the PDMS during the reticulation, with the same geometry of the reservoir fabricated in the Lithium Niobate (Figure 1). The use of additional PDMS around the tubes allows a hermetic closure.

3.6. Functionalization

The first experiments with the droplets generation were taken without any further treatment of the channel, using three hydrophobic walls of LN and one of PDMS. First images took with the set-up explained in section 4.1 exhibited a co-flow regime (Figure 17.Up) between water and hexadecane, a regime that we did not expect. The conditions of the flows were varied in a wide range (flow rates from same μL/min to about 200 μL/min), but the regime did not change. Furthermore, we noticed that the water flow was irregular along the channel, and in some point was slower. This anisotropy was due to an irregular wettability along the channel, which in some points caused the pinning of the water at the walls. It was clear that the wettability of water on LN was still too high, and therefore the oil phase was not able to completely wet the channel walls. Hence, co-flowing was a more stable regime in comparison to squeezing or dripping. This kind of problems can affect microfluidic devices also in other materials like PDMS [51], and can be solved with a surface treatment able to increase and homogenize the hydrophobicity of the walls, that could have changed during the fabrication process. In fact both the acid cleaning and the O_2-plasma treatment used to bond the PDMS can change the surface energy of the LN increasing its hydrophilicity. We decide to flow into the device a solution of OTS molecule (Octadecyltrichlorosilane) in toluene ($C_6H_5CH_3$) with a concentration equals to 10 mM for about 30 s, then we flow the solvent alone to remove the exceeding molecules. By heating the device at 65°C for 20 minutes we assure the toluene evaporation. The toluene solvent swells the PDMS but after the treatment we observe that the channel comes back to its initial dimension without damages. We report in Figure 17 a comparison between the flow in a channel before and after the OTS treatment, the images shows a complete change in the flow regime with the same flow rate, that indicates

that the OTS can silanize the PDMS resulting in grafting of the octadecyl chain onto the surfaces. This allows us to confirm that the LN and PDMS surfaces can be silanizated (see section 3.2)[52] resulting in a more lipophilic surfaces, and also assuring a more homogeneous hydrophobic surface. We choose to use toluene instead of other solvents (for examples hexadecane) because the solution of OTS in toluene was already used in the laboratory for other experiments. The resulting coating of OTS ensures the reproducible behaviour of droplets in the junction. However, other solvent should be tried in future, in order to decrease the swelling of PDMS and to improve the homogeneity of the wetting properties on the surfaces. The cleaning of the channels, after experiments and when necessary, was achieved using isopropyl alcohol (CH_3CH_3CHOH) at a concentration ≥ 95 %, this because its low swelling coefficient in PDMS (only 1.09 [53]), and because it evaporates quickly from the channel taking the device at 70°C for a couple of hours.

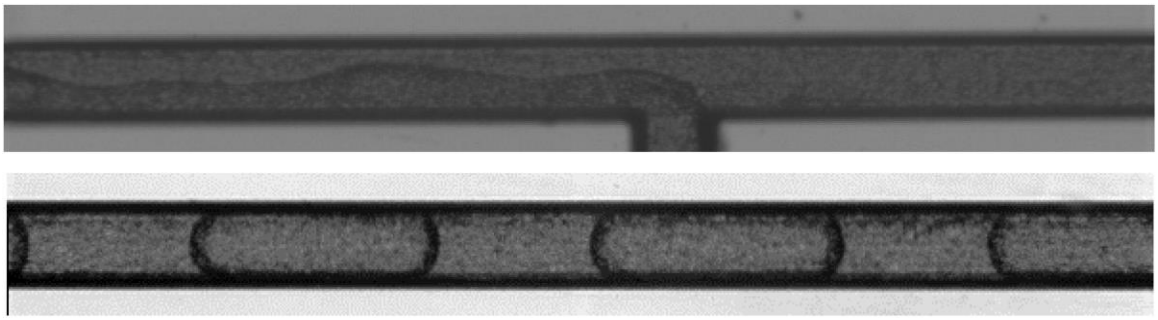

FIGURE 17. UP) CO-FLOW REGIME IN A T-JUNCTION WITHOUT HYDROPHOBIC FUNCTIONALIZATION (Q_c=5 ML MIN^{-1} AND Q_D=5 ML MIN^{-1}); DOWN) SQUEEZING REGIME IN THE SAME CONDITION AFTER THE FUNCTIONALIZATION OF THE CHANNEL WALLS.

4. T-junction characterization

In this section the process of generation of water droplets in oil, as commonly used in biological applications, is characterized and the microfluidic performances of our $LiNbO_3$ based T-junctions prototypes (TJ1 and TJ2) is discussed, demonstrating a high process reproducibility and low dispersion of droplet size distribution. Moreover we compare our data with the Cristopher et al. model [21] finding an excellent agreement for Capillary number higher than $8 \cdot 10^{-3}$. The oil used for the continuous phase was hexadecane with different concentrations of a surfactant (SPAN® 80) in order to change the surface tension between the liquids.

Furthermore, we present the set-up used for the characterization, in particular the liquids and the surfactan; the pump used to control the flow rates of the two liquid phases; and the set-up for the acquisition and elaboration of the droplets images and videos.

4.1. Setup

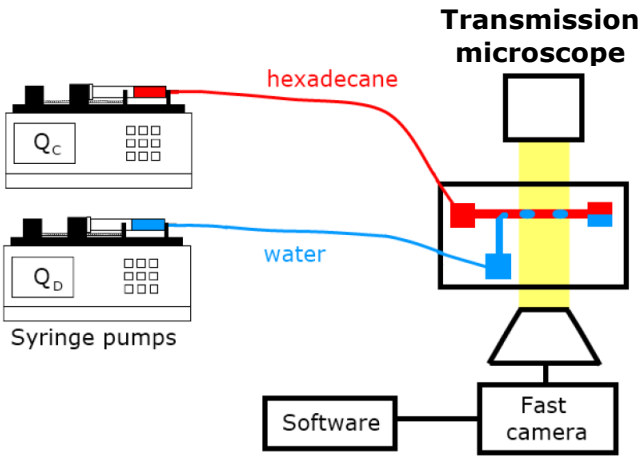

FIGURE 18 SET-UP FOR THE CHARACTERIZATION OF T-JUNCTION DROPLETS GENERATORS.

T-junction TJ2 (Table 4) was chosen to characterize the droplet generation performance and to study in depth the agreement of our devices with the Christopher et al. model. Therefore, two immiscible liquids were introduced into the microfluidic devices through flexible polyethylene tubes (0.5 mm ID) by using two independent automated syringe pumps (PHD 2000, Harvard

Apparatus) (Figure 18), which allow working at constant flow rates between 1 and 500 L/min with a nominal accuracy of 0,5%. Hexadecane ($CH_3(CH_2)_{14}CH_3$, CAS number: 544-76-3, viscosity 3cP, density 0,77 g/cm^3) and distilled water were used as continuous phase and dispersed phase, respectively [6]. Moreover we characterize the behaviour of the devices in function of the surface energy, therefore we added SPAN® 80 surfactant to hexadecane to decrease the surface energy at the water-oil interface and facilitate droplets formation [6]. The surfactant concentration was set to 0,08% (w/w), which is above the critical micelle concentration (0.03% (w/w) [6][23] for hexadecane, and the results were compared with the ones without surfactant. The images of the droplet generated (Figure 13.c) by the T-junctions were obtained using a monochrome camera (MV D1024 CMOS, Photonfocus) coupled to an inverted microscope (Eclipse Ti-E, Nikon), whereas the videos were acquired by using the fast camera (Phantom VRI v7.3). Every video was acquired with a different sample rate in function of the droplets velocity, so that a suitable number of frames (more than 100) were collected for every droplet during its transit in the range of vision of the camera. Later, all the videos were divided in single frame and then analysed with a software, made by the LaFsi group of the University o Padova [6], which is able to detect the shape of the droplets and to follow their movement through the subsequent frames; therefore it can derivate the length of every droplet and the frequency of generation (section 4.2). Different videos were collected changing the flow rates of the two phases and the surfactant concentration in the continuous phase. For both hexadecane with and without surfactant the flow rate of the continuous phase (Q_c) was fixed at the values of 5, 7, 10, 12, 20, 30, 35, and 40 μL min^{-1}. Then the flow rates of the dispersed phase (Q_D) was set to the different ratios (Q_D/Qc) of: 0,1; 0,3; 0,5; 0,7; 1; 1,5; and 2.

4.2. Software analysis

The software adopted for the droplet detection was based on the colour contrast analysis of the video sequences collected for the droplet flowing through microfluidics channels. A Phantom VRI v7.3 video camera was used for the video collection and the video splitting into different sequences was

performed with the software imagej (http://imagej.nih.gov/ij/), the goal of which was the object recognition using their colour contrast. In this section the analysis procedure adopted in this thesis is discussed considering only the software functions necessary for our work, i.e. the droplet data transfer from a video to a numerical format. At first the software gave a brightness value to each pixel of the image background. In order to distinguish the background pixels from the droplet ones the software automatically compared two consecutive video sequences: the background pixels were which remained similar in the two sequences. Consequently from the difference between the value of the background pixels and the pixel of every single frame the software was able to recognize the objects, in this case the droplets. Only the pixel with a difference value above a given threshold (which can be set up) were taken into account as objects by the software, we call this pixel object-pixel. Therefore the software by the mean of another threshold value categorized the object-pixel in recognized and excluded, in Figure 19 they are represented in magenta and blue respectively. After the identification the next step was the object tracking, i.e. the measurement of the droplets parameters.

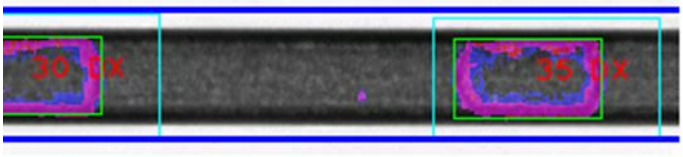

FIGURE 19 IMAGE OF THE SOFTWARE SHAPE DETECTION OF TH 35TH DROPLETS OF A SET, IN MAGENTA AND BLUE THE SOFTWARE DETECTION OF THE DROPLET BORDER. IN GREEN THE RECTANGLE THAT REPRESENTS THE DROPLETS DIMENSIONS. IN CYAN THE RECTANGLE AREA WITH THE CHARACTERISTIC DIMENSION OF THE DROPLET SET UP BY THE USER.

First of all the users drew 3 rectangles which defined

- the area in which the software had to work, in order to exclude the useless zone out from the channel borders;
- the characteristic dimensions of our object (Figure 19);
- a dimensional limit in order to exclude object with lower dimensions.

Finally we could proceed to the automatic tracking of the droplets from which we got these parameters:

- the length between the two extremities of a droplet for every frame in which it was tracked;

- the position of the droplet compared to the channel length;
- the number assigned to every droplet.

Therefore the equation of motion of every droplet was calculated from the linear interpolation of the droplet positions (in pixels) in function of the frame number (which is a time measure). From the law we could calculate the velocity and the frequency as the inversion of a reference time of transit at the half-channel length. In conclusion the software estimated the average value of length for every droplet, its standard deviation, its velocity and the reference time of transit, which were then converted in suitable units of measurement.

4.3. Results and Discussion

The T-junction TJ2 performance was tested in terms of the droplet formation frequency and droplet size distribution. The analysed devices have a dispersed to continuous channel width ratio of 1 within 2%, a viscosity ratio of 1/3, and were tested in a range of Capillary Number (Ca) between 0.0004 and 0.07. We remind that the Capillary number can be calculated as:

$$Ca = \frac{\mu_c v_c}{\sigma} = \frac{\mu_c Q_c}{\sigma w_c h}$$

EQUATION 10

where μ_c is the viscosity of the continuous phase (hexadecane), v_c the velocity of the continuous phase, and σ the surface tension between the two liquids respectively [23][12]. The values of w_c and h for the T-junctions are reported in Table 4; and the value of the interface energy between the liquids σ is 50.7 ± 0.3 mN m^{-1} for the pure hexadecane, and 10 ± 0.3 mN m^{-1} for the 0,08% surfactant concentration [12] about 5 times lower. Finally μ_C is 3.0041 mPa s at 25◦C (www.ddbst.com).

4.3.1. Frequency droplets generation

The droplet generation frequency *f* depends on the flow rates of the two immiscible liquids Q_C and Q_D. The highest value of *f* is therefore usually limited by the maximum pressure (typically a few bars) the microfluidic channels are able to sustain. In particular, in a T-junction geometry the

frequency does scale in a nonlinear manner with the ratio Q_D/ Q_C (Equation 7) [12], [23], [54], [55].

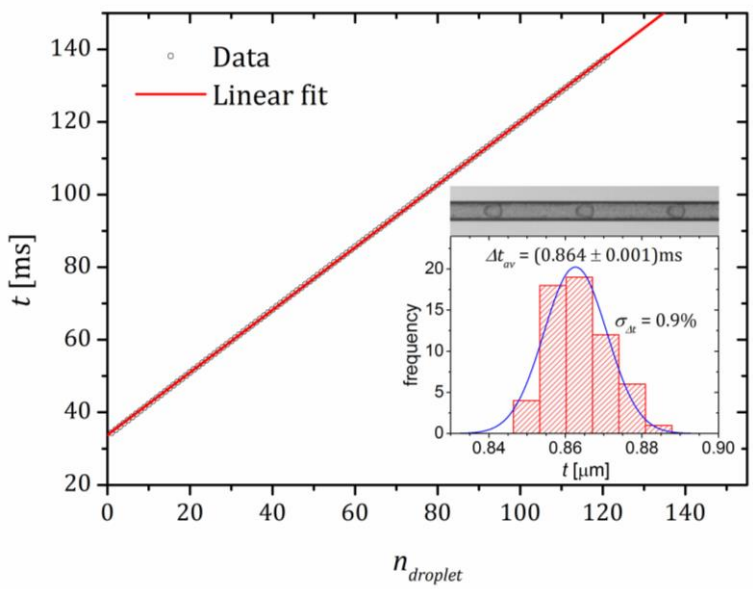

FIGURE 20 EXAMPLES OF THE MEASUREMENT OF THE DROPLET FORMATION FREQUENCY. THE TIME INTERVAL AT WHICH EACH DROPLET PASSES THROUGH A REFERENCE POSITION IS REPORTED, AS A FUNCTION OF DROPLET NUMBER; THE CORRESPONDING LINEAR FIT IS ALSO SHOWN WITH THE DERIVED FREQUENCY OF (1157 ± 9) HZ. THE INSET PRESENTS THE HISTOGRAM OF THE TIME INTERVAL BETWEEN SUBSEQUENT DROPLETS.

We determined the frequency *f* by measuring the time intervals δt between the transit of two subsequent droplets. In order to avoid bias and therefore systematic errors, the time intervals refer to distinct pairs, i.e. $\delta t_j = t_{2j} - t_{2j-1}$, where j=1…N/2 and N is the total number of droplets. Figure 20 shows the histogram of the time intervals corresponding to the highest total flow rate achievable with our set-up, that is $Q_C + Q_D$= 380 μl/min. The average of this distribution yields $\Delta t_{av} = (0.864 \pm 0.001)\, ms$, which corresponds to the maximum value of the droplet generation frequency *f*=(1157 ± 9) Hz. However, the majority of our measurements stay in a range of frequencies from few Hz to about 350 Hz. This to avoid the risk of leakage of the device. The statistical dispersion of the frequencies was never over the 5%, except for flow rates lower than 7 μL min^{-1} in which it has a maximum of 10%. Similarly, the velocities dispersions are always lower than 7% (Figure 21).

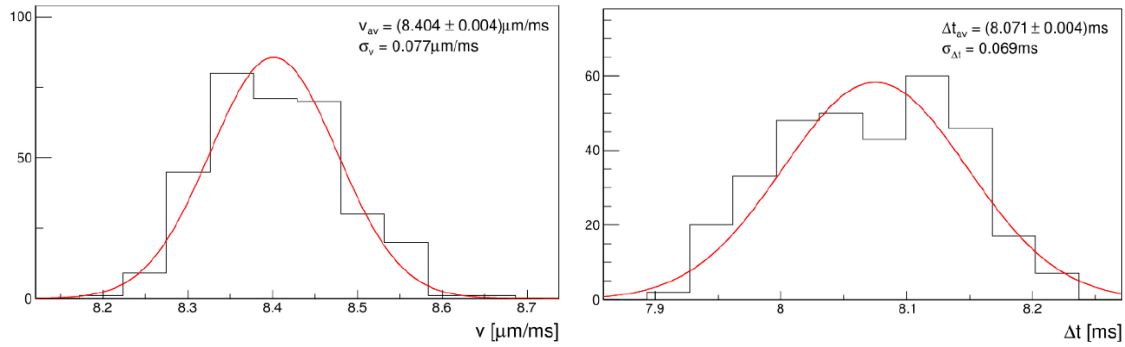

FIGURE 21 THE TWO IMAGES ARE THE HISTOGRAMS OF THE VELOCITY (LEFT) AND ΔT (RIGHT) FOR Q_D=30µL MIN^{-1}, Q_C=20µL MIN^{-1}. IN BOTH THE FIGURES THE AVERAGE VALUE AND THE STANDARD DEVIATION ARE REPORTED WITH THE GAUSSIAN FITS.

4.3.2. Lengths of the droplets

The droplet length *L* was estimated by analysing each droplet image extracted from a video lasting a period of time sufficiently high to obtain at least 200 droplet measurements, one from every frame of the video. In particular, *L* was determined referring to the front and back menisci of each droplet respectively (Figure 19): since this procedure is affected by the grey contrast level of the recorded image, the light intensity and camera exposure time had to be properly tuned in each video recording in order to obtain the best image contrast. Figure 22 shows an example of the histograms obtained in the case of low (a), intermediate (b) and high (c) droplet generation frequency for the T-junction TJ2 with a 1% of surfactant, respectively. Moreover the maximum droplet length obtained was 761 µm and the minimum 187 µm for a surfactant concentration of 0,08%, and 833 µm and 199 µm for the case without surfactant. The dispersion of the length of the droplets was obtained as the standard deviation of the length distribution: in all the analysed cases it was better than 3%, in most cases lower that 2%. These values are comparable with those reported in literature (Table 7) for T-shaped droplet generators realized with PDMS, thus highlighting the potentialities offered by $LiNbO_3$-based structures realized by laser ablation for microfluidic applications. Moreover, the three graphs clearly show that the dispersion of droplet lengths does not significantly change (less than 33%) by increasing the droplet generation frequency in the range between 92 Hz to 1157 Hz. The fact that the dispersion values remain below 1% in all the three investigated cases confirms the good microfluidic performances of our droplet

generators and the possibility to employ them also as high-frequency droplet generators.

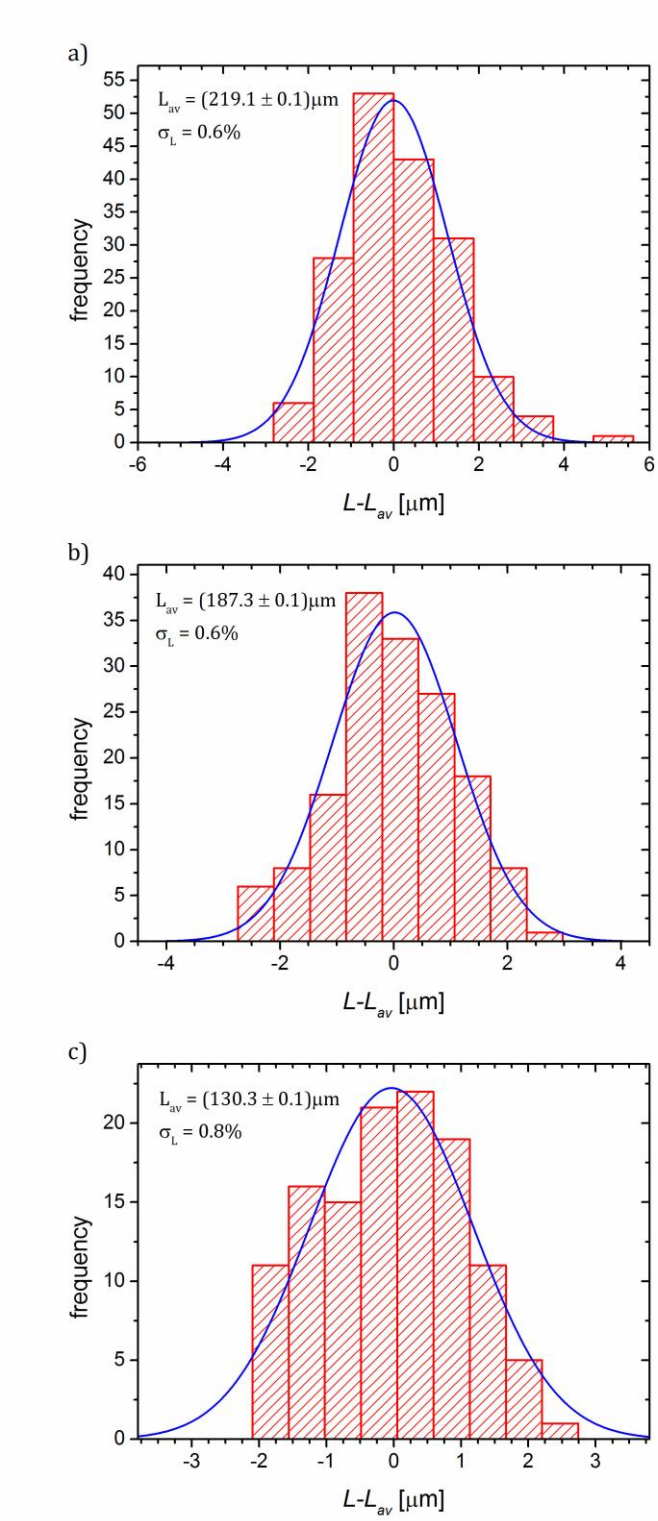

FIGURE 22 THE HISTOGRAMS RELATIVE TO THE DISPERSION OF THE DROPLET LENGTH *L* ARE REPORTED. THE DATA WERE OBTAINED IN THE T-JUNCTION TJ2 AT A DROPLETS GENERATION FREQUENCY OF 92 HZ (A), 467 HZ (B) AND 1157 HZ (C), SHOWING DISPERSIONS LOWER THAN 1%.

It is worth mentioning that the grey contrast of each video can affect the accuracy in the estimation of *L* by introducing a systematic error; this contribution eventually shifts the *L* value distribution but not its dispersion. In particular, by measuring the droplet meniscus thickness *m* and assuming that the values of droplet border positions follow a uniform probability density as wide as the width *m,* the random error σ_c in the droplet border estimation can be calculated as $m/\sqrt{12}$ [29]: the images analyses show that σ_c is about 5μm. Finally we did a test for eventual systematic errors due to temporal changes in the set-up, in particular fluctuating variations of the flow rates. In Figure 23 we report, as an example, a graphic of the time intervals Δt in function of the droplet numbers. It can be easily see that all the Δt are casually distributed, hence even if there can be systematic errors, they will be lower than the casual error.

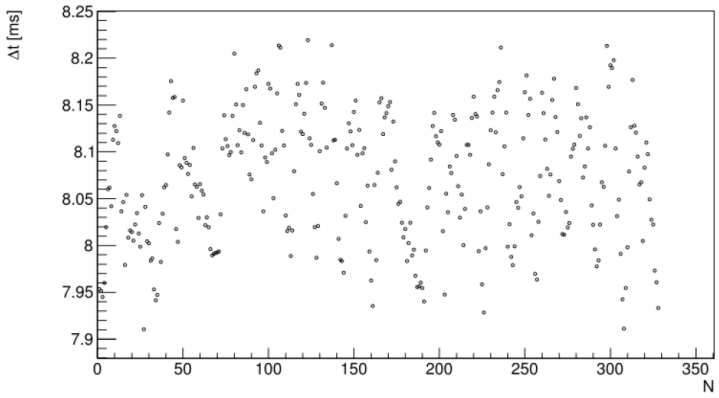

FIGURE 23 THE TIME INTERVALS (ΔT) ARE REPORTED IN FUNCTION OF THE DROPLET NUMBER, THE GRAPHIC SHOWS A CASUAL TREND OF ΔT

4.4. Data elaboration and model validation

In order to compare our results with the literature, the production of droplets was also tested as a function of the ratio $\varphi=Q_D\backslash Q_C$. In this analysis the droplets are generated in the squeezing regime, where the dynamics of their formation (break-up) is dominated by the pressure drop across the droplet as it forms [12], [23], [54], [55]. Therefore, the length *L* of the droplets can be conveniently expressed with the scaling Equation 5. In Figure 24 we report the dependence of the ratio $\bar{L}/\mathrm{wC}$ with respect to the relative flow rate Q_D/Q_C: in particular $\bar{L}$ was taken as the average value derived from two hundred droplets. The measurements were performed at two different

constant values of continuous flow rate Q_C: 5, 7, 10, 12, 20, 30, 35, 40 μL min^{-1}. While the value of Q_D was set to different ratios of Q_D/Qc: 0,1; 0,3; 0,5; 0,7; 1; 1,5; and 2. The data were then interpolated excluding the points out of 5σ from the function of interpolation, with the exception of the measures with the lower value of Q_C (5 μL min^{-1}) for which 3 points of 7 were excluded from the fit. Therefore for flow rates of the continuous phase greater than 7μL min^{-1} our T-junctions perfectly reproduce the typical microfluidic performances of T-shaped droplet generators realised with PDMS. Indeed, the linear relation between *L* and Q_D/Q_C was widely investigated and characterized for PDMS-based T-junctions and the results presented in [22][21] show a good agreement with those obtained in our study.

For what regards the experimental data at Q_C = 5μL min^{-1}, we can suppose both: that the different behaviour could be due to possible systematic errors; or that there is a different regime at lower flow rates ratio. Unfortunately we have not sufficient data to discern the question, therefore new studies need to be done in future.

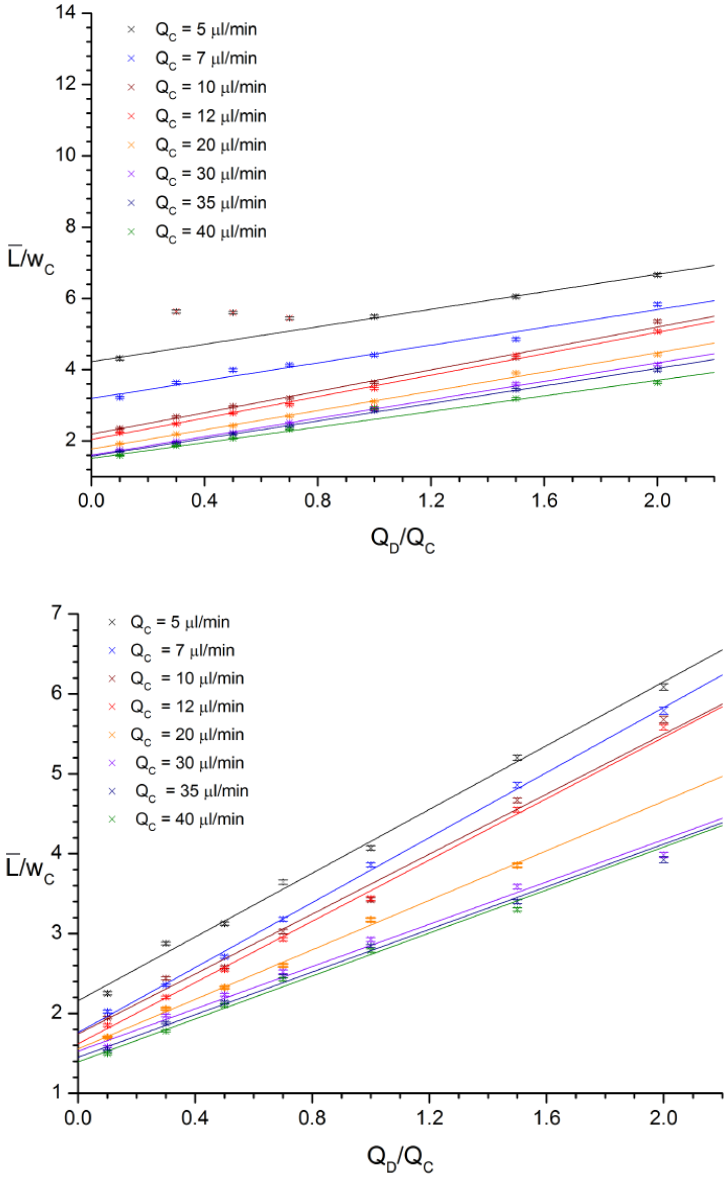

FIGURE 24 THE TWO FIGURES RAPPRESENT THE AVERAGE VALUE OF THE EFFECTIVE LENGTH IN FUNCTION OF THE FLOW RATES RATIO. EVERY SET OF VALUES WITH THE SAME Q_c, AND THEREFORE OF Ca, IS LINEARLY FITTED. THE UPPER IMAGE IS RELATED TO THE CASE WITHOUT SURFACTANT, THE LOWER TO THE CASE WITH SURFACTANT CONCENTRATION 0,08%.

4.4.1. Frequency droplet generation

Another important parameter to characterize our devices is the frequency of droplet generation *f*; as previously discussed the relation between the effective frequency and the Capillary number is given by Equation 7. For Ca higher than $8 \cdot 10^{-3}$ the model fit very well our data (Pearson's r value always greater than 0,985); in Figure 24 two exemplifying graphics are presented: in (a) the case without surfactant, and in (b) the case with a surfactant concentration of 0,08% in weight. In the first case the Ca lower than $6 \cdot 10^{-4}$

are detached from the model, instead in the second figure the model is confirmed by the fit. In all the cases we found a good agreement of the model for Ca higher than $6 \cdot 10^{-4}$.

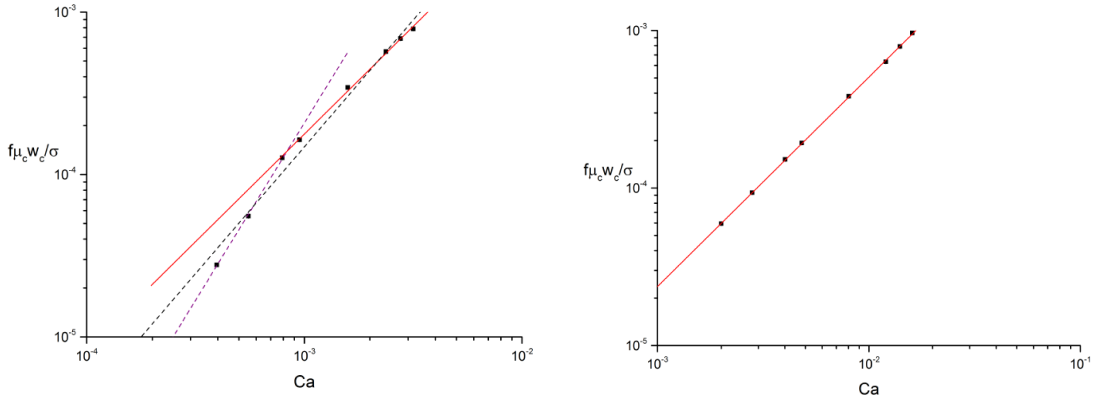

FIGURE 25 THE DATA RAPRESENTS THE VALUES OF THE EFFECTIVE FREQUENCIES IN FUNCTION OF THE CAPILLARY NUMBER (CA) IN A LOGARITHMIC SCALE. ALL THE ERRORS ARE LOWER THAN THE POINT SYMBOLS (■). THE LEFT IMAGE IS RELATED TO THE CASE WITHOUT SURFACTANT, THE RED LINE FITS THE POINT WITH CA MAJOR THAN $6 \cdot 10^{-3}$, THE DOTTED BLACK LINE FITS ALL THE POINT, AND THE VIOLET DOTTED LINE FITS THE CA LOWER THAN $6 \cdot 10^{-3}$. IN THE RIGHT FIGURE THE CASE WITH SURFACTANT CONCENTRATION 0,08% IS PRESENTED WITH ITS LINEAR FIT (RED LINE).

We can see in Figure 25 that the Ca lower than $6 \cdot 10^{-4}$ have a systematic detachment from the model. We can suppose that this behaviour is due to a different regime, in fact the trend is exhibited by different sets of data. Moreover these values of Ca are not in the range of the Christopher dissertation, therefore this behaviour cannot be predicted. In addition the change of behaviour is exhibited for both the value of surface energy at the same Ca but at different flow rates, therefore the relation is correlated to the Ca and not to the flow rates. Finally we suggest that the same regime change could be responsible for the deviation from linearity of the droplet lengths for Q_C=5μL min^{-1} previously discussed. In fact these measures are a subset of the previously one at low Ca (Figure 24). Nevertheless, to explain this change of behaviour a deeper study is necessary. Therefore the Christopher model was used only for dataset with Ca major of $8 \cdot 10^{-4}$ (for every set of frequencies, flow ratios, and surface energy) and the agreement with the data was defined with a linear fit in logarithm scale graphics. Then the value of α (Equation 7) was calculated for every different set of $\varphi = Q_D/Q_C$, in Figure 26 all the values are compared resulting all compatible in the range of the standard deviation (1σ). Moreover, also the average value of α for the two

surface energies (surfactant concentration) are compatible in the range of 1 σ and all the data were furthermore compatible with the value calculated by Christopher: 1.31 ± 0.03 [21]. Therefore we confirm the Christopher et al. model for Capillary number higher than $6 \cdot 10^{-4}$, and moreover we can suppose that α is independent of the value of the surface tension σ, a parameter that was not investigated in ref. [21].

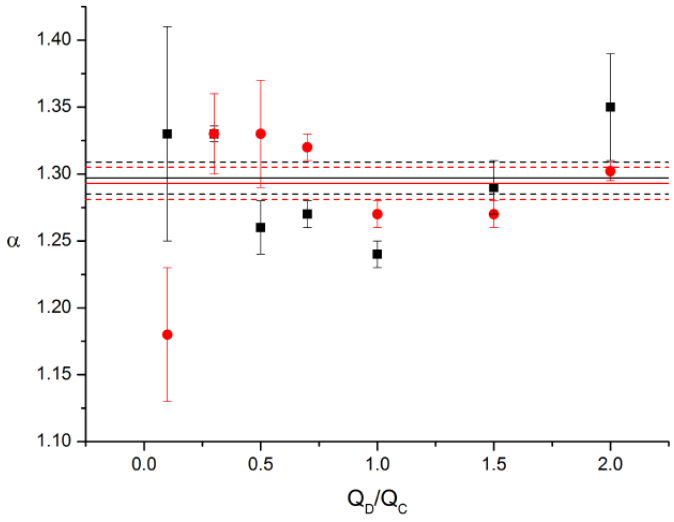

FIGURE 26 IN THE IMAGE ARE REPORTED THE VALUES OF α FOR EVERY FIT OBTAINED FROM FIGURE 25. IN BLACK ARE SHOWN THE DATA FOR THE SURFACTANT CONCENTRATION OF 0,08%, WITH THEIR AVERAGE VALUE (BLACK LINE), AND 3 TIMES ITS STANDARD DEVIATION (DOTTED BLACK LINE). IN RED THE SAME VALUES ARE REPORTED FOR THE CASE WITHOUT SURFACTANT.

4.4.2. Relation between Volume and Ca

Therefore the relation between the volumes V of the droplets and the Capillary number Ca (Equation 8) was analysed. We calculated the volume of the droplets with the following equation

$$V = Lhw_c - \Delta V$$

EQUATION 11

Where ΔV is the difference of volume between the real volume of the droplet and the parallelepiped of dimensions L, h, and wc. The two droplet extremities were approximated as half-ellipsoids, with the semi-axis orthogonal to the side wall equal to w_c, the semi-axis orthogonal to the bottom surface equals to h/2, and the axis parallel to the flow approximated to w_c. The difference ΔV was then given by

$$\Delta V = 2\left(\frac{hw_c^2}{2} - \frac{2}{3}\pi\frac{hw_c^2}{8}\right)$$

EQUATION 12

And finally the value of the droplet volume V could be estimated as

$$\hat{V} = \hat{L} - \left(1 - \frac{\pi}{6}\right)$$

EQUATION 13

Where $\hat{V}$ is the effective volume $\hat{V} = \frac{V}{hw_c^2}$

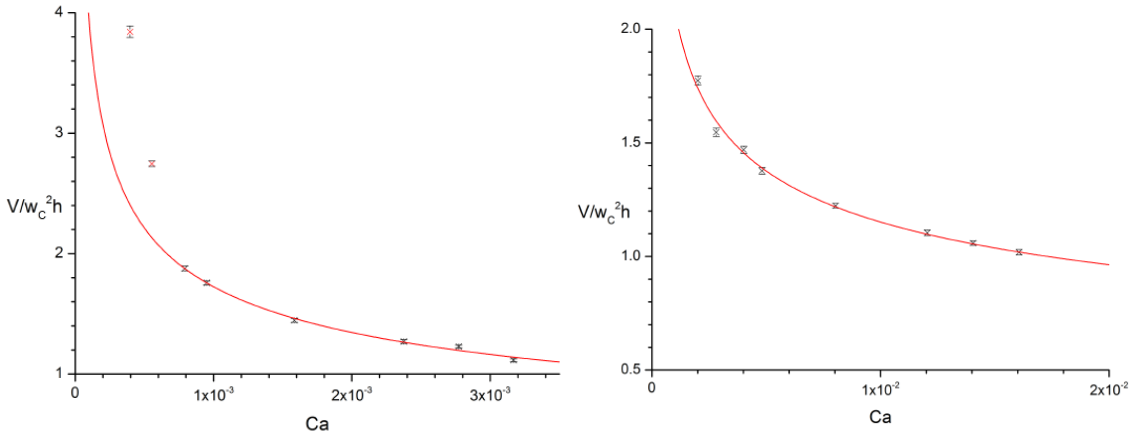

FIGURE 27 THE DATA RAPRESENTS THE VALUES OF THE EFFECTIVE VOLUME IN FUNCTION OF THE CAPILLARY NUMBER (CA) IN A LOGARITHMIC SCALE. THE IMAGE ON THE LEFT IS RELATED TO THE CASE WITHOUT SURFACTANT, AND THE ONE ON THE RIGHT TO THE CASE WITH SURFACTANT CONCENTRATION 0,08%. FOR BOTH THE RED CURVE RAPPRESENTS THE FIT OF THE RELATION IN EQUATION 8

In Figure 27 two graphics of the effective volume in function of the Capillary number are reported. In comparison with the other graphics this theoretical model fits the data worse than the other (frequency and length). However, the curve trend reflects the data and the farthest point is in the range of 4 times its error from the fit. This worse behaviour is probably due to the approximations used to calculate the volume of the droplets, which surely introduced a systematic error in the data. However, also for this relation we calculated the value of the α parameter; as it could be expected the volume approximations affect also these results, with the values calculated for the surfactant at 0,08% and without surfactant incompatible (Figure 28).

4.4.3. The Value of α

Finally, in Figure 29 we compare all our results for the value of α, in particular we present their weighted average values for every set, finding a good compatibility taking in consideration the volume approximation previously discussed. All the values are compatible in a range of 3σ with the value in ref. [21], and in particular the results from the frequency relation (Figure 25) are comparable into 1 σ. Therefore all our data confirm the model of Christopher et al. in a range of Capillary number between 0.0008 and 0.016. While at lower Ca, as previously discussed, we need a new study that could confirm or deny the presence of a different regime.

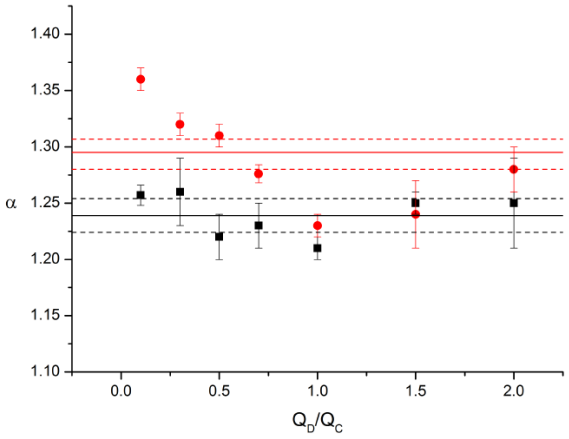

FIGURE 28 IN THE IMAGE THE VALUES OF α FOR EVERY FIT OBTAINED FROM FIGURE 27 ARE REPORTED: IN BLACK THE DATA FOR THE SURFACTANT CONCENTRATION OF 0,08%, WITH THEIR AVERAGE VALUE (BLACK LINE), AND 3 TIMES ITS THE STANDARD DEVIATION (DOTTED BLACK LINE); AND IN RED THE SAME VALUES FOR THE CASE WITHOUT SURFACTANT.

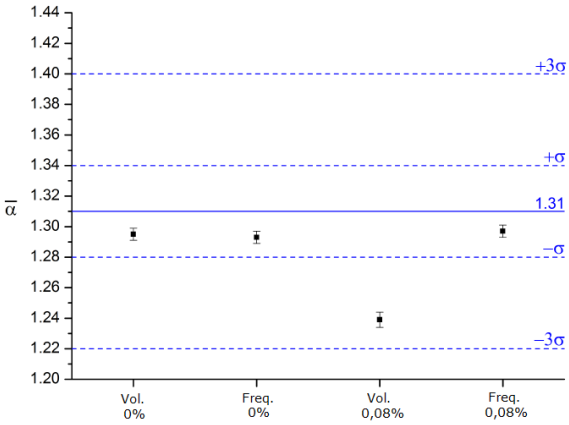

FIGURE 29 THE GRAPHIC REPORTS THE AVERAGE VALUES OF α FOR THE DIFFERENT DATASETS PREVIOUSLY CALCULATED (VOLUME AND FREQUENCY, 0% AND 0,08% OF SURFACTANT CONCENTRATION). THE BLUE LINE RAPRESENT THE VALUE OF LITERATURE [21], WHILE THE DOTTED BLUE LINE ARE ONE TIME AND THREE TIMES THE VALUE OF ITS STANDARD DEVIATION.

4.4.4. TJ1 and TJ2 comparison

After the previously reported characterization of the TJ2 in a wide range of condition, we measured also the behaviour of the TJ1 for a lower set of different parameters, in order to compare two different devices realized with the same technique. In Figure 30 we report the dependence of the ratio *L*/w with respect to the relative flow rate Q_D/Q_C for both TJ1 and TJ2: in particular *L* was taken as the average value derived from one hundred droplets. The measurements were performed at two different constant values of continuous flow rate Q_C, 30 μl/min and 10 μl/min respectively, while the value of Q_D was varied between 1 μl/min and 30 μl/min, the concentration of the surfactant was 1% in weight.

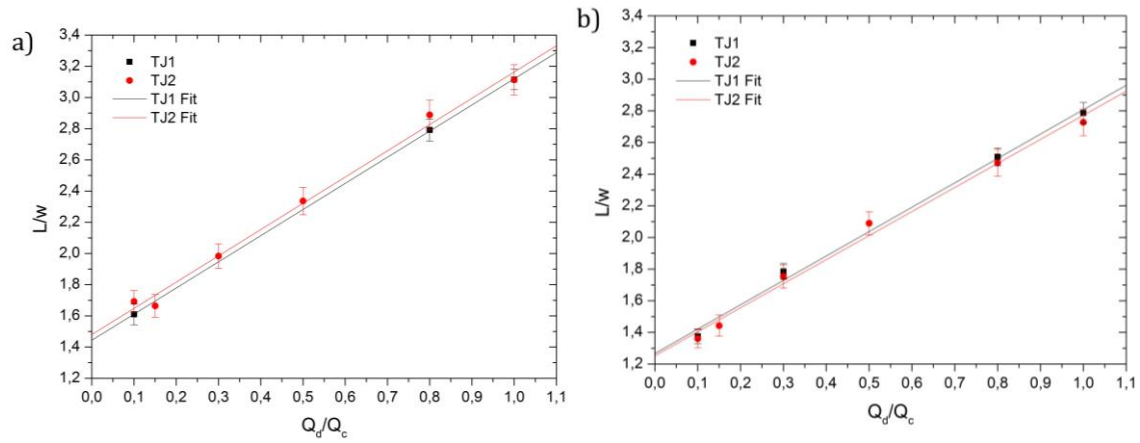

FIGURE 30 THE VALUES OF L/w_C ARE REPORTED AS A FUNCTION OF THE RATIO BETWEEN THE DISPERSED AND CONTINUOUS FLOW RATES, Q_D/Q_C. THE VALUE OF Q_C IS FIXED TO 10 μL/MIN (A) OR 30 μL/MIN (B), WHILE THE VALUE OF Q_D IS PROPERLY VARIED. THE STRAIGHT LINES REPRESENT THE LINEAR FITS OF THE EXPERIMENTAL DATA, FOR BOTH TJ1 AND TJ2.

The experimental points are well fitted by a linear regression (Pearson's r value greater than 0.995), whose coefficients A and B are reported in Table 5. Moreover, for each value of Q_c the intercept (A) and the slope (B) of the linear regression are fully compatible (compatibility better than 0.3 [29]) for the two T-junctions and with the Christopher model, demonstrating the high reproducibility of the femtosecond laser technique used to realize the microfluidic device in the $LiNbO_3$ substrate. Nevertheless, in Figure 30 it is evident that both the values of A and B vary with the flow rate Q_c of the continuous phase. However, this difference is forecasted by Equation 5, since the parameters A and B depend not only on the geometry of the channels, which is almost the same in graphs (a) and (b), but also on the capillary

number of the microfluidic device, which in turn increases with increasing Q_c, especially in the case of a high viscosity ratio [12], [23], [54], [55].

T-junction	w_c (μm)	h(μm)	Q_C= (10.00 ± 0.04) μl/min		$Q_{C=}$(30.00 ± 0.11) μl/min	
			A	B	A	B
TJ1	126±2	89 ± 6	1.44±0.01	1.68 ±0.01	1.27 ±0.05	1.54 ±0.07
TJ2	125±3	100 ±1	1.48±0.04	1.68 ±0.07	1.25 ±0.04	1.52 ±0.07

TABLE 5 SIZES OF THE MICROCHANNELS FOR THE T-JUNCTIONS TJ1 AND TJ2, THE VALUES OF WIDTH (W_C) AND DEPTH (H) WERE OBTAINED BY PROFILOMETRY. VALUES OF THE PARAMETERS A (INTERCEPT) AND B (SLOPE) OBTAINED BY PERFORMING A LINEAR FIT OF THE DATA REPORTED IN FIG.30 FOR THE TWO INVESTIGATED T-JUNCTIONS.

5. Conclusion

The objectives of this task were the fabrication and the characterization of the first T-junction directly engraved in Lithium Niobate, with suitable roughness for the implementation of an optical stage. Moreover also the fluidic characterization of the devices was an important issue in order to measure their performance in relation with published results and the Christopher et al. model [21].

The fabrication was divided in three different phases: the realization of the channels with a femtosecond laser technique and their geometrical characterization; the sealing of the device with a PDMS layer; and the functionalization of the surfaces with OTS in order to increase their hydrophobicity. A feasibility study of the microstructuration techniques for the realization of microchannel in Lithium Niobate was done. The comparison between different techniques supported the exploitation of laser ablation with femtosecond laser operating at a wavelength of 800 nm as a suitable technique to get high performant microfluidic channels engraved in lithium niobate crystals (section 3.3). In particular we showed that among the different scanning velocities (100-500μm/s) and laser pulse energies (1-20 μJ) exploited, the best results were obtained at 500μm/s and 5μJ. Moreover, since the material is proposed as an optofluidic substrate also the optical quality of the walls of the channels is fundamental, especially for the good coupling between the waveguides and the droplets in the final device. As a matter of fact a first AFM study, still in progress, supports the use of laser ablation, since we found an average roughness of about 50 nm for the sidewalls.

Fabrication time	Scanning speed	Beam diameter at 5μJ	Translation stage resolution	Vertical/horizontal scanning step	Sidewall roughness R_a	Fabrication costs
< 3 h	500 μm/s	≈25 μm	30nm	15/10 μm	51,2 nm	≈20-25 €/T-junction

TABLE 6. FABRICATION PARAMETERS RELATIVE TO THE T-JUNCTIONS INVESTIGATED IN THE PRESENT WORK.

Furthermore, we study the wettability of the Lithium Niobate in different condition: six crystallographic directions; different liquids (water and hexadecane); and also with a hydrophobic functionalization of the surfaces (OTS). The material exhibits good fluidic properties for our purposes, since it is moderately hydrophobic with an average contact angle of 62°, it is lipophilic with a angle between 10° and total wetting, and it could be functionalized with standard SAM techniques (solvent immersion and vapour deposition), showing the possibility to increase the hydrophobicity to 101° and also to homogenize the surfaces properties (section 3.6). Moreover, the crystallographic directions do not seem to exhibit different wettability properties on every different surface, since the values of all the different measures are all compatible. However it cannot be possible to evaluate the difference of wettability between every different surface, this because the measurement of the contact angle was not repeatable in that case. Therefore to study this behaviour a control of pressure, temperature and humidity in a glow box should be done.

The microfluidic performances of these devices were then characterized in a wide range of droplet generation frequencies, from a few Hz to about 1 kHz. The frequencies, the velocities, and droplet lengths distributions were analysed in different conditions and showed a low dispersion with a standard deviation less than 10%, 7%, and 3% respectively, an optimal results for a new fabrication technique and a new material. As reported in Table 7 our values are totally comparable with the literature, and are compatible in its range of validity with the Christopher et al. model [21]. In fact, for Ca higher than $6 \cdot 10^{-4}$ all the equation for frequency, length and volume presented in section 2.3 are confirmed with a very good agreement of the fits with our data (Figure 29). Moreover we found a different systematic behaviour for the measures at lower Ca, we suppose that this behaviour could be due to a different regime for which the model is not valid. However, further studies need to be done and the question has not found an answer yet. Furthermore, the microfluidic performance of our two different T-junctions (TJ1 and TJ2) suggests that laser ablation guarantees a high reproducibility and good quality channel shape (Table 7). In fact the frequency and the droplet length stay in a range of 1Hz-5kHz like the other devices taken into account,

nevertheless the droplet length results different in our device, with an effective length several times (from 1 to 600) higher then the other references, that its probably due to the use of the surfactant which lower the surface energy of our droplets.

All the major objectives of this task were achieved, so we can conclude that, for what explained in this chapter, our approach paves the way toward a direct integration on a single $LiNbO_3$ substrate of passive microfluidic devices and then of active optical components, like waveguides, holographic filters and droplet actuators driven by light. The realization of optofluidic platform, therefore, is not limited by the fluidic properties of the material, on the contrary its compatibility with all our fluidic experiments shows excellent perspectives, in particular with the exploration of the crystals also as active material for fluidic purpose (trapping, droplets control, liquid mixing, liquid waveguide, etc.).

Channel dimension (μm) CP=cont. phase; DP=disp. Phase	Frequency (Hz)	Droplet Length (μm)	L/wc	ref.
125 X 100 (CP-DP)	1-1157	187-833	1,5-6,7	TJ2
150 X 100 (CP-DP)	2	130	0,87	[57]
150 X 50 (CP); (65 : 375) X 50 (DP)	0,3-5000	50-100	0,0025-0,83	[21]
60 X 9 (CP-DP) and 35 X 6,5 (CP-DP)	20-80	10-40	0,16-0,67	[11]
500 X 100 (CP); 100 X 100 (DP)	20-2000	100-400	0,2-0,8	[14]
150 X 50 (CP); (65 : 375) X 50 (DP)	0,3-5000	50-100	0,0025-0,83	[21]

TABLE 7 COMPARISON BETWEEN OUR RESULTS FOR THE T-JUNCTION TJ2 (FIRST LINE) AND ANALOGOUS RESULTS FROM LITERATURE.

Bibliography

[1] H. Song, D. L. Chen, and R. F. Ismagilov, "Reactions in droplets in microfluidic channels.," *Angew. Chem. Int. Ed. Engl.*, vol. 45, no. 44, pp. 7336–56, Nov. 2006.

[2] K. Jensen and A. Lee, "SPECIAL ISSUE FOREWORD," *Lab Chip*, vol. 4, no. 4, p. 31N, 2004.

[3] C. N. Baroud, M. R. de Saint Vincent, and J.-P. Delville, "An optical toolbox for total control of droplet microfluidics.," *Lab Chip*, vol. 7, no. 8, pp. 1029–33, Aug. 2007.

[4] V. Chokkalingam, B. Weidenhof, M. Krämer, W. F. Maier, S. Herminghaus, and R. Seemann, "Optimized droplet-based microfluidics scheme for sol-gel reactions.," *Lab Chip*, vol. 10, no. 13, pp. 1700–5, Jul. 2010.

[5] J.-C. Baret, V. Taly, M. Ryckelynck, C. A. Merten, and A. D. Griffiths, "[Droplets and emulsions: very high-throughput screening in biology].," *Med. Sci. (Paris).*, vol. 25, no. 6–7, pp. 627–32.

[6] E. Piccin, D. Ferraro, P. Sartori, E. Chiarello, M. Pierno, and G. Mistura, "Generation of water-in-oil and oil-in-water microdroplets in polyester-toner microfluidic devices," *Sensors Actuators B Chem.*, vol. 196, pp. 525–531, Jun. 2014.

[7] P. Watts and S. J. Haswell, "The application of micro reactors for organic synthesis.," *Chem. Soc. Rev.*, vol. 34, no. 3, pp. 235–46, Mar. 2005.

[8] V. Noireaux and A. Libchaber, "A vesicle bioreactor as a step toward an artificial cell assembly.," *Proc. Natl. Acad. Sci. U. S. A.*, vol. 101, no. 51, pp. 17669–74, Dec. 2004.

[9] M. S. Long, C. D. Jones, M. R. Helfrich, L. K. Mangeney-Slavin, and C. D. Keating, "Dynamic microcompartmentation in synthetic cells.," *Proc. Natl. Acad. Sci. U. S. A.*, vol. 102, no. 17, pp. 5920–5, Apr. 2005.

[10] H.-J. Choi and C. D. Montemagno, "Biosynthesis within a bubble architecture," *Nanotechnology*, vol. 17, no. 9, pp. 2198–2202, May 2006.

[11] T. Thorsen, R. W. Roberts, F. H. Arnold, and S. R. Quake, "Dynamic Pattern Formation in a Vesicle-Generating Microfluidic Device," *Phys. Rev. Lett.*, vol. 86, no. 18, pp. 4163–4166, Apr. 2001.

[12] C. N. Baroud, F. Gallaire, and R. Dangla, "Dynamics of microfluidic droplets.," *Lab Chip*, vol. 10, no. 16, pp. 2032–45, Aug. 2010.

[13] S.-Y. Teh, R. Lin, L.-H. Hung, and A. P. Lee, "Droplet microfluidics.," *Lab Chip*, vol. 8, no. 2, pp. 198–220, Feb. 2008.

[14] T. Nisisako, T. Torii, T. Takahashi, and Y. Takizawa, "Synthesis of Monodisperse Bicolored Janus Particles with Electrical Anisotropy Using a Microfluidic Co-Flow System," *Adv. Mater.*, vol. 18, no. 9, pp. 1152–1156, May 2006.

[15] C. Cramer, P. Fischer, and E. J. Windhab, "Drop formation in a co-flowing ambient fluid," *Chem. Eng. Sci.*, vol. 59, no. 15, pp. 3045–3058, Aug. 2004.

[16] S. Yeom and S. Y. Lee, "Size prediction of drops formed by dripping at a micro T-junction in liquid–liquid mixing," *Exp. Therm. Fluid Sci.*, vol. 35, no. 2, pp. 387–394, Feb. 2011.

[17] S. L. Anna, N. Bontoux, and H. A. Stone, "Formation of dispersions using 'flow focusing' in microchannels," *Appl. Phys. Lett.*, vol. 82, no. 3, p. 364, 2003.

[18] A. Gupta and R. Kumar, "Effect of geometry on droplet formation in the squeezing regime in a microfluidic T-junction," *Microfluid. Nanofluidics*, vol. 8, no. 6, pp. 799–812, Oct. 2009.

[19] A. Gupta and R. Kumar, "Flow regime transition at high capillary numbers in a microfluidic T-junction: Viscosity contrast and geometry effect," *Phys. Fluids*, vol. 22, no. 12, p. 122001, 2010.

[20] M. DE MENECH, P. GARSTECKI, F. JOUSSE, and H. A. STONE, "Transition from squeezing to dripping in a microfluidic T-shaped junction," *J. Fluid Mech.*, vol. 595, Jan. 2008.

[21] G. F. Christopher, N. N. Noharuddin, J. a. Taylor, and S. L. Anna, "Experimental observations of the squeezing-to-dripping transition in T-shaped microfluidic junctions," *Phys. Rev. E*, vol. 78, no. 3, p. 036317, Sep. 2008.

[22] P. Garstecki, M. J. Fuerstman, H. a Stone, and G. M. Whitesides, "Formation of droplets and bubbles in a microfluidic T-junction-

scaling and mechanism of break-up.," *Lab Chip*, vol. 6, no. 3, pp. 437–46, Mar. 2006.

[23] R. Seemann, M. Brinkmann, T. Pfohl, and S. Herminghaus, "Droplet based microfluidics.," *Rep. Prog. Phys.*, vol. 75, no. 1, p. 016601, Jan. 2012.

[24] G. F. Christopher and S. L. Anna, "Microfluidic methods for generating continuous droplet streams," *J. Phys. D. Appl. Phys.*, vol. 40, no. 19, pp. R319–R336, Oct. 2007.

[25] C. L. Sones, S. Mailis, W. S. Brocklesby, R. W. Eason, and J. R. Owen, "Differential etch rates in z-cut LiNbO3 for variable HF/HNO3 concentrations," *J. Mater. Chem.*, vol. 12, no. 2, pp. 295–298, Jan. 2002.

[26] Y. Yun, L. Kampschulte, M. Li, D. Liao, and E. I. Altman, "Effect of Ferroelectric Poling on the Adsorption of 2-Propanol on LiNbO 3 (0001)," vol. 3, no. 0001, pp. 13951–13956, 2007.

[27] N. Ohnishi and T. Iizuka, "Etching study of microdomains in LiNbO3 single crystals," *J. Appl. Phys.*, vol. 46, no. 3, p. 1063, 1975.

[28] A. B. Randles, M. Esashi, and S. Tanaka, "Etch rate dependence on crystal orientation of lithium niobate.," *IEEE Trans. Ultrason. Ferroelectr. Freq. Control*, vol. 57, no. 11, pp. 2372–80, Nov. 2010.

[29] "Bureau International des Poids et Mesures, Evaluation of measurement data – Guide to the expression of uncertainty in measurement." 2005.

[30] M. Chauvet, L. Al Fares, and F. Devaux, "No Title," 2012, p. 84340Q–84340Q–7.

[31] C. Canali, a. Carnera, G. Della Mea, P. Mazzoldi, S. M. Al Shukri, a. C. G. Nutt, and R. M. De La Rue, "Structural characterization of proton exchanged LiNbO3 optical waveguides," *J. Appl. Phys.*, vol. 59, no. 8, p. 2643, 1986.

[32] R. Cheng, T. Wang, and W. Wang, "Wet-Etched Ridge Waveguides in -Cut Lithium Niobate," vol. 15, no. 10, pp. 1880–1887, 1997.

[33] H. Hu, R. Ricken, W. Sohler, and R. B. Wehrspohn, "Lithium Niobate Ridge Waveguides Fabricated by Wet Etching," *IEEE Photonics Technol. Lett.*, vol. 19, no. 6, pp. 417–419, Mar. 2007.

[34] V. Dobrusin, S. Ruschin, and L. Shpisman, "Fabrication method of low-loss large single mode ridge Ti:LiNbO3 waveguides," *Opt. Mater. (Amst).*, vol. 29, no. 12, pp. 1630–1634, Aug. 2007.

[35] N. Courjal, B. Guichardaz, G. Ulliac, J.-Y. Rauch, B. Sadani, H.-H. Lu, and M.-P. Bernal, "High aspect ratio lithium niobate ridge waveguides fabricated by optical grade dicing," *J. Phys. D. Appl. Phys.*, vol. 44, no. 30, p. 305101, Aug. 2011.

[36] V. A. Fedorov, S. M. Kostritskii, A. N. Alkaev, E. I. Maslennikov, E. M. Paderin, D. V Apraksin, and F. Laurell, "P roton exchanged LiNbO 3 and LiTaO 3 optical waveguides and integrated optic devices," vol. 69, pp. 228–236, 2003.

[37] H. Hu, R. Ricken, and W. Sohler, "Low-loss ridge waveguides on lithium niobate fabricated by local diffusion doping with titanium," *Appl. Phys. B*, vol. 98, no. 4, pp. 677–679, Jan. 2010.

[38] T.-L. Ting, L.-Y. Chen, and W.-S. Wang, "Wet etchingX-cut LiNbO3 using diluted joint proton source," *Microw. Opt. Technol. Lett.*, vol. 48, no. 10, pp. 2108–2111, Oct. 2006.

[39] Y. N. Korkishko and V. A. Fedorov, *Ion Exchange in Single Crystals for Integrated Optics and Optoelectronics*. Cambridge International Science Publishing, 1999.

[40] Y. N. Korkishko, V. A. Fedorov, and O. Y. Feoktistova, "LiNbO3 Optical Waveguide Fabrication by High-Temperature Proton Exchange," *J. Light. Technol.*, vol. 18, no. 4, p. 562–, 2000.

[41] T. Wang, C. Huang, W. Wang, and P. Wei, "A Novel Wet-Etching Method Using Electric-Field-Assisted Proton Exchange in LiNbO 3," vol. 22, no. 7, pp. 1764–1771, 2004.

[42] Z. Ren, P. J. Heard, J. M. Marshall, P. a. Thomas, and S. Yu, "Etching characteristics of LiNbO[sub 3] in reactive ion etching and inductively coupled plasma," *J. Appl. Phys.*, vol. 103, no. 3, p. 034109, 2008.

[43] M. Bianconi, F. Bergamini, G. G. Bentini, a. Cerutti, M. Chiarini, P. De Nicola, and G. Pennestrì, "Modification of the etching properties of x-cut Lithium Niobate by ion implantation," *Nucl. Instruments Methods Phys. Res. Sect. B Beam Interact. with Mater. Atoms*, vol. 266, no. 8, pp. 1238–1241, Apr. 2008.

[44] M. Sridhar, D. K. Maurya, J. R. Friend, and L. Y. Yeo, "Focused ion beam milling of microchannels in lithium niobate.," *Biomicrofluidics*, vol. 6, no. 1, pp. 12819–1281911, Mar. 2012.

[45] M. Tamura and S. Yoshikado, "ADVANCED Etching characteristics of LiNbO 3 crystal by fluorine gas plasma reactive ion etching," vol. 563, pp. 2–9.

[46] M. Roussey, M.-P. Bernal, N. Courjal, and F. I. Baida, "Experimental and theoretical characterization of a lithium niobate photonic crystal," *Appl. Phys. Lett.*, vol. 87, no. 24, p. 241101, 2005.

[47] R. Osellame, H. J. W. M. Hoekstra, G. Cerullo, and M. Pollnau, "Femtosecond laser microstructuring: an enabling tool for optofluidic lab-on-chips," *Laser Photon. Rev.*, vol. 5, no. 3, pp. 442–463, May 2011.

[48] P. Sivarajah, C. a. Werley, B. K. Ofori-Okai, and K. a. Nelson, "Chemically assisted femtosecond laser machining for applications in LiNbO3 and LiTaO3," *Appl. Phys. A*, vol. 112, no. 3, pp. 615–622, Jul. 2013.

[49] J.-W. Lee, Y.-K. Cho, M.-W. Cho, G.-H. Kim, and T.-J. Je, "Optical transmittance recovery of powder blasted micro fluidic channels on fused silica glass using MR polishing," *Int. J. Precis. Eng. Manuf.*, vol. 13, no. 11, pp. 1925–1930, Oct. 2012.

[50] V. Maselli, J. R. Grenier, S. Ho, and P. R. Herman, "Femtosecond laser written optofluidic sensor: Bragg grating waveguide evanescent probing of microfluidic channel," *Opt. Express*, vol. 17, no. 14, p. 11719, Jul. 2009.

[51] F. Tesser, "Production of monodispersed droplets in a T-junction device," Padova, 2012.

[52] B. J. Adzima and S. S. Velankar, "Pressure drops for droplet flows in microfluidic channels," *J. Micromechanics Microengineering*, vol. 16, no. 8, pp. 1504–1510, Aug. 2006.

[53] J. N. Lee, C. Park, and G. M. Whitesides, "Solvent compatibility of poly(dimethylsiloxane)-based microfluidic devices.," *Anal. Chem.*, vol. 75, no. 23, pp. 6544–54, Dec. 2003.

[54] J. H. Xu, S. W. Li, J. Tan, and G. S. Luo, "Correlations of droplet formation in T-junction microfluidic devices: from squeezing to dripping," *Microfluid. Nanofluidics*, vol. 5, no. 6, pp. 711–717, May 2008.

[55] J. H. Xu, S. W. Li, J. Tan, Y. J. Wang, and G. S. Luo, "Controllable preparation of monodisperse O/W and W/O emulsions in the same microfluidic device.," *Langmuir*, vol. 22, no. 19, pp. 7943–6, Sep. 2006.

[56] R. Zamboni, "Caratterizzazione microfluidica di un generatore di gocce a T-junction integrato in niobato di litio," Padova, 2014.

[57] B. Zheng, L. S. Roach, and R. F. Ismagilov, "Screening of protein crystallization conditions on a microfluidic chip using nanoliter-size droplets.," *J. Am. Chem. Soc.*, vol. 125, no. 37, pp. 11170–1, Sep. 2003.

Optical stage

1. Preface

The first objective of this task is the fabrication of monomodal optical waveguides by Titanium in-diffusion in Lithium Niobate crystals. The waveguides were exploited to connect the different stages of our optofluidic platform, in particular the coupling with the microfluidic channels, the collection of the emitted light from the channel, and its transmission to the analytical stage. Moreover the realization of custom-designed laser source would be an important improvement in our platform, in fact the possibility of use taylorable wavelength in the visible range with a compact set-up will surely improve its range of application. Therefore the second objective of the project was a feasibility study on the fabrication and characterization of a high-efficiency integrated frequency converter in the visible range. The proposed prototype was realized on substrates that could be also doped in order to have an enhanced optical damage resistance in a waveguide configuration [1]. The frequency converter that the project aimed to realize represented the first stage for obtaining an integrated coherent light-emitting source, and therefore should have all the characteristics to obtain a compact laser source in the visible range, for direct application in the optofluidic platform as building block for more complicated integrated optical circuits (Figure 1). Among the others, the second harmonic generation (SHG) process (i.e. the generated waves have twice the frequency of the pump) attracted great interest because of the inherent possibility of generating visible light starting from a pump operating in the near infrared spectral region where low cost, high power light sources are commercially available. Therefore the main objective of this part was the fabrication and characterization of a high-efficiency integrated frequency converter prototype based on PPLNs (Periodic Poled Lithium Niobate) waveguide operating in the visible range. The proposed prototype was realized on substrates that also could be suitably doped in order to have an enhanced optical damage resistance, and moreover in a waveguide configuration performed by Titanium in-diffusion.

1.1. The circuit

The device prototype was constituted by a periodic pattern of ferroelectric domains (PPLN) realized on both congruent Lithium Niobate crystals (cLN) and a Zirconium doped Lithium Niobate crystals (Zr-LN), a dopant which can assures a high resistance against optical damage (see section 3.2.5). These structures were able to generate a frequency conversion through the Quasi-Phase Matching technique (QPM) with high efficiencies. On these PPLN substrates a waveguide structure by Titanium in-diffusion was needed, in order to confine the light of the pump and of the second harmonic in order to extend the interaction length of the two beams through the entire device. The frequency converter would therefore work in a waveguide configuration in order to assure a spatially confined frequency conversion and so a stable, high conversion efficiency even at high intensities. Therefore the waveguides should be single-mode in the range of operation, in order maximize the power confinement and so the efficiency of the system. The wavelength of the pump signal was 1064 nm in order to obtain a SH wavelength of 532 nm in the visible range (green), so that the period of our PPLN was equals to 6,8 µm.

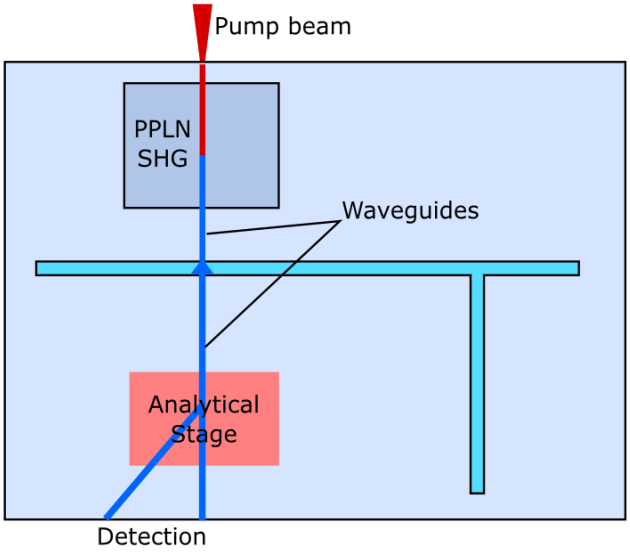

FIGURE 1 SCHEME OF THE OPTICAL CIRCUIT OF THE OPTOFLUIDIC PLATFORM

1.2. Objectives

The objectives and the expected results of this task can be summarized as follow:

- Realisation and characterization of optical waveguides on by Titanium in-diffusion on Lithium Niobate Crystals. This part considers the design of the optical waveguide geometry with UV-photolithography; the relative sputtering deposition and lift-off process; the high temperature diffusion to get the best optical confinement in the visible/NIR ranges (SHG and pumps frequency respectively). The characterization was achieved with the near-field and the m-lines techniques.
- Preparation and characterization of Periodically Poled Doped Lithium Niobate (PP-doped-LN) structures. This task considers the preparation of lithium niobate crystals with a periodic pattern of ferroelectric domains on crystals undoped and doped with Zr using photolithography and electrical poling. The PPLN crystal were designed to act as efficient frequency converter in visible spectral range via SHG with a period of 6,8 μm. Finally the structures were characterized with polarized microscopy and wet etching and then the SHG efficiency was measured.
- Test of the optical performances of the integrated PPLN structure: the measurement of the conversion efficiency for a specific nonlinear process.

The expected results of the project can be summarized as follows:

- Setting up of a new facility for micro-patterning of lithium niobate samples by photolithographic patterning and poling.
- Realisation of periodically poled structures with a period of 6,8 μm in order to obtain optical conversion in the visible spectral region with efficiencies of 0,1% W^{-1}.
- Realisation and characterization of single-mode optical waveguides in the visible range.
- Realisation and testing of an integrated waveguide frequency converter with high conversion efficiency and strong endurance.
- Realization of PPLN in Zr-doped lithium niobate crystals.

In this thesis we discuss the realization and characterization of the two different stages of the optical circuit (PPLN and waveguide), but unfortunately there are no data on the integration between the two different stages, as this work regards the last months of the ongoing project. However, the realization of monomodal waveguides in the visible range is the key point for the realization of the opto-microfluidic circuit and the first results on the microchannel/waveguide coupling are presented in Chapter 4.

2. Waveguides

2.1. Introduction

Waveguides are the basic element in an integrated optical device and in particular also in a system realized in Lithium Niobate. Lithium Niobate is one of the most popular dielectric materials for integrated optics, that because it is characterized by low optical absorption (~0.1 dB/cm). The refractive index increase to realize an optical waveguide is usually achieved by locally doping the $LiNbO_3$ crystal with titanium at high temperature [2]; or by Proton-Exchange (PE) in which lithium ions of the substrate material are exchanged by hydrogen ions protons of the acid [3]; or by ion implantation [4]. A large variety of integrated optical devices has been demonstrated where these three techniques have been employed [5]. For the realization of our optical stage we choose to use Ti-indiffused waveguides, this for several reasons: the first is that even if PE give refractive index variation of one order of magnitude greater than Ti-indiffusion ($\delta n_e \sim 0{,}1 \div 0{,}12$), it seriously damages the electro-optical properties of the crystals and therefore it is not suitable for the integration with the photorefractive holographic gratings which we want to realize in our project. The second is that the fabrication of ion-implanted waveguides is expensive being performed in external facilities. The third is that Ti indiffusion process is quite known and it was deeply investigated in the past (significant contribute to the understanding of the Ti indiffusion process came from the Group of Padua in the ninetees [6]–[10], therefore the procedure and the parameters used to fabricate high quality Ti:$LiNbO_3$ optical devices were well known. In particular the diffusion behavior of titanium, the relation between Ti concentration and the refractive index change, and the also the predictive models were completely studied in the past years [11]–[13]. In this thesis we started from the works cited, and therefore we implemented a complete procedure for the realization single-mode channel waveguides, thanks to the use of the different techniques employed in this work: photolithography, heat treatments, sputtering deposition.

Therefore in this section we discuss the fabrication and characterization of optical standard waveguides in Lithium Niobate. Firstly we present the diffusion of slab waveguides on x-cut crystals and their compositiona characterization –using the Secondary Ion Mass Spectrometry (SIMS) and the Rutherford Backscattering Spectrometry (RBS)– to achieve the in-depth profile and consequently estimate the diffusion coefficient. We measure the number of modes supported by the waveguides to characterize the optical response of the doped region. Finally we discuss multimodal and monomodal channel waveguides realized by the mean of photolithography and their optical characterization with the Near Field technique.

In the next section we briefly discuss the diffusion behavior of the Ti in $LiNbO_3$ and the numerical solution of the waveguide modes; therefore we show our procedure and results.

2.2. Titanium Diffusion in Lithium Niobate

The thermal diffusion of thin films of titanium evaporated or sputtered onto the substrate surface [14] is a widely used method for waveguide formation in $LiNbO_3$, and most of the integrated optical devices available today are based on titanium-diffused $LiNbO_3$ waveguides. A large number of other metals can be diffused into $LiNbO_3$ to form waveguiding layers, for example, vanadium, nickel, niobium, cobalt, silver, or gold [14], but the best results were obtained by using titanium. Titanium diffusion was studied in details [15][10] and it was reported that into $LiNbO_3$ is the following: at a temperature of about 500°C, titanium is oxidized to TiO_2, and above 600°C $LiNb_3O_8$ epitaxial crystallites are formed at the surface, connected with a loss of lithium. For temperatures larger than 950°C a $(Ti_{0.65}Nb_{0.35})O_2$ mixed oxide appears, which acts as the diffusion source for titanium indiffusion. With increasing annealing time titanium diffuses deeper into the crystal, and the titanium–niobium oxide layer decomposes. The diffusion process follow the Fick's Laws and therefore the diffusion profile can be described by

$$C(x,t) = C_0 \operatorname{erfc}\left(\frac{x}{\sqrt{4Dt}}\right)$$

EQUATION 1

for infinite dopants source, and by

$$C(x,t) = C_0 \exp\left(\frac{x^2}{4Dt}\right)$$

EQUATION 2

for thin layer, as it is in our case. Where C(x,t) is the depth concentration of the Ti ions, C_0 the superficial concentration, and D the diffusion coefficient. Therefore the depth of diffusion can be controlled varying the diffusion time for a determined temperature. In fact the diffusion coefficient D depends on the temperature of diffusion with an Arrhenius relation. Therefore it is necessary to measure the value of D(T) and of the superficial concentration (C_0) to determine the waveguide geometrical parameter. The diffusion coefficient and the superficial concentration measurements are discussed in section 2.5.2, together with the measure of the depth of diffusion.

Finally, to simulate the refractive index profile of the waveguide we have to know also the relation between C(x,t) and n. Some papers dealt with the problem of the determination of refractive index changes in Ti-diffused $LiNbO_3$ optical waveguides [11][12]. A linear dependence between the extraordinary refractive index change and titanium concentration was obtained by Minakata et al. [11], whereas a nonlinear relationship was found by Fouchet et al. [12] and Caccavale et al. [13]. These relations were used in the simulation discussed in section 2.3.

2.3. Numerical simulation

A numerical simulation was used to find the fabrication parameters of a single-mode channel waveguide. The simulation was done using COMSOL software by Dr. Nicola Argiolas of the Department of Physics and Astronomy of the University of Padova. The modes supported by the waveguide were calculated as the solution of the Maxwell's equation in a graded-index waveguide. Therefore, the solutions of the Maxwell's equations were searched in the hypothesis of harmonic monochromatic planar waves, then only the spatial component of the wave function was taken into account. The problem was solved only for the electric field component, as the magnetic field can be simply derived from its solution. Therefore we suppose that the

waveguide is invariant along the propagation direction (z), while the amplitude of the function varies only in the transversal plane (x,y): $\bar{E} = \bar{E}_{x,y} e^{ik_z \cdot z}$. Consequently the solutions of the system, for insulating and paramagnetic materials, can be found as the eigenvalues and eigenvectors of the following equation:

$$\bar{\nabla} \times (\bar{\nabla} \times \bar{E}) - k_0^2 \varepsilon_r \bar{E} = 0$$

EQUATION 3

Where $\varepsilon_r = \varepsilon_r(x, y)$ and depends on the Titanium concentration profile of the waveguide, as it is related to the square of the refractive index for non-absorbent materials, and it depends on the concentration as $n_e^{Ti} = n_e + cost._e \cdot C(x, y)$, $n_o^{Ti} = n_o + cost._o \cdot C(x, y)^{\gamma_o}$ for extraordinary and ordinary polarization respectively [11]–[13]. The eigenvalues are therefore the effective refractive index of propagation and the eigenvectors the electric field vectors. Since ε_r varies in the plane (x,y) the solutions of the Equation 3 can be found only with a numerical method (COMSOL software).

Therefore from the compositional characterization presented in section 2.5 we calculate the refractive index profile of a y-propagating channel waveguide on x-cut obtained from Ti diffused at 1030°C for 2,2 hours (approximating the lateral diffusion equal to the depth diffusion) for a total Ti dose of $1{,}5 \cdot 10^{17}$ atoms/cm^2. We tried different width of the starting Ti strip photolithographically deposited on the LN surface, in order to find at which dimension the waveguide simulated would be single-mode. We found a single mode for a 5μm-width strip. In Figure 2 we present the only one physical meaningful solution of Equation 3 in TE polarization, for the 5μm-width waveguide. The relative effective refractive index calculated is 2,2032. In figure we also present the effective dimension of the waveguide, as the difference between the refractive index and the effective refractive index.

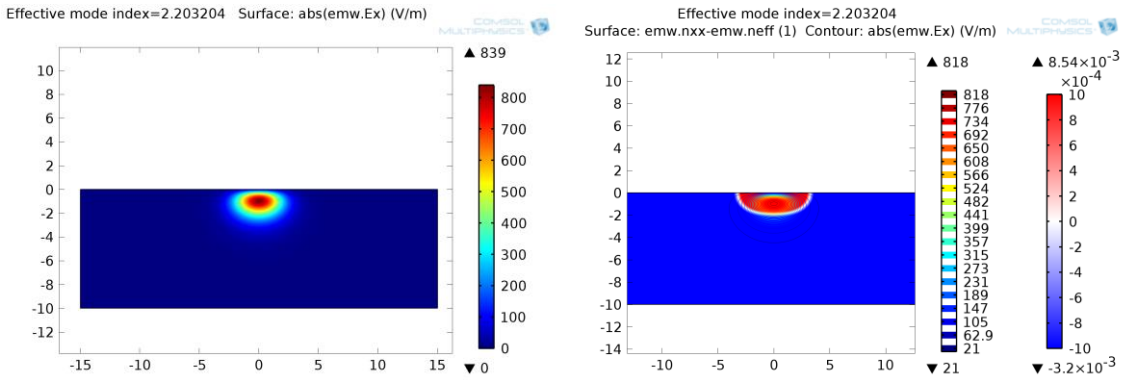

FIGURE 2 ON THE LEFT THE NUMERICAL SIMULATION OF A TE SINGLE-MODE RADIATION PROPAGATING IN A NOMINAL 5 μm WAVEGUIDE. ON THE RIGHT THE REPRESENTATION OF THE EFFECTIVE DIMENSION OF THE WAVEGUIDE, I.E. THE DIFFERENCE BETWEEN THE REFRACTIVE INDEX AND THE EFFECTIVE REFRACTIVE INDEX OF THE CALCULATED MODE. FOR BOTH THE FIGURE THE SCALE IS IN MICROMETERS.

2.4. Fabrication

This section is devoted to the presentation of the experimental procedures used to prepare and characterize Ti in-diffused samples. In the first part of the section the main steps involved in the preparation of a diffused Ti:LN x-cut samples are presented, then the usual techniques exploited to characterize the compositional and structural properties of each realized sample are briefly discussed. Finally the best experimental conditions to realize monomodal diffused Ti:LN waveguides are summarized. The parameter of Ti in-diffusion samples are shown in Table 2 and Table 3. Although this doping process was already known, the implementation of channels waveguides instead of planar one was a new issue for the group, and literature is not exhaustive in this topic since Ti:LN channel waveguides are the base of commercial modulators, and therefore, a patented process.

Sample cutting and cleaning: The first stage of the samples preparation is the cutting of the substrates. The congruent lithium niobate crystals are obtained by a commercial x-cut wafer, 1mm thick, and polished on both faces. A South Bay 540 cutting machine, equipped with a diamond-coated Cu-alloy blade, is used to cut the wafer, whose crystallographic axes can be aligned with respect to the blade by using a protractor. Therefore the lithium niobate wafer is cut along its $\hat{y}$ and $\hat{z}$ directions and, according to their experimental purpose, substrates with different sizes can be obtained. After the cutting, just before the beginning of the deposition process, each sample was washed

with soap and distilled water, then cleaned with the propanol, and finally immersed in acetone in an ultrasonic cleaner for about ten minutes.

Titanium thin film deposition: In this work, to realize titanium thin films on lithium niobate substrates it was exploited the magnetron sputtering technique, which is one of the most widely used surface coating technique. Sputtering is basically the removal of atoms from a solid material by bombardment of its surface with energetic particles. The process occurs in a vacuum chamber, where the substrate and the target are located and, once the appropriate pressure is reached, and inert gas is introduced. When a negative voltage is applied to the target, it attracts the positive ions of the gas which collide with the surface atoms of the material, leading to an energy transfer which results with the sputtering of some atoms. Then the sputtered neutral atoms tend to deposit on all the surfaces present in the chamber, therefore also on the considered lithium niobate substrate. Besides from the sputtering of a target atom, another important phenomenon involved in this process is the emission of secondary electrons from the target surface. If permanent magnets are positioned under the target, the secondary electrons are trapped around the magnetic field lines undergoing more ionizing collisions with neutral gas than would otherwise occur. This enhances the ionization of the inert gas near the target, leading to a higher sputter rate. The sputtering machined used was provided by Thin Film Technology and it is equipped with three sources: a DC (diode) magnetron for metallic targets and two RF (radio frequency) magnetron for semiconducting ones. In the cylindrical chamber the vacuum is achieved by using two pumps: first a rotary vane vacuum pump is activated to reach a pressure of about $9\text{-}10 \cdot 10^{-2}$ mbar, then a turbomolecular one is switched on to obtain and maintain a pressure less than $3 \cdot 10^{-6}$ mbar. The sample is mounted in a sample-holder located at the opposite side of the Titanium target and during the sputtering process it is rotated, in order to achieve a good homogeneity in the thickness of the deposited film. The used inert gas is Ar and, before starting with the deposition process, a pre-sputtering of about 2 minutes is usually performed, to remove all the possible impurities present on the surface of the solid target. Finally, when the deposition is completed, all the pumps are stopped and, to return to the atmospheric pressure, Ar gas is still introduced in the

chamber. The Rutherford Backscattering Spectrometry discussed in section 2.5.1 gave a flux of deposition of $8{,}3 \cdot 10^{14}$ molecules s^{-1} cm^{-2}.

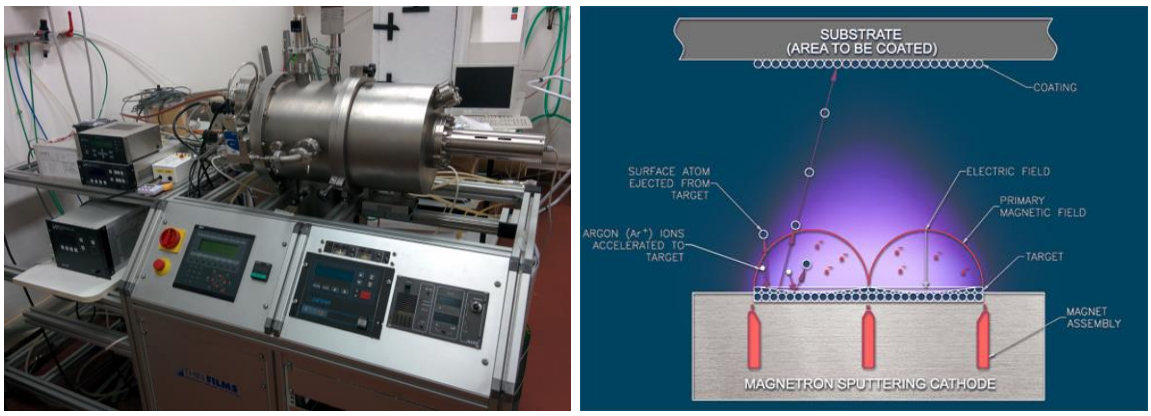

FIGURE 3 MAGNETRON SPUTTERING APPARATUS ON THE LEFT. SCHEME OF THE MAGNETRON SPUTTERING DEPOSITION ON THE RIGHT.

The thermal treatments: After the deposition of the Ti film, the dopant is completely diffused inside the $LiNbO_3$ substrate by performing thermal treatments. The diffusion process occurs in a tubular furnace, by Gero Hochtemperaturofen Gmbh (model F-VS 100-500/13), and the heating tube consists of an uncovered FeCrAl heating coil, mounted on a ceramic fiber module whose low thermal conductivity guarantees low energy consumption and allows high heating rates, up to 600 °C/h. The furnace is equipped with all the necessary to realize thermal treatments in vacuum or different gases: water-cooled flanges, gas inlet and outlet and two rotameters to adjust the gas flux at the entrance of the furnace. The rotameter scale is in Nl/h and the gases used are provided by Sapio in cylinders of 40L and purity 5.0. At the center of the tubular furnace there is a region, long some centimeters, where the highest temperature is homogeneous, thus the sample is located in that zone by using a quartz rod with at the end a square support. Moreover, between the support and the $LiNbO_3$ sample a Platinum support layer is fixed, to avoid a possible high-temperature reaction between SiO_2 and the sample, which would dissolve the crystal. Each sample is positioned on the support with the Ti film upward and heating/cooling rates of 300 °C/h and 400°C/h respectively are used, in order to avoid an excessive thermal stress on the sampe. The diffusion of Ti into the substrate can occur in vacuum or in different atmospheres. In our case the gas used during the diffusion process was oxygen, this to reduce the damage of the surface [16]. Unfortunately the

use of a wet atmosphere was not possible in our set-up, and therefore the optimal conditions that avoid the Lithium out-diffusion was not achievable. The samples were then diffused at a temperature of 1030°C.

FIGURE 4 THE TUBULAR FURNACE GERO HOCHTEMPERATUROFEN GMBH (MODEL F-VS 100-500/13)

Lapping and polishing: The Near-Field characterization (section 2.10) of the waveguide needs lateral surface of the samples with a roughness of an optical quality, therefore after the realization of the waveguides all the samples were polished and lapped. Lapping and polishing are processes by which material is precisely removed from a workpiece to produce a desired dimension, surface finish, or shape. These processes have been applied to a wide range of materials and applications and they are useful due to the precision and control with which material can be removed. Surface finishes in the nanometer range can be produced using these techniques, which makes lapping and polishing an attractive method for materials processing. In particular the lapping is the removal of material to produce a smooth, flat, unpolished surface and a midrange abrasive particle (5-20m) is typically used, while polishing is exploited to produce a scratch-free, specular surface using fine (<3μm) abrasive particles. The machine used to polish and lap the samples of this work is a professional one by Logitech. The machine uses a rotating disc and a device, called JIG, on which one or more samples are mounted and that allows to regulate the force with which the sample is pressed on the disc. The lapping process is divided into two steps and it is used to remove the subsurface damage caused by the cutting of the sample from the original commercial wafer. In these stages an iron disc is used to remove material from the surface of the sample with a rate of 10 μm/min by

using first an aqueous solution of 9μm alumina particles and then a 3 μm one. Moreover at each step, before changing to the next one, a microscopy is used to verify that at the surface of the sample they are present only damages whose size is about the same of the alumina suspension used. Finally, in the third stage a polyurethane disc is used with a SF1 alumina colloidal suspension (0.1 μm) and a polished sample is obtained with a surface roughness less than about 1 μm.

2.5. Compositional Characterization

Different samples diffused with a planar layer of Titanium were compositional characterized in order to determine fundamental diffusion parameters. First of all, the deposited dose of Titanium was measured using the Rutherford Backscattering Spectrometry (RBS), therefore the Diffusion coefficient at 1030°C and the concentration profiles of the Ti inside the Lithium Niobate were obtained using the Secondary Ion Mass Spectrometry (SIMS). In the following section we present the two techniques and the main results obtained.

2.5.1. Rutherford Backscattering Spectrometry (RBS)

Rutherford backscattering technique (RBS) was used to quantify the absolute amount of titanium deposited. The knowledge of the dose of Ti, together with the knowledge of the thickness by profilometry, allows determining the density of the film before the diffusion; moreover, assuming that Ti does not evaporate during diffusion, it allows converting the SIMS yeld into a concentration profile (section 2.5.2). Finally, knowing the time of deposition, we can calculate the flux of the sputtering deposition.

In a RBS measurement, few MeV light ions collide on a sample surface, the incident ions undergo collisions with target atoms and are therefore scattered. Finally the backscattered ions are then collected by a Mass spectrometer. The number N_s of target atoms per unit area is determined by the probability of a collision between incident particle and target atoms as measured by the total number of detected particles Q_D for a given number Q of incident particles. The connection between number of target atoms per unit area N_s and number of detected particles is given by the scattering cross

section σ(θ,Ω) which is tabulated in literature. Therefore for small solid angle Ω of detection we have

$$Q = \sigma(\vartheta) \cdot \Omega \cdot Q \cdot N_s$$

EQUATION 4

Where σ(θ) is an average cross section for small solid angle.

The RBS experiments were performed at the National Laboratory of Legnano (LNL-INFN) on a two as-deposited samples on glass (SiO_2) substrate. The detector was placed at 170° with respect to the incident beam, with a detection solid angle (measured with calibration standard) equal to 1,966 mstrad.

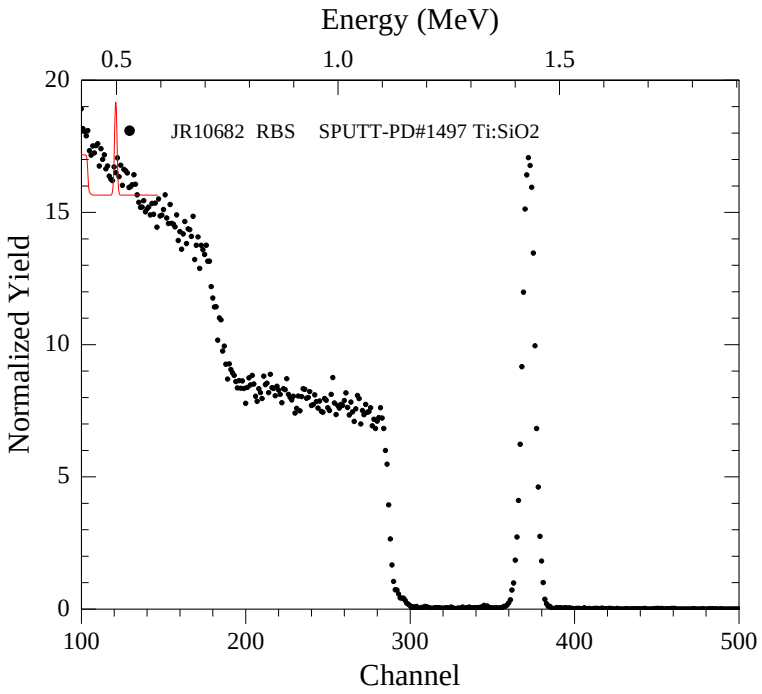

FIGURE 5 RBS SPECTRUM IN CHANNELING CONDITION OF AN AS-DEPOSITED SAMPLE OF TI ON GLASS (SiO_2). ABSCISSA REPORTS THE CHANNEL NUMBER, EACH CHANNEL DETECT AN ENERGY RANGE OF BACKSCATTERED PARTICLES.

In Figure 5 a typical RBS spectra in channeling condition with x axis is reported. The Ti peak is clearly distinguishable from the background signal due to Si, and O backscattering, which rises going from higher to lower energies. Since Ti atoms are located in a very thin layer on the surface, they give rise to a narrow peak whose width depends only on the energy resolution of the detector. By means of the Rutherford cross-section, the solid angle of detector acceptance, the Ti screening factor, and the incident

ion charge, it is possible to relate linearly the integral area of the Ti peak to the fluence of $150 \cdot 10^{15}$ molecules cm^{-2} for both the samples measured. Therefore the flux of deposition calculated is $8{,}3 \cdot 10^{14}$ molecules s^{-1} cm^{-2}. Moreover the spectra evidence also the partial oxidation of the sputtered layer ($TiO_{0,8}$), which in our case is not a problem, since the oxidation of the Titanium is an essential step to achieve the diffusion inside the Lithium Niobate. Finally we calculate, from the measure of the thickness of the Ti layers using a profilometer, a bulk concentration of 4,06 ± 0,08 molecules cm^{-3}.

2.5.2. Secondary Ion Mass Spectrometry (SIMS)

Secondary ion mass spectrometry (SIMS) is a powerful analytical tool to study the in-depth profile of dopants, for its extremely high sensitivity and significant depth resolution. The fundamental basis of SIMS analyses is the measurement of the mass and intensity of secondary ions produced in a vacuum by sputtering the sample surface with energetic ion or neutral beams. The sputtering beam is referred to as the primary beam and typically has a kinetic energy of several thousand electron volts. The primary beam removes atomic or molecular layers at a rate determined principally by the intensity, mass, energy of the primary species and the physical and chemical characteristics of the sample. Sputtering of the sample produces a variety of particles including electrons, photons, atoms, atomic clusters, molecules and molecular fragments. A small fraction of these sputter products is ionized, and these ions are the secondary ions in secondary ion mass spectrometry. In a typical Dynamic SIMS analysis, the samples are sputtered by a focused energetic primary ion beam which is rasted over a square area, usually a few hundred microns on a side. Secondary ions formed during the sputtering process are accelerated away from the sample surface by electrostatic fields (in particular the sample voltage is close to -4500 V). Fractions of the secondary ions are accepted for analysis by a mass spectrometer and are collected from a circular area centered in the rasted region. This field of view is defined by an adjustable field aperture in the ion optic column. This aperture provides an optical gate that is used to improve depth resolution by rejecting secondary ions emitted from the wall of the sputtered crater where material at different depths is exposed simultaneously. The transmission

(sensitivity) of the spectrometer is further controlled by a second adjustable aperture in the secondary ion optic column. Adjustable entrance and exit slits are used to adjust the mass resolution of the spectrometer when it is necessary to separate interfering ions of the same nominal mass/charge ratio. The secondary ions are energy focused by an electrostatic analyzer and mass-filtered by a magnetic sector analyzer. After passing through the analyzers, the ions are detected either in an analog current mode using a faraday cup or in a pulse counting mode using an electron multiplier.

Dopant profiles of the diffused samples were measured by SIMS using a CAMECA ims4f equipped with a normal incidence electron gun used to compensate the surface charge build-up while profiling insulating samples without any need to cover the surface with a metal film. Concentration profiles were obtained by 14.5 keV Cs positive ion bombardment and by negative secondary ion detection. The calibration of the Ti profiles was made by means of the measurement of the total Ti dose in the as-deposited films using RBS (section 2.5.1). In fact, the integral of each profile was normalized to the fluence, known from RBS measurements, to obtain the absolute concentration profile, i.e. for each profile the proportionality factor between normalized signal and concentration was determined. This constant is usually called relative sensitivity factor RSF, defined by the equation:

$$C[atoms/cm^3] = RSF \cdot I$$

EQUATION 5

Therefore a typucal concentration profiles is presented in Figure 6, with its good Gaussian fit (R^2= 0,9998) which yelded the value of the diffusion coefficient D and of the superficial concentration C_0 (Table 1). Moreover the SIMS profile fitting allows determining the depth of the waveguide which is related to the Diffusion coefficient by

$$\sigma = \sqrt{4Dt}$$

EQUATION 6

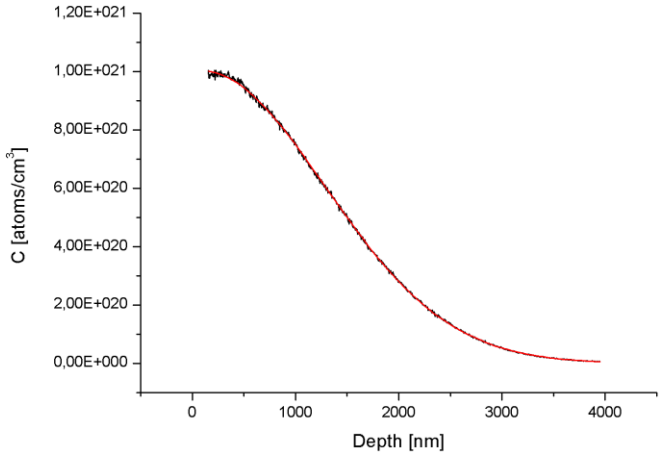

FIGURE 6 PROFILE TI CONCENTRATION ELABORATED FROM A SIMS MEASURE (BLACK) AND THE RELATIVE GAUSSIAN FIT (RED)

In the past years other SIMS and RBS measurements -done by Dr. M.V. Ciampolillo in the same conditions- gave a value of the diffusion coefficient of 88±3 nm^2/s, fully comparable with our measures.

	Value	Error
σ	1203 nm	6 nm
C_0	$1{,}00 \cdot 10^{21}$ at/cm^3	$2 \cdot 10^{19}$ at/cm^3
D	91 nm^2/s	2 nm^2/s

TABLE 1 PARAMETER OF THE TI DIFFUSION OBTAINED FROM THE GAUSSIAN FIT

2.6. Planar waveguides

After the characterization of the sputtering and diffusion processes, planar waveguides on x-cut crystals were realized with the same set-up and different parameters (Table 3) in order to optimize the production of monomodal waveguides in the visible range. This was the first step necessary to obtain the channel waveguide that are discussed in section 2.9. After the production, the samples were characterized with the m-lines technique in order to measure the number of modes guided. In Table 2 the main parameters for the production of the planar waveguides are reported

Sputtering Pressure	Sputtering Power	Diffusion Temperature
5,00E-03 mbar	80 W	1030 °C

TABLE 2 PARAMETERS OF DEPOSITION AND DIFFUSION OF THE TI

2.7. Optical characterization

2.7.1. m-lines

The numbers of modes of the waveguides were determined by the means of m-lines spectroscopy [17], which is based on a standard prism-coupling method that uses the setup illustrated in Figure 7, equipped with a rotating stage. The m-lines spectroscopy is a non-destructive method. The light source was a He–Ne laser at 632 nm and solid-state laser at 532 nm. Waveguide modes are selectively excited through the coupling prism by varying the incidence angle, and the coupling angles are determined by collecting the light in total reflection from the sample (dark-lines mode). An automatized system allows scanning the incidence angle interval within which the modes are excited with an uncertainty of 0.01°. The signal from the waveguide, collected by a photodiode, is filtered through a lock-in system and displayed in real time on the system display as a function of the rotation angle.

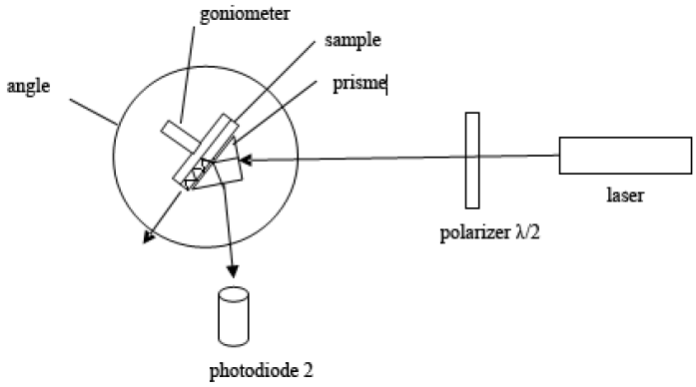

FIGURE 7 THE M-LINES SETUP: THE LIGHT SOURCE IS A HE-NE LASER AT 632 NM OR A SOLID STATELASER AT 532 NM. THE POLARIZER λ/2 IS USED TO CHOOSE THE TE OR THE TM MODES, THE ROTATING TABLES CHANGES THE INCIDENCE ANGLE OF THE LASER BEAM WITH THE PRISM, THE PHOTODIODE MEASURE THE INTENSITY OF REFLECTION LIGHT (DARK LINES). THE PRIMES USUALLY USED THE ANGLE TO 90° OR 60°.

In Figure 8 a single-mode planar waveguide m-lines spectrum is showed, the negative peak corresponds to a TE mode guided by the Ti layer. The peak is due to the light coupling at the prism-waveguide interface, with the consequent reduction of the reflected intensity.

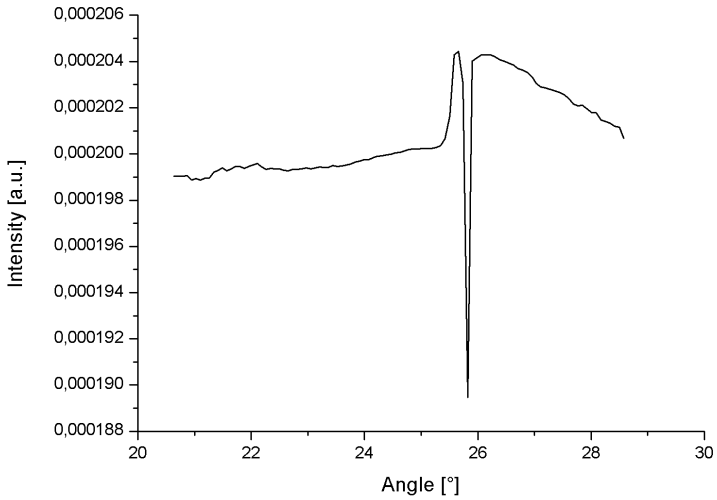

FIGURE 8 DARK M-LINES AT 633NM FOR A PLANAR WAVEGUIDE OBTAINED WITH 2,75 S OF SPUTTERING AND 2,2 HOURS OF ANNEALING AT 1030°C.

2.8. Results and Discussion

Sample	Sputtering time	Diffusion time	Number of modes	Number of modes
	minutes	hours	At 532 nm	At 633 nm
140.7	5,5	2,2	2	2
140.10	4	2,2	2	2
140.11	3	2,2	2	1
140.14	2,75	2,2	1	0

TABLE 3 PARAMETERS OF FABRICATION AND NUMBER OF MODES FOR PLANAR WAVEGUIDES AT TWO DIFFERENT WAVELENGTHS.

In Table 3 the parameters of production and the number of modes guided at 633nm and at 532 nm are presented. The sample 140.11 was the best of the samples analyzed, however we were not able to achieve the monomodal guiding at both the wavelength. We report in Table 4 the parameters and characteristics of the waveguide. Therefore sample 140.11 was chosen as the starting point used to achieve monomodal channel waveguides.

Dose	Annealing time at 1030°C	Calculated depth	Measured depth (SIMS)	Number of modes	Number of modes
(atoms/cm^2)	(h)	(μm)	(μm)	at 532 nm	at 633 nm
1,5 10^{17}	2,2	1,2	1,4	2	1

TABLE 4 OPTIMIZED PARAMETERS TO OBTAIN A MONOMODAL PLANAR WAVEGUIDE WITH TI IN-DIFFUSION IN LITHIUM NIOBATE AT 1030°C (DIFFUSION COEFFICIENT 88±3 NM^2/S).

2.9. Channel waveguides

As previously reported the realization of channel waveguides was a process to be settled. A titanium film was deposited onto an x-cut $LiNbO_3$ substrate and patterned photolithographically using the procedure described in section 3.3.2. The parameters of diffusion and the width of the waveguides were chosen using the simulation discussed in section 2.3, therefore a width of 5 μm was used to achieve monomodal waveguides with the same diffusion conditions of the monomodal planar waveguides of section 2.8, Table 4. Three kinds of waveguides were realized, multimodal 12-μm and 10-μm; and monomodal 5-μm waveguides. Therefore the samples were lateral lapped and polished to allow the optical characterization using the Near Field technique.

In Table 5 we report the samples produced and analyzed. Different parameters were explored: geometrical dimensions, direction of propagation, parameters of production. Therefore we characterize the channel waveguides in order to find the best condition to achieve monomodal channel waveguides at 633 nm.

Channel waveguide width	Atmosphere and Temperature of Annealing	Propagation direction
13.0 ± 0.3 μm	Air, 1030 °C, 2h	z
11.5 ± 0.5 μm	Air, 1030 °C, 2h	y
9.8 ± 0.5 μm	O_2, 1030 °C, 2h	z
12.6 ± 0.4 μm	O_2, 1030 °C, 2h	z
5.9 ± 0.2 μm	O_2, 1030 °C, 2h	z
5.3 ± 0.3 μm	O_2, 1030 °C, 2h	y

TABLE 5 STRIP WIDTH OF THE DEPOSITED TI AND ANNEALING PARAMETERS OF WAVEGUIDES WITH DIFFERENT DIRECTION OF PROPAGATION

2.10. Near Field

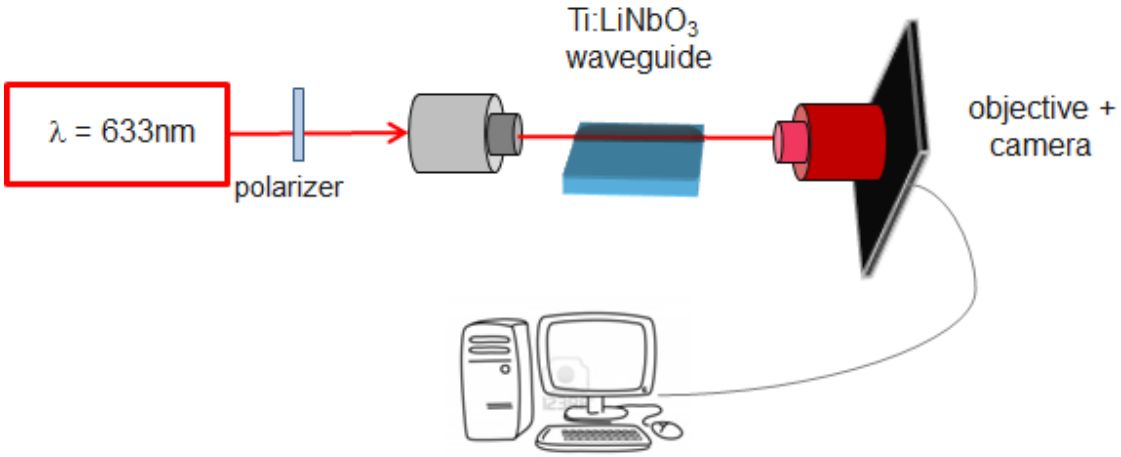

FIGURE 9 NEAR FIELD APPARATUS SCHEME, A LASER DIODE AT 633 NM IS POLARIZED AND FOCALIZED (20X) INSIDE THE WAVEGUIDES, THEN THE LIGHT IS COLLECTED AT THE WAVEGUIDE END BY A 20X OBJECTIVE AND THEREFORE RECORDED BY A DIGITAL CAMERA.

The channel waveguides realized were characterized using the near field technique. The method, sketched in Figure 9, consist on a fiber-coupled laser diode at 633 nm which is polarized TE or TM and then focalized with a 20x objective to the head of the waveguide. Therefore at the output of the optical waveguide the near-field image is collected by a Vidicon tube by using a 20x (f=10mm) objective lens and recorded by a digital camera (LaserCam-HR, Coeherent), which allows measuring the intensity distribution of the guided beam and therefore the number of modes transmitted.

In Figure 10 three samples with different widths of the waveguides are compared, it can be easily seen that reducing the width from 11,5 to 5 μm allows passing from a multimode waveguide to a single-mode waveguides. In particular in Figure 11 we compare the image of a single TE mode 5 μm waveguides with its simulation that was previously calculated as explained in section 2.3, demonstrating the good behavior of our simulation tool to forecast the light propagation in our waveguides.

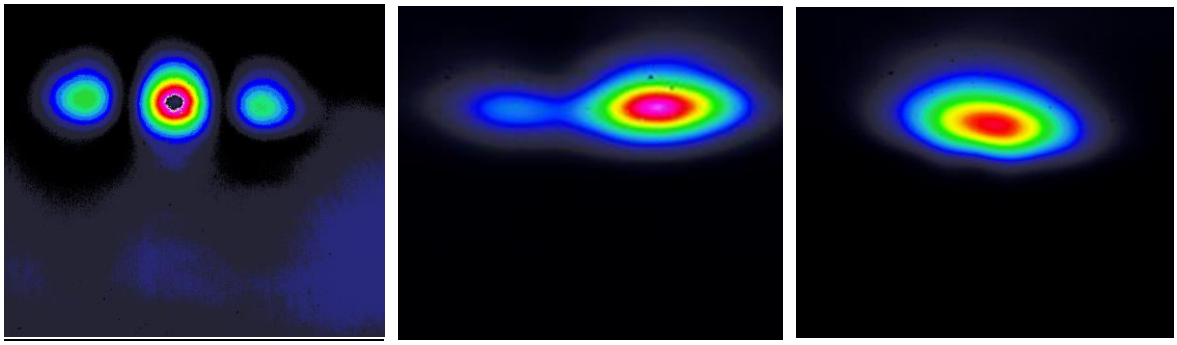

FIGURE 10 NEAR-FIELD IMAGES OF THREE 1,4 µM DEPTH Y-PROPAGATING WAVEGUIDES ON X-CUT SAMPLES (λ=633 NM, NO POLARIZATION). LEFT) MULTIMODE WAVEGUIDE (NOMINAL WIDTH 11,5 µM); CENTER) MULTIMODE WAVEGUIDE (NOMINAL WIDTH 10 µM) RIGHT) SINGLE-MODE WAVEGUIDE (NOMINAL WIDTH 5 µM).

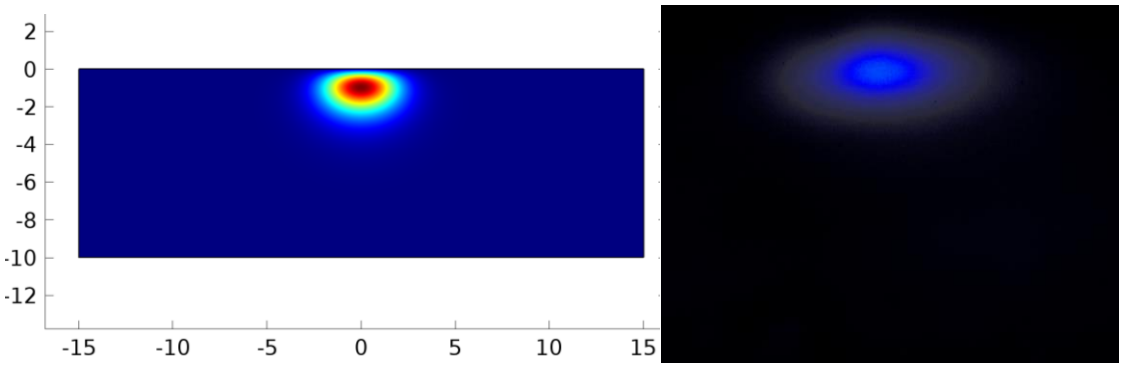

FIGURE 11 COMPARISON BETWEEN THE SIMULATION OF A 5 µM WAVEGUIDE TE SINGLE-MODE (ON THE LEFT) AND THE NEAR FIELD IMAGE OF A TE MODE IN A 5 µM WAVEGUIDE.

Finally, in Figure 12 we present a comparison between a y propagating and a z propagating 5 µm waveguides, both the samples are single-mode and therefore we can use the same production process also for the z propagating waveguides.

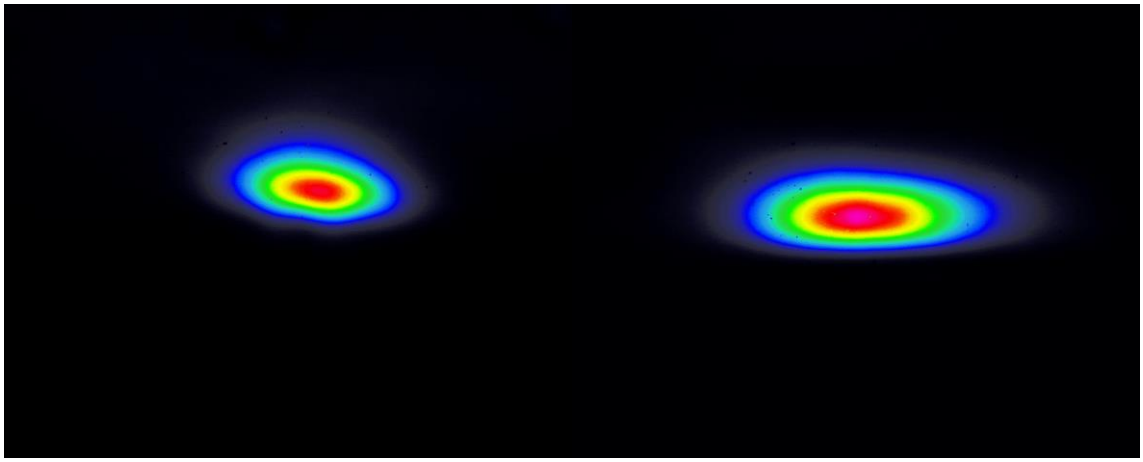

FIGURE 12 ON THE LEFT THE NEAR FIELD IMAGE OF A 5 µM Y-PROPAGATING WAVEGUIDE, ON THE RIGHT THE NEAR FIELD IMAGE OF A 5 µM Z-PROPAGATING WAVEGUIDE. BOTH THE WAVEGUIDES WERE PRODUCED WITH THE SAME PROCEDURE (1030°C, 2.2 HOURS, O_2 ATMOSPHERE).

3. PPLN Frequency Converter

3.1. Introduction

Many applications in different fields (e.g. optofluidic, biomedical, optical data storage, telecommunications, printing and displays, etc…) would greatly benefit from the availability of compact and low-cost, solid-state sources emitting in the visible range. Nowadays semiconductor lasers allow covering a large fraction of the visible spectrum, but the availability of green-light sources is still limited, and green laser light is generally produced by exploiting nonlinear optical processes, such as the second harmonic generation (SHG) of lasers emitting in the infrared. Very efficient SHG can be performed by exploiting quasi-phase matching (QPM) technique in ferroelectric materials [18][19], which allows to phase-match the desired nonlinear interaction, and to exploit large χ^2 nonlinear coefficients [20]. The QPM technique requires to periodically reversing the material spontaneous polarization, which is the sign of the χ^2 coefficient, with a period matching an even multiple of the coherence length [21]. In ferroelectric crystals, such as lithium niobate (LN), this process creates a periodic structure of ferroelectric domains (so called periodically-poled lithium niobate, PPLN). In the past decades, several techniques were developed for the fabrication of PPLN [22][23], and currently electric-field poling is the most commonly used system [24][25]. According to this technique, an electric field higher than LN coercive field is applied to selected regions of the sample where patterned electrodes are deposited, yielding a localized polarization reversal. Although high quality PPLNs are now commercially available, their application to the generation of high-power visible radiation is still limited. This is mainly due to the photorefractive effect occurring in LN, which may produce beam deformation, increase of propagation losses and a strong decrease of the nonlinear efficiency. In order to avoid this effect, it is necessary to use low-intensity beams (both in the visible and in the infrared range [26], or to operate the PPLN at temperatures above 100 °C. In both cases the performance is severely reduced: in the first case in terms of efficiency, and in the second case in terms of device reliability and power consumption. To

overcome this problem a possible solution is to use Magnesium doped LN [23], [27]–[29] that however requires high level of doping (about 6 mol%), that affects the crystal quality and homogeneity. As an alternative to Mg-doped crystals, in this work we evaluate the exploitation of Zr-doped lithium niobate, as this substrate can withstand high optical intensities, without exhibiting appreciable photorefractivity even when the Zr content is as low as 3 mol% [1], [30], [31]. Crystals with the same composition of those considered in this manuscript (Zr:LN crystals doped with 3.0 mol%) were characterized in order to evaluate their optical damage resistance, and the obtained results demonstrated that green light intensities up to 50 kW/cm^2 don't induce any measurable beam smearing (Figure 13) [26][1]. Several papers regarding the properties of Zr-doped LN crystals were published in the last few years, but, to the best of our knowledge, no data has ever been reported on the post-growth periodic-poling of this material, and about the nonlinear performance of Zr-doped periodically-poled LN.

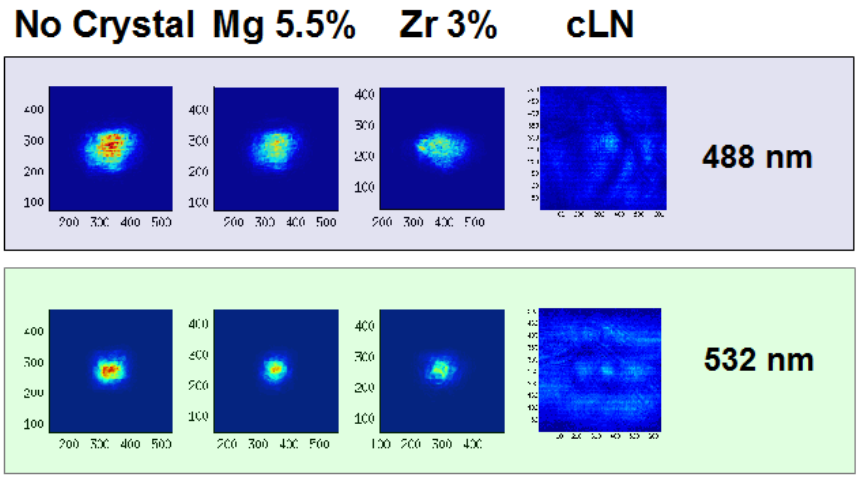

FIGURE 13 THE IMAGES PRESENT THE DISTORTION OF A LASER BEAM COLLECTED AFTER THE TRANSMISSION THROUGH DIFFERENT MATERIALS AND AT TWO DIFFERENT WAVELENGTHS. THE COMPARISON CONFIRMS THAT THE ZR DOPING LN AT 3% MOL. IS AN EXCELLENT OPTICAL-DAMAGE RESISTANT MATERIAL.

In this section we describe the realization of periodically-poled LN crystals both undoped (cLN:PPLN) and doped (Zr:PPLN) with a 6.8 μm period, and then characterization of the structure and the efficiency of the different samples realized with the described poling set-up. However, first of all a theoretical introduction to SHG, QPM, and poling of LN is discussed.

3.2. Poling

Several techniques have been developed for the fabrication of such systems. Some exploit the direct growth procedures which consist in growing lithium niobate boules under the periodic action of some external influence (such as an alternate current flowing through the crystal while pulling), and post-process electrical treatments. In alternative, by off-centering the crystal growth axis with respect the temperature field, PPLN can be achieved in a Czochralski growth apparatus. In the past this last technique was extensively exploited since, depending on the modulation type, it is able to produce quite easily domain structures on the whole boule volume. Unfortunately the process reproducibility is far from being exported into the in industries for large production. A different approach to obtain PPLNs relies instead on inverting the $LiNbO_3$ spontaneous polarization after the growth [23]. By applying an electric field higher than the lithium niobate coercive field, the ferroelectric domains can be reversed according to the field versus. Among this technique the direct "writing" by electron beams or by High Voltage AFM tips [22] were used but the most exploited is the direct polarization reversal under patterned electrodes. Due to the high value of the coercive field required for reversing domains in crystal thicker than some hundreds of micrometers (up to 21 kV/mm), the periodicities which can be obtained are limited by the spreading of the electric field inside the material. The state of the art of commercial PPLN fabrication using this technique is now 6 μm period in 0.5 mm thick wafers and 17 μm in 1 mm thick wafers.

In this section we will explain the principal characteristic of ferroelectric switching of Lithium Niobate and the correlated characteristic of ferroelectric domains. First of all, we will present thermodynamic and kinetic models describing behavior of uniaxial ferroelectric material like $LiNbO_3$. Then we will discuss the role of dopants in these models. For an instrumental and practical description of the poling process (ferroelectric switching) we remand to section 3.4.

3.2.1. Thermodynamic model

The Landau-Ginsburg theory can explain the spontaneous polarization (P_s) of uniaxial ferroelectric crystal with two antiparallel polarization directions like

$LiNbo_3$. Particularly we will concentrate on the switching process and ferroelectric domains. The phenomenology of a ferroelectric second-order phase transition is described with a thermodynamic potential [23], a Gibbs function with the independent variable temperature and the order-parameter polarization (P). Function G(P, T) for reasons of symmetry is approximated with a polynomial in P having at least terms up to the fourth order.

$$G(P,T) = G_0 + \frac{A(T)}{2}P^2 + \frac{B(T)}{4}P^4$$

EQUATION 7

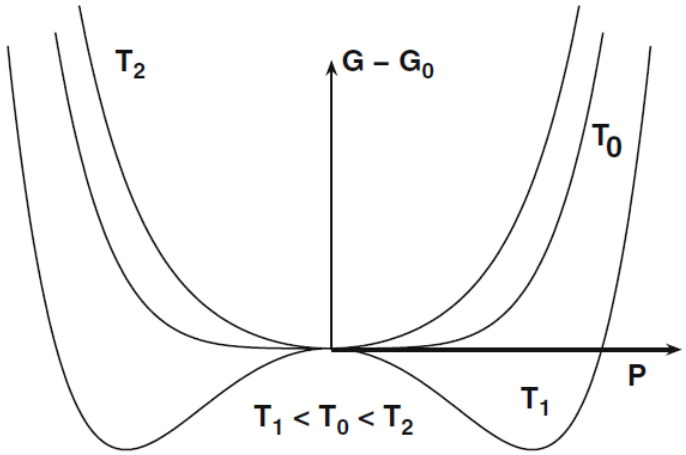

FIGURE 14. GIBBS EQUATIONS AT TEMPERATURE UP AND LOW TEMPERATURE OF CURIE (T_0) FOR IDEAL FERROELECTRIC CRYSTAL

In Figure 14 it is described the ferroelectric phase transition with the appearance of two possible polarization directions ($\pm P_s$) under the Curie temperature (T_0). From the Gibbs equation results the theoretical values of the spontaneous polarization (P_s) and coercive field (E_c)

$$P_s = \pm\sqrt{\frac{-A(T)}{B(T)}}$$

EQUATION 8

$$E_c = \pm\frac{2}{3\sqrt{3}}A(T)P_s$$

EQUATION 9

Applying an external field bigger than the coercive field the crystal inverts its spontaneous polarization (poling). Ferroelectric switching is explained by the displacement of the system from one minimum to the other. Microscopically the polarization reversal requires movement of Lithium ions along the polar

axis through the plane of the oxygen. As consequence crystal presents a hysteresis loop of external field versus polarization. Nevertheless, as it is illustrated in Figure 15, hysteresis loop of real congruent $LiNbO_3$ is shifted along the E-axis, while stoichiometric $LiNbO_3$ seems symmetrical. This is a first deviation of the ideal model just presented, and will be explained in section 3.2.4 with the presence of defects. In fact, stoichiometric Lithium Niobate has less intrinsic defects than congruent one. This shift is described in termed of bias internal field (E_{int})

$$E_{int} = \frac{E_{c1+}E_{c2}}{2}$$

EQUATION 10

Where E_{c1} and E_{c2} are the two different coercive fields for respectively the forward (first polarization of the crystal) and the reverse poling (second polarization to return at the initial state).

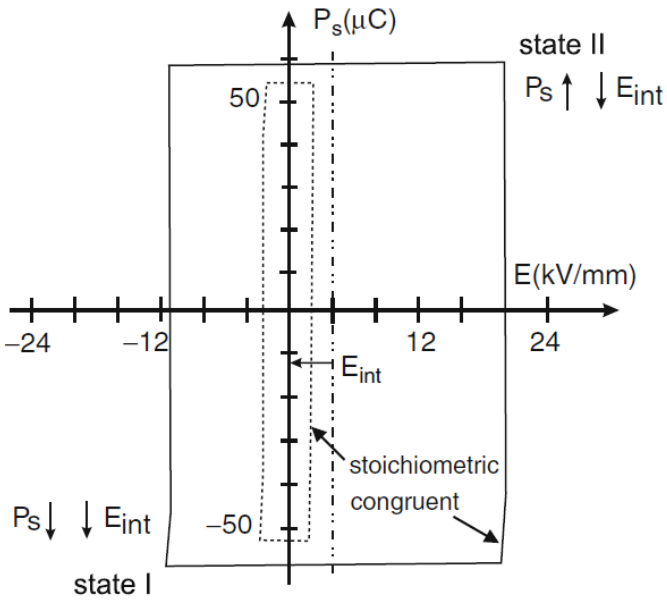

FIGURE 15. P-E HYSTERESIS LOOP FOR STOICHIOMETRIC AND CONGRUENT LITHIUM NIOBATE

Another problem of this first model is that it does not consider contribution of domains in ferroelectric switching. Therefore we have to take into account the depolarizing energy and the energy of the domain walls, with the depolarizing energy depending on the crystal geometry and the surface domain configuration. For a case of periodically poled domain structure it is obtained:

$$w = \sqrt{\frac{\sigma d}{\varepsilon^* P_s^2}}$$

EQUATION 11

with w the domain width, σ is the energy for unit of domain wall area, d the crystal thickness, and ε* a coefficient depending on dielectric constant. The dependence of w to $\sqrt{d}$ was actually observed in some crystals [23]. Moreover the crystal symmetry imposes limitations on the orientation of the domain walls with regard to the crystallographic axes. According to calculations [32][33] and experimental studies the most energetically favorable domain walls are that which lying in the yz plane. Calculations were performed without consider contribution of defects, so they are more appropriate for the stoichiometric crystals.

3.2.2. Domains Kinetic

Kinetic of the domains formation during a poling process is described with Miller–Weinreich model [23]. It consists on several stages of the domain evolution with different velocity contributing at the switching velocity. Optical studies reveal four steps of the domain kinetics under external fields [34]:

- *Nucleation of new domains*: The mechanism of the domain nucleation has not been clarified yet. Usually it is presented as a statistical process with the probability depending on the external field E directed oppositely to Ps

$$p \propto \exp\left(\frac{E_{coercive}}{E_{loc}}\right)$$

EQUATION 12

Nucleation probability is determined by a coercive field E_{ac}, which depends on material properties, shape of nuclei and temperature; and electric field averaged over the volume of the nucleus E_{loc}. It has been observed that the nucleation sites are related to surface defects [34] and that the domains starts always from the +z face. The encrease of the nucleation rate can be related to different phenomena: a spatial inhomogeneity of E_{ac} due to the presence of structural defects; singularities of E_{loc} along the edges of the electrodes; and E_{loc} created

by field concentrators resulting from pits at the surface. Furthermore it is a still unknown if the initial domain state is (or contains) nano-scale residual domains. In fact, spontaneous appearance of antiparallel domains on the polar face may be related to the screening effects of charges on the polar surface, high surface screening fields could lead to a partial polarization reversal [35]. This might be a possible reason of the surface initiating of the domain nucleation.

- *Forward growth*: After the nucleation from the +z face the formed domains expand in the polar direction (z axis). At this stage the domain walls are needle-shaped.
- *Sideways domain growth*: Domains expand in orthogonal direction to the polar axis by wall motion. The wall motion is anisotropy, so we obtain the formation of polygon domains with sides oriented along crystallographic directions. Calculation demonstrated that the real lateral domain wall movement under moderate fields is energetically unfavorable [23]. So, this process is described as a generation of antiparallel domain nuclei on an already existing domain wall, and their subsequent coalescence [36]. Some developments to the model are introduced considering the pinning effect. This effect happens when the domain wall motion is stopped due to the wall coupling with a defect, which causes the formation of a potential barrier. To overcome this barrier (depinning) it required to increase the applied field or heating the crystal. Pinning effects manifest themselves in $LiNbO_3$ and are responsible for extremely high coercive field of these crystals [23].
- *Domain coalescence*: At this step the wall motion decelerates and residual region between walls disappears very rapidly after certain rest time. This process is the causes of a jump-like switching behavior of the crystal and it is known as a noise component of the switching current, called Barkhausen noise [36][37].

3.2.3. Backswitching

Backswitching means a partial or total depoling of a reversed crystal after turning-off the poling field. There are different explanations for this phenomena, complementary rather than conflicting. One is related to the

existence of a critical time (t*) required to depin the wall. In fact, to provide the depinning at a given field, the length of the field pulse should exceed t*, otherwise a domain would come back to its initial boundaries [23]. Another explanation of the backswitching is given by Shur model [37], which describes the role of bulk charges screening. The nucleation probability, as seen, depends exponentially on E_{loc}, which in a ferroelectric capacitor is determined by the following sum of components

$$E_{loc}(r,t) = E_{ex}(r) + E_{dep}(r,t) + E_{scr}(r,t) + E_{b}(r,t)$$

EQUATION 13

where $E_{ex}(r)$ is the external field produced by the voltage applied to the electrodes; $E_{dep}(r,t)$ is the depolarization field produced by bound charges existing at the polar surfaces and at the charged domain walls which is opposite to E_{ex}; $E_{scr}(r,t)$ is the external screening field originating from the redistribution of the charges at the electrodes; and $E_b(r,t)$ is the bulk screening field governed by bulk screening processes [37] explained successively.

The cooperative action of E_{dep}, E_{scr} and E_b could lead to the backswitching after switch-off of the external field. In fact the external screening is opposite to the depolarization field, but it could never compensate completely E_{dep} due to existence of the dielectric surface layer [37]. So bulk screening is the only process that could compensate completely E_{dep} and so avoid the backswitching. There are three different bulk screening mechanisms: redistribution of the bulk charges [37], reorientation of the defect dipoles [38], and injection of carriers from the electrode through the dielectric gap [39]. The time constants (τ_b) of all mechanism considered has a range from milliseconds up to months. So if external field impulse are shorter than τ_b the bulk screening doesn't change and remain quite the same of old state, than switching is ineffective and no irreversible change of the domain structure occurs, and as a consequence the domains backswitch. For pulses longer than τ_b the bulk screening field could change sign thus stabilize the reverse domain. It is important to note that high temperatures could decrease τ_b by increasing the defect mobility.

Defects are involved in both the model we had presented, as cause of the pinning effect, or as origin of the bulk screening field. In the following chapter role of defects and dopants on ferroelectric switching properties will be discussed.

3.2.4. Dopants Dependence

The polarization reversal in $LiNbO_3$ containing structural defects cannot be presented simply as a symmetry inversion of the single-domain matrix [23], as experiments revealed different structure between antiparallel domain [40]. This is the origin of the internal field, and therefore of the shift along the E-axis of the P-E hysteresis loop of Lithium Niobate (Figure 15). In some studies internal field is attributed to the dipole moments of defect clusters $[Nb_{Li}–4V_{Li}]$ [32], moreover Kim et al. [23] also proposed a model in which at room temperature it is postulated that the point defects Nb_{Li} are fixed by Li vacancies, so the cluster dipoles cannot be reoriented and conserve the initial direction of E_{int}. These dipoles may be realigned only at T > 100–150°C where the defects mobility is increased. So the reason of the observed reorientation of E_{int} at elevated temperatures is a reorientation of the cluster $[Nb_{Li}–4V_{Li}]$ dipoles, which is attributed to a thermo-activated mobility of the Li vacancies and their hopping over equivalent Li sites. Moreover, we knew that doping $LiNbO_3$ with [Mg] or [Zn] above the thresholds sharps decrease E_c and E_{int}, but this is scarcely explained by this model. That because, even if Magnesium or Zinc reduce the concentration of Nb_{Li} and V_{Li}, in the other hand new intrinsic defects Mg_{Nb} or Zn_{Nb} are formed, which themselves could serve as pinning centers.

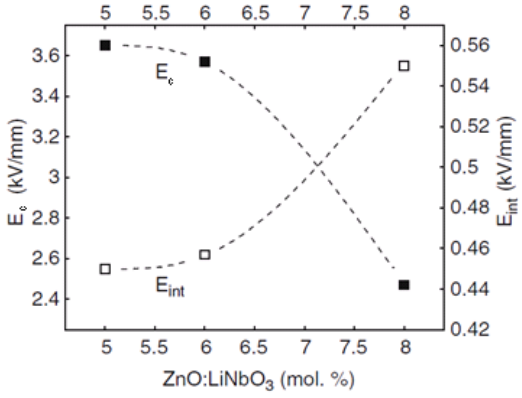

FIGURE 16. VARIATION OF COERCIVE FIELD (E_c) AND INTERNAL FIELD (E_{INT}) IN FUNCTION OF ZINC CONCENTRATION

We have illustrated some qualitative mechanisms that may regulated switching parameter in terms of structural defects, but the knowledge of this phenomena is nowadays still far from comprehension.

Crystal	E_c(KV cm^{-1})	E_{int}(KV cm^{-1})
CLN	210	2-33
SLN	60-65	→0
CLN:5%MgO	60-68	5
CLN:8%ZnO	25-35	5
SLN:1%MgO	25	→0

TABLE 6. COERCIVE FIELD AND INTERNAL FIELD FOR PRINCIPAL KIND OF LITHIUM NIOBATE

3.2.5. Zirconium doping

As far as the first point is concerned, traditional dopants used to improve the optical damage resistance include Mg and Zn. The optical damage drastically falls off by more than two orders of magnitude when a doping threshold of about 5% mol. for Mg and about 6% for Zn in congruent lithium niobate is used respectively. Although even In and Sc and Hf were found to play the same role [41], Mg, Zn, In, Sc and Hf have segregation coefficient less than one and therefore the growth of good quality crystals is rather difficult and the growth process is very expensive (a 3" Mg:$LiNbO_3$ wafer costs higher than 1000 Euros). Very recently [30] it has been published that the incorporation of zirconium (Zr) in $LiNbO_3$ crystals satisfies the requirement of increasing the optical damage resistance but with a lower threshold concentration (2 mol%) and with a segregation coefficient close to one. This allows for obtaining a high crystal quality with a high rate of reproducibility. Moreover Zr incorporation has the additional advantage of lowering the coercive field (one third of that of the pure congruent $LiNbO_3$), a very promising aspect for the PPLN realization. These preliminary results clearly indicate that Zr represents an excellent alternative for obtaining a $LiNbO_3$ substrate with higher optical damage resistance and with less critical value on the electric polarization reversal.

3.2.6. Poling Process

The orientation of the ferroelectric domains, so called poling, is the procedure with which Lithium Niobate polarization could be switched in one of the two possible direction of the z axis. In fact by applying to a crystal a suitable electric field like those reporting in Figure 17, all the crystal domains could be

oriented to the same polarization direction. This happens when potential exceeds a threshold voltage related to the coercive field.

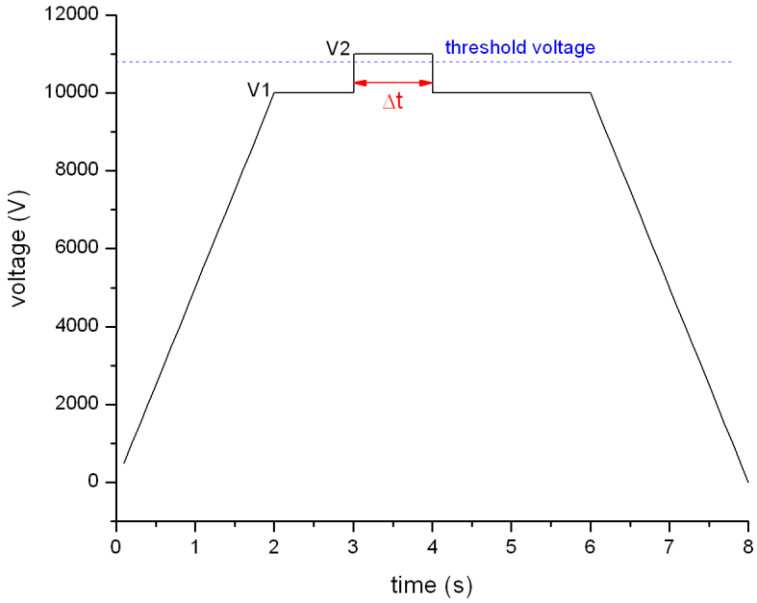

FIGURE 17. TYPICAL VOLTAGE PROGRAM FOR POLING PROCESS

By monitoring the electric potential and intensity of the electric current during the poling process, we can note that corresponding to the polarization reversing a current impulse is measured. The great part is composed by superficial charges that were electrostatic bounded to neutralize the spontaneous superficial charge of Lithium Niobate. If we use a photolithographic pattern as electrode, using a voltage slightly above the threshold we could manage to exceed the coercive field only under the electrodes and not under the insulating regions, so we could achieve a Periodically Poled Lithium Niobate. As explained in the section 3.2.2 the periodic poling could be described by six steps (Figure 18): (a) Domain nucleation at the electrode edges because of the higher electric field. (b) Domain tip propagation toward the opposite face of the crystal. (c) Termination of the tip at the opposite side of the crystal. (d) Rapid coalescence under the electrodes. (e) Propagation of the domain walls under the photoresist. (f) Stabilization of the new domains.

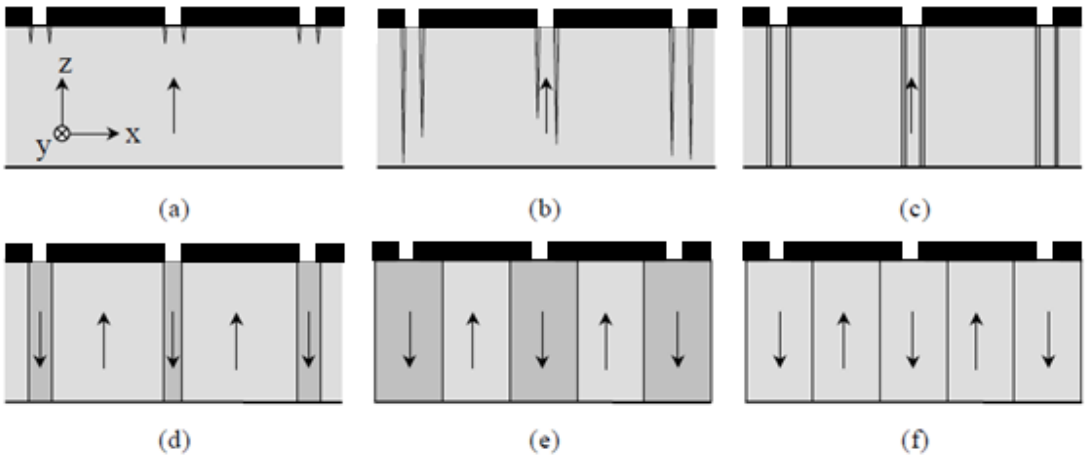

FIGURE 18. STEPS OF THE DOMAINS FORMATION: (A) NUCLEATION; (B) Z AXIS PROPAGATION; (C) TERMINATION OF THE TIPS; (D) GROWTH UNDER THE ELECTRODES; (E) PROPAGATION UNDER THE PHOTORESIST; (F) STABILIZATION

So it is inevitable that a part of the domains grown under the photoresist. Anyway, 50% optimal duty cycle could be obtained starting from a pattern duty cycle lower than 50%.

It is important to note that a different behavior can be found if the Lithium Niobate is poled at high temperature. As a matter of fact previous studies on high temperature poling [42] showed that for temperature of 100-200°C the inverted domains started from the +z surface but are not able to reach the +z face probably because of a charged layer that is build due to the higher conductivity of charges in the high-temperature crystal. Therefore only superficial domains are achievable. In Figure 19 a comparison between the results of literature and our domain inversion is presented, our results confirm the literature and show an irregular depth of the domain inversion, with deeper tips that almost reach the other side and other of only a hundred of micrometers.

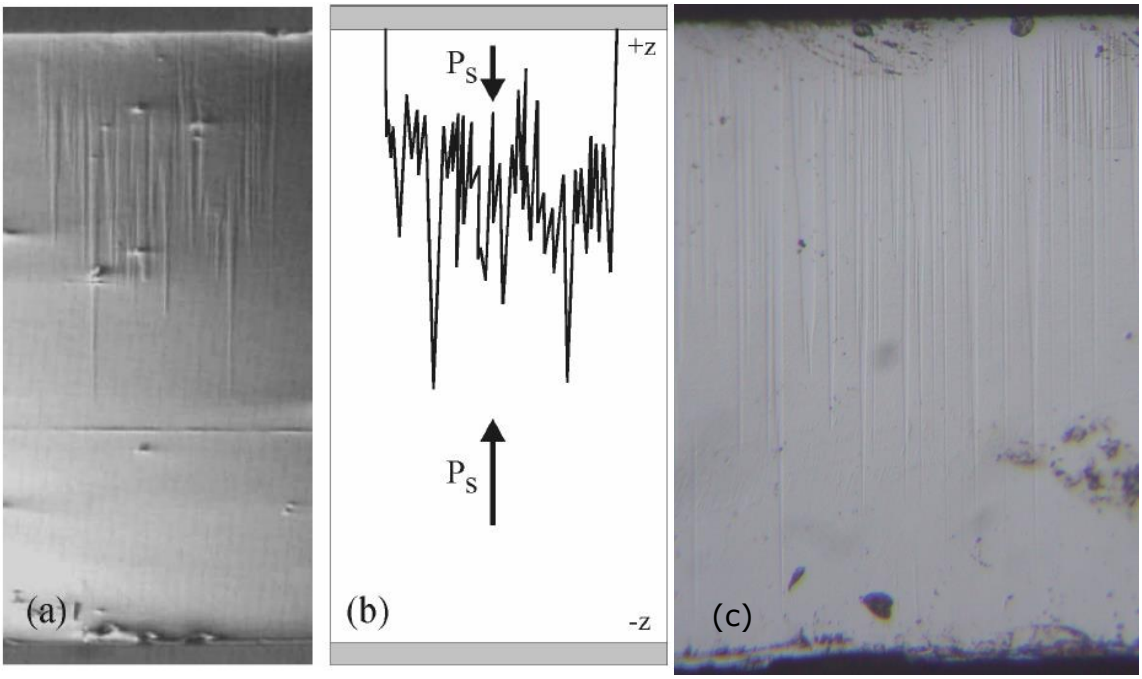

FIGURE 19 (A) AND (B) AN EXAMPLE OF SUPERFICIAL DOMAINS OF A HIGH-TEMPERATURE (120°C) POLED CLN CRYSTAL FROM LITERATURE [42]**(C) LATERAL SECTION (0,5 MM) OF A POLED CLN AT 150°C AFTER WET ETCHING (SECTION 3.7.1).**

3.3. Microfabrication

The microfabrication of a periodic polymeric grating using UV-photolithography is the first of the two fundamental steps necessary for the realization of a pattern of periodic ferroelectric domains. The periodic pattern of photoresist can be exploited in two different configuration, the first is the use of the photoresist as insulating layer, so that during the poling process the electric field under the resist is reduced and when the voltage applied is just above the critical threshold only the areas uncovered will reverse their polarization leading to the formation of the periodic ferroelectric domains. In this case liquids electrodes are used (solution of LiCl in water) and therefore this configuration can be use only at low temperature (<100°C). A second possibility is to deposit a conductive layer after the photolithography (Cr, Al) and therefore to lift-off the photoresist obtaining a metal grating that is then used as electrode for the poling. In both the cases we need the implementation of photolithographic process able to achieve structures of few nanometers. So that, the first part of our work was focused to implement and improve UV-photolithography and lift-off process. As it can be seen in (Figure

20) we obtained good photolithographic structures of the purposed period dimension (6,8 μm).

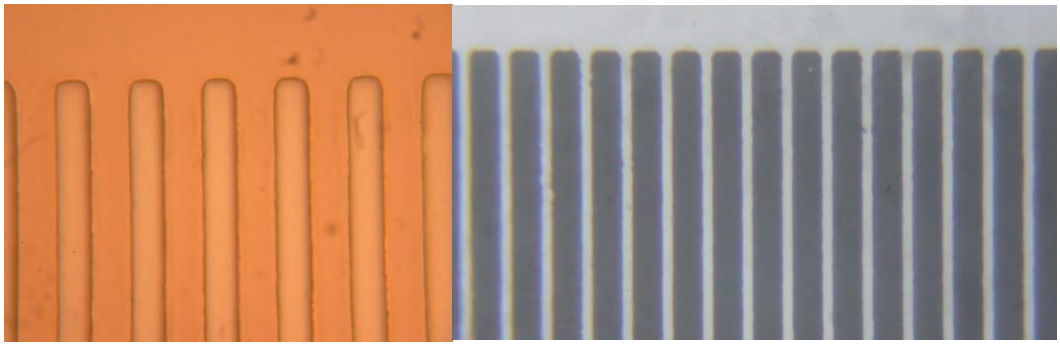

FIGURE 20. LEFT: EXAMPLE OF A PERIODIC GRATING (6,8 μM, DUTY CYCLE 20%) OBTAINED WITH THE OPTIMIZATION OF THE PHOTOLITHOGRAPHY PARAMETERS. RIGHT: PICTURE OF AL PATTERNED ELECTRODES (LIGHT ZONES) ON ZRLN SUBSTRATES (DARK ZONE): PERIOD 6.8 μM, DUTY CYCLE EQUAL TO 20%.

In the next sections we present the instrumentation, the materials, and the procedures used for the microfabrication of the electrodes.

3.3.1. Instrumentation and Materials

Lithium Niobate Crystals

During the optimization of all the steps of the photolithographic process we used commercial congruent z-cut Lithium Niobate wafer. When the optimization was reached, the process was studied also on the zirconium doped oriented crystals of Lithium Niobate grown by Czochralski technique and then cut and polished at an optical grade. The samples were cut orthogonal to the z axis (z-cut) because it is the ferroelectric direction of the crystal. Commercial wafers have thickness of 0,5 mm and diameter of about 76 mm. Doped samples have diameter of about 15 mm and thickness of about 0,6 mm (depending on the cutting and the polishing stages).

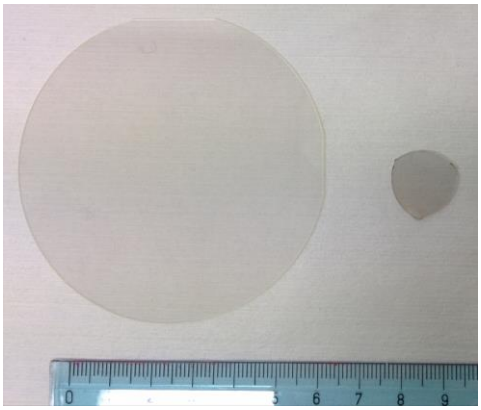

FIGURE 21 ON THE LEFT A CRYSTAL OF COMMERCIAL CONGRUENT Z-CUT LITHIUM NIOBATE, ON THE RIGHT A Zr DOPED LITHIUM NIOBATE Z-CUT

Photolithographic Masks

We designed three masks of 4x4 inch with 18 different patterns with CAD software. Masks are realized with a laser patterned chrome layer of 980 Å on a plate of Soda Lime glass by a specialized company (Delta Mask B.V.). The final masks were designed to contain different patterns each with several parameters modified: period, open width, and outline (Table 7). The first two masks (Figure 22/left) were thought for liquid electrodes configuration with period dimension from 100 μm to 6,8 μm and duty cycle of 50%; for smaller periods (mask D,E,F) also duty cycle was changed, this to overcoming the domains grown under the photoresist layer during the poling stage. Masks with duty cycle of 40%, 30% and 20% were realized to consent a study of the open width broadening. The size of every mask pattern is 5x5 mm and was designed with signs that show the right crystallographic placement of the sample.

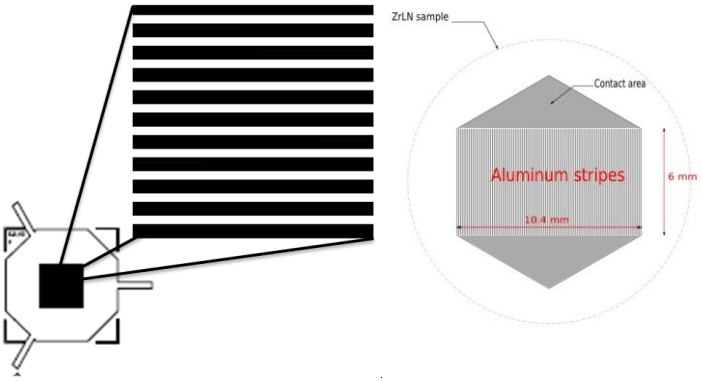

FIGURE 22. ILLUSTRATION OF MASK PATTERNS, ON THE LEFT FOR ROOM TEMPERATURE POLING, ON THE RIGHT FOR HIGH TEMPERATURE POLING

Since the most stable orientation of domain walls is parallel to the yz plane, the correct orientation of the mask with respect to crystallographic axes is fundamental [32][33]. In Figure 23 we show a PPLN obtained with an optimal orientation, in fact we could see that all the domains walls follow the y crystal directions at 120° one to the other (energy minimum). The third mask realized was designed for the metal electrodes, with a negative configuration in comparison with the liquid electrodes masks (Figure 22/right). Moreover a hexagonal zone around the periodic pattern was planned in order to permit the contact of the metal layer with the poling circuit described later (section 3.6.1).

	Pattern	Period (μm)	Duty cycle (%)
First Mask	A	100	50
	B	50	50
	C	30	50
	D	20	50
	E	20	40
	F	20	25
Second and third Mask	A1	10	40
	A2	8	40
	A3	6,8	40
	A4	6,8	40
	B1	10	30
	B2	8	30
	B3	6,8	30
	B4	6,8	30
	C1	10	20
	C2	8	20
	C3	6,8	20
	C4	6,8	20

TABLE 7 MASK PATTERNS PARAMETERS

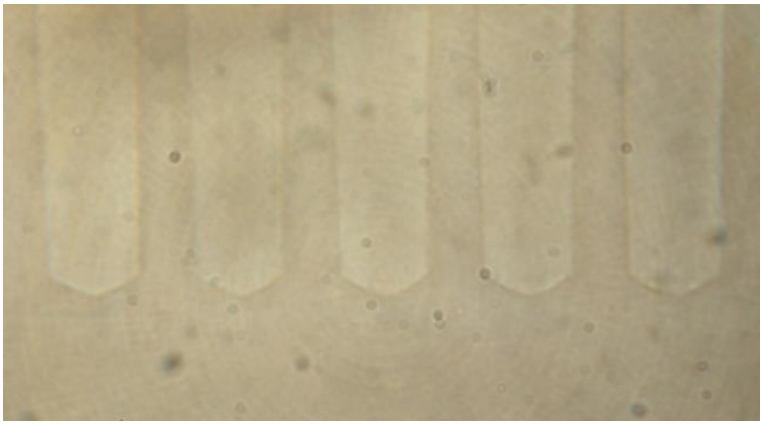

FIGURE 23. FERROELECTRIC REVERSE DOMAINS ON PPLN, WITH WALLS LYING IN THE YZ PLANE, 120° Y DIRECTIONS CAN BE SEEN AT THE ENDS OF THE DOMAINS.

Photoresist

We use the Microposit S1800 G2 series as photoresists, in particular S1813. They are positive photoresists engineered to satisfy microlithography applications on silicon, however, they showed good performance also on lithium niobate surfaces. In order to improve the adhesion of the photoresist to Lithium Niobate surface a primer was used, i.e. a chemical reagent that produces a layer able to improve the adhesion between the substrate and the photoresist. The primer must be deposited and spinned on the substrate before the deposition of photoresist. We used a Microposit primer based on hexamethyldisilizane (HMDS), a chemical pre-treatment developed for oxide materials.

Property	
Sizing energy	150 mJ/cm^2
Resolution	0,48 µm

TABLE 8. PHOTOLITHOGRAPHIC RESPONSES SUMMARY FOR MICROPOSIT S1813 PHOTORESIST

S1813 is a good photoresist for our purpose, since its absorbance spectrum (Figure 24) is compatible with our lamp emission, and it has an optimal resolution of 0,48 µm that is more than sufficient for our application. We collected a spectrum of the primer and of the resist before and after the UV exposition to compare them with the literature (Figure 24), we did not observe any variation.

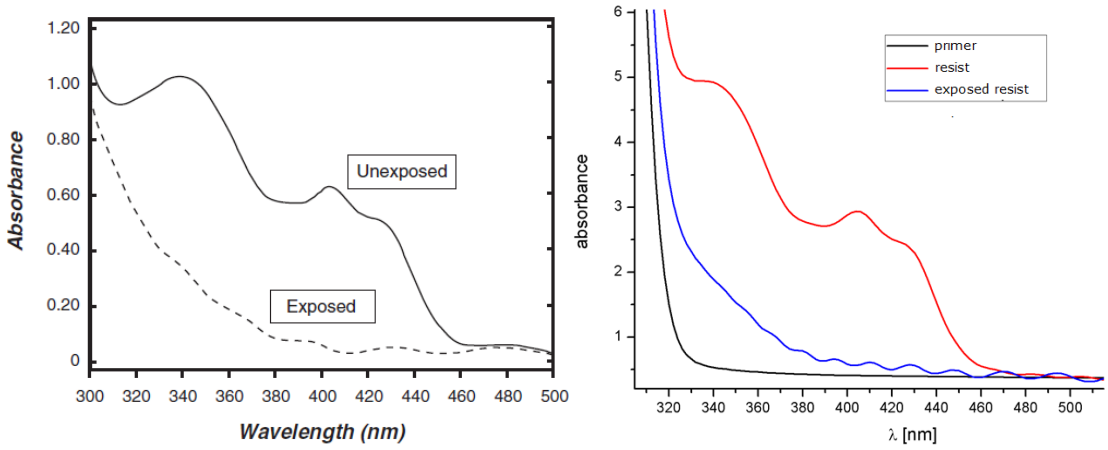

FIGURE 24. (LEFT) ABSORTION SPECTRUM OF S1813 FROM THE PHOTORESIST DATASHEET; (RIGHT) ABSORTION SPECTRA OF RESIST, EXPOSE RESIST AND PRIMER.

UV Lamp

A collimated UV lamp system was used to expose the photoresist, it is composed by a 300 W mercury-vapor lamp followed by a mirror and a quartz

lens, so that the projected light rays follow parallel paths to the same plate. In this way, shadows cast by a mask in the light path are faithfully reproduced on the sample. All the system emits at the I line (365,4 nm) with a power of 9 mW cm^{-2} (it is included the mask absorption).

Developer

We used Microposit MF-300 series developer that is specifically formulated to work with a wide range of positive photoresists including MICROPOSIT S1800 (Microposit Materials - Rohm and Haas company).

Sputtering

We use a sputtering chamber with three different torches for magnetron sputtering, one DC and two RF respectively (see section 2.4). The geometry is horizontal and the sample holder is opposite to the torches. The chamber can achieve a pressure of around 10^{-6} mbar, and all the deposition were performed at $50 \cdot 10^{-3}$ mbar in Argon atmosphere after a clean of the chamber at a pressure of at least $3 \cdot 10^{-6}$ mbar. All the targets (Al, Cr, ITO) were used in the DC configuration, the sample always rotating during the deposition.

Lift-off solution

The lift-off of the samples after the sputtering deposition was done using the SVC(TM)-14 positive photoresist stripper, a product developed for this purpose.

3.3.2. Procedure: Proximity Photolithography

The photolithographic procedure was optimized starting from the literature [43] and the information of the datasheet. All the follow steps were improved and optimized by a systematic study of spinning, exposure, development, and treatments of the samples (cutting, cleaning, and approaching of the mask). All the steps except cutting were performed in the ISO 7 class clean-room financed by the MISCHA project (Microfluidics laboratory for scientific and technological application

The following procedure has been adopted:

- *Samples preparation*: Two kinds of z-cut samples were used: commercial wafers undoped and Czochralsky zirconium doped crystals. In both cases they were cut with a diamond saw to obtain the desired

size. In the case of commercial polished wafer after the cut we got rectangular samples of 14x14 mm and 0,5 mm thick. The Zr-doped LN boules were first grown by the Czochralski technique (performed in our lab as well) with a nominal ZrO_2 concentration of 3.0 mol%, and then cut and polished to obtain optical-quality Z-cut slices [44] (crystal thickness in the range 0.55-0.65 mm and a diameter of about 15 mm) that have three ridges at 120° to each other that indicate the y axis. Therefore all the samples were cleaned in clean room with washing cycles of distilled water and acetone until the sample did not present any observable stain or grain of dust.

- *Primer and photoresist deposition (spin coating)*: before the deposition of S1813, the primer has to be spinned to improve the adhesion of the photoresist. Photoresist deposition needs to wait about 10 s after the primer spinning to permit the adhesion of the layer of primer. On Table 9 we report the parameter usually adopted in this step. The mainly problem of this step was the square shape of the samples that strongly influences the homogeneity of the resist flow in the different radial directions of every square sample.

	Primer (Microposit)		Resist (Microposit S1813)	
	Spin rate (rpm)	**Duration (s)**	**Spin rate (rpm)**	**Duration (s)**
First rate	200	20	800	20
Second rate	1000	20	4000	20
Third rate	2000	50	8000	50

TABLE 9 SPIN COATING PARAMETERS

- *Mask approaching*: a factor that could modify the exact reproduction of the mask pattern and also limits the final dimensions is related to interference phenomena. In fact, the lamp light is partially diffracted on the plane of the resist and if the mask pattern is small (10 μm or less), the interference effects can strongly alter the photoresist pattern. A critical step of this procedure is the mask approaching to the sample, in fact it was necessary to reduce as much as possible the gap between sample and mask without breaking the crystal. When the mask is removed after the exposure, the crystal may remain stuck to the mask and has to be removed delicately.

- *UV exposure*: exposure of a photoresist involves the absorption of radiation and subsequent photochemical change, generally resulting in a modification of dissolution properties. Both maximum light transmission (to reach to the bottom of the resist) and absorption (to achieve the highest sensitivity) are desired. Our lamp has a power of about 9 mW/cm^2, and as reported in Table 8 the sizing energy for S1813 MICROPOSIT photoresist is 150 mJ/cm^2, so the calculated time of exposure is 17 s. Experimentally an optimal time of about 15 s has been found, this is due to the different experimental setup used for the literature measure.
- *Developing*: experimentally, after the exposure the sample was removed from the mask and dipped for about 20-40s on a gently stirred developing bath (Microposit MF-300) and suddenly plunged in a distilled water bath. After those steps, the samples were dried with a nitrogen flow.
- *First microscopic observation*: a first check of the outcome of the process was made with simple optical microscopy. This step allowed to roughly recognize unsuccessful samples and then clean them and repeat again all the procedure without leaving the clean room.
- *Sputtering deposition*: eventually a layer of Cr or Al was sputtered in the case of metal electrodes. On the opposite side (-z face) a layer of ITO (Indium Tin Oxide) was also deposited as transparent and conductive layer that allow to see the evolution of the poling with a microscope during the treatment. The sputtering conditions are reported in Table 10.
- *Lift-off*: In the case of metal electrodes after the deposition on the photoresist gratings the samples were then put in a bath of SVC(TM)-14 stripper at 60°C under sonication for 5 minutes and then clean with acetone. The results of the lift-off procedure are reported in Figure 20.

Target	Power (W)	Deposition time (min)	Thickness (nm)
Al	30	30	200
ITO	30	11	50
Cr	40	15	20

TABLE 10 MAGNETRON SPUTTERING PARAMETERS FOR DIFFERENT TARGETS.

A sketch of the electrodes configuration is reported in Fig.1 (left), together with a picture of the final deposited pattern acquired by a microscope (right).

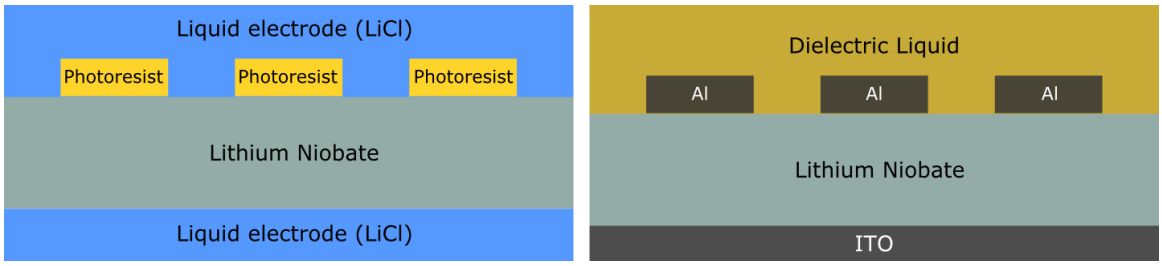

FIGURE 25 PATTERNED ELECTRODES SCHEME FOR THE PERIODICALLY POLING AT ROOM TEMPERATURE (LEFT) AND HIGH TEMPERATURE (RIGHT).

3.4. Poling at room temperature

The first study on the ferroelectric domains switching was performed on congruent lithium niobate crystals using a room temperature poling set-up with liquid electrodes. This configuration allows a low breaking-rate of the samples compared to metal electrodes and it is also the most used configuration in literature [42]. It is worth mentioning that previous measurements determined at 10,5 kV the threshold voltage for congruent Lithium Niobate thick 0,5 mm (coercive field of 21 kV/mm [23]. Therefore $LiNbO_3$ was poled with patterns of period 100 μm and duty cycle 50% for a first study of the domains behavior. At the same time, also some Zirconium doped crystals have been poled to determine the threshold voltage. It is known (section 3.2.4) that optical-damage resistance dopants cause a reduction of the coercive field, particularly its dependence on Zr concentration is not known. Therefore in section 3.5.2 measurements were performed to quantify E_c indicating that for a 3 mol. % Zr Lithium Niobate the coercive field is of about 7-8 kV/mm, one third of the congruent coercive field.

In the following we discuss the poling set-up and materials for both congruent and Zr doped crystals, then we present and discuss s our results and the motivations that lead us to implement a different set-up of poling at higher temperature.

3.4.1. Poling Cell

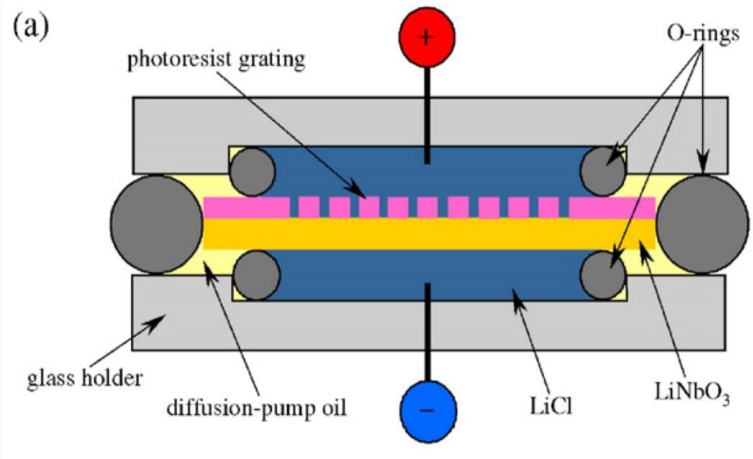

FIGURE 26. SCHEME OF THE POLING CELL

The poling cell (Figure 26) was designed to maintain the sample between two sections (closed by two O-rings) that contain an electrolytic solution, in this way we insulate the faces of the crystal one from the other avoiding a possible electric arc. The insulating was increased using, around the O-rings, a gap full of distilled water. The poling cell structure was made of Poly-methylmethacrylate (PMMA or Plexiglas) since it is a good insulator and it is transparent (so we could observe directly the poling process). Two electrodes are plunged into the electrolytic solutions (one for every z face of the crystal), the mass electrode is connect to the +z face, the one without the photoresist; instead the electrode at high voltage was connected to the –z face. Both the electrode rods were made of brass covered with a titanium and gold layer, this to passivate the surface and to avoid that electrolytic corrosion occurs from electrolytic solution. The electrolytic solution was a saturated water solution of Lithium Chloride (0,82 g/ml), that was chosen thanks to its good conductivity (146 mS/cm).

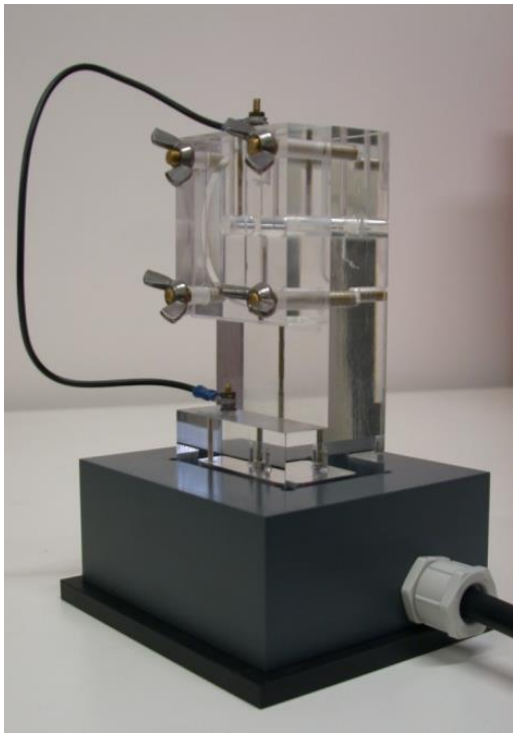

FIGURE 27. PHOTO OF THE POLING CELL

3.4.1.1. The Circuit

The poling circuit has to give a potential of up to 11 kV in order to reverse the polarization of a congruent crystal thick 0,5 mm (Coercive field of 21 kV/mm). Moreover, it has to measure electric voltage and the current during the poling stage; discharge the electric potential at ground in case of missing contact in the poling cell; and limit the current in case of short circuit.

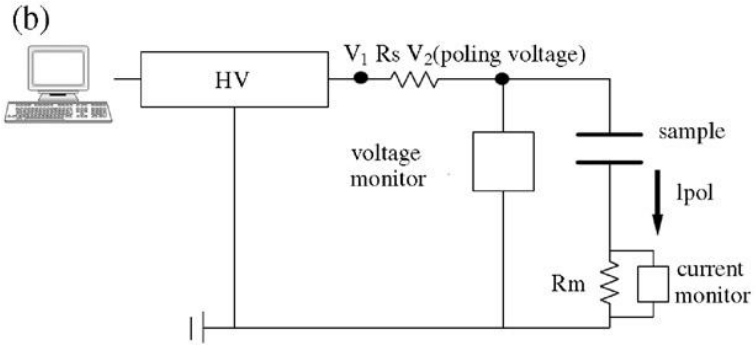

FIGURE 28. POLING ELECTRIC CIRCUIT

The circuit (Figure 28) is composed of a high voltage amplifier (0-15 kV) controlled by a specifically home-made computer software, whose output is a square wave like the one in Figure 29. The shape of the wave was chosen in order to minimize the piezoelectric stress (lower potential ramps) and, after

the over-thresholds impulse of few seconds, to stabilize the new reverse domains at a high under-threshold voltage for tens of seconds (section 3.2.3). A resistance (R_s) is put in series configuration with the sample, in order to limit the intensity of the current passing through the circuit.

3.4.1.2. Procedure

The procedure of poling in carried out in three steps: the insertion of the sample in the cell; the pouring of the LiCl saturated solution and of the distilled water; and finally the high-voltage application. The insertion of the sample could be a critical step, in fact if the O-ring are not perfectly aligned one over the other, the pressure of the O-rings on the crystal and therefore the piezoelectric stress are able to break the sample due to the developed shear stresses. Also the liquid pouring has to be well controlled, in fact the formation of bubbles has to be avoided in order to prevent the formation of electric arcs that could melt the PMMA (Plexiglas) and damage the electric circuit. We develop software in order to automatically control the application of the voltage, the software allows to set the following parameters: under-threshold voltage (V_1), over-threshold impulse voltage (V_2), pre-poling time, duration of the pulse (t_{pol}), and post-poling time ($t_{postpol}$) respectively. The parameters are reported in Figure 29.

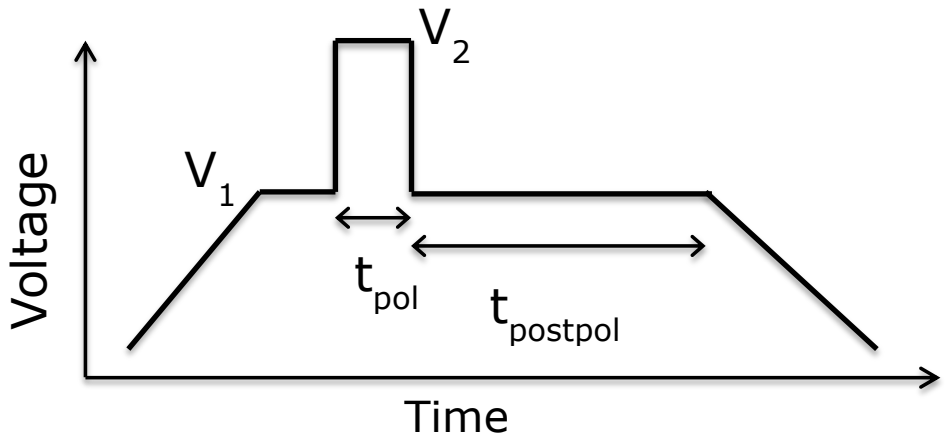

FIGURE 29. POLING PARAMETERS: UNDER THRESHOLD VOLTAGE (V_1), OVER THRESHOLD IMPULSE VOLTAGE (V_2), DURATION OF THE PULSE (T_{POL}), POST-POLING TIME (T_{PPOL}).

3.4.2. Characterization

Characterization methods may be divided into surface and volumetric. All the surface methods are based on describing a distribution of the surface charge,

which replicates the near-surface domain distribution. These methods include the chemical etching, powder deposition and colloidal decoration methods, the scanning force microscopy (SFM) and scanning electron microscopy (SEM). In addition to the SEM method, the transmission electron microscopy (TEM) method can be used for these aims, but it requires very thin samples. The bulk methods are first of all the structure studies. Domain observation by X-ray diffraction methods based on the anomalous dispersion of the X-rays resulting from a difference of the diffracted intensities from positive and negative domains [45]. But also optical methods based on the variation of refractive index at the domain borders. For our current purposes optical and chemical etching are sufficient to determine the domains sizes.

Optical method

Optical methods belong to the volumetric ones and permit to probe the switching process and the domain distribution over the crystal bulk. If strong mechanical strains occur next to the domain walls, they affect the refractive indices via the elasto-optic effect. So, when a polarized light wave impinges normally to the crystal domain, walls are visible because of the variation of refractive index. This case occurs in $LiNbO_3$, especially for a non-equilibrium (freshly formed) domain structure [23]. The elasto-optic effect also allows recording videos during the poling process.

Etching

The etching method is a destructive technique universal for all ferroelectrics and it is based on a different etching rate for the positive and negative ends of the domains by an individual etchant. In $LiNbO_3$ the -z face is etched much faster than the +z face, therefore the poling domains after the etching can be measured with both microscopy and profilometry. In our case the etching was achieved with an immersion of the samples in a water solution of hydrofluoric acid at room temperature for few minutes.

3.5. Results and Discussion

A systematic study of the poling process parameters was first carried out using commercial undoped lithium niobate crystals in order to compare the results with those reported in literature. The study was performed on the

bare photolithographic pattern and also on the pattern covered by a metal thin film of Cr. Once optimized the parameters, the poling process was investigated also on Zr doped crystals.

3.5.1. Congruent Lithium Niobate

As a typical result we present the realization of a 100 μm periodic PPLN. The samples were covered with a photolithographic pattern of period 100 μm and an average open width of 47,5 ±0,3 μm (Table 12). Then one cycle of poling has been sufficient to obtain a PPLN with a poling voltage of 10,6 kV. We measured the total charge by integrating the current signal as a function of the time, obtaining 24,3 μC. The theoretical total charge is given by the relation:

$$|Q| = |P_s| \cdot A_{Poling}$$

where Q is the total charge, P_s the spontaneous polarization and A_{Poling} is the poling area, which is

$$A_{Poling} = 2 \cdot DC \cdot A_{Pattern}$$

where DC is the Duty Cycle and $A_{Pattern}$ the total area of the photolithographic pattern. Obtaining a theoretical value of 20,9 μC that is comparable to the experimental.

Mask	OW pattern (μm)	V_1 (kV)	V_2 (kV)	t poling (s)
A	47,5 ±0,3	9,1	10,6	8

TABLE 11. PARAMETERS OF POLING: OPEN WIDTH OF THE PHOTOLITHOGRAPHIC PATTERN (OW); UNDER THRESHOLD VOLTAGE (V_1); POLING VOLTAGE (V_2); DURATION OF THE PULSE (T POLING)

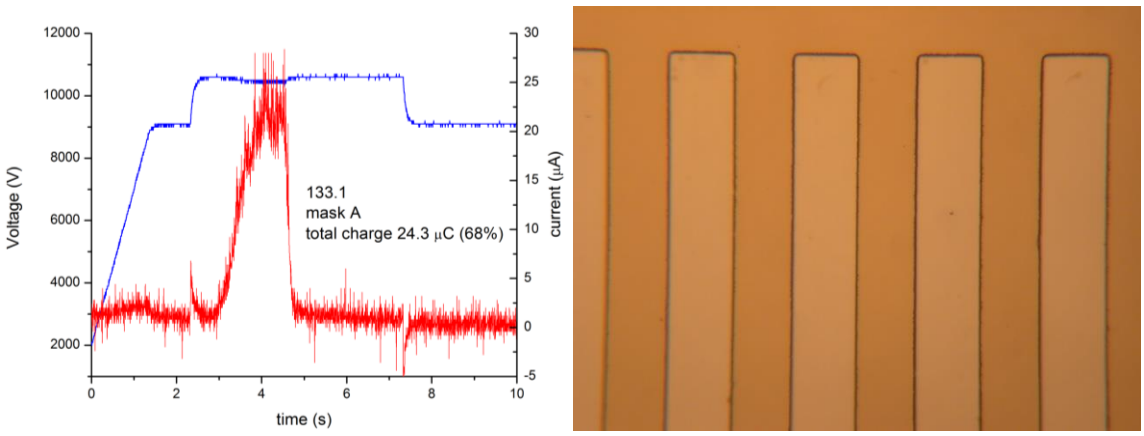

FIGURE 30. (LEFT) VOLTAGE (BLUE) AND CURRENT (RED) MEASUREMENTS DURING THE POLING; (RIGHT) MICROSCOPE IMAGE OF THE PHOTORESIST PATTERN

After the poling, the domain pattern was observed under polarized light microscope, then etched with HF, an open width of 59,1±0,7 μm was measured using profilometry. This confirms that domains grow also under the photoresist, in this case of about the 25% of the photolithographic open width. Figure 31 show the as-poled and the etched PPLN, even if open width is large compared to what we need, the entire domain pattern is uniform in period and open width. Moreover the periodic structures were found in both the z faces of the crystal, so that our domains pass through the entire crystal. Therefore the poling procedure associated to photolithographic patterning was proved to be a powerful technique that can be easily used to fabricate PPLN. Similar results were found for other samples with an average open width widening of 24%.

OW pattern (μm)	OW etching (μm)	ΔOW (μm)	Total charge (μC)
47,5 ± 0,3	59,1 ± 0,7	12 ± 1	24,3

TABLE 12. COMPARISON BETWEEN PHOTOLITHOGRAPHIC PATTERN OPEN WIDTH AND DOMAINS SIZE (OW ETCHING).

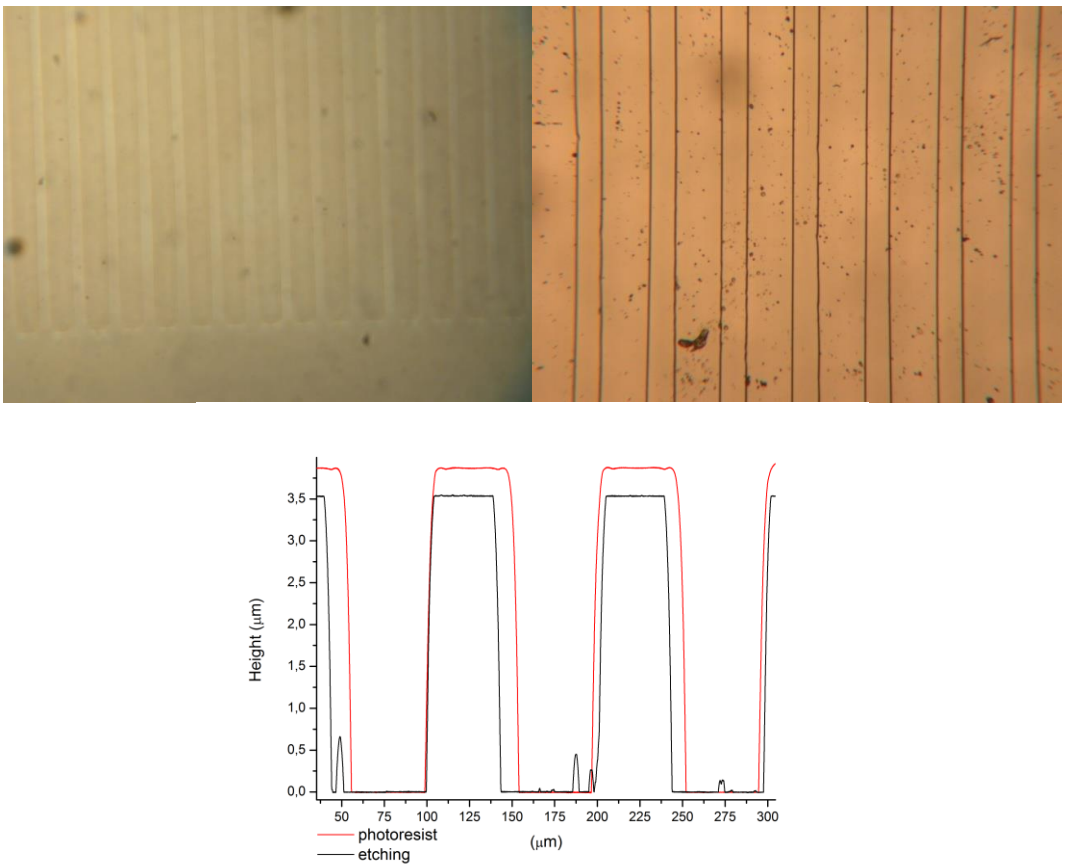

FIGURE 31 (UP LEFT) POLARIZED LIGHT MICROSCOPY ON PPLN. (UP RIGHT) MICROSCOPE IMAGE OF PPLN AFTER THE ETCHING. (DOWN) COMPARAISON OF PHOTORESIST AND ETCHED PATTERNS.

Moreover the poling of the sample was performed with the same experimental setup after a chrome metallization of the pattern surface via sputtering deposition. Our aim was to check if the metallization had some effect on the poling results, especially on the PPLN duty cycle. The sample was covered with a pattern with period 100 μm and an average open width of 48,6 ± 0,7 μm (Table 14) compatible with the parameter used in the previous PPLN. Then two cycles of poling of 1 and 5 seconds were sufficient to obtain the PPLN with a poling voltage of 10,6 kV. We measured the total charge by integrating the current signal as a function of time, obtaining 24,7 μC, comparable with the previous non-metallized sample (24,3 μC).

Mask	OW grating (μm)	V_1 (kV)	V_2 (kV)	t poling (s)
A	48,6 ±0,7	9,1	10,6	6

TABLE 13 PARAMETERS OF POLING: OPEN WIDTH (OW) OF THE PHOTOLITHOGRAPHIC PATTERN; UNDER THRESHOLD VOLTAGE (V1); POLING VOLTAGE (V2); DURATION OF THE PULSE (T POLING)

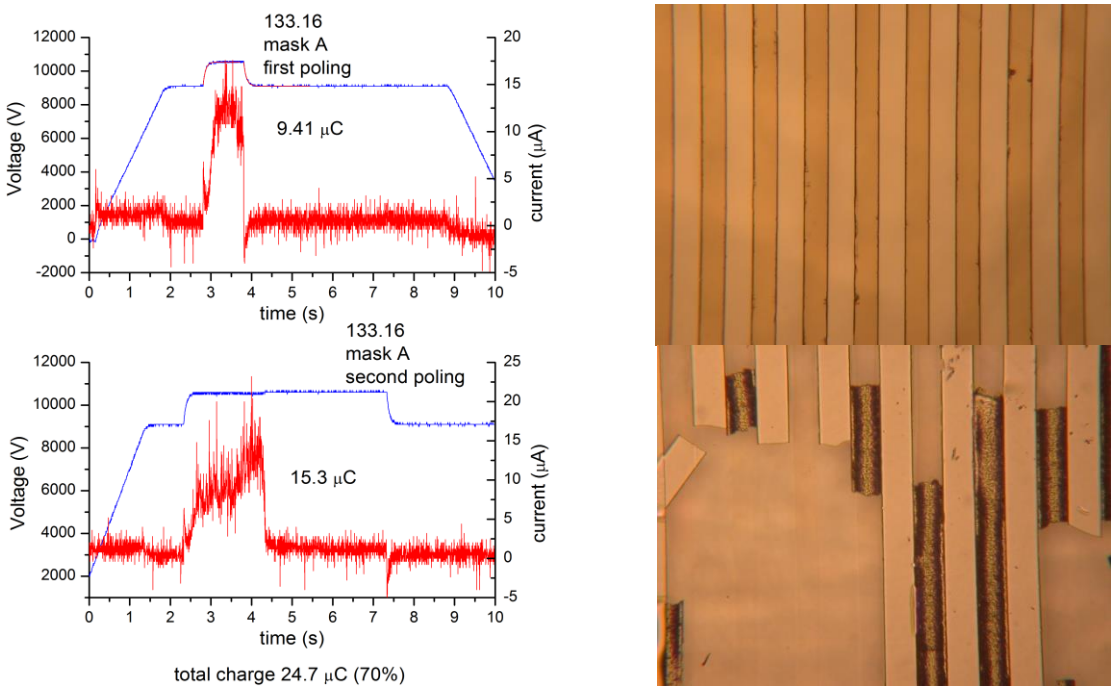

FIGURE 32. (LEFT) VOLTAGE AND CURRENT MEASUREMENT DURING THE POLING; (RIGHT) MICROSCOPIC IMAGE OF THE PHOTORESIST PATTERN AND OF THE METALIZED PATTERN AFTER THE POLARIZATION.

Some photos with polarized light microscope were taken and after the etching of the PPLN an open width of 60 ± 1 μm was measured, so the domains growth under the photoresist is about the 23% of the open width. Photos in Figure 33 shows a worse quality of the PPLN compared to non-metalized sample. This is probably due to the roughness of the metal-LN

interface. In fact, peaks could locally increase the external electric field and cause a non-uniform nucleation density. Also in this case, the periodic structures were found in both the z faces demonstrating that our domains pass through the entire crystal. In conclusion, metallization does not improve our results, and we choose to use the simple LiCl solution as electrode.

OW pattern (µm)	OW etching (µm)	ΔOW (µm)	Total charge (µC)
48,6 ± 0,7	60 ± 1	11 ± 2	24,7

TABLE 14. COMPARISON BETWEEN THE PHOTOLITHOGRAPHIC PATTERN OPEN WIDTH (OW PATTERN) AND THE DOMAINS SIZE (OW ETCHING).

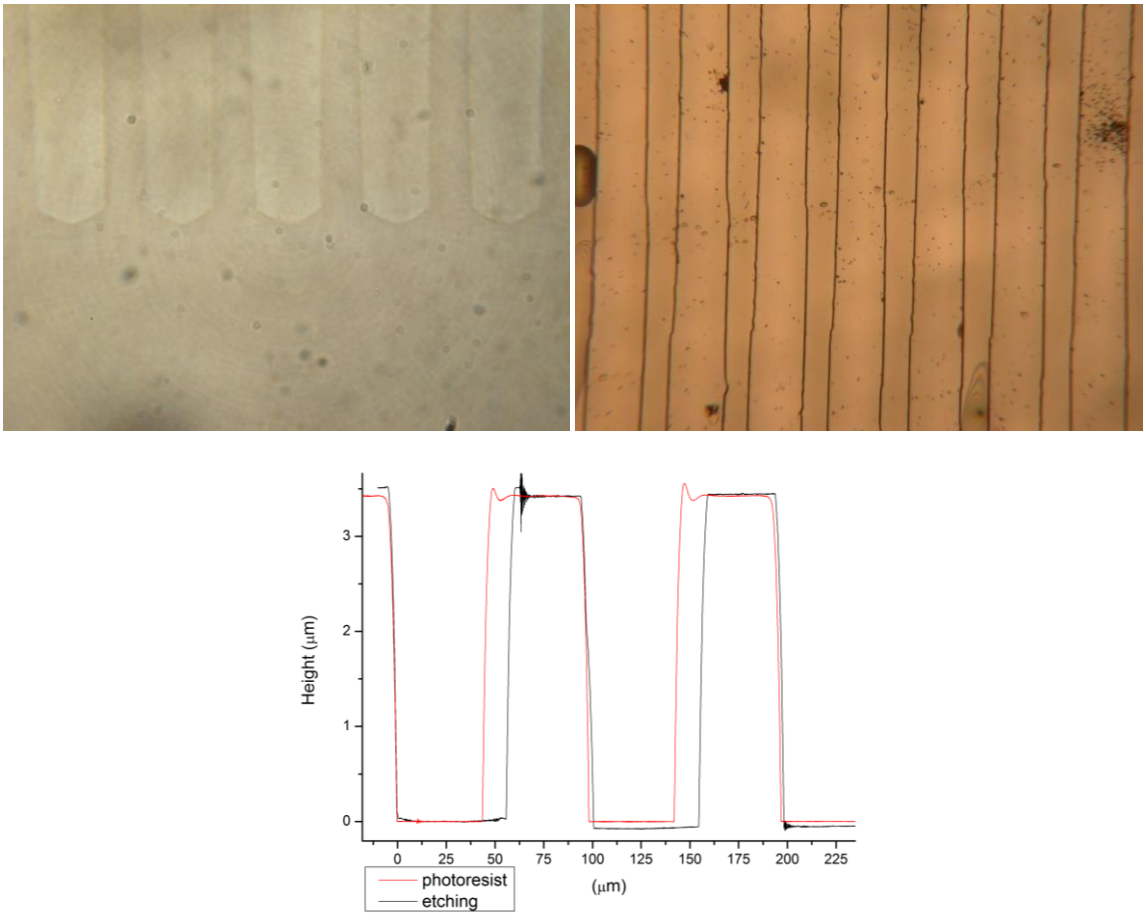

FIGURE 33. (UP LEFT) POLARIZED LIGHT MICROSCOPY ON PPLN. (UP RIGHT) MICROSCOPIC IMAGE OF PPLN AFTER THE ETCHING. (DOWN) COMPARISON OF THE PHOTORESIST AND THE ETCHED PATTERNS.

Several PPLNs were achieved with the same procedure of the two presented, also with lower periodicity down to 6,8 µm. Therefore we demonstrated the effectiveness of the experimental setup to realize PPLN. Next step will be the optimization of poling parameters, in particular poling time (t_{pol}) and poling voltage (V_2), with the aim of minimizing the lateral grown under the photoresists. Before the optimization of these steps, other problems related

to the poling of Zr doped crystals need to be fixed. In the next section these problems are discussed.

3.5.2. Zirconium doped Lithium Niobate

The poling of Zr doped LN resulted a complex phenomenon that still presents some unclear aspects that we have just started to study. In fact, first poling tests on patterned samples gave a non-zero poling current over the threshold voltage, but characterization didn't show any inverted domain. In order to understand what happens during poling, the current measurement is not sufficient: therefore we recorded with a videocamera fixed on the polarized light microscope the image of the samples during the poling cycles. We applied a poling cycle to a sample 0,6 mm thick with a pattern with 100 μm period and 50% duty cycle (mask A). We found a current pulse at V_2=4,5kV. During the pulse we observed a non-homogeneous nucleation of micro-domains that suddenly grew and merged without respecting the geometry of the patterns (Figure 34/b). After 5 s of poling the domains didn't stop and continued to grow during the post poling at 3 kV. After that, voltage was removed and crystal backswitched to the starting uniform polarization (Figure 34/c). As explained in section 3.2.3 backswitching is due to internal fields generated by crystal defects that, because of the low coercive field of the Zr-doped-LN (4,5 kV corresponds to 7, 5 kV/mm) can probably reverse the polarization.

V_1 (kV)	V_2 (kV)	t_{pol} (s)	$t_{postpol}$ (s)
3,0	4,5	5	45

TABLE 15. PARAMETERS OF POLING

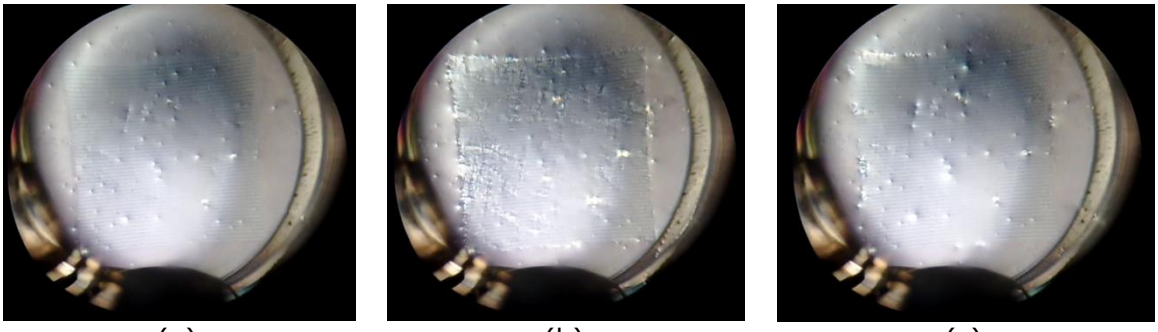

(a) (b) (c)

FIGURE 34. ZIRCONIUM DOPED LITHIUM NIOBATE (A) BEFORE THE POLING PULSE, (B) DURING THE POLING, (C) AFTER THE POLING (FIELD SWITCH OFF).

Then we investigated the value of the poling parameters: we raised V_2 to 5,5 kV to increase the rate of nucleation (section 3.2.2) of micro-domains with

the aim to improve the homogeneity of the domains nucleation. We also decreased the time of poling (t_{pol}) at 0,5 s to inhibit the domains growth under the photoresist. Lastly, post poling voltage was reduced to 2 kV with the aim of stopping the domains expansion. Crystal was poled with these new parameters and therefore observed during the poling cycle.

V_1 (kV)	V_2 (kV)	t_{pol} (s)	$t_{postpol}$ (s)
2,0	5,5	0,5	50

TABLE 16. PARAMETERS OF POLING

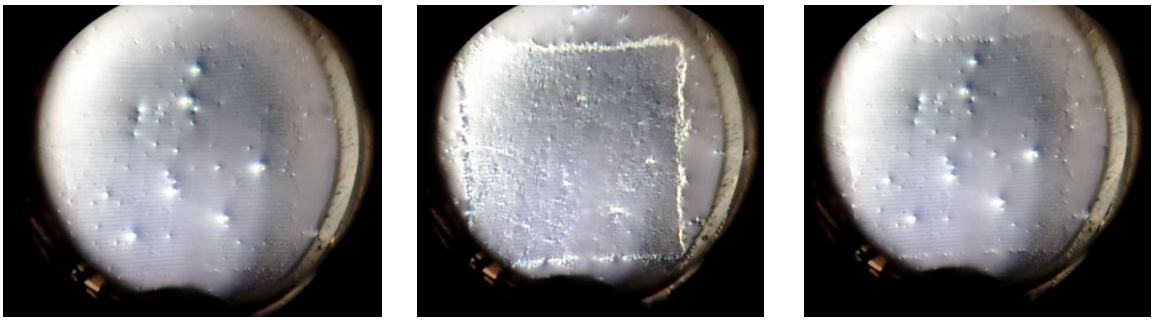

(a) (b) (c)

TABLE 17. ZIRCONIUM DOPED LITHIUM NIOBATE (A) BEFORE THE POLING PULSE, (B) DURING THE POLING, (C) AFTER THE POLING (FIELD SWITCH OFF).

Our purposes were partially reached; in fact expansion during the poling was limited and domain walls were "frozen" during the post poling. Moreover, we tried to stabilize domains by increasing the time of post poling up to 2 hours, but this was not sufficient to avoid backswitching.

Furthermore, considering that back-switching required several minutes in the case of large poled areas, a study of the voltage threshold was done on six samples by measuring repeatedly coercive fields for direct and reverse poling (hysteresis loop) until dielectric breakdown of the samples. From these measurements, we applied cyclic triangular ramps of voltage and we measured the current pulse: the coercive field is determined as the field at which the current pulse starts. We obtained an average value of the coercive field for the 3 mol. % Zirconium doped Lithium Niobate, that is 7,8 ± 0,4kV/mm that is about one-third of pure congruent lithium niobate (CLN, 21.2 kV/mm), in agreement with previously reported data Table 20 [46].

	E_{for} (kV/cm)	E_{rev} (kV/cm)	E_{int} (kV/cm)
1	80.0	4.2	37.9
2	78.3	12.5	32.9
3	77.5	21.7	27.9
4	75.0	20.0	27.5
5	73.3	24.2	24.6

	E_{for} (kV/cm)	E_{rev} (kV/cm)	E_{int} (kV/cm)
1	79.2	19.2	30.0
2	74.2	20.8	26.7
3	73.3	18.3	27.5
4	73.3	22.5	25.4

TABLE 18. MEASURE OF INTERNAL FIELD (E_{INT}) AND COERCIVE FORWARD/REVERSE FIELDS (E_{FOR}, E_{REV}) FOR REPEATED HYSTERESIS LOOPS FOR TWO OF SIX SAMPLES. THICKNESS OF THE SAMPLES = 0.600 MM; V_1 = 7 KV; V_2 = 7KV; T_{POL} = 1S; T_{POST} = 0.5S; RAMP=0.57KV/S

We note that parameters of the hysteresis loops are asymmetric as expected (Figure 15). Therefore, we determined the internal field as the semi-difference between the direct and the reverse coercive fields for each cycle of forward and reverse poling. By looking at the data of Table 18 we observe that the internal field decreases as we increase the progressive number of cycles and the hysteresis loop becomes more symmetric. This is probably due to the modification of the defects that, driven by the alternating external field, tends to reverse also the bulk screening field (section 147), thus reducing the internal field. Backswitching is due to external field pulse that are shorter than time of defect reorientation (τ_b). So, we have to decrease τ_b to stabilize the domains, since a post poling time of two hours wasn't sufficient. Consequently, to help the stabilization of domains we decide to realize a poling cell for high temperature (up to 200°C) in order to improve the defect mobility and therefore to stabilize the inverted domains. In section 3.6 we discuss the set-up, the procedure and the results of high temperature poling.

3.6. High Temperature Poling

As previously discussed, the study of the poling dynamics under different temperature conditions demonstrated that the temperature of the crystal is a critical parameter for the poling process in ZrLN. In fact at room temperature domain back-switching prevented the formation of stable periodically poled structures in Zr doped samples, differently from what happens in pure LN. In

Zr–doped samples, at room temperature, it is indeed possible to induce the nucleation of a large number of inverted domains immediately at the beginning of t_{pol}. However as the poling went on, they merged and formed one single domain as large as the whole poling area. Moreover, although the inverted domains remained stable during the post-poling time, they back-switched during (or after) the ramp used to bring the applied field down to zero, independently of the post-poling field stage duration. Back-switching required several minutes for large poled areas, but less than 1 s for poled stripes under patterned electrodes. In order to prevent this effect high-temperature poling was performed, and the periodically-poled ZrLN samples were cooled down to room temperature during the post-poling period. On the opposite side, by operating at high temperature stable periodically-poled ZrLN were successfully obtained and no back-switching could be observed.

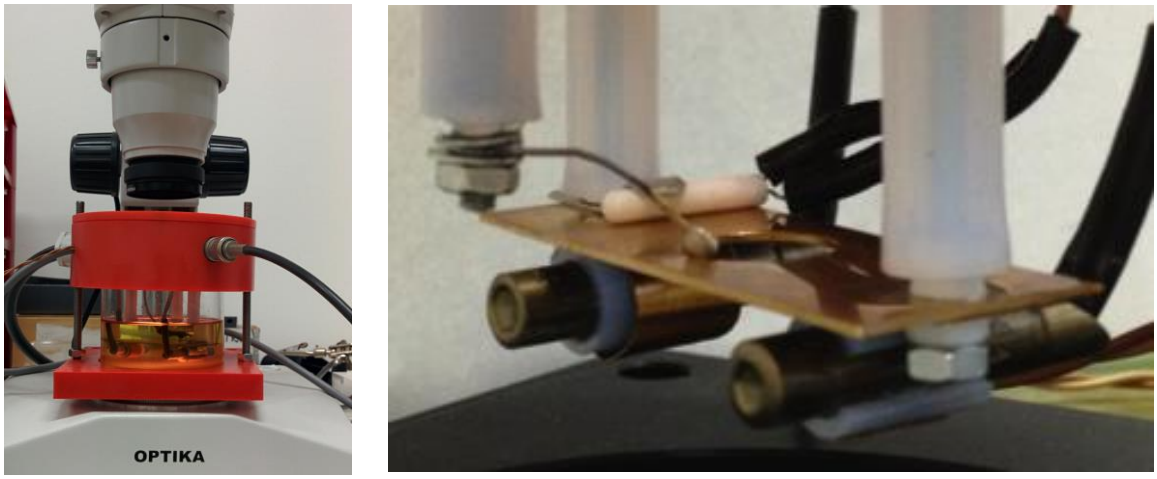

FIGURE 35 (LEFT) HIGH TEMPERATURE POLING CELL UNDER A POLARIZED MICROSCOPY (RIGHT) PICTURE OF THE POLING SET-UP BEFORE IMMERSING IN THE DIELECTRIC OIL: THE COPPER SLAB IS VISIBLE. THE POSITIVE ELECTRODE, VISIBLE ON THE LEFT SIDE, WAS A STEEL SPRING WITH A ROUNDED END. RIGHT: POLING CYCLE: T_{POL} REFERS TO THE POLING TIME AT APPLIED FIELD E_2 WHILE T_{PPOL} INDICATES THE POST-POLING TIME WHEN THE APPLIED FIELD IS E_1.

3.6.1. Poling Cell

The electric field poling was performed using a poling-cell specifically designed in order to operate also at high temperature (up to 150°C, with temperature stability ±1°C), and equipped with a real-time polarization-reversal monitoring system. In our set-up the ZrLN samples were immersed in dielectric oil, as proposed for the PP:Mg:LN [32], and laid on a copper slab that acted simultaneously as sample holder, ground electrode and heat conductor. Two resistors placed below the copper slab were exploited to heat

the sample, and a PT100 thermo-resistor near the sample measured the temperature (Figure 35). The designed circuit applied a programmable voltage time profile as depicted in Figure 29, while monitoring the current flowing through the poling cell, with the same software and electric circuit described in section 3.4.1.1.

Procedure

After a pattern electrodes with period 6,8 μm and duty cycle 20% were deposited with a photolithographic technique (section 3.3), the periodic poling procedure was carried out applying a poling cycle as sketched in Figure 29, similarly to what reported for CLN [33], [35], [37], where $E_1<E_c$ and $E_2>E_c$. When the applied electric field exceeded the coercive field, the domain switching started. The poling field E_2 was maintained for a time interval t_{pol} long enough to complete the polarization reversal. After the switching process, a post-poling step was used to stabilize the inverted domains (the applied field being E_1 for a duration t_{ppol}) thus suppressing the domain back-switching process. In order to determine the best working conditions to get periodically poled ZrLN crystals we investigated the process parameters, and we found that the best results were achieved by applying an electric field E_2 = 4.5 kV/mm, for t_{pol}=180 s and a post-poling electric field E_1=2.3 kV/mm with a ramp of 0,05 V/s. Then the samples were cooled down to room temperature during the post-poling in about 30 minutes. In fact, it is known that, due to fringe effect, the field intensity is maximum at the edges of the electrodes: for this reason the nominal threshold field (applied voltage divided by thickness) needed to start poling can be lower than coercive field as in this case. Finally the Al and the ITO layers were etched using a solution of HCl/HNO_3 at 40°C for 1 hour.

3.6.2. Results

As a first step by using uniform large electrodes, we measured the mean coercive field E_c in a pure and Zr doped samples at 150°C. At room temperature the coercive field of ZrLN crystals (7.8 kV/mm) is about one-third of pure congruent lithium niobate (CLN, 21.2 kV/mm), instead at 150°C, the difference between the two coercive fields was found to be slightly lower, as in ZrLN and CLN crystals we measured coercive fields

values of about 4.6 and 10.8 kV/mm respectively. Moreover we try to reverse the sample to the starting polarization (reverse poling), but the domains cannot switch, not even at coercive field of 8 kV/mm, also this behavior was expected from literature as the extreme stabilization of the domains was measured in different conditions also by Scrymgeour [42]. Therefore we could exploit only one doped sample for this measure because of the low number of crystals at our disposal.

T poling	Pure LN	Zr 3 mol %
25°C	21,2	7,8
150°C	10,8	4,6

TABLE 19 COERCIVE FIELD MEASURED BOTH AT ROOM TEMPERATURE AND AT 150 °C FOR PURE CONGRUENT LN, AND FOR 3 MOL. % ZR-DOPED

After this investigation four different samples of Lithium Niobate (two congruent and two doped at the 3% mol.) were poled with a period of 6,8 μm and duty cycle of 20%, as expected [42] we measured a current during the poling of about 42 mA, that corresponds to a total released charge of $2{,}8 \cdot 10^{3}$ C, order of magnitude over the charge presents at the polar surfaces of 71 μC cm^{-1} (Figure 36). This is due to the charge conductivity enhancement that occurs at high temperature, that lead to superficial and more extended domain surfaces (Figure 38) stabilized by screening bulk charges attracted to the domain walls. The process resulted in a giant increase of the total poling current. This phenomenon occurred for all the samples. Therefore the polarized microscopy showed the realization of periodic structures in both the materials and, more important, the stabilization of the domains also in the Zirconium doped crystals.

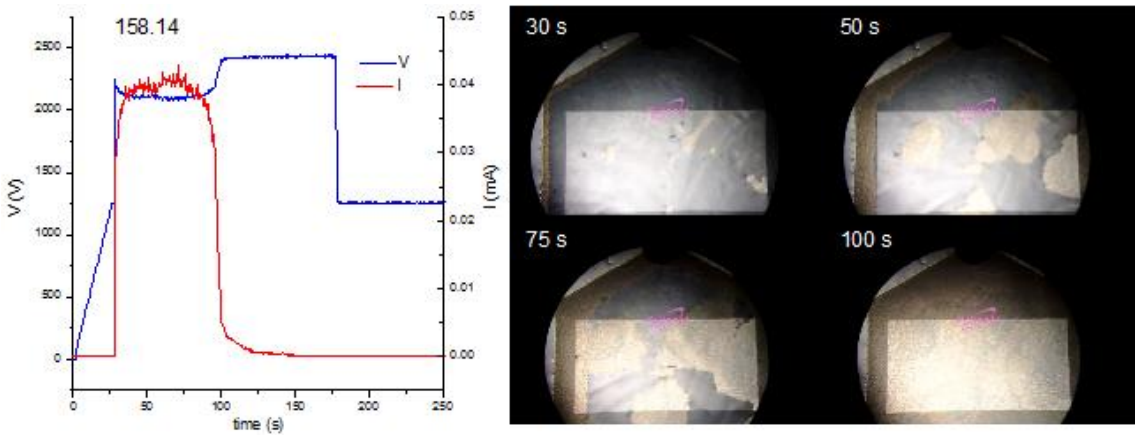

FIGURE 36 VOLTAGE AND CURRENT VS TIME PLOTS AND SNAPSHOT TAKEN FROM THE RECORDED VIDEOS AT DIFFERENT POLING STAGES.

3.7. Characterization

3.7.1. Wet Etching

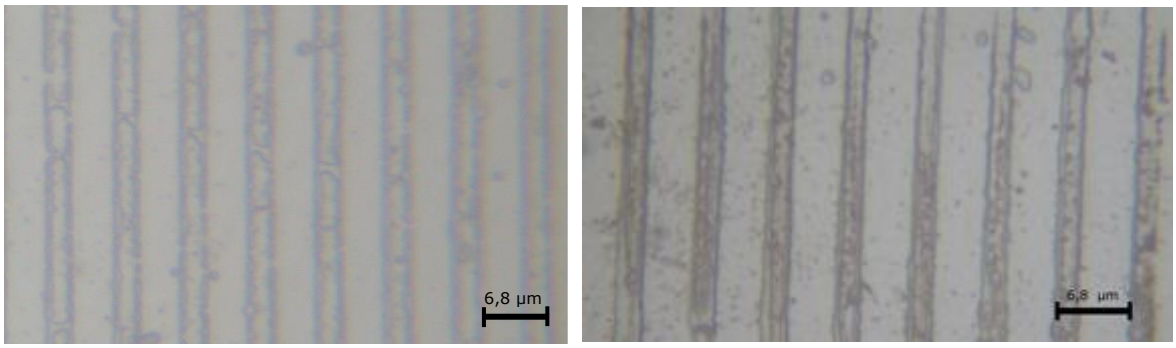

FIGURE 37 IMAGES OF 6,8 µm PPLN AFTER THE WET ETCHING FOR A CONGRUENT CRYSTAL (LEFT) AND A Zr DOPED CRYSTAL (RIGHT)

As for the room temperature samples (section 3.4), also in this case we report pictures of the +z surface of two of the four PPLN, one Zr doped and one congruent after the chemical etching in HF, performed by standard methods [36], where the periodic structure can be easily seen. Since the wet etching is a destructive technique only two samples were etched, one cLN and one ZrLN. The period of 6.8 µm was confirmed and the measured open width for the first was 1,9±0,2 µm and 2,4±0,2 µm for the second, i.e. a duty cycle of 27% and 35% respectively. Differently from the low-temperature poling in this case the structures were etched only in the +z surface, this is due to the superficial structure of the domains as it was expected from literature [42]. Moreover the sample without periodic pattern used to measure the coercive field at 150°C was lateral etched in order to confirm the superficial structure (Figure 38).

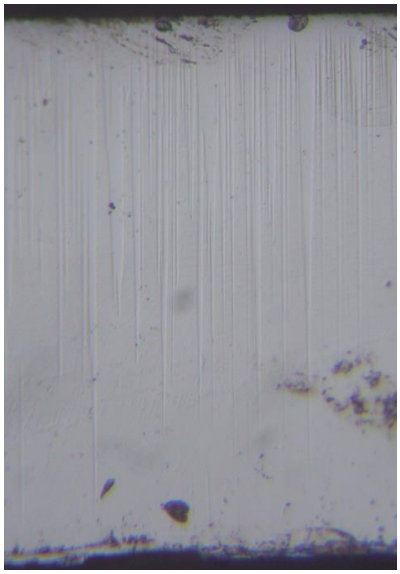

FIGURE 38 LATERAL ETCHING OF A CONGRUENT CRYSTAL POLED AT 150°C.

3.7.2. SHG efficiency

The SHG efficiency of the last two samples, one doped and one undoped, was tested using a CW Yb-doped fiber with an emission wavelength of 1070 nm, and a maximum output power of 5 W, at the Laboratory of Quantum Electronics and Nonlinear Optics Electronics Department of the University of Pavia. The scheme of the experimental setup is reported in the following figure.

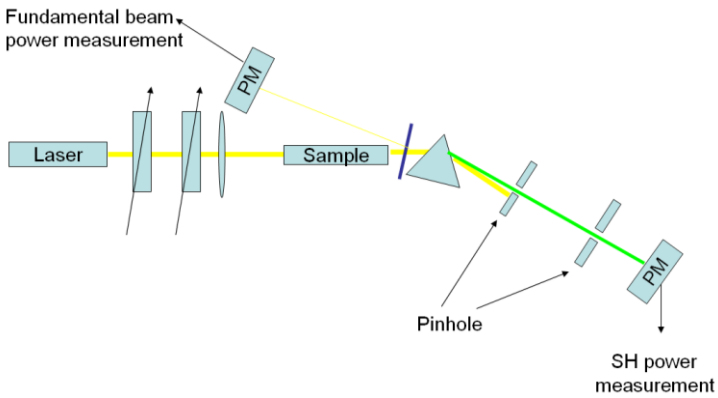

FIGURE 39 SKETCH OF THE SHG EXPERIMENTAL SET-UP.

We positioned two polarizers after the beam collimator at the fiber output to fix the polarization again instabilities: the second polarizer is used to align the beam polarization with the extraordinary axis of the sample, while the first one is used to modify the beam power incident on the sample. The

1070-nm beam was focused by a lens with focal length of 150 mm, thus producing a beam waist of 60 μm. The Rayleigh length was larger than 2 cm, allowing to easily center the beam on the sample facet and guarantee that the beam size is almost constant along the whole crystal (length L ≈ 11 mm). The crystal itself was mounted on a temperature-controlled holder to finely tune the phase-matching condition. After the sample a wedge glass was used to reflect a small fraction of the pump and SH beams, while the transmitted beam was first spatially separated by a prism, and subsequently by two pin holes and an IR-blocking filter. Thanks to the use of two separate power-meters and to an accurate calibration of all the losses, we could measure at the same time both the SH power and the pump beam power. In order to evaluate the SHG process efficiency it is useful to exploit Equation 14 relating the SH beam power (P_{SH}) to that of a fundamental beam (P_F), having a beam waist w, under the hypothesis of the pump is undepleted and the phase-matching condition is satisfied:

$$\frac{P_{SH}(L)}{P_F^2} = \eta = L^2 \frac{8\pi d_{eff}^2}{w^2 \lambda^2 n_{SH} n_F^2 c \varepsilon_0}$$

EQUATION 14

In the above equation d_{eff}, given by $2\times(d_{33}/\pi)$, represents the effective nonlinear coefficient in case of first order QPM, n_{SH} and n_F are the material refractive indexes at the second harmonic and at the fundamental wavelength respectively. Measuring the losses in the experimental setup and substituting the appropriate values to the constants in Equation 14, it is possible to obtain both the experimental η values and the theoretical ones. Given that the length of the periodically poled area (L) is the same for both the congruent and the Zr-doped samples, and neglecting the small differences (<1%) that could affect the extraordinary refractive index curve, the theoretical η value derived by Equation 14 for both materials is $9\cdot10^{-3}$ W^{-1}. On the other hand the experimental values allowed estimating $\eta \approx 1\cdot10^{-3}$ W^{-1} for both samples. It is interesting to highlight that the SHG efficiency in the Zr-doped LN is exactly the same observed in the CLN sample, but lower than the efficiency expected by exploiting first-order QPM in a cLN sample.

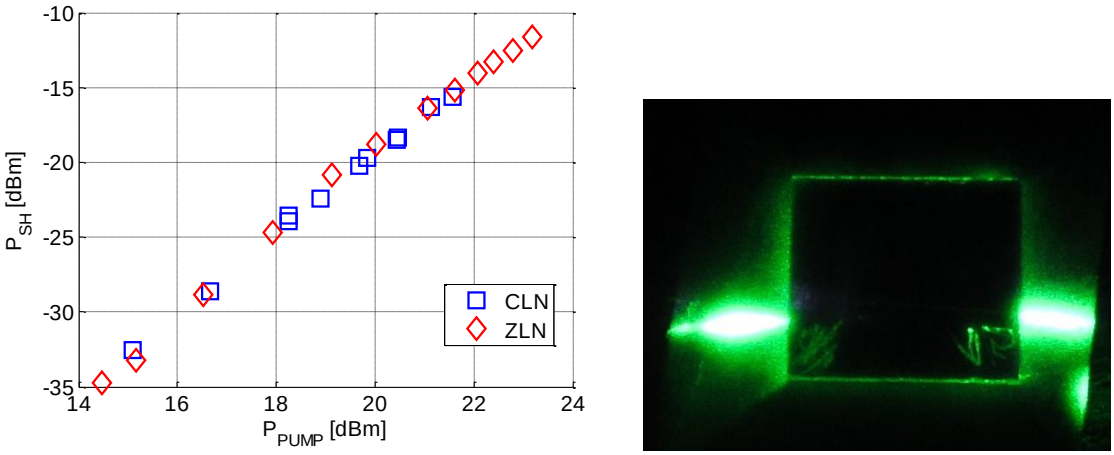

FIGURE 40 SECOND HARMONIC GENERATION MEASUREMENT OF TWO SAMPLES: CONGRUENT PPLN (CLN) AND Zr DOPED PPLN (ZLN). ON THE RIGHT A PHOTO OF THE SH GENERATION DURING THE PROCESS.

Taking into account the poling duty cycle, i.e. the actual ratio between the width of the inverted domain and the structure period (l/Λ), the effective nonlinear coefficient for first-order QPM, can be written as:

$$d_{eff} = \frac{2d_{33}}{\pi} sin\left(\pi \frac{l}{\Lambda}\right)$$

EQUATION 15

It is worth underlining that for PPLN realization the duty-cycle was set to 20%, as domain broadening seemed to appear when the domains were observed exploiting the HF-etching technique. The resulting duty cycles were of 27% and 35% for the cLN and Zr:LN respectively, instead of the ideal 50%. Therefore these values could reduce the SHG efficiency of the 56% and 79% respectively. Which in any case are still not sufficient to completely justify the difference between theoretical and observed SHG values. We suggest that the residual discrepancy is due to the non-homogenous depth structure of the domains, in fact this leads to a duty-cycle change in depth as domains become narrower, and also to missing rods as more superficial domains end.

4. Conclusion

4.1. Waveguides

The production and the characterization of planar and channel waveguides by Ti-indiffusion were achieved on x-cut Lithium Niobate crystals in both the possible direction of propagation, y and z. The planar waveguides were characterized using structural (SIMS and RBS) and optical (m-lines) methods, the firsts confirm the fickian behavior of the titanium diffusion inside the Lithium Niobate, with a diffusion coefficient of 91±2 nm^2/s, comparable with the previous measure of 88±3 nm^2/s; and a superficial concentration of $(1{,}00\pm0{,}02)\cdot10^{21}$ at/cm^3, comparable with literature [7]. The second allowed finding the fabrication parameters to achieve a single-mode planar waveguide (Table 4). Moreover we characterize our deposition process finding a flux of the sputtering deposition of $8{,}3\cdot10^{14}$ molecules s^{-1} cm^{-2}.

Therefore by means of a photolithographic process, settled up and optimized in the PhD thesis, we produce channel waveguides using the same diffusion condition of the planar single-mode waveguides. Firstly we simulate, using a numerical approach (section 2.3), different starting width of the Ti strip deposited, finding that for a width of 5 μm (the lower dimension of our photolithographic mask) a TE single-mode y-propagating channel waveguide was achievable. Therefore we produce such a kind of waveguides confirming the TE polarized single-mode using the Near-Field technique (section 2.10). Moreover we find that also non-polarized beams both y and z propagating were single-mode in these kinds of waveguides.

Finally we achieve our goal of production a single-mode waveguide in x-cut crystals by Ti in-diffusion, furthermore the next steps will be the measurement of the intensity losses of the waveguides. After the complete characterization of this standard process, we will do the same study on z-cut substrate in order to obtain waveguides for different kind of devices, PPLN-based or photorefractive-based. Moreover a study of Ti co-diffusion in Zr or Fe doped sample will be fundamental for the integration of the waveguides with PPLN or holographic filters respectively. Furthermore the first good

results of the coupling of a microchannel with this kind of waveguides are reported in chapter 4, an important step toward the Lithium Niobate Optofluidic Platform.

4.2. Frequency converters (PPLN)

The realization of a frequency converter integrated in LN is a fundamental step for the achievement of the optical stage of our microfluidic platform. As discussed previously the realization of this PPLN structure can be achieved in two kinds of substrate cLN and Zr:LN, as the second allow obtaining optica-damage resistant devices. Therefore the Zr:PPLN could be realized in two possible ways, the first is to implement all the structures, both optical and fluidic, in a bulk doped crystal of LN. The second is to diffuse at high temperature Zr only in the area where the PPLN are realized. Since the realization of periodic structures on Zr:LN has not been reported in literature yet, and the implementation of these structures on a varying Zr profile as that observed in in-diffused sample is a strong complication, we decided to investigate the real possibility of getting PPLN on Zr doped samples as a first step. However the first possibility is surely less flexible compared to a tailorable doping but is necessary to understand the unknow phenomena observed in the Zr periodic poling. Therefore we started to study the behavior of the poling in the bulk Zr doped crystal, as they are the simplest model in which operate.

In conclusion we realized photolithographyc patterns with useful size on the sample (6,8 μm), and we were able to obtain periodic poled domains of suitable dimensions in congruent Lithium Niobate crystals. Next steps will concern the measurements of the efficiency of SHG and the realization of PPLN in channel-waveguide configuration, since these structures are well known in literature we expected high efficiency PPLN, but only for low intensity because of the optical damage.

The formation of domains in Zr doped crystals results more different and complicated than in the undoped samples. In fact in the low-temperature configuration this domains are not stable and tend to return to initial polarization state. This problem probably depends on the wall dynamics and domain nucleation in Zr doped $LiNbO_3$ crystals, which are still unknown topics

in Lithium Niobate research. Some models suggest that the internal field is due to dipole moments of defect clusters [Nb_{Li}–$4V_{Li}$] [32], or it is postulated that at room temperature the point defects Nb_{Li} are fixed by Li vacancies [23], so the cluster dipoles cannot be reoriented and maintain the initial direction of E_{int}. These dipoles may be realigned only at T>100–200°C. So the reason of the observed reorientation of E_{int} at elevated temperatures could be a reorientation of the cluster [Nb_{Li}–$4V_{Li}$] dipoles, which is attributed to a thermo-activated mobility of the Li vacancies and their hopping over equivalent Li sites.

Crystal	E_c(kV cm^{-1})	E_{int}(KV cm^{-1})
CLN	210	2-33
SLN	60-65	→0
CLN:5%MgO	60-68	5
CLN:8%ZnO	25-35	5
SLN:1%MgO	25	→0
CLN:3% ZrO_2	78 ± 4	24-38

TABLE 20. COERCIVE FIELD AND INTERNAL FIELD FOR PRINCIPAL KIND OF LITHIUM NIOBATE

Moreover, we found a value of the coercive field of about 7,8 ± 0,4 kV/mm for the congruent Lithium Niobate doped with 3 mol. % with Zirconium (CLN:3 mol. %Zr). A comparison with the coercive fields of LN with different stoichiometry and different dopants is reported in Table 20: the coercive field of CLN:3%Zr is about the 37% of the CLN coercive field, and it is comparable with the 5 mol. % MgO CLN, but with a lower threshold concentration. Furthermore the coercive field is the one measured at first forward poling, so it is possible that samples with lower internal field give lower value of forward poling. The solution to Zr:LN backswitching was the implementation of a high-temperature poling set-up that allowed the realization of a stable periodic inversion of the ferroelectric domains at 150°C, for both doped and undoped crystals. Moreover we measured the coercive fields of ZrLN also at 150°C (Table 19). As expected the PPLNs obtained at high temperature were stabilized but superficial, as discussed the mobility of charges and defect inside the material could be the explanation of both the phenomena [42]. Moreover the domains stabilization itself could be explained not only by the reorientation of the polar defects, but also by the charges compensation of the instable domain walls. In support of this hypothesis we find furthermore that after the poling process a reverse poling is not possible for high-

temperature samples both congruent and doped, a behavior that is not explainable only considering the internal field generated by polar defects.

In summary, we achieved the periodic poling of Lithium Niobate crystals by exploiting both room-temperature and high-temperature (150°C) electric-field poling, thanks to the use of a dedicated apparatus that allows also monitoring the domain formation during the process. In the first case better structures were achieved for congruent crystals, since the ferroelectric domains pass through the whole crystal width, as demonstrated by the wet etching.

The Quasi-Phase Matching Second-Harmonic Generation (QPM-SHG) operating at room temperature was then tested for high-temperature-poling crystals both congruent and Zr doped. A comparison between the efficiencies of doped and undoped PPLN results in a comparable efficiency, demonstrating that Zr-doped substrates are a valid alternative to Mg-doped. Moreover we found a low efficiency in comparison from what expected from theory, probably due the superficial structures of the domains that is related to the poling at high temperature. The depth of the domains is still unknown for the periodic structures, but considering the measure took for the poling of the entire surface it is probably of around one hundreds of micrometers (Figure 38) with a beam waist of 60 μm. Therefore two possibilities may be explored to improve our efficiency: the first is to improve our high-temperature poling set-up so that deeper domains are achieved, for example we could exploit the poling at lower temperature (i.e. deeper domains) and then achieve their stabilization increasing the temperature during the post-poling phase. The second is to use directly this kind of structures with waveguides able to confine the light in few micrometers, a region in which the domains probably could be considered uniform also in depth.

Finally it is important to note that other kind of optical-damage resistant dopants like Mg are not compatible with ion diffusion technique for the realization of waveguides, on the contrary first studies on Zr doped samples demonstrated its compatibility with proton exchange technique [47]. Therefore a study also on the Titanium diffusion in Zr doped crystal would be interesting and will be done in the next months.

Bibliography

[1] G. Nava, P. Minzioni, W. Yan, J. Parravicini, D. Grando, E. Musso, I. Cristiani, N. Argiolas, M. Bazzan, M. V. Ciampolillo, A. Zaltron, C. Sada, and V. Degiorgio, "Zirconium-doped lithium niobate: photorefractive and electro-optical properties as a function of dopant concentration," *Opt. Mater. Express*, vol. 1, no. 2, p. 270, May 2011.

[2] D. P. Birnie, "Analysis of diffusion in lithium niobate," *J. Mater. Sci.*, vol. 28, no. 2, pp. 302–315, 1993.

[3] C. Canali, a. Carnera, G. Della Mea, P. Mazzoldi, S. M. Al Shukri, a. C. G. Nutt, and R. M. De La Rue, "Structural characterization of proton exchanged LiNbO3 optical waveguides," *J. Appl. Phys.*, vol. 59, no. 8, p. 2643, 1986.

[4] G. G. Bentini, M. Bianconi, a. Cerutti, M. Chiarini, G. Pennestrì, C. Sada, N. Argiolas, M. Bazzan, and P. Mazzoldi, "Integrated Mach-Zehnder micro-interferometer on LiNbO3," *Opt. Lasers Eng.*, vol. 45, no. 3, pp. 368–372, Mar. 2007.

[5] W. P.K. and W. W.S., "A TE-TM mode splitter on lithium niobate using Ti, Ni, and MgO diffusions," *IEEE Photonics Technol. Lett.*, vol. 6, no. 2, pp. 245–248, Feb. 1994.

[6] F. Caccavale, P. Chakraborty, A. Quaranta, I. Mansour, G. Gianello, S. Bosso, R. Corsini, and G. Mussi, "Secondary-ion-mass spectrometry and near-field studies of Ti:LiNbO3 optical waveguides," *J. Appl. Phys.*, vol. 78, no. 9, p. 5345, 1995.

[7] F. Caccavale, "Secondary ion mass spectrometry and optical characterization of Ti : LiNbO 3 optical waveguides," pp. 195–201, 1999.

[8] F. Caccavale, F. Segato, I. Mansour, and M. Gianesin, "A finite differences method for the reconstruction of refractive index profiles from near-field measurements," *J. Light. Technol.*, vol. 16, no. 7, pp. 1348–1353, Jul. 1998.

[9] F. Caccavale, A. Morbiato, M. Natali, C. Sada, F. Segato, and I. Introduction, "Correlation between optical and compositional properties of Ti:LiNbO 3 channel optical waveguides," vol. 87, no. 3, pp. 1007–1011, 2000.

[10] M. De Sario, M. N. Armenise, C. Canali, A. Carnera, P. Mazzoldi, and G. Celotti, "TiO2, LiNb3O8, and (TixNb1−x)O2 compound kinetics during Ti:LiNbO3 waveguide fabrication in the presence of water vapors," *J. Appl. Phys.*, vol. 57, no. 5, p. 1482, 1985.

[11] M. Minakata, S. Saito, M. Shibata, and S. Miyazawa, "Precise determination of refractive-index changes in Ti-diffused LiNbO3 optical waveguides," *J. Appl. Phys.*, vol. 49, no. 9, p. 4677, 1978.

[12] S. Fouchet, A. Carenco, C. Daguet, R. Guglielmi, and L. Riviere, "Wavelength dispersion of Ti induced refractive index change in LiNbO<inf>3</inf>as a function of diffusion parameters," *J. Light. Technol.*, vol. 5, no. 5, pp. 700–708, 1987.

[13] F. Caccavale, P. Chakraborty, a. Quaranta, I. Mansour, G. Gianello, S. Bosso, R. Corsini, and G. Mussi, "Secondary-ion-mass spectrometry and near-field studies of Ti:LiNbO3 optical waveguides," *J. Appl. Phys.*, vol. 78, no. 9, p. 5345, 1995.

[14] R. V. Schmidt, "Metal-diffused optical waveguides in LiNbO3," *Appl. Phys. Lett.*, vol. 25, no. 8, p. 458, 1974.

[15] R. J. Holmes and D. M. Smyth, "Titanium diffusion into LiNbO3 as a function of stoichiometry," *J. Appl. Phys.*, vol. 55, no. 10, p. 3531, 1984.

[16] H. Search, C. Journals, A. Contact, M. Iopscience, and I. P. Address, "Water Vapor Effects on Titanium Diffusion into LiNbO3 Substrates," vol. 2180.

[17] P. K. Tien, "Integrated optics and new wave phenomena in optical waveguides," *Rev. Mod. Phys.*, vol. 49, no. 2, pp. 361–420, Apr. 1977.

[18] J. Armstrong, N. Bloembergen, J. Ducuing, and P. Pershan, "Interactions between Light Waves in a Nonlinear Dielectric," *Phys. Rev.*, vol. 127, no. 6, pp. 1918–1939, Sep. 1962.

[19] R. L. Byer, "Quasi-Phasematched Nonlinear Interactions and Devices," *J. Nonlinear Opt. Phys. Mater.*, vol. 06, no. 04, pp. 549–592, Dec. 1997.

[20] P. Martelli, P. Boffi, M. Ferrario, L. Marazzi, P. Parolari, R. Siano, V. Pusino, P. Minzioni, I. Cristiani, C. Langrock, M. M. Fejer, M. Martinelli, and V. Degiorgio, "All-optical wavelength conversion of a 100-Gb/s polarization-multiplexed signal.," *Opt. Express*, vol. 17, no. 20, pp. 17758–63, Sep. 2009.

[21] M. M. Fejer, G. a. Magel, D. H. Jundt, and R. L. Byer, "Quasi-phase-matched second harmonic generation: tuning and tolerances," *IEEE J. Quantum Electron.*, vol. 28, no. 11, pp. 2631–2654, 1992.

[22] G. Rosenman, P. Urenski, A. Agronin, Y. Rosenwaks, and M. Molotskii, "Submicron ferroelectric domain structures tailored by high-voltage scanning probe microscopy," *Appl. Phys. Lett.*, vol. 82, no. 1, p. 103, 2003.

[23] T. Volk and M. Wöhlecke, *Lithium Niobate*, vol. 115. Berlin, Heidelberg: Springer Berlin Heidelberg, 2008.

[24] M. Houe and P. D. Townsend, "An introduction to methods of periodic poling for second-harmonic generation," *J. Phys. D. Appl. Phys.*, vol. 28, no. 9, pp. 1747–1763, Sep. 1995.

[25] V. Pruneri, S. D. Butterworth, J. Webjörn, P. S. J. Russell, and D. C. Hanna, *Ultrafast Processes in Spectroscopy*. Boston, MA: Springer US, 1996.

[26] G. Nava, P. Minzioni, I. Cristiani, N. Argiolas, M. Bazzan, M. V. Ciampolillo, G. Pozza, C. Sada, and V. Degiorgio, "Photorefractive effect at 775 nm in doped lithium niobate crystals," *Appl. Phys. Lett.*, vol. 103, no. 3, p. 031904, 2013.

[27] D. A. Bryan, R. Gerson, and H. E. Tomaschke, "Increased optical damage resistance in lithium niobate," *Appl. Phys. Lett.*, vol. 44, no. 9, p. 847, 1984.

[28] Y. Kong, S. Liu, and J. Xu, "Recent Advances in the Photorefraction of Doped Lithium Niobate Crystals," *Materials (Basel).*, vol. 5, no. 12, pp. 1954–1971, Oct. 2012.

[29] M. Nakamura, M. Kotoh, H. Taniguchi, and K. Tadatomo, "Bulk Periodically Poled MgO-doped LiNbO3 by External Electric Field Application," *Jpn. J. Appl. Phys.*, vol. 38, no. Part 2, No. 5A, pp. L512–L514, May 1999.

[30] Y. Kong, S. Liu, Y. Zhao, H. Liu, S. Chen, and J. Xu, "Highly optical damage resistant crystal: Zirconium-oxide-doped lithium niobate," *Appl. Phys. Lett.*, vol. 91, no. 8, p. 081908, 2007.

[31] N. Argiolas, M. Bazzan, M. V. Ciampolillo, P. Pozzobon, C. Sada, L. Saoner, A. M. Zaltron, L. Bacci, P. Minzioni, G. Nava, J. Parravicini, W. Yan, I. Cristiani, and V. Degiorgio, "Structural and optical properties of zirconium doped lithium niobate crystals," *J. Appl. Phys.*, vol. 108, no. 9, p. 093508, 2010.

[32] V. Gopalan, V. Dierolf, and D. A. Scrymgeour, "Defect–Domain Wall Interactions in Trigonal Ferroelectrics," *Annu. Rev. Mater. Res.*, vol. 37, no. 1, pp. 449–489, Aug. 2007.

[33] D. Scrymgeour, V. Gopalan, A. Itagi, A. Saxena, and P. Swart, "Phenomenological theory of a single domain wall in uniaxial trigonal ferroelectrics: Lithium niobate and lithium tantalate," *Phys. Rev. B*, vol. 71, no. 18, p. 184110, May 2005.

[34] A. I. Lobov, V. Y. Shur, I. S. Baturin, E. I. Shishkin, D. K. Kuznetsov, A. G. Shur, M. A. Dolbilov, and K. Gallo, "Field Induced Evolution of Regular and Random 2D Domain Structures and Shape of Isolated

Domains in LiNbO 3 and LiTaO 3," *Ferroelectrics*, vol. 341, no. 1, pp. 109–116, Oct. 2006.

[35] V. Janovec, "Anti-parallel ferroelectric domains in surface space-charge layers of BaTiO3," *Czechoslov. J. Phys.*, vol. 9, no. 4, pp. 468–480, Jul. 1959.

[36] R. Miller and G. Weinreich, "Mechanism for the Sidewise Motion of 180° Domain Walls in Barium Titanate," *Phys. Rev.*, vol. 117, no. 6, pp. 1460–1466, Mar. 1960.

[37] V. Y. Shur, "Kinetics of ferroelectric domains: Application of general approach to LiNbO3 and LiTaO3," *J. Mater. Sci.*, vol. 41, no. 1, pp. 199–210, Jan. 2006.

[38] P. V. Lambeck and G. H. Jonker, "The nature of domain stabilization in ferroelectric perovskites," *J. Phys. Chem. Solids*, vol. 47, no. 5, pp. 453–461, Jan. 1986.

[39] A. K. Tagantsev, I. Stolichnov, E. L. Colla, and N. Setter, "Polarization fatigue in ferroelectric films: Basic experimental findings, phenomenological scenarios, and microscopic features," *J. Appl. Phys.*, vol. 90, no. 3, p. 1387, 2001.

[40] T. Jach, S. Kim, V. Gopalan, S. Durbin, and D. Bright, "Long-range strains and the effects of applied field at 180° ferroelectric domain walls in lithium niobate," *Phys. Rev. B*, vol. 69, no. 6, p. 064113, Feb. 2004.

[41] E. P. Kokanyan, L. Razzari, I. Cristiani, V. Degiorgio, and J. B. Gruber, "Reduced photorefraction in hafnium-doped single-domain and periodically poled lithium niobate crystals," *Appl. Phys. Lett.*, vol. 84, no. 11, p. 1880, 2004.

[42] David Scrymgeour, "LOCAL STRUCTURE AND SHAPING OF FERROELECTRIC DOMAIN WALLS FOR PHOTONIC APPLICATIONS," The Pennsylvania State University, 2004.

[43] Chakraborty and Suman, *Microfluidics and microfabrication*. 2009.

[44] T. R. Volk and N. M. Rubinina, "A new optical damage resistant impurity in lithium niobate crystals: Indium," *Ferroelectr. Lett. Sect.*, vol. 14, no. 1–2, pp. 37–43, May 1992.

[45] M. Bazzan, N. Argiolas, C. Sada, P. Mazzoldi, S. Grilli, P. Ferraro, P. De Natale, and L. Sansone, "High Resolution X-Ray Characterization of Sub-Micron Periodic Domain Structures in Lithium Niobate Crystals," *Ferroelectrics*, vol. 352, no. 1, pp. 25–34, Jul. 2007.

[46] G. I. Malovichko, V. G. Grachov, and E. P. Kokanyan, "Low-symmetry Fe-Mg complexes in LiNbO 3 :Mg," *Ferroelectrics*, vol. 125, no. 1, pp. 289–294, Jan. 1992.

[47] C. Langrock, R. V. Roussev, and M. M. Fejer, "Nonlinear diffusion model for annealed proton-exchanged waveguides in zirconium-doped lithium niobate," in *IEEE Photonics Conference 2012*, 2012, pp. 416–418.

Conclusion

1. Latest Results

With the aim of prove the possibility of integration between the optical stage and the fluidic stage, that is one of the main challenges of our project, we present the first results of the coupling between a single-mode waveguide and a microfluidic channel. Different x-cut sample with single-mode waveguides were realized with the optimized procedure and the parameters discussed in Chapter 3. Therefore two samples were tested to host T-juntion structures realized with the femtosecond laser ablation; and other two samples prepared with single channel realized with a precision saw (Disco DAD 321) at the University of Franche-Comté, Besançon (France) in order to assure a high optical grade dicing.

Since polished faces are requested at both the entrance and exit sides as well as at the walls of the trenches, in order to limit losses due to light diffusion, a polymer blade with diamond particles was used. Cutting parameters have been experimentally determined to give optical quality cuts in $LiNbO_3$. The blade, with a diameter of 56 mm and a thickness of 200μm, rotates at 10 Krpm and the cutting speed was fixed at 0.2 mm s^{-1}. A constant and high flow of water was exploited, keeping a constant and low temperature for both the blade and the sample during the process. Such a process constitutes a straightforward way to simultaneously dice and polish 200 μm wide by 50 μm deep trenches oriented along the z-axis, with smooth walls and realized in a single step process.

The microchannel cut was then characterized with an AFM (Figure 1) in order to measure the roughness of the lateral and the bottom walls. The results, reported in Table 1, are excellent with an average roughness of the lateral wall of about 7 times lower than the laser-ablated channels. These preliminary measurements are surely encouraging and we could probably change the fabrication technique in favour of the optical-grade dicing, or of a mixed procedure between the laser ablation and the dicing.

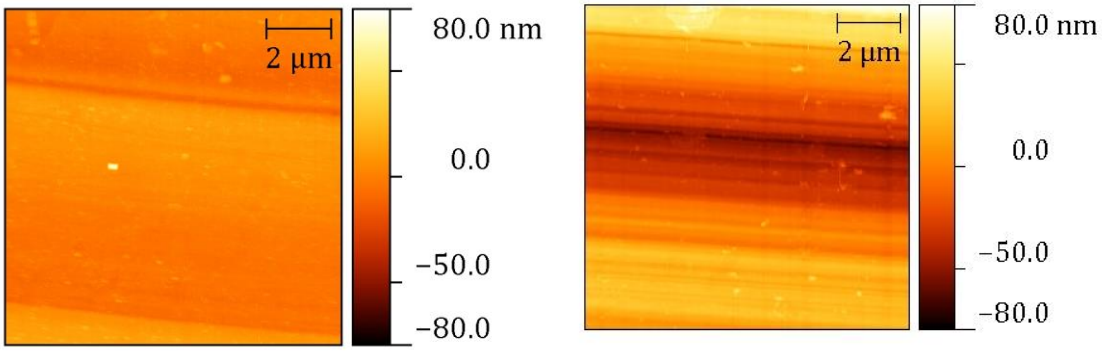

FIGURE 1 AFM MEASUREMENTS OF THE LATERAL SIDE (LEFT) AND BOTTOM SIDE (RIGHT) OF A MICROCHANNEL REALIZED USING A PRECISION SAW (DISCO DAD 321).

	Lateral side (nm)		Bottom side (nm)	
	Average	Error	Average	Error
Ra	6,8	0,5	19	6
Rq	8,5	0,9	23	7

TABLE 1ROUGHNESS AVERAGE MEASUREMENTS OF THE LATERAL AND BOTTOM FACES OF A MICROCHANNEL REALIZED USING A PRECISION SAW (DISCO DAD 321)

After the surface characterization we collected the Near Field images for a waveguide passing through the channel. A Near Field measurement was taken also before the channel cut and therefore in Figure 2 we present a comparison between the same waveguides at the same input intensity ($2{,}2 \cdot 10^5$ W/m^2) before and after the channel realization. As it can be easily seen the presence of the channel, filled with hexadecane, slightly affect the emission of the waveguide, with a ratio between the two measured output intensities of 0,46. The coupling between the microchannels and the waveguides was therefore demonstrated, and therefore the last part of the project – the integration between the optical and the fluidic stages – could be implemented in the next months.

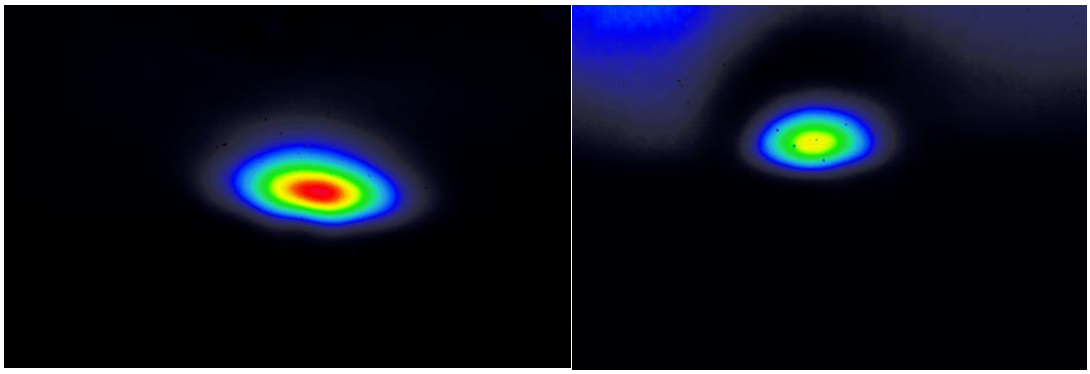

FIGURE 2 NEAR FIELD IMAGES OF THE MONOMODAL WAVEGUIDE BEFORE (LEFT) AND AFTER (RIGHT) THE MICROCHANNEL CUTTING. THE CHANNEL IS FILLED WITH HEXADECANE.

2. Conclusion

From the work presented in this thesis Lithium Niobate has demonstrated one more time its extremely adaptability as material for optical and, in our case, also for optofluidic applications. As a matter of fact, a wide set of different technologies was explored in order to tailor the material for different application: chemical functionalization, doping, ion exchanging, etching, domains engineering, and microfabrication. A little subset of possibility, since a lot of other techniques were not explored in the project (for example ion implantation) or discussed in this thesis (photorefractive trapping). Moreover also properties like piezoelectricity or the electro-optic effect - that are well known and used to realize microfluidic or optical circuits respectively – were not taken into account in this project. However they extend the range of tools that it is possible to implement in an optofluidic platform in Lithium Niobate. We obtained therefore both optical and fluidic devices in the same kind of substrate. The first type of device was taken from literature a and were implemented (Ti in-diffused waveguides, PPcLN) or improved by us (Zr:PPLN); the second one (T-junction) was the first device of this kind realized in LN crystals and demonstrated performance and behaviors completely comparable to classical microfluidic materials. Finally the first coupling between a Ti waveguide and a microchannel was achieved, demostrantig that Lithium Niobate have really good perspective as a material for optofluidics.

For what concerns the optical stage of our project we were able to obtain single-mode Ti-indiffused waveguides, starting from the state of the art of our group (20 years of work on the Ti-indiffusion waveguide study and fabrication). Therefore we obtained for the first time, at the best of our knowledge, the coupling between a Ti single-mode channel waveguide and a microfluidic channel. Therefore we measured a loss due to the transmission through the channel of the 46%, which is quite good for a first experiment. We completely characterize the procedure of waveguide fabrication, therefore we were able to reproduce our sample with a good confidence. The next step will be the implementation of the same procedure on z-cut crystals with the aim to integrate the waveguides with the PPLN, moreover also the study of

the diffusion of Ti in Zr bulk doped sample will be implemented in order to achieve high efficient optical-damage resistant frequency converters. Finally the co-diffusion of Ti and Fe will be strategic for the realization of holographic Bragg gratings which can be used in the analysis of the signal.

The implementation of a frequency converter in Lithium Niobate plays a key role in the development of our optofluidic platform. In fact it can be used to integrate a laser source in the green-blue range that could found application particularly in the biological field. Moreover PPLN could also be used to produce multifrequency emission, which could have interesting application, for example the simultaneous analyis of our droplets with different wavelengths. Therefore we achieved the realization of PPLN structure for the SHG in the QPM configuration. PPLN were realized in congruent LN using photolithography and a room-temperature poling cell. Moreover our aim was to achieve also high intensity and high efficiency of conversion, therefore we needed to dope the material with ions able to contrast the optical damage and a new kind of dopant, Zirconium, was chosen. This was the first study on the realization of PPLN on substrate doped with Zr, therefore we found that the implementation of a high-temperature poling cell was necessary, because of the backswitching phenomenous accouring after the poling at room temperature. We successfully obtained both congruent and Zr doped PPLN with the suitable periodicity (6,8 μm) able to achieve the SHG from 1064 nm to 532 nm. Unfortunately the ferroelectric domains were too superficial, this because of the high temperature process, and therefore the efficiencies of SH conversion ($9 \cdot 10^{-3}$ W^{-1}) were not satisfactory for both the kind of material realized at high temperature. Therefore the next step will be the optimization of the poling process at high temperature in order to obtain better and deeper domains. Finally also the integration of a channel waveguide can increase the efficiency of conversion and will be another step toward a higher integration, therefore the study of the Ti diffusion in Zr bulk doped LN will be an important task.

In the fluidic stage the first study on the realization of a T-Junction droplets generator directly engraved in Lithium Niobate was completely achieved. First we find a useful fabrication technique from a feasibily study: femtosecond laser ablation, which demonstrated a good reproducibility, flexibility on the

pattern writing, and good roughness of the channel walls. Then for this first prototype, we close the microchannels with a layer of PDMS, using a O_2-plasma bonding. Therefore we characterize the fluidic properties of the T-Junctions finding extremely good performances in both the control of the droplet generation frequency and the control of the their dimensions. In particular we reached frequencies generation of about 1 kHz and a dispersion of the length lower than 3% in the majority of the cases. Moreover we found the bottom bound of application of the model used, as for $Ca<6\cdot10^{-4}$ the Christopher et al. model started to evidence its limits. In addition the study of the wettability and of the functionalization showed how the material is easily adaptable to different needs, in our case the increase of the hydrophobicity. Moreover with different functionalization it could be probably easy to turn the LN surfaces hydrophilic. Lithium Niobate is therefore comparable to other standard material for microfluidic like PDMS, glass or silicon; but with better and well-known optical properties. The major problem that still needs to be study is the one relative to the roughness of the channel sidewall. In fact, the laser ablation gives surfaces with an average roughness of about 50 nm, a value that is good but could still affect the coupling of the waveguide with the channel. However the first waveguide/microchannel samples are under fabrication and the consequence of the roughness will be analyzed. Nevertheless, in order to improve the optical quality of the channel polishing technique for the sidewall will be implemented, as magnetorheological finishing or optimizing the combination of laser damaging and wet-etching. Furthermore we recently obtained an excellent sidewall roughness with a different technique: the optical-grade dicing. In this samples we recently demonstrated for the first time the possibility of coupling a Ti-indiffused waveguide and a microchannel. Therefore, if femtosecond laser ablation will not be able to achieve similar results, a combination of the two techniques could probably be a good solution, exploiting the pattern flexibility of the laser to achieve the T-juntion, or other channel geometries, and the low roughness of the dicing technique to fabricate waveguide-coupling zone of the fluidic circuit.

In conclusion all the fundamental steps for the fabrication of the fluidic and the optical stages were implemented. In particular during our work we were

able to achieve the realization of the first T-junction devices engraved in Lithium Niobate, of the first PPLN frequency converters realized in Zr doped Lithium Niobate, and the first coupling between a Ti indiffused single-mode channel waveguide and a microfluidic channel. All this devices can be realized on the same substrate, paving the way to an extreme integration of optofluidic tools in Lithium Niobate. Therefore in the next months the principal issue will be the integration between all these different devices in order to achieve the final optofluidic platform. In the next section we discuss the next steps and the future objectives of our work.

2.1. Future perspectives

As previously discussed the next main objective will be the improvement of the coupling of the single-mode waveguide with the microfluidic channel, and in this context first results are encouraging, as discussed in section 1. In particular we are going to analyze also waveguides coupled with the laser-ablated channel in order to found which is the best method of microchannel fabrication. Moreover also the fabrication of a T-junction using the optical-grade dicing will be taken into account. After these studies the realization of a droplets counter used to measure the performance of the T-junction will allow realizing a first simple prototype able to measure frequency and dimensions of the droplets.

A second objective will concern the realization of a PPLN/waveguide/microchannel system in which the radiation emitted from the PPLN excite a dye dissolved in a water droplet and therefore the opposite waveguide collect the light emitted from the droplets. This will be the first step toward the realization of a sensor, as the realization of an analytical stage (Bragg gratings) realized with microfabrication, or photorefractive holographic techniques, will allow separating the different wavelength contribution of the collected light and therefore to identify the presence of the dye in the droplets.

Finally also an improvement on the channel fabrication is forecast, in fact we will try to close the upper side of the channels using another layer of Lithium Niobate instead of PDMS, this will consent to increase the design possibility, as the two LN crystal could have different crystallographic orientation, and

moreover to increase the frequency of droplets production and the flux achievable as the closure layer is rigid and do not bend at high fluxes as PDMS.

2.2. Acknowledgements

This work would not be possible without the help of many people that contributed to the project in different ways. First of all I would like to thank my supervisor Prof. Cinzia Sada for the support and for the elevated degrees of freedom that she granted me. Then I would like to acknowledge my research group, the Lithium Niobate Group of the Department of Physics and Astronomy, and in particular Dr. Giacomo Bettella and Dr. Annamaria Zaltron without whom I would surely not be able to complete this multidisciplinary work; Dr. Marco Bazzan, Dr. Nicola Argiolas for the simulation and the Czochralski crystals, and Dr. Maria Vittoria Ciampolillo who started the work on the PPLNs and the waveguides, and Luca Bacci for the realization of the poling cells. Moreover I would like to thank Renzo Storti and the degree students Carlo Montevecchi e Riccardo Zambon for their good work.

Then a particular thank is due to the LaFsi group of the Department for the help in the closure of the channels and the characterization of the microfluidic devices and of the lithium niobate wettability, in particular Prof. Giampaolo Mistura, Dr. Matteo Pierno, Dr. Paolo Sartori, Dr. Enrico Chiarello, and Dr. Silvia Varagnolo. Therefore I would like to thank the Nonlinear Photonics Group of the Institute of Applied Physics of the University of Münster (Germany) of Prof. Cornelia Denz for the realization of the microfluidic channels using the femtosecond laser ablation. And Prof. Mathieu Chauvet of the University of Franche-Comté, Besançon (France) for the realization of the diced microchannel.

Finally I would acknowledge CARIPARO foundation for the economic support given with the Excellence Project 2011-2012.

Appendices

1. Optical damage resistance

An important target for Lithium Niobate optical applications is the increasing of optical stability under intensive illumination, in particular a protection against the optical damage. The doping of the crystal with several different ions (Mg^{2+}, Zn^{2+}, In^{3+}, Sc^{3+}, Hf^{4+}, Zr^{4+}) has been demonstrated a successful way for obtaining optical damage resistance Lithium Niobate crystals. These ions seems to vary the amount of the Nb antisites [1] and therfore control the Lithium Niobate defects. As a consequence, many optical properties depending on that defect could be altered by the doping with this optical damage resistant ions.

Magnesium: The first useful dopants which assure low optical damage with excellent optical transparency has been $LiNbO_3$:Mg [2]. A critical threshold concentration of 5 mol.% MgO was found for the congruent Lithium Niobate, above which the optical damage decrease of two orders of magnitude. Stability of $LiNbO_3$:Mg against pulse-laser intensities arrives up to 100 $MWcm^{-2}$ [3]. It has been observed that in Li-enriched $LiNbO_3$:Mg crystals the threshold of Mg concentration is lower, that because of fewer concentration of Niobium antisites, that decrease also the impurity concentration required to replace them. This effect is a prove of the role of these defects in optical property.

Zinc: $LiNbO_3$:Zn belong to the same bivalent family of the Magnesium doped crystals. Also Zinc shows an increased optical damage resistance [4], with a particularly strong effect at ZnO concentrations above 6 mol.% for the congruent melt [5]. Highly doped $LiNbO_3$:Zn crystals revealed no optical damage under irradiation with 532nm pulses of 10 ns up to 100 $mWcm^{-2}$ [4].

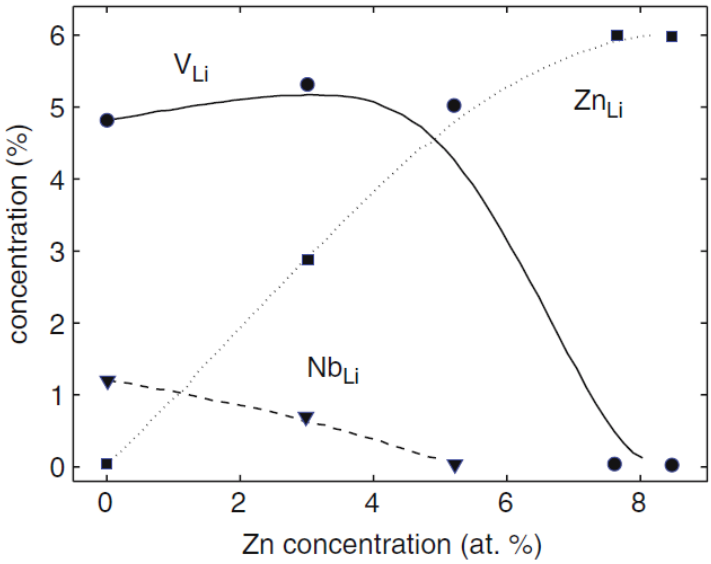

FIGURE 1 VARIATION OF LITHIUM VACANCY, NIOBATE ANTISITE AND ZINC ANTISITE DEFECTS IN FUNCTION OF ZINC CONCENTRATION

Magnesium and Zinc optical damage resistant ions operate as controllers of the concentration of the intrinsic defects Nb_{Li} and V_{Li} (Figure 1**Errore. L'origine riferimento non è stata trovata.**). As discuss in the previously optical properties, photorefractive effect and even ferroelectric coercive fields depending on the variation in the intrinsic defect structure. Moreover, it has been observed that Fe impurities and Fe_{Nb}^{3+} centers appear in the crystal during the substitution of Nb_{Li} by Mg [6]. The change of the Fe^{3+} lattice site is another important cause of the origin of the optical damage resistance, in fact, as previous discuss, Fe_{Li}^{3+} in the congruent $LiNbO_3$ is the dominant electron trap. The alteration of the Fe^{3+} lattice with the decreasing of the Niobium antisite affect the charge transport properties and so the photorefrective effect.

Trivalent ions (In^{3+}, Sc^{3+}): Another family of optical damage resistance ions is composed of In^{3+} and Sc^{3+}[1]. This dopants ensure a drastic decrease of the photorefraction at concentration below 2mol.% oxides for the congruent melt. The effect of 1,7 mol.% In_2O_3 [7] and 1,5 mol.% Sc_2O_3 [8] is comparable to the effect of 4,5–5 mol.% MgO.

Tetravalent ions (Hf^{4+}, Zr^{4+}): $LiNbO_3$:Zr is the most recently investigated optical-damage-resistant composition [9], with a threshold of elevated optical damage resistance at concentration of

less than 2 mol.% ZrO_2. $LiNbO_3$:2%Zr crystals show no optical damage up to intensities of 20 $MWcm^{-2}$ [I], in Figure 2 a comparison between Mg, Zr and cLN is reported in order to prove the optical-damage resistance of Zr [10]. The threshold for Hf is about 2 mol.% in the crystal [1]. A reduction of the photorefractivity in $LiNbO_3$:Hf and $LiNbO_3$:Zr with concentrations of Hf or Zr [9] above the thresholds is more pronounced than in $LiNbO_3$:6.5%Mg for equal light intensities.

Difference in the threshold of ions with different valences may be explained in terms of charge compensation effects. No speculation can be proposed concerning the incorporation of the Hf and Zr in the crystal lattice, except for the observation of the occupation of Li sites with Hf ions at low concentrations , it is probably that at high concentrations it occupies both cation sites [1].

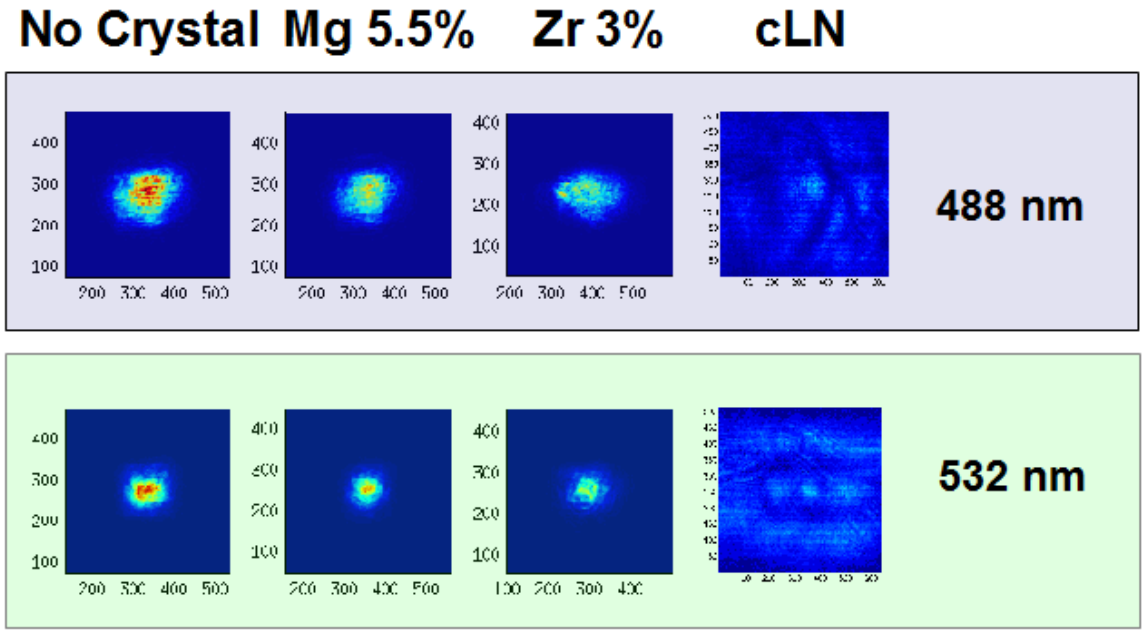

FIGURE 2 COMPARISON OF THE LASER TRANSMISSION BETWEEN CONGRUENT, ZIRCONIUM DOPED, AND MAGNESIUM DOPED LITHIUM NIOBATE AT TWO DIFFERENT WAVELENGTHS. THE EFFECT OF THE OPTICAL DAMAGE IS VISIBLE ONLY FOR THE CONGRUENT LITHIUM NIOBATE CRYSTAL[11].

2. Quasi-Phase Matching

We anlyze SHG as a second-order non linear interaction. We assume low conversion efficiency, loose focusing, long-pulse interaction and no losses for the fundamental or second harmonic waves. The varying amplitude equation governing the growth of the SH field under this conditions is

$$\frac{dE_{2\omega}}{dz} = \Gamma d(z)\exp(-i\Delta k' z)$$

EQUATION 1

$$\Gamma = \frac{i\omega E_{\omega}^2}{n_2 c}$$

EQUATION 2

Where $E_{2\omega}$ is the SH field amplitude and E_{ω} the fundamental, z the distance along the propagation direction, d(z) the spatially varying nonlinear coefficient for SHG. Δk', the wave vector mismatch caused by dispersion in the material, is defined by $\Delta k' = k_{2\omega} - 2k_{\omega} = \pi/l_c$ where l_c is the coherence length: $l_c = \lambda/4(n_{2\omega} - n_{\omega})$. Integrating Equation 3, we find that SH field at the end of a sample of length L is given by

$$E_{2\omega}(L) = \Gamma \int_0^L d(z)\exp(-i\Delta k' z)\, dz$$

EQUATION 3

For perfect phase matching Δk'=0 and $d(z)=d_{eff}$, so SH electric field wil be

$$E_{2\omega}(L) = \Gamma d_{eff} L$$

EQUATION 4

So the intensity grows quadratically with the sample length.

For QPM interaction we consider the Fourier transform approach. Let us write the normalized form of d(z) as $g(z) = d(z)/d_{eff}$ with g(z) between -1 and 1 for z between 0 and L. Than Equation 4 takes the form

$$E_{2\omega}(L) = \Gamma d_{eff} L G(\Delta k')$$

EQUATION 5

Where G(Δk') is the Fourier transform of g(z) given by

$$G(\Delta k') = \frac{1}{L}\int_0^L g(z)\exp(-i\Delta k' z)dz$$

EQUATION 6

If g(z) is a function periodic in z with period Λ, than

$$g(z) = \sum_{m=-\infty}^{\infty} G_m \, e^{i\,K_m z}$$

EQUATION 7

Whose mth-harmonic grating wave vector

$$K_m = \frac{2\pi m}{\Lambda}$$

EQUATION 8

Is close to Δk', so the integral in Equation 6 is dominated by this mth term, and thus Equation 5 can be written

$$E_{2\omega} \approx \frac{iexp(-\frac{\Delta k L}{2})}{\Gamma} d_Q L sinc(\Delta k L/2)$$

EQUATION 9

Where $d_Q = d_{eff} G_m$ is the amplitude of the relevant harmonic of d(z).

$$\Delta k \equiv k_{2\omega} - 2k_{\omega} - K_m$$

EQUATION 10

Is the total wave vector mismatch, and sinc(x)= sin(x)/x. So the behavior of QPM interaction is similar to that of a conventionally phase-matched interaction, but with an effective mismatch Δk shifted of K_m with respect to $\Delta k'$, and an effective non linear coefficient d_Q in place of d_{eff} .

Assuming $\Delta k' = K_m$, than

$$G_m = \frac{2}{\pi m}\sin(\pi m D)$$

EQUATION 11

With D the Duty Cycle $D = l/\Lambda$, so since $d_Q = d_{eff} G_m$ then, if m=1 we would have maximum of d_Q at D=50%. With d_Q^2 proportional to the conversion efficiency.

Bibliography

[1] T. Volk and M. Wöhlecke, *Lithium Niobate*, vol. 115. Berlin, Heidelberg: Springer Berlin Heidelberg, 2008.

[2] G.-G. Zhong, J. Jin, and Z.-K. Wu, "Measurements of optically induced refractive-index damage of lithium niobate doped with different concentrations of MgO," *J. Opt. Soc. Am.*, vol. 70, p. 631, 1980.

[3] D. A. Bryan, R. Gerson, and H. E. Tomaschke, "Increased optical damage resistance in lithium niobate," *Appl. Phys. Lett.*, vol. 44, no. 9, p. 847, 1984.

[4] T. R. Volk, V. I. Pryalkin, and N. M. Rubinina, "Optical-damage-resistant LiNbO_3:Zn crystal," *Opt. Lett.*, vol. 15, no. 18, p. 996, Sep. 1990.

[5] Y. Zhang, Y. . Xu, M. . Li, and Y. . Zhao, "Growth and properties of Zn doped lithium niobate crystal," *J. Cryst. Growth*, vol. 233, no. 3, pp. 537–540, Dec. 2001.

[6] G. I. Malovichko, V. G. Grachov, and E. P. Kokanyan, "Low-symmetry Fe-Mg complexes in LiNbO 3 :Mg," *Ferroelectrics*, vol. 125, no. 1, pp. 289–294, Jan. 1992.

[7] T. R. Volk and N. M. Rubinina, "A new optical damage resistant impurity in lithium niobate crystals: Indium," *Ferroelectr. Lett. Sect.*, vol. 14, no. 1–2, pp. 37–43, May 1992.

[8] J. K. Yamamoto, T. Yamazaki, and K. Yamagishi, "Noncritical phase matching and photorefractive damage in Sc2O3:LiNbO3," *Appl. Phys. Lett.*, vol. 64, no. 24, p. 3228, 1994.

[9] Y. Kong, S. Liu, Y. Zhao, H. Liu, S. Chen, and J. Xu, "Highly optical damage resistant crystal: Zirconium-oxide-doped lithium niobate," *Appl. Phys. Lett.*, vol. 91, no. 8, p. 081908, 2007.

[10] G. Nava, P. Minzioni, W. Yan, J. Parravicini, D. Grando, E. Musso, I. Cristiani, N. Argiolas, M. Bazzan, M. V. Ciampolillo, A. Zaltron, C. Sada, and V. Degiorgio, "Zirconium-doped lithium niobate: photorefractive and electro-optical properties as a function of dopant concentration," *Opt. Mater. Express*, vol. 1, no. 2, p. 270, May 2011.

[11] G. Nava, P. Minzioni, I. Cristiani, N. Argiolas, M. Bazzan, M. V. Ciampolillo, G. Pozza, C. Sada, and V. Degiorgio, "Photorefractive effect at 775 nm in doped lithium niobate crystals," *Appl. Phys. Lett.*, vol. 103, no. 3, p. 031904, 2013.

List of Publications

- G. Pozza, S. Kroesen, G. Bettella, A. Zaltron, M. Esseling, G. Mistura, P. Sartori, E. Chiarello, M. Pierno, C. Denz, and C. Sada, "T-junction droplet generator realised in lithium niobate crystals by laser ablation", *Optofluidics microfluidics nanofluidics* 3, 34–42 (2014);
- G.Nava, P. Minzioni, I. Cristiani, N. Argiolas, M. Bazzan, M.V. Ciampolillo, G. Pozza, C. Sada, V. Degiorgio, "Photorefractive effect at 775 nm in doped lithium niobate crystals", *Applied Physics Letters* 103, 031904 (2013);
- M. Bazzan, M. Michieletto, L. Bacci, N. Argiolas, A. Zaltron, M.V. Ciampolillo, G. Pozza, C. Sada, "Giant increase of the photorefractive effect in lithium niobate: a novel approach", *Proceedings of SPIE Conference on Micro-Optics,* 84281X (2012).